TR 3205 S

Stellingen

behorende bij het proefschrift

Modelling of Amorphous Silicon Single- and Multi-Junction Solar Cells

door

J.A. Willemen

Delft, 16 oktober 1998

1. De 'mobility gap' van amorf silicium is binnen experimentele foutgrenzen gelijk aan de, met de methode van Tauc bepaalde, optische bandafstand.

   Dit proefschrit, hoofdstuk 6.

2. Het belang van de 'mobility gap' van amorf silicium manifesteert zich pas als de temperatuurafhankelijkheid van diode-karakteristieken beschouwd wordt.

   Dit proefschrift, hoofdstuk 4.

3. De voorwaartse stroom in een amorf-silicium *pin* diode wordt vrijwel uitsluitend door recombinatie in de depletielaag veroorzaakt. Ten onrechte wordt vaak op basis van de waarde van de diode-idealiteitsfactor geconcludeerd dat er ook sprake is van een aanzienlijke diffusiestroom.

   Dit proefschrift, hoofdstuk 4.

4. Het gebruik van de termen 'serie-weerstand' en 'shunt-weerstand' om de gradiënten in de stroom-spanningscurve van belichtte amorf-silicium zonnecellen bij respectievelijk de doorsnijding van de spannings- en stroom-as aan te geven, is verwarrend en daarom af te raden. De fysische oorzaak voor deze gradiënten is veelal niet aan weerstandseffecten toe te schrijven.

5. De generatie van door licht geïnduceerde defecten in amorf-silicium zonnecellen kan het best onderzocht worden door meting van diodestroom-karakteristieken in het donker.

   Dit proefschrift, hoofdstuk 4.

   B. Rech, *Solarzellen aus amorphem Silizium mit hohem stabilem Wirkungsgrad*, 1997.

6. Dunne amorf-silicium zonnecellen zijn stabieler dan dikke cellen; de juiste fysische verklaring hiervoor is niet dat er in dunne cellen minder recombinbatie optreedt, waardoor de generatie van meta-stabiele defecten lager is, maar dat in dunne cellen de invloed van die defecten op het omzettingsrendement kleiner is.

7. De term 'current matching', waarmee aangeduid wordt dat in beide deelcellen van een tandem-zonnecel een gelijke fotostroom wordt opgewekt, is ongelukkig gekozen, omdat — strikt genomen — de conditie van gelijke stromen ('matching currents') zich in een tandem-zonnecel met twee elektrische aansluitingen altijd voordoet.

8. De term 'Back Surface Field', waarmee het aanwezig zijn van een hogere dotering aan de achterzijde van een zonnecel wordt aangeduid, is niet correct, omdat de beoogde verbetering van het omzettingsrendement van dergelijke zonnecellen niet een veld- maar een diffusie-gerelateerd effect is.

9. Het beschouwen van het energie-bandendiagram en de quasi-Fermi-niveaus in plaats van de ladingsdragerconcentraties en het elektrische veld leidt veelal tot beter inzicht in de werking van een halfgeleider-component.

10. In tegenstelling tot wat vaak gesteld wordt[1–3], vindt in een tandem-zonnecel met een slechte tunnel-recombinatie-junctie geen ladings-accumulatie bij de genoemde junctie plaats.

    [1] M. von der Linden, *Electronic Defects in Amorphous Silicon Materials and Devices*, 1994.

    [2] D.S. Shen *et al.*, Appl. Phys. Lett. 56, pp. 1871–1873, 1990.

    [3] J. Dutta *et al.*, Proc. EPVSEC-11, pp. 545–548, 1992.

11. De schijnbare sprong die kan optreden in de quasi-Fermi-niveaus bij simulaties van voorwaarts ingestelde diodes met grote, abrupte sprongen in de geleidings- of valentieband, wordt veroorzaakt door een abrupte verandering van de gradiënt in de quasi-Fermi-niveaus. De consequentie van deze schijnbare sprong is dat de stroom bij een bepaalde aangelegde spanning kleiner is dan op grond van Shockley's theorie voor de ideale diode wordt verwacht.

12. Als de grenzen van de optische lithografie bereikt zijn, zal het eindelijk lonen te investeren in de betrouwbaarheid van software.

    G.D. Hutcheson *et al.*, Scientific American, Special issue vol. 8, nr. 1, pp. 66–73, 1997.

13. Helaas is de stelling bij het proefschrift van Den Boer[1], "Metingen aan amorfe halfgeleiders leveren zelden kristalheldere resultaten op," thans — 15 jaar later — nog glashard waar.

    [1] W. den Boer, *Interference Effects and Space-charge-limited Conduction in Amorphous Silicon Devices*, 1983.

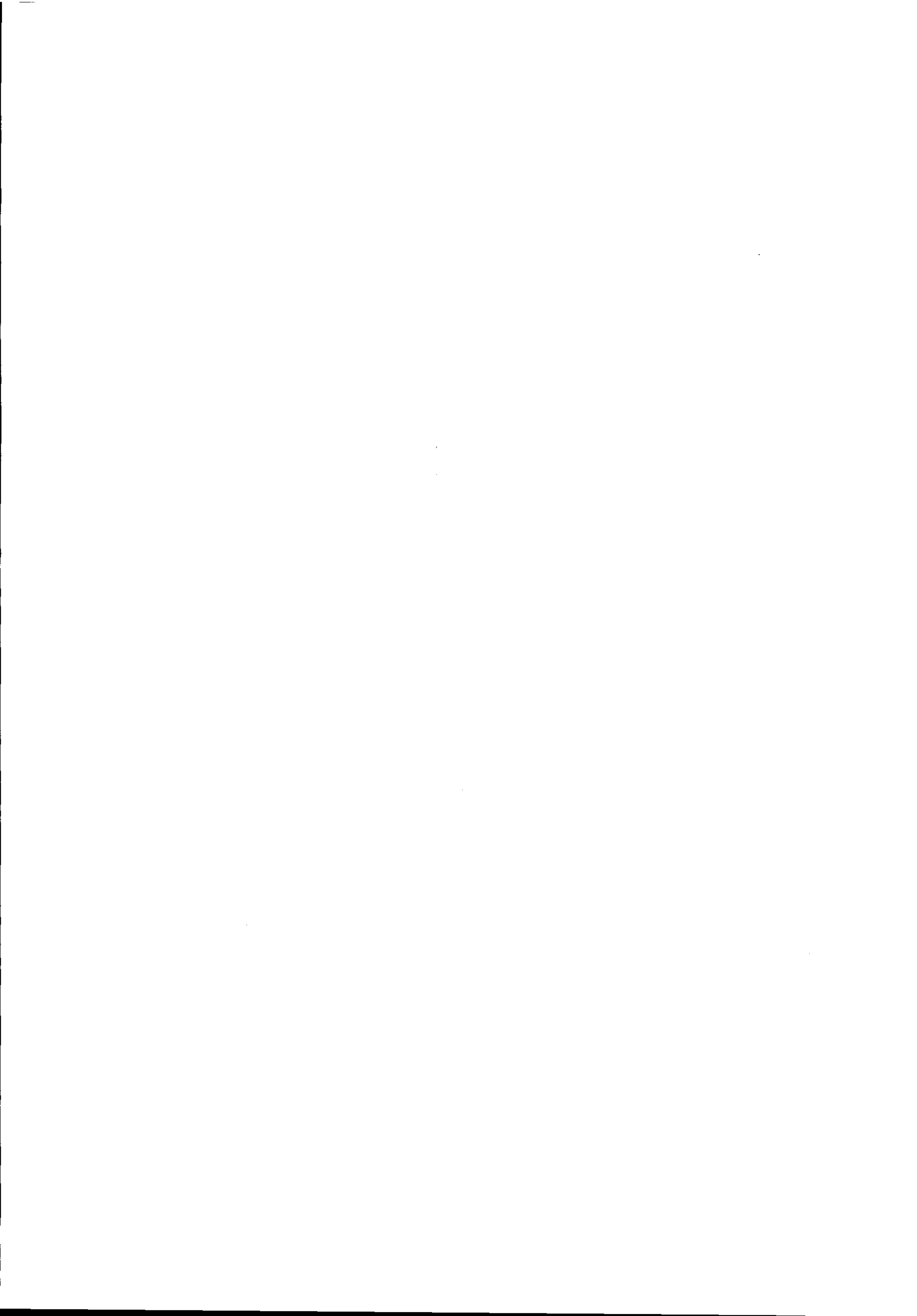

706963
3205
TR 3205

Modelling of Amorphous Silicon Single- and Multi-Junction Solar Cells

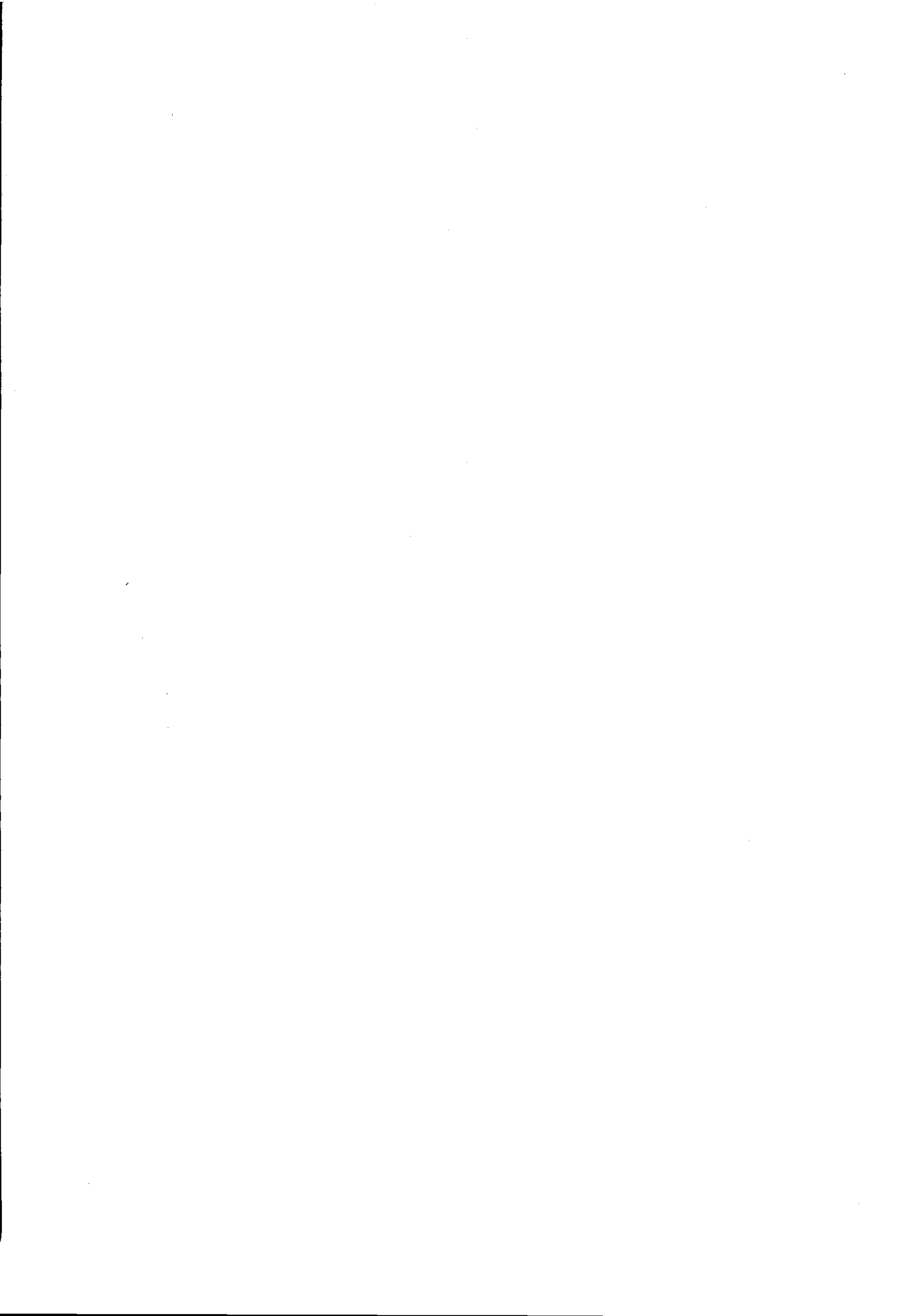

Modelling of Amorphous Silicon Single- and Multi-Junction Solar Cells

PROEFSCHRIFT

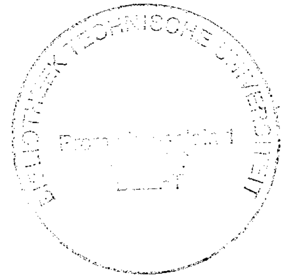

ter verkrijging van de graad van doctor
aan de Technische Universiteit Delft,
op gezag van de Rector Magnificus prof.ir. K.F. Wakker,
in het openbaar te verdedigen ten overstaan van een commissie,
door het College voor Promoties aangewezen,
op vrijdag 16 oktober 1998 te 10:30 uur

door

Joost Adriaan WILLEMEN

elektrotechnisch ingenieur

geboren te Schijndel

Dit proefschrift is goedgekeurd door de promotoren:

Prof.dr. M. Kleefstra
Prof.dr.ir. J.W. Slotboom

Samenstelling promotiecommissie:

Rector Magnificus	Voorzitter
Prof.dr. M. Kleefstra	Technische Universiteit Delft, promotor
Prof.dr.ir. J.W. Slotboom	Technische Universiteit Delft, promotor
Prof.dr. C.I.M. Beenakker	Technische Universiteit Delft
Prof.dr. W.C. Sinke	Universiteit Utrecht
Dr. R.E.I. Schropp	Universiteit Utrecht
Dr. M. Zeman	Technische Universiteit Delft
Dr. C. Beneking	Rheinisch-Westfälische Technische Hochschule Aachen
Prof.dr. W.Th. Wenckebach	Technische Universiteit Delft, reservelid

Dit werk is mede tot stand gekomen door financiële ondersteuning van de Nederlandse Onderneming voor Energie en Milieu (NOVEM).

Willemen, J.A.
Modelling of Amorphous Silicon Single- and Multi-Junction Solar Cells/
J.A. Willemen, PhD. thesis Delft University of Technology. - With ref. -
With summary in Dutch.

ISBN 90-9011963-9

COPYRIGHT ©1998 by J.A. Willemen

All rights reserved.

No part of this publication may be reproduced, stored in a retrieval system, or transmitted in any form or by any means — optical, electronic, magnetic, mechanical, photocopying, or any other recording system — without the prior written permission of the copyright owner.

Aan Kirstin, Felien en Jiri

Contents

1 Introduction 1
1.1 Background and motivation 1
1.2 Amorphous silicon solar cells 5
1.3 Material and solar cell characterisation 21
1.4 Modelling of amorphous silicon solar cells 28
1.5 Scope and outline of this thesis 34

2 Review of amorphous silicon solar cell simulation models 37
2.1 Transport equations 37
2.2 Modelling of the gap states 40
2.2.1 Recombination and charge trapping in an arbitrary distribution of states 45
2.2.2 Recombination and trapping modelling of *a*-Si:H gap states 47
2.3 Charge trapping, recombination and thermal generation modelling 48
2.3.1 Shockley-Read-Hall recombination statistics 48
2.3.2 Taylor and Simmons approximation 51
2.3.3 Recombination and charge trapping at amphoteric states . 56
2.3.4 Amphoteric states modelled by a pair of uncorrelated states 60
2.3.5 Trap-assisted tunnelling recombination model 61

3 Simulation program for amorphous silicon devices: ASA 65
3.1 Simulation modes 65
3.2 Definition of the simulation structure 66
3.3 Heterojunctions 67
3.4 Mobilities 67
3.5 Doping profile 67
3.6 Recombination and charge trapping models 68
3.7 Contact models 69
3.8 Optical models 70

3.9 Temperature-dependent models 71
3.10 Numerical and implementational aspects 72
3.11 Other features 74

4 Amorphous silicon solar cell model parameters 75
4.1 Qualitative discussion of distribution of active recombination states in *pin* structures 76
4.2 Analytic analysis of model parameter dependences 87
4.2.1 Derivation 88
4.2.2 Numerical examples 93
4.2.3 Discussion 98
4.3 Assessment of the abrupt mobility edge approximation 100
4.4 Model parameter sensitivities 103
4.5 Parameter extraction by inverse modelling 115
4.5.1 Inverse modelling 116
4.5.2 Calibration exercises 118
4.5.3 Discussion 124
4.5.4 Proposed additional experiments 127
4.5.5 Conclusion 130

5 Modelling of amorphous silicon tandem cells 131
5.1 Device physics of tandem cells and tunnel recombination junctions 131
5.1.1 Operating principles of a tandem cell 131
5.2 Review of tunnel-recombination junction technologies 142
5.3 Review of tandem cell models 145
5.4 New model for tandem cells 148
5.5 Modelling of tandem cell degradation 153

6 Experiments for modelling 157
6.1 Accurate measurements of dark and light *IV*-curves 157
6.1.1 Lateral leakage currents in *a*-Si:H *pin* cells 158
6.1.2 Influence of trap charging on dark *IV*-measurements . . . 160
6.1.3 Influence of lateral leakage currents on low illumination level *IV*-measurements 165
6.1.4 Accurate measurements of tandem cell *IV*-characteristics . 167
6.2 Extraction of mobility gap 168
6.3 Stability of back contacts 169

7 Conclusions 175

A List of symbols **181**

B Comparison of different physical models **185**

B.1 Shockley-Read-Hall vs. Taylor and Simmons approximation . . . 185

B.2 Amphoteric dangling bonds model vs. decoupled approach 189

References **195**

Summary **211**

Samenvatting **213**

Acknowledgements **217**

Biography **219**

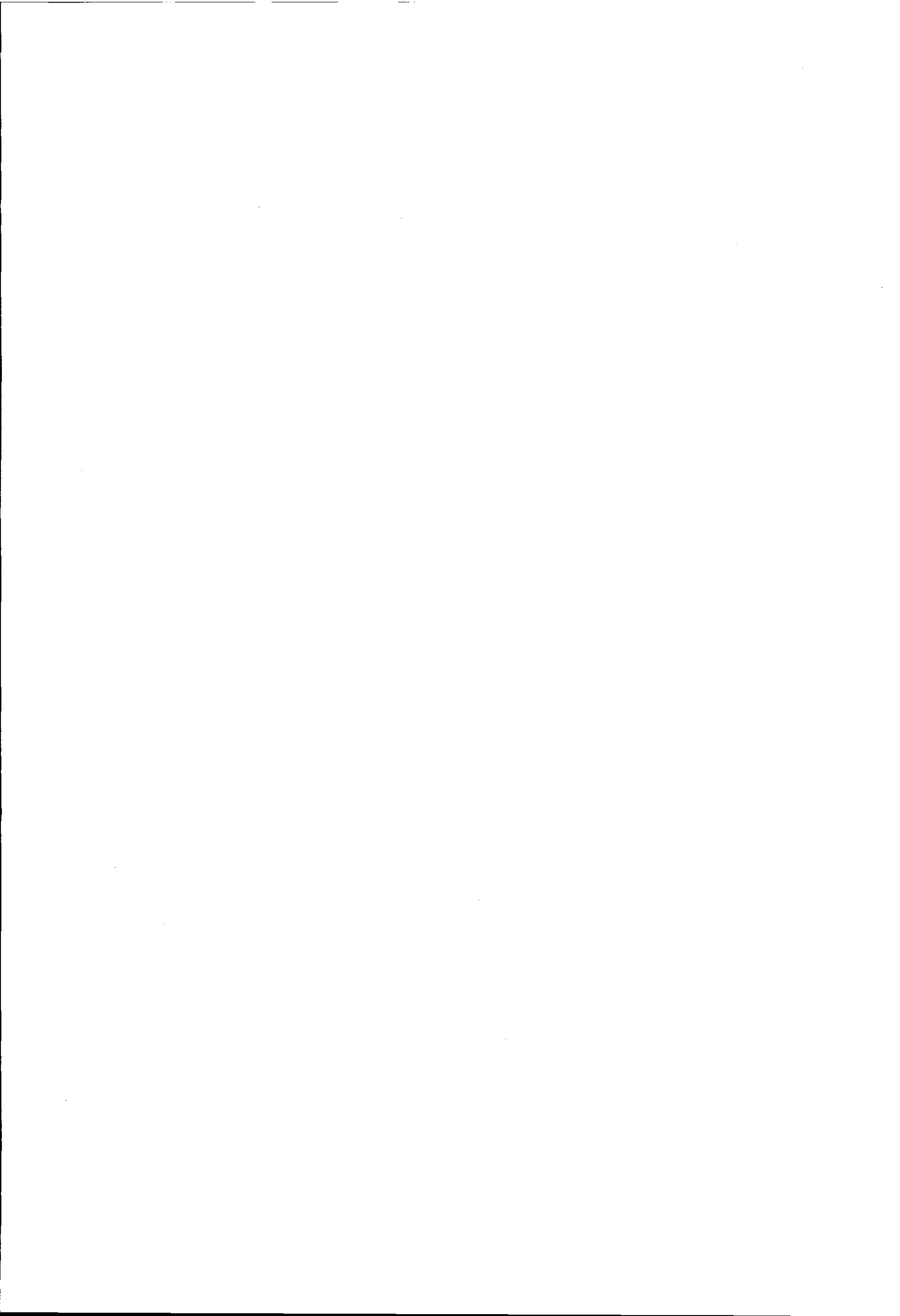

Chapter 1

Introduction

This thesis is the result of research on hydrogenated amorphous silicon solar cells. In this chapter we give a general introduction. After a short discussion of the social relevance of solar cell research we introduce hydrogenated amorphous silicon as a semiconductor for photovoltaic applications. Subsequently, we discuss the basics of amorphous silicon solar cells, followed by short introductions to solar cell characterisation methods and solar cell device modelling. Finally, we present the outline of the rest of this thesis.

1.1 Background and motivation

The present-day awareness of the environmental risks and limited availability of fossil and nuclear fuels is a strong driving force for the search for renewable energy sources. Unless a drastic change takes place in the ways energy is produced, a sustaining growth of the world's economy and a more equal spread of welfare amongst all world's nations is threatened. This awareness has given a large impulse to the research in the field of tomorrow's energy sources, comprising sources as hydro-power, biomass, wind energy and photovoltaics.

By photovoltaic power conversion the light of the sun is transformed directly into electrical energy. This process occurs inside a solar cell and does not involve moving parts or use fuel. Furthermore, the conversion process does not produce waste products. Therefore, photovoltaic energy can be considered as a clean energy source if the following conditions are fulfilled: (1) the materials used for the solar cell module production must be environmentally harmless, and (2) the production process must use significantly less energy than is generated during the operational life of the module. Since — on the time scale of human evolution — the energy supply of the sun is eternal, photovoltaic solar power can be considered

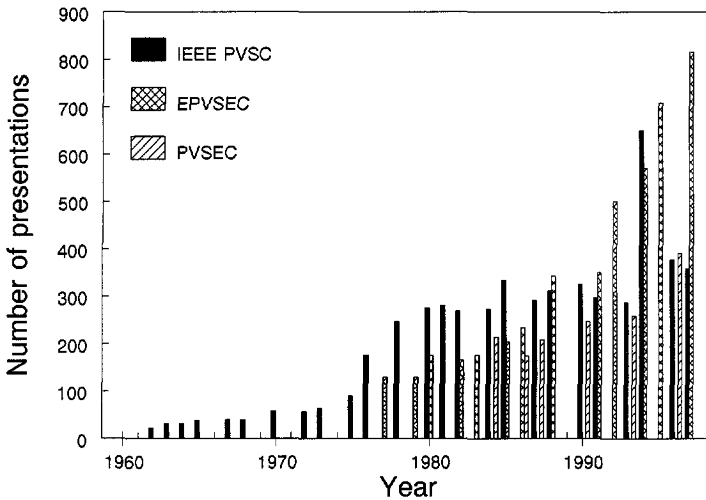

Figure 1.1: Overview of the number of papers presented at the three large international photovoltaic conferences: IEEE-PVSC, Photovoltaic Specialists Conference; EPVSEC, European Photovoltaic Solar Energy Conference; and PVSEC, Photovoltaic Science and Engineering Conference.

as an unlimited source of energy.

In the past two decades interest in photovoltaic power has grown continuously. This is — for instance — reflected in the strongly increasing number of papers presented at the three large international scientific conferences on photovoltaic power conversion (Fig. 1.1). Note the strong increase in the mid-1970's; after the oil crisis many countries have started research activities in the field of photovoltaics because they recognized the potential of solar energy as an alternative for conventional fuels. Before this time, photovoltaic power was mainly used in space applications (satellites), as the contents of the older conference proceedings reflect.

The extensive research and development activities in the past decades have led to a certain level of maturity of solar cells technologies. The state-of-the art solar cells have a much higher conversion efficiency than those of two decades ago. For example, the first amorphous silicon solar modules for commercial applications had an efficiency of 2–2.5%, as presented by Sanyo Electric Co. in 1980 [69]. Present commercial module production at United Solar Systems Corp. is targeted at more than 10% efficiency [39]. At the same time the cells have become less expensive. Nevertheless, the price of photovoltaic energy is still about 5 times higher than the present-day cost of electrical energy produced with traditional sources. This means that it is not yet economically appealing to apply

photovoltaic conversion as a large-scale utility power source in the industrialised world. On the other hand, the following applications are already economically viable: powering of portable consumer products, electrification of rural areas without connection to the electricity grid, local electricity production in developing countries for domestic lighting, communication apparatus, water pumping, refrigeration, etc.

Presently, we see a shift from governmentally funded research towards a strong expansion of industrial activity. As examples of this we can mention:

- United Solar Systems Corp. and Solarex started new production lines in 1997 with annual capacities of 15 MW [39] and 10 MW [19], respectively.
- Shell has founded a new business unit for renewable energy production and has increased its Dutch solar module production capacity to 5 MW/year; further production units with a 20–25 MW capacity are projected for the future [144].
- Akzo Nobel started ambitious activities which target at a production capacity of 70 MW to be realised in 5 years [61].

These numbers reflect a substantial increase in production capacity, if we compare them with the total world production of photovoltaic modules that amounted to 70 MW in 1994. The reasons [144] for this increased industrial interest are:

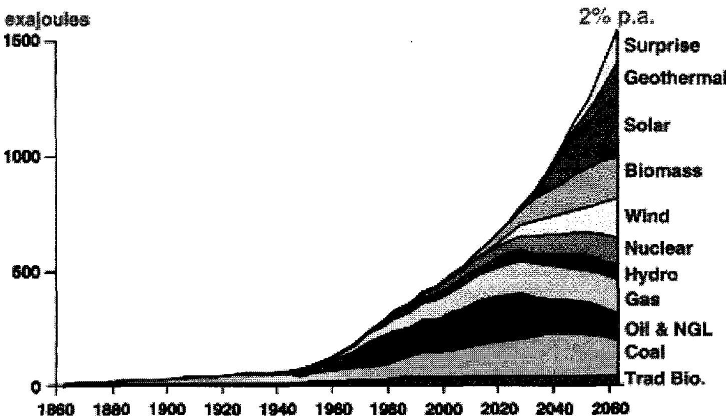

Figure 1.2: Forecast of diversification of energy sources in the first half of the 21st century [144].

(1) photovoltaic technology has reached a level of maturity; (2) large industrial companies have become aware of the enormous commercial potential of photovoltaics (see Fig. 1.2); and (3) it is expected that producing solar panels in large quantities will result in a considerable decrease of the cost of solar energy. Shell expects a 70% reduction of the price for photovoltaic energy over the next 10 years [144]. This opens a new era for large scale application of a clean energy source.

To obtain insight in the numbers large-scale photovoltaic energy production involves, we carry out some simple calculations. Let us consider the situation in the Netherlands, where the sun shines about 1000 hours per year, and let us estimate the maximum price of a photovoltaic power system that can be competitive with conventional electricity. For non-industrial users the electricity price is currently about Dfl 0.22 per kWh. If we assume a solar irradiation of 1000 W per square meter and a 10% system conversion efficiency, a photovoltaic installation (consisting of solar modules and all additional systems) is capable of generating 100 kWh per square meter per year. If we estimate a lifetime of 15 years, the maximum price of a photovoltaic system is approximately Dfl 330,- per square meter area of solar panel. The maximum *system price* per Watt delivered power is Dfl 3.30. The system price includes: cost of the solar panel and additional systems, installation and maintenance costs and in some cases the cost of the occupied land and the cost of energy storage systems[1].

As another example we calculate the total area of solar cells needed to generate all electrical power consumed in the Netherlands. The total electricity consumption in 1995 amounted $75 \cdot 10^9$ kWh [32]. If we assume the power generation per unit area of solar module as estimated above, an area of 750 square kilometers of solar panels must be installed. Although one square meter of solar panel will in general occupy more than one square meter of land (shadowing by neighbouring cells must be avoided) it is illustrative to compare this with the total area of the Netherlands: the required 750 km^2 corresponds to 1.8%.

As a final example we compute the area of solar panels required to produce the annual electricity consumption of the household of the author. Again we use the results calculated above and find that, for the 1700 kWh/year, 17 square meters of solar panels are required.

[1]This is a rather rough estimation. In a more accurate estimation one should account for: (1) price rises of conventional electricity, interest and inflation rates; (2) a module with a fixed orientation cannot continuously capture the highest flux density of solar energy; and (3) the fluctuation in solar irradiation with the time of year.

1.2 Amorphous silicon solar cells

The basic principle of photovoltaic conversion is the generation of an electron-hole pair in a semiconductor after absorbing a photon, and the subsequent separation and collection of the generated charge carriers. This gives rise to an electric current and voltage, thus to power generation. This process can take place in a suitable semiconductor material, such as silicon (Si), gallium-arsenide (GaAs), cadmium telluride (CdTe) or copper indium diselenide ($CuInSe_2$). Silicon occurs in different forms which are suitable for photovoltaics. In order of decreasing electronic quality and decreasing cost, these forms are mono-crystalline silicon, poly-crystalline silicon and hydrogenated amorphous silicon (*a*-Si:H). The latter material is the semiconductor used for the solar cells that are the subject of this thesis.

Historic overview of amorphous silicon solar cells

Shortly after Spear and LeComber [121] reported that the conductivity of *a*-Si:H could be changed effectively by introducing dopants such as boron and phosphorus, the first amorphous silicon solar cells were made. Carlson and Wronski reported the first solar cell with 2.4% efficiency in 1976 [20]. The structure of this cell was a *pin* diode consisting of an intrinsic *a*-Si:H layer of about 1 μm thickness that is sandwiched between a *p*- and *n*-doped layer with thicknesses of several tens of nanometers. This achievement has initiated a period of increased interest in *a*-Si:H solar cells during which conversion efficiencies increased rapidly. In 1977, a Pt-*a*-Si:H Schottky barrier solar cell was reported with an efficiency of 5.5% [18, 21]. In the same year Staebler and Wronski published their findings about the metastable behaviour of *a*-Si:H [122]. Prolonged illumination of amorphous silicon degrades the electrical conductivity, but this can be fully restored by an annealing step at temperatures of about 150 °C. This effect is ascribed to the creation of light-induced metastable defects that can degrade the solar cell efficiency by 10% to 50% of its initial efficiency. This behaviour is named the *Staebler-Wronski effect* after the researchers who first reported it. Its discovery led to the search for materials with better stability or solar cells designs that are less susceptible to material degradation. One of the approaches for obtaining highly efficient stable cells is the multi-junction cell concept. In these cells two or three *pin* cells are stacked on one another, thus forming a monolithic, multi-layered structure. Hamakawa [50] reported the first multi-junction cell in 1979. The research activities of the past two decades have led to a world-record efficiency of small, laboratory-scale cells of 14.3% initial and 13% stabilised efficiency [152]. In the field of the large area cells the present-day record is 11.8% initial and 10.2% stabilised efficiency on one square foot area [40].

Amorphous silicon based materials for solar cell applications

Due to its amorphous nature the electronic properties of hydrogenated amorphous silicon are quite different from those of crystalline silicon. The differences in atomic structure and the consequences for the electronic properties are discussed with the help of Fig. 1.3. Figure 1.3a shows the structure of crystalline silicon schematically. Each atom is covalently bonded to four neighbours; all bonds have the same length and the angles between the bonds are equal. From the figure it is obvious that we can distinguish a *unit cell*, which is repeated periodically. In contrast, amorphous silicon does not have this ordered structure, as depicted schematically in Fig. 1.3b. Nevertheless, on a local atomic scale there is a

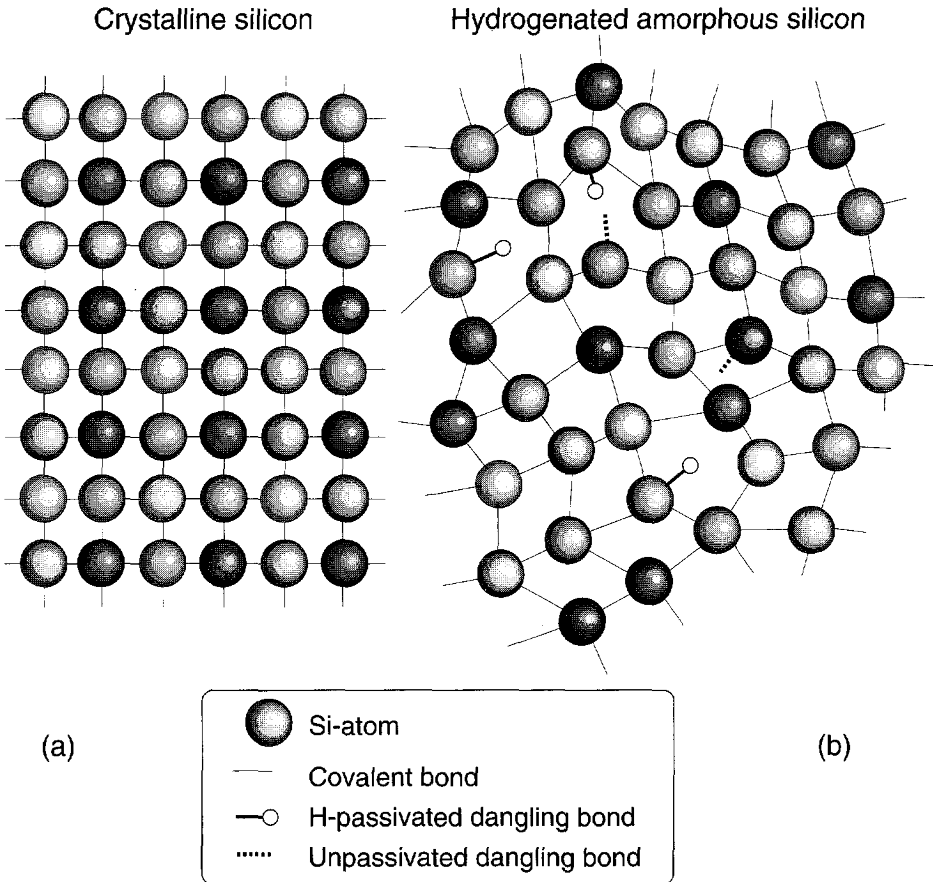

Figure 1.3: Schematic drawing of the atomic structure of: (a) crystalline silicon; (b) hydrogenated amorphous silicon.

resemblance to crystalline silicon: most of the atoms have covalent bonds with four neighbours. This local order gives *a*-Si:H its semiconducting properties. However, small deviations in bond angles and lengths occur in amorphous silicon. Due to these deviations the orderly structure, that is present locally, is completely lost when the separation between atoms exceeds a few atomic distances. Instead of a periodic structure, we now have a random, disordered network. In the random network of amorphous silicon, defects are present in the form of silicon atoms that have only three covalent bonds with neighbours. The fourth bond is a so-called dangling bond. Some of these defects are shown in Fig. 1.3b. In *un-hydrogenated* amorphous silicon, the dangling bond concentration is in the order of 10^{19}–10^{20} cm^{-3} [86], which renders this material quite useless for electronic applications (for reasons that will be apparent shortly). Atomic hydrogen can passivate dangling bonds effectively; it can be built into the network during material deposition or by a post-deposition treatment. High-quality *hydrogenated* amorphous silicon contains in the order of 1–10% atomic hydrogen. Most of this hydrogen is bonded at sites where so-called strained or weak bonds were broken; strained or weak bonds are bonds with lengths and/or angles that are far from the energetically optimal values, as are present in crystalline silicon. However, the most important effect is that the dangling bond concentration is reduced to values around 10^{15}–10^{16} cm^{-3}. Figure 1.3b shows a few hydrogen-passivated dangling bonds as well.

The periodic structure of crystalline silicon gives rise to an energy band of free electron states (conduction band) and a band of free hole states (valence band). The separation between the sharply defined bottom of the conduction band and the top of the valence band is the bandgap, which has a value of 1.12 eV in silicon at room temperature. Ideally, the bandgap does not contain energy states that can be occupied by electrons. As shown in Fig. 1.4 this is not the case in hydrogenated amorphous silicon. Due to the local order there is a valence and a conduction band present in *a*-Si:H (region I and V in the figure). However, instead of sharply defined band edges, these have tails entering into the bandgap (regions II and IV). These tails are caused by the lacking periodicity (the *disorder*) of the amorphous network. Further, the dangling bonds cause electronic states in the central region of the bandgap (region III). As is apparent from the figure there is a quasi-continuum of electronic states in the bandgap of *a*-Si:H.

The electron and hole wavefunctions in the extended states (regions I and V) are non-localised, hence the carriers can be considered as free carriers. However, as soon as an electron occupies a state in the conduction band tail below E_c its wavefunction becomes localised and its mobility decreases strongly, as Fig. 1.4b depicts. The same applies to holes in the valence band tail. The energies E_c and

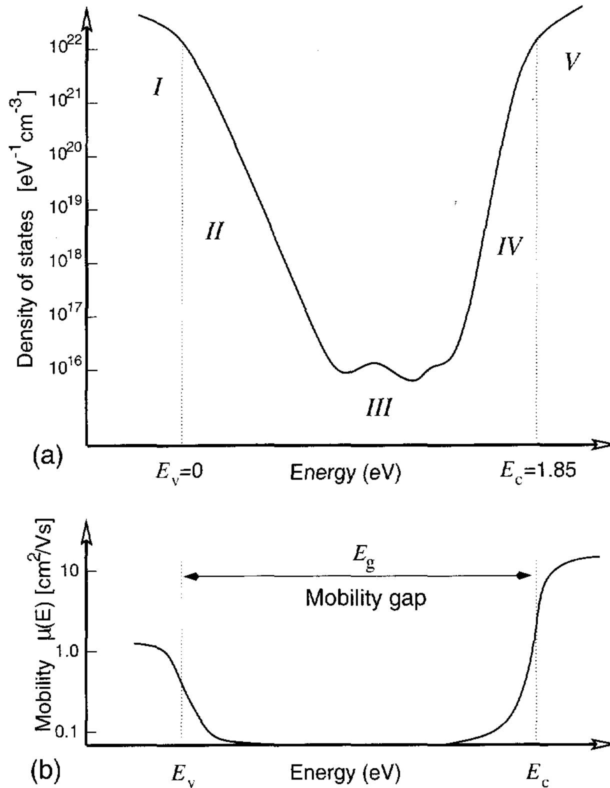

Figure 1.4: (a) Schematic representation of the density of states in hydrogenated amorphous silicon. Region I: extended valence band states, Region II: valence band tail states, Region III: dangling bond defect states, Region IV: conduction band tail states. Region V: conduction band extended states. (b) Schematic graph of the electron and hole mobilities as a function of energy in *a*-Si:H.

E_v are called the conduction band and valence band mobility edge, respectively, and form the boundary between the localised gap states and extended band states. Since we may expect that carriers in states deep in the tails are more localised than in states close to the mobility edges, the transition from localised to extended states will be gradual. Consequently, the mobility edges are not sharply defined and the mobility as a function of energy will be increasing smoothly, as is shown schematically in Fig. 1.4b. However, details about the change of the mobilities around the mobility edges are not known, since there is no way to measure the mobilities as a function of electron energy. The mobility edges define the bandgap of amorphous silicon. This gap is generally denoted by the term *mobility gap*, because the presence of a considerable density of electronic states conflicts with the term bandgap. The mobility gap of *a*-Si:H is larger than the bandgap of crystalline silicon. Generally, a value of about 1.85 eV is assumed for the mobility gap in device quality *a*-Si:H; its precise value depends on the hydrogen content. However, in this work we will show that this value is too high: from experiments we have extracted a mobility gap of 1.70 to 1.75 eV (see Sect. 6.2). In *a*-Si without hydrogen the mobility gap is about 1.6 eV [86].

Due to the disorder in the material the mobilities of the charge carriers in the extended states are about two orders of magnitude lower than in crystalline silicon. Typically, the electron mobility is 10 cm^2/Vs, and the hole mobility is 1 cm^2/Vs.

For a long time, researchers assumed that the electronic properties of amorphous silicon could not be changed by doping with group III and V elements such as boron, phosphorus, and arsenic. It was predicted that dopants would be built into the amorphous network with their optimal valency, instead of at a fourfold-coordinated substitutional location. However, the results of Spear and LeComber showed the contrary [121]. They succeeded in changing the conductivity of *a*-Si:H by adding to the silicon source gas, silane, up to 1 volume % of phosphine or diborane (a short overview of deposition of *a*-Si:H will be given below). Nevertheless, the doping efficiency of *a*-Si:H is low: in heavily doped *a*-Si:H only a small fraction (about 1%) of all dopant atoms occupies a fourfold-coordinated location and is active as a dopant [126]. Because the density of localised tail states is high, it is impossible to move the Fermi level closer to the conduction band mobility edge than approx. 150 meV and 300 meV to the valence band mobility edge. In combination with the low carrier mobilities in the extended states this explains the low conductivity of doped *a*-Si:H (typically 10^{-2} S/cm for *n*-type and 10^{-5} S/cm for *p*-type *a*-Si:H). An important effect related to doping of *a*-Si:H is the doping-induced defect creation [126]. The defect density increases with increasing concentration of dopants.

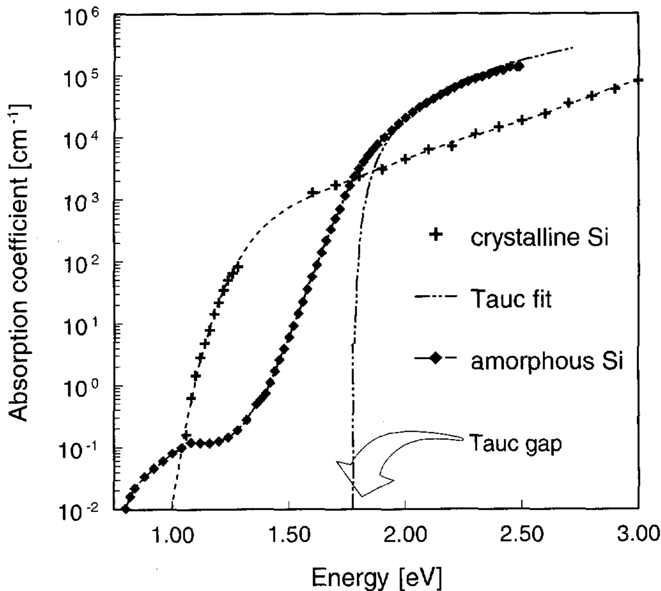

Figure 1.5: Absorption spectra of hydrogenated amorphous silicon and crystalline silicon. Absorption data of crystalline silicon from Ref. 31.

In contrast to crystalline silicon, which is an indirect bandgap semiconductor, *a*-Si:H has a direct bandgap. The lack of long range order is the reason why the crystal momentum $\vec{k}$ is not a proper quantum number. Therefore, no conservation of crystal momentum is required for an optical transition of an electron from the valence band to the conduction band. As a consequence *a*-Si:H is a better absorber for visible light than crystalline Si, which the higher absorption coefficient in the energy range above 1.75 eV reflects (Fig. 1.5). The optical bandgap of the material can be extracted from the absorption spectrum. Various definitions of the optical bandgap exist; the Tauc gap is most commonly used (to be defined in Eq. 1.3, page 23). It is generally assumed that the optical gap of *a*-Si:H is about 0.1-0.2 eV smaller than the mobility gap[2]. However, in Sect. 6.2 of this thesis we show that the mobility gap is approximately equal to the optical bandgap. Typical values of the Tauc gap are in the range of 1.70–1.75 eV. The importance of the optical gap is that it can be used to estimate the minimum energy of photons that are absorbed and contribute to the photovoltaic conversion. With decreasing optical bandgap an increasing part of the solar spectrum is absorbed. Figure 1.6

[2]In this thesis often the 'generic' term *bandgap* will be used if there is no explicit need to differentiate between the *mobility gap* and *optical bandgap*.

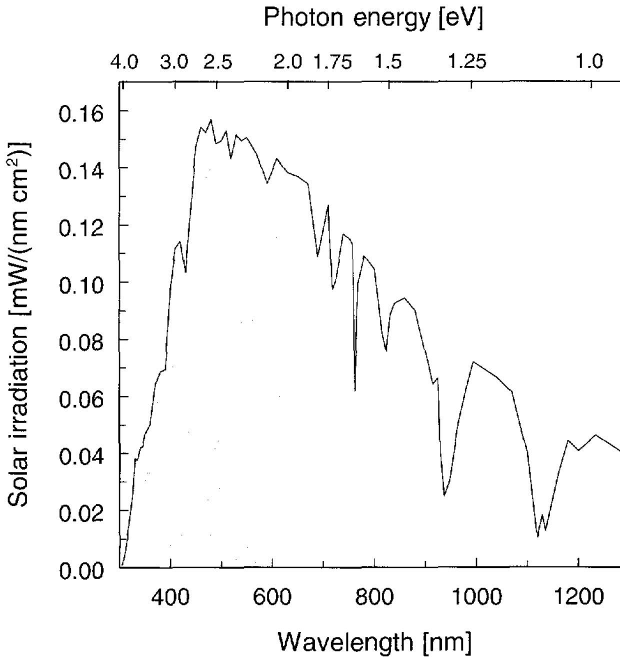

Figure 1.6: Spectral irradiance of the AM1.5G spectrum. Amorphous silicon with an optical bandgap of 1.71 eV can absorb half of the energy of the AM1.5G spectrum; this is indicated by the shaded area. Data after Hulstrom *et al.* [59].

shows the standard solar spectrum, the Air Mass 1.5 Global (AM1.5G) spectrum, which has a normalised total irradiation of 100 mW/cm^2. Half of the power is due to photons with energies exceeding 1.71 eV, which are strongly absorbed in *a*-Si:H. Information about the tail states and the defect states can be obtained from the absorption of photons with less energy than the optical bandgap (*i.e.* the *sub-bandgap* absorption). The exponential part of the absorption spectrum just below the bandgap energy (between 1.4 and 1.7 eV in Fig. 1.5) is called the Urbach edge and is correlated with the width of the valence band tail. The midgap defect states give rise to absorption in the energy range below 1.4 eV.

State-of-the-art amorphous silicon-based solar cells do not only contain silicon as the semiconducting material; nowadays, the amorphous silicon-based materials encompass a large group of related materials as well. To name a few: micro-crystalline silicon (μc-Si); alloys of hydrogenated amorphous silicon with germanium (*a*-SiGe:H), oxygen (*a*-SiO:H), nitrogen (*a*-SiN:H), or carbon (*a*-SiC:H); and hydrogenated fluorinated amorphous silicon (*a*-Si:H:F).

Microcrystalline silicon is a material containing two solid phases; volumes of

crystalline material are embedded in an amorphous network. The crystallites are in the order of 10 nm diameter. The fraction of crystalline material depends on the deposition conditions. The properties of μc-Si:H are quite different from those of amorphous silicon. Doped μc-Si:H can reach a much higher conductivity than a-Si:H (in the order of 10-100 S/cm for n-type μc-Si:H compared with 10^{-2} S/cm for n-type a-Si:H). Application of μc-Si:H as the doped layers in solar cells has led to improved efficiencies. However, it is difficult to deposit *thin* layers of microcrystalline material.

Alloying amorphous silicon with other elements is a very effective method to adjust the optical bandgap, but in general the alloys have poorer electronic properties. Alloying amorphous silicon with germanium reduces the bandgap; good quality material with Tauc gap values between 1.35 eV and 1.65 eV can be obtained by choosing different Ge-fractions. The reduced optical gap leads to an increased absorption, especially in the red and near infrared part of the solar spectrum. In contrast alloying with nitrogen, oxygen or carbon increases the bandgap and reduces the absorption in the visible part of the light spectrum.

Deposition of amorphous silicon

The most common technology for device quality hydrogenated amorphous silicon deposition is RF-PECVD (Radio-Frequency Plasma Enhanced Chemical Vapor Deposition) at 13.56 MHz. This method was first reported by Sterling and Swann [123], while Chittick *et al.* [26] showed that this method is very useful for a-Si:H deposition. In PECVD the source gas, usually silane SiH_4 for a-Si:H deposition, is decomposed in a plasma; the silane radicals reaching the substrate surface give rise to the growth of a hydrogenated amorphous silicon layer.

At present a capacitively coupled plasma system is most widely used for a-Si:H deposition. In principle this type of reactor consists of a vacuum chamber in which a plasma is generated between two electrodes in a capacitor-like configuration. The gap between the capacitor "plates" is in the order of 10-30 mm. The substrate for film growth is attached to a temperature-controlled electrode. One of the plates is grounded and the other is connected to the RF-power generator. A gas system provides the control and mixture of the source gases. The pressure during deposition is set to a fixed value. In a small-area ($\approx$100 cm^2) deposition system high-quality amorphous silicon is grown with the following typical process settings: pressure 0.5-2.0 mbar, substrate temperature 150-220 °C, RF power 10–30 mW per cm^2 of electrode area, SiH_4 flowrate 20 sccm. With these settings typical growth rates of 1.5–3 Å/s are obtained.

Other technologies for a-Si:H deposition are: vhf PECVD, photo CVD, plasma-arc CVD, hot-wire CVD, reactive sputtering.

The properties of amorphous silicon depend to a large extent on the process parameters. The values of the mobilities, sub-bandgap density-of-states, hydrogen content, optical bandgap, and the growth rate depend much on e.g. the temperature, plasma power density, and dilution of the process gases by hydrogen or argon. This means that the parameter space for material and device optimisation is very large.

Structure of amorphous silicon solar cells

Charge carriers generated in quasi-neutral, doped material give the main contribution to the photovoltaic effect in *crystalline* solar cells. The minority carriers diffuse in the quasi-neutral semiconductor to a *pn*-junction, which effectuates the actual separation of the electron-hole pairs. In *amorphous* silicon solar cells this mechanism of charge collection is not very effective: the diffusion lengths in undoped *a*-Si:H are in the order of 100 nm, because of the low carrier mobilities and short lifetimes. In doped *a*-Si:H the diffusion lengths are even shorter. Therefore, only charge carriers absorbed in a depletion layer will be effectively separated with the aid of the built-in electric field. The *pin*-diode is the structure generally used in *a*-Si:H solar cells to create a relatively thick depletion layer in which charge carriers have relatively long lifetimes. In this structure an *i*-layer of several hundreds of nanometers is sandwiched between two doped layers with thicknesses in the order of 10 nm. The doped layers have to be as thin as possible because of the poor electronic properties of these layers; the carriers generated optically in these layers do not contribute to the photocurrent. As discussed above *a*-Si:H is a very good absorber of visible light. Therefore, amorphous silicon can be utilised for solar cells with useful conversion efficiencies, despite of its relatively bad electronic properties; the thickness of the intrinsic *a*-Si:H layer can be kept low, hence the recombination losses are limited.

In general, *a*-Si:H *pin* solar cells are designed such that light enters through the *p*-layer. This design results in higher conversion efficiencies than a structure where the light enters through the *n*-type layer. Since the optical generation in the *i*-layer is higher at the side of light entrance, on average the holes have to traverse a shorter distance through the *i*-layer towards the *p*-layer if the light enters through the *p*-layer instead of the *n*-layer. This leads to higher efficiencies because the electrons, which now have to move the longest path, have better transport properties than the holes.

The structures used in *a*-Si:H solar cells are sketched in Fig. 1.7. Figure 1.7a shows a pin structure deposited on a transparent substrate such as glass or plastic foil. The light enters the solar cell through the substrate, which gives the cell its mechanical support. It is coated with a Transparent Conductive Oxide (TCO)

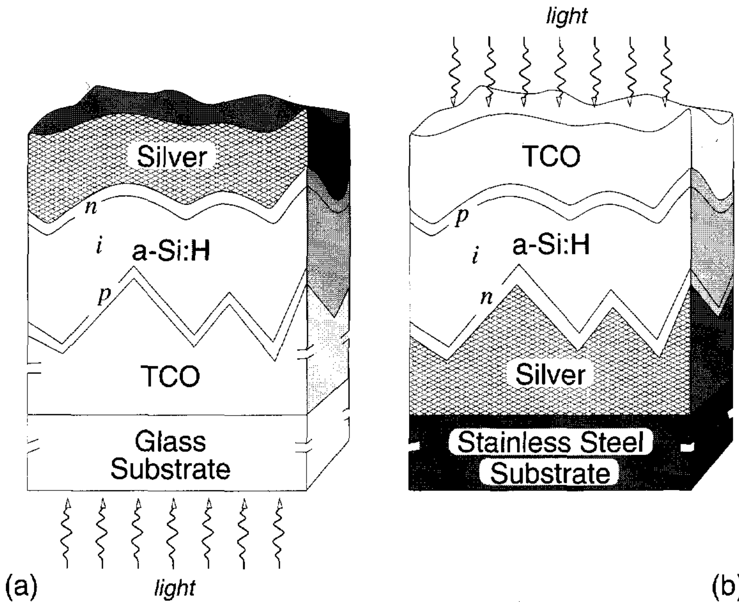

Figure 1.7: Schematic drawing of *a*-Si:H solar cell structures. (a) *pin* structure deposited on a transparent substrate. The light enters the cell through the substrate. (b) *nip* structure deposited on an opaque substrate. For this type of cell, the light enters at the side of the deposited layers. In both figures the substrate is positioned at the bottom.

layer of 500–1000 nm. The TCO serves as the front contact and must have high optical transmission and high electrical conductivity. Usually, fluor doped tin oxide, SnO_x:F is used as TCO material. For high-efficiency cells *textured* TCO layers are used (Fig. 1.7). The texturisation causes scattering of the incoming light in order to increase the optical path length of light rays through the amorphous silicon layers. This enhances the absorption of weakly absorbed (red) light and thus increases the solar cell efficiency. Typical sizes of the TCO peaks and grain widths are in the order of several 100 nanometers. On the TCO a *p*-doped layer of about 10 nm is deposited. Usually boron doped silicon carbide, *a*-SiC:H, is used, because it has less optical absorption than *p*-type *a*-Si:H (boron doping of *a*-Si:H decreases the optical bandgap; alloying with carbon increases it to values around 1.95–2.00 eV). After the *p*-layer an intrinsic layer of 300–500 nm is deposited, followed by an amorphous or microcrystalline, phosphorus doped *n*-layer of about 20–30 nm thickness. The *pin* structure is covered by a sputtered or evaporated aluminium or silver layer serving as the back electrode and reflector for light that is not yet fully absorbed. In terms of reflectivity silver is superior to

aluminium. To enhance the reflectivity further, a TCO layer such as doped ZnO or ITO (Indium Tin Oxide) can be inserted between the *n*-layer and metal back contact (not shown in the figure).

Figure 1.7b shows an alternative structure consisting of a *nip* diode deposited on an opaque substrate such as stainless steel foil. In this structure the sequence of layer depositions (metal, *a*-Si:H, TCO) is inverted. Here, the metal back contact is deliberately texturised to improve optical absorption. Usually ITO is used as front contact for this type of solar cells.

Degradation effects in amorphous silicon solar cells

The light-induced degradation of the conductivity of *a*-Si:H, the Staebler-Wronski effect, has already been briefly mentioned before. Light-induced changes degrade the solar cell efficiency too. The degradation effects are metastable: thermal annealing at temperatures of about 150 °C restores the initial properties.

It is now generally recognised that the degradation of the material properties is caused by creation of additional dangling bonds. Evidence of this is that the absorption of degraded material in the sub-bandgap energy range has clearly increased compared to the absorption of material that has not been subjected to degrading conditions. The defect concentration increase has a pronounced influence on *a*-Si:H material and device properties. Because midgap states act as charge trapping and recombination centres, the effect is twofold.

1. Carrier lifetimes decrease as additional defects are created which act as recombination centres. Because material degradation reduces the lifetimes in *a*-Si:H layers, their photoconductivity decreases. The shorter carrier lifetimes reduce the efficiency of solar cells; a larger number of the optically generated electron-hole pairs will recombine before they are collected in the doped layers.

2. The position of the Fermi-level in the bandgap of neutral bulk material, as well as the space-charge distribution in devices changes because the concentration of trapped charges changes due the additional defects. Therefore, the dark conductivity of bulk layers changes; usually it decreases because the increase of the midgap density-of-states forces the Fermi-level towards midgap to preserve charge neutrality. In *pin* solar cells the higher defect concentration changes the built-in electric-field distribution; this influences the conversion efficiency negatively.

The creation of metastable defects is explained by the breaking of weak or strained Si-Si bonds. Although the mechanism is not yet fully understood,

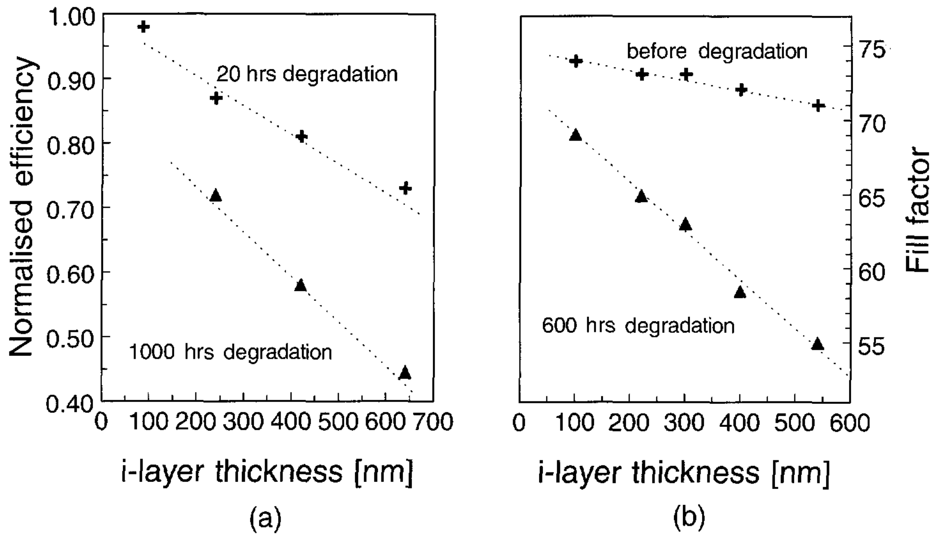

Figure 1.8: Dependence of single-junction *pin* solar cell degradation behaviour on *i*-layer thickness. (a) Efficiency degradation vs. *i*-layer thickness after 20 and 1000 hours of degradation. Efficiencies are normalised by the undegraded values. Data after Bennett and Rajan [10]. (b) Fill factor as a function of *i*-layer thickness, before and after 600 hours degradation. (The fill factor will be defined on page 26; this device parameter is correlated with the quality of a solar cell.) Data after Rech [101].

researchers believe that hydrogen plays a role in the bond breaking process. It is assumed that recombination of excess carriers can cause bond-breaking. However, there is also evidence that charge trapping due to a shift of the Fermi-level may cause metastable defects [89, 90] [126, page 220] [147, page 89]. Therefore, not only illumination causes extra defects, but also charge carrier injection, which occurs for example in un-illuminated *pin* structures under forward biasing conditions.

Important topics in amorphous silicon cell research are the development of intrinsically more stable *a*-Si:H-based materials and solar cell structures that are less sensitive to material degradation. It has been observed in experiments that reducing the thickness of *a*-Si:H solar cells reduces the degradation of the conversion efficiency (see Fig. 1.8). However, reduction of the cell thickness affects the optical absorption in a negative way. Therefore, optical absorption-enhancement techniques must be applied; for instance, the use of highly reflective back contacts or the use of light scattering to cause multiple internal passes of weakly absorbed light rays can increase the photocurrent generation in a thin solar cell.

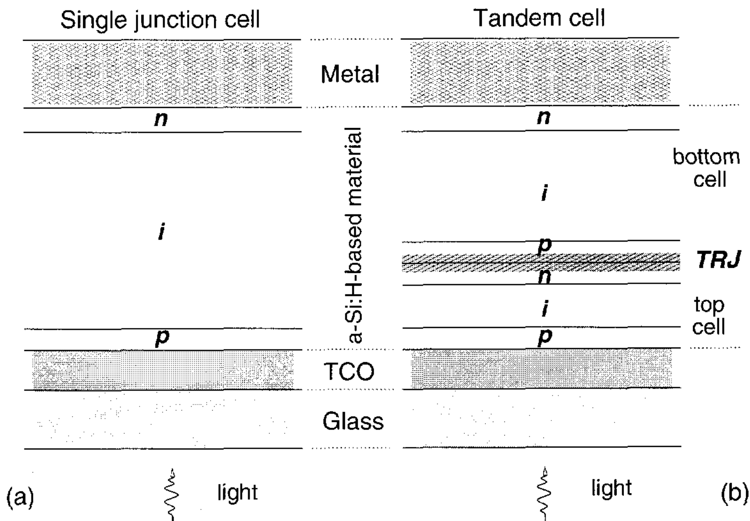

Figure 1.9: Schematic drawing of (a) single-junction cell and (b) tandem cell (*TRJ* = *T*unnel *R*ecombination *J*unction).

In multi-junction cells, the stacking of several *pin* subcells that are thinner than a single-junction cell gives the desired combination of better stability (due to thinner *i*-layers) and high efficiency (due to large total cell thickness). In the field of material research it is found that *a*-Si:H deposition from highly H_2-diluted SiH_4 gas mixture exhibits less light-induced degradation. Using this material in solar cells results in devices which are more stable (see for instance Ref. 101).

Multi-junction *a*-Si:H-based solar cells

A multi-junction solar cell is considered as a good candidate for a stable, highly efficient *a*-Si:H solar cell. It consists of two or three *pin* diodes, called a tandem or a triple cell, respectively. The stack of individual *pin* diodes, the subcells, forms a monolithic multi-layered structure. Because there are no fundamental differences between tandem and triple cells we will restrict our discussion to tandem cells in the rest of this thesis. Figure 1.9 shows the schematic structure of a single-junction cell and a tandem cell side by side. In this figure the substrate texture as drawn in Fig. 1.7 is omitted for clarity. The subcell at the light entrance side is usually called the top cell, while the other subcell is called the bottom cell. Different *a*-Si:H-based materials can be utilised as *i*-layer material for the individual subcells. A tandem cell is usually called an *a*-Si/*a*-Si tandem cell, if both subcells are made with the same *a*-Si:H-material. In the case that materials with different

bandgaps are applied, the tandem cell is called a *multi-bandgap* tandem cell. An example of this type of cell is an *a*-Si/*a*-SiGe tandem cell. For use in the bottom cell *i*-layer a lower bandgap material is chosen than for the top cell; in this way, the bottom cell effectively absorbs the photons of the longer wavelength range for which the higher-bandgap top cell is relatively transparent.

The total thickness of a single-junction cell and a tandem cell designed for high stabilised efficiency are in the same order of magnitude. However, the thicknesses of the individual subcells of a multi-junction cell must be carefully optimised to obtain the maximum power conversion efficiency. Because the subcells are connected in series the current is the same in each subcell. Therefore, the photocurrents generated in each subcell must be the equal to a first-order approximation. The subcell photocurrent can be estimated from purely optical considerations: the total number of photons absorbed in the *i*-layer of a subcell (*i.e.* the active region) is more or less equal to the number of charge carriers in the photocurrent. Hence, the thicknesses of the individual subcells can be optimised approximately by optical analysis of the tandem cell. For instance, in an equal bandgap *a*-Si/*a*-Si tandem cell the top cell is about five times thinner than the bottom cell because the highest optical absorption occurs at the side of the cell where the light enters; here, the photons of the blue part of the spectrum are strongly absorbed. The absorption near the back contact is much lower, because only photons of the red part of the spectrum can penetrate the total cell (due to the lower absorption coefficient for these photons).

In Fig. 1.9 we can see that the connection between two subcells is formed by a highly doped *np* interface. Various names are used for this interface: tunnel junction, recombination junction and tunnel-recombination junction (TRJ). We prefer the use of the latter term for reasons that will become obvious in Ch. 5. As discussed above the current in the subcells is equal due to the series connection. Therefore, if we want to extract the photovoltaic power generated in the individual subcells optimally, the photovoltages of the subcells must be added without losses. This imposes requirements on the TRJ, which will be discussed in Ch. 5.

There is much experimental evidence that multi-junction cells have the potential of achieving higher stabilised efficiencies than single-junction cells do. Especially the use of different bandgap materials for the photovoltaically active *i*-layers leads to an efficiency increase. The advantage tandem cells have over single-junction cells has two origins:

- The application of semiconductors with different bandgaps in multi-junction cells has a fundamental advantage over the use of one single bandgap. This is elucidated by physical intuitive reasoning, which does not pretend to provide a detailed physical model. We consider three different cases

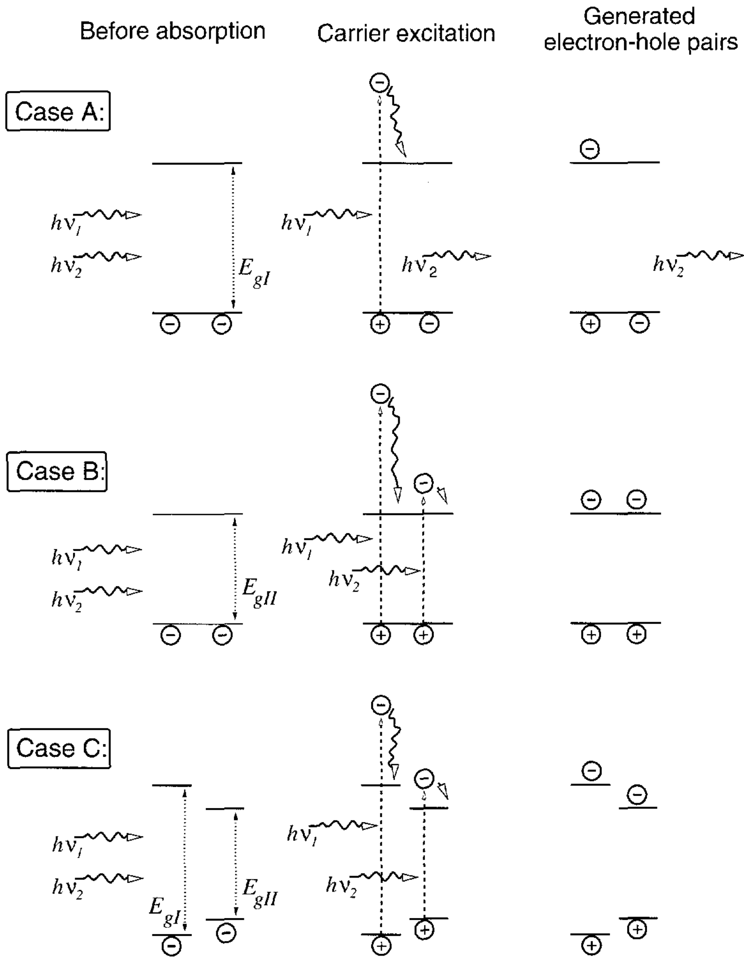

Figure 1.10: Optical carrier generation in semiconductors with different bandgaps. This figure illustrates that the use of two materials with different bandgaps in a tandem cell can give a fundamentally higher conversion efficiency. For an explanation see the text

as sketched in Fig. 1.10. We assume two different semiconductor materials with bandgaps E_{gI} and E_{gII}, respectively, and consider two photons; one with energy $h\nu_1$ and another with energy $h\nu_2$. The energies of bandgaps and photons obey the following relation: $h\nu_1 > E_{gI} > h\nu_2 > E_{gII}$, which means that $h\nu_1$ can be absorbed in both materials, but $h\nu_2$ can only be absorbed in material II.

Case A shows the absorption processes in semiconductor I. The left graph shows the situation before absorption, where there are two photons and no electron-hole pairs (all electrons occupy valence band states). In the central graph, the photon $h\nu_1$ excites a valence electron to an energy high in the conduction band that subsequently loses its excess energy, $h\nu_1 - E_{gI}$, and 'falls down' to the conduction band edge, as indicated by the wavy arrow. After this process we have *one* electron-hole pair, which 'contains' an energy E_{gI}, as drawn in the right graph. Material I is transparent for photon $h\nu_2$, because it has not enough energy to create an electron-hole pair. Hence this photon is not absorbed.

In case B the absorbing material is replaced by material II. In this semiconductor both photons are absorbed and *two* electron-hole pairs are created. However, the energy of each of these pairs is *less* than in case A: instead of E_{gI} the energy is now only E_{gII}. From this difference in optical electron-hole pair creation in material I and II we can conclude that a solar cell made of semiconductor II is capable of generating a *larger* photocurrent, but a *smaller* photovoltage than a solar cell made of material I. Because of the lower bandgap, in case B a larger fraction of the photon energy $h\nu_1$ is lost than in case A.

Case C combines the benefits of both semiconductors: photon $h\nu_1$ is absorbed in material I, where it creates an electron-hole pair with energy E_{gI} and photon $h\nu_2$ passes material I to be absorbed in material II, where it creates an electron-hole pair with energy E_{gII}. Now, the final situation as depicted in the bottom right graph of Fig. 1.10 is energetically preferable to the other two cases, because there are now two electron-hole pairs, as in case B, but one of the pairs contains more energy. In terms of photovoltaic power conversion, this means that a tandem cell combining a higher-bandgap top cell and a lower-bandgap bottom cell can generate more power than a tandem cell with equal-bandgap *i*-layer materials.

- As discussed above in the section on degradation, thinner cells show relatively less degradation. Therefore a tandem cell, that contains subcells that are *thinner* than a single-junction cell with equal *initial* power conversion,

is less sensitive to light-induced degradation. In other words, tandem cells have higher stabilised efficiencies than single-junction cells. Even tandem cells using equal *i*-layer materials in both subcells have a higher stabilised efficiency than single-junction cells using the same material. We discuss tandem-cell stability in detail in Sect. 5.5.

Finally, we give some numbers to illustrate the superiority of multi-junction cells over single-junction cells. Presently, the world record multi-junction cell is an *a*-Si/*a*-SiGe/*a*-SiGe triple cell with 13.0% stabilised efficiency [152]. The single-junction record efficiency is considerably less: 8.9% [56]. To illustrate that even with same bandgap materials in tandem cells higher stabilised efficiencies can be obtained, we mention some efficiencies of the Jülich group for *a*-Si:H single and tandem cells; they have obtained 7.9% and 9.0% for single-junction and tandem cells, respectively [101].

1.3 Material and solar cell characterisation

A detailed coverage of the characterisation techniques for *a*-Si:H-based materials and solar cells is beyond the scope of this work. We give a brief overview of the main measurement techniques with emphasis on those that are relevant to *a*-Si:H solar cell device modelling. First, we discuss the material characterisation measurements; from these measurements material parameters can be extracted that serve as simulation input parameters. Secondly, the measurements of device characteristics are discussed, which are the reference for the simulated device. Finally, a brief discussion of degradation experiments is given.

The interpretation of measurements of *a*-Si:H-based materials and devices is difficult for several reasons: e.g. the complexity of the material, the sensitivity of material properties to process parameters, the small thicknesses of layers as applied in devices, the inhomogeneities of materials inside devices, the role of interfaces between materials. Because of these reasons physical models — on which the interpretation of experiments is generally based — often have to be simplified by approximations and assumptions, to enable a comprehensible and direct extraction of physical parameters from measurements. Unfortunately, the approximations and assumptions are not always valid, thus leading to physical material parameters that cannot be used directly in other models, such as a device simulator.

Material characterisation:

Dark conductivity. In general, the conductivity, σ, of a semiconductor is expressed by:

$$\sigma = q(\mu_n n + \mu_p p). \tag{1.1}$$

In an un-illuminated homogeneous semiconductor in which no excess carrier are injected, the carrier concentrations have their equilibrium values, n_{eq} and p_{eq}. Substitution of the equilibrium carrier concentrations in Eq. 1.1 yields the dark conductivity, σ_d. The basic information obtained from σ_d is the product of mobility, μ_n or μ_p, and equilibrium free carrier concentration, n_{eq} or p_{eq}. The latter quantity depends strongly on the distance between the Fermi level and the conduction band or valence band, respectively.

Measurement of the dark conductivity as a function of temperature yields the conductivity activation energy, E_{act}, which is related to σ_d by

$$\sigma_d(T) = \sigma_0 \exp\left(-\frac{E_{act}}{kT}\right). \tag{1.2}$$

The activation energy, E_{act}, equals the distance between Fermi level and the mobility edge of the majority carriers, if we assume that this distance does not depend on temperature. Therefore, this measurement is often used to estimate the position of the Fermi level in a material.

Photoconductivity. The steady-state photoconductivity, σ_{ph}, of *a*-Si:H is the bulk conductivity of the illuminated material. Usually standard AM1.5G illumination or red light illumination is used; with red light electron-hole pairs are generated more uniformly in the material. Basically, the photoconductivity measurement shows to what extent optical generation is able to change the free carrier concentrations. This is related to the carrier lifetimes, because in steady-state the recombination rate equals the optical generation rate. Therefore, σ_{ph}-measurements are used to quantify the quality of intrinsic *a*-Si:H based materials.

Besides this basic steady-state photoconductivity measurement there are numerous other experiments which are based on photoconductivity measurements. A few examples are:

- Photoconductivity as a function of illumination intensity. Because of the quasi-continuum of gap states the carrier lifetimes and thus the photoconductivity depend on the strength of the optical excitation.

Therefore, the results of this measurement are related to the distribution of energy states in the mobility gap.

- Photoconductivity transients. This measurement yields the time-dependent decay of the photoconductivity after an abrupt termination of the optical excitation. It provides direct quantitative data of the carrier lifetimes.
- Modulated photoconductivity. This technique measures the small-signal response of the photocurrent caused by an intensity-modulated optical excitation. The trapping and emission processes and gap state spectrum can be studied by using various modulation frequencies and steady-state bias-illumination intensities.
- Time-resolved photoconductivity or Time-of-Flight (TOF). With this technique the time-resolved photocurrent is measured following a short light pulse. The tail state properties and mobilities can be extracted from the current response.

Reflection and Transmission. From reflection and transmission spectra the refractive index and absorption coefficient can be extracted. The latter is used to determine the optical bandgap. It is most common to use the Tauc gap for intrinsic-*a*-Si:H characterisation. The Tauc gap is determined from the fit of the following expression to the absorption data [135] (see also 1.5).

$$\sqrt{h\nu\alpha(h\nu)} = A(h\nu - E_g). \tag{1.3}$$

By measuring the temperature dependence of the reflection-transmission spectra, the optical bandgap as a function of temperature can be determined.

Sub-bandgap absorption measurements. Several types of measurements are used to determine the absorption of photons with less energy than the optical bandgap, the sub-bandgap absorption. The most commonly used techniques are: Constant Photocurrent Method (CPM), Dual Beam Photoconductivity (DBP) and Photothermal Deflection Spectroscopy (PDS). The sub-bandgap absorption is correlated to the density of states distribution in the mobility gap, because these states enable optical electron-hole pair creation by photons with less energy than the mobility gap. Absorption of photons with energies just below the optical bandgap is due to the band tails (refer to Fig. 1.5). The characteristic energy of the exponential slope of the absorption spectrum is called the Urbach energy. The absorption through valence band tail states dominates this part of the absorption spectrum, because the valence band tail is broader than the conduction band tail (see

Fig. 1.4). Therefore, the Urbach energy provides quantitative information about the valence band tail density of states. The absorption of photons with energies below 1.4 eV is due to the defect states. Therefore, the density of dangling bonds can be estimated from the low energy part of the absorption spectrum.

The Urbach energy as a function of temperature can be determined with temperature-dependent sub-bandgap absorption measurements. This gives a quantitative measure for the temperature dependence of the valence band tail width.

Electron Spin Resonance. This measurement is the most direct way to measure dangling bond concentrations. However, a disadvantage of this method is that only singly occupied dangling bonds contribute to the measurement signal.

Internal Photo Emission. With this technique one can measure optical transitions between *e.g.* the Fermi level in a metal and the conduction or valence band in an adjacent semiconductor, or between extended states at both sides of a heterojunction interface. It is used to determine band offsets and mobility gaps.

Solar cell characterisation techniques:

Illuminated IV-characteristics. The most important characterisation technique for solar cells is the current-voltage (IV) measurement under illumination, because with this measurement the conversion efficiency can be determined. For this measurement usually the standard AM1.5G solar spectrum is used at an intensity of 100 mW/cm^2. A typical illuminated IV-curve is

Parameter	Description
I_{sc}	Short circuit current
V_{oc}	Open circuit voltage
I_{mpp}	Current at maximum power point
V_{mpp}	Voltage at maximum power point
P_{max}	Maximum output power ($P_{max} = V_{mpp} \cdot I_{mpp}$)
P_{irr}	Power of incident irradiation
FF	Fill factor ($FF = P_{max}/(V_{oc} \cdot I_{sc})$)
η	Conversion efficiency ($\eta = P_{max}/P_{irr}$)

Table 1.1: Parameters of illuminated solar cells.

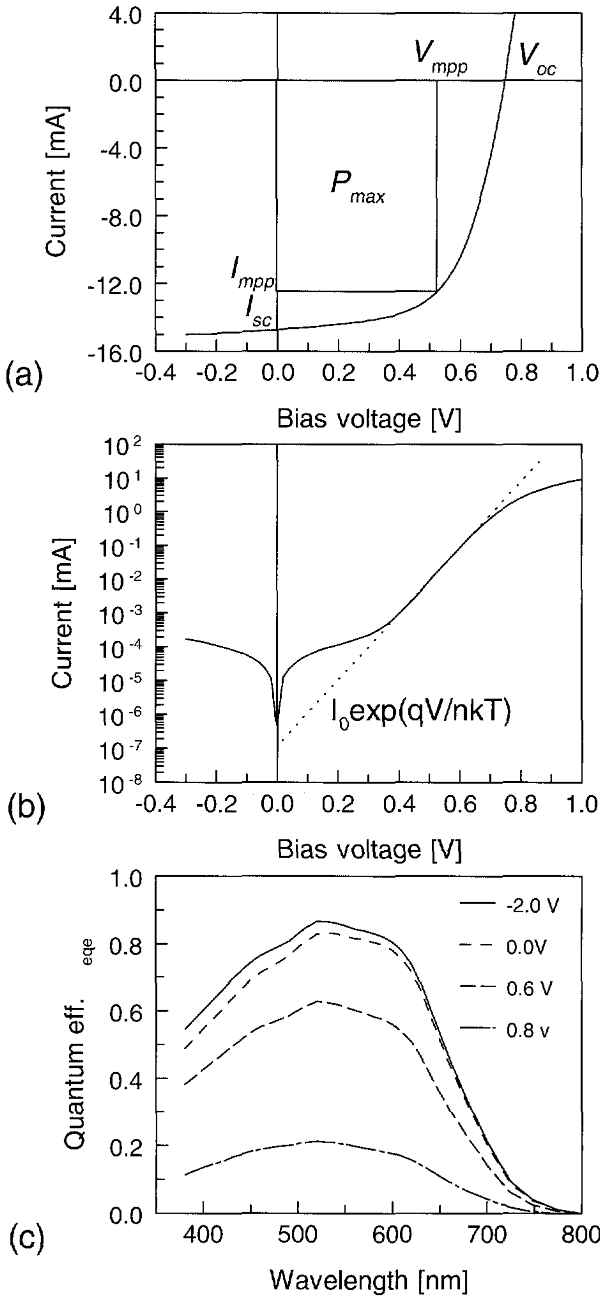

Figure 1.11: Typical measurement results of the main solar cell characterisation techniques: (a) illuminated IV-measurements with standard AM1.5G irradiation; (b) dark IV-measurements; (c) external quantum efficiency spectrum.

depicted in Fig. 1.11a. Table 1.1 lists the most important solar cell parameters; if the definitions are not obvious from the figure these are given in the table.

Dark IV-characteristics. Less frequently used is the IV-measurement without illumination, because it has no direct correlation with the solar cell as a photovoltaic power generator. Nevertheless, qualitative information can be extracted from dark IV-characteristics. Like crystalline semiconductor diodes amorphous silicon diodes are rectifying devices; the IV-characteristics of *a*-Si:H *pin* diodes are similar to the characteristics of crystalline diodes. In the forward bias region the current increases exponentially with increasing bias voltage. In Fig. 1.11b an example of a dark IV-curve is shown. In this curve we can distinguish three regions:

- Between 0.4 and 0.7 V forward bias the curve can be approximated by $I = I_0 \exp(qV/nkT)$. By fitting this exponential function to the measurement data, the saturation current, I_0, and diode quality factor or diode ideality factor, n, can be determined. These parameters are correlated with electronic material properties such as the bandgap and defect density.

  According to the theories for *crystalline* diodes we can obtain qualitative information about the physical mechanisms that give rise to the current flow in a diode. These theories are often applied to explain the behaviour of *amorphous silicon-based* diodes; based on the value of n which is usually between 1 and 2 for good-quality *a*-Si:H diodes, often the conclusion is drawn that the current mechanism in these devices must be a combination of diffusion and recombination. However, we will show in Sect. 4.1 that the current in *a*-Si:H-based diodes is a *pure recombination* current.

- The deviation of the 'ideal' exponential IV-characteristics at voltages below 0.4 V and in reverse bias is usually ascribed to a "shunting" effect. This effect will be discussed in detail in Ch. 6.

- In the region above 0.8 V forward bias there is also a deviation from the ideal exponential characteristics. This is commonly ascribed to series resistance effects or Space Charge Limited Current (SCLC) effects.

External Quantum Efficiency. The External Quantum Efficiency (EQE) measurement is an electric-optical measurement by which the spectral sensitivity of a solar cell is determined. In principle the external quantum efficiency,

η_{eqe}, is the number of electrons in the photocurrent I_{ph}/q divided by the number of photons, n_{ph}, of certain wavelength λ that impinge on the cell,

$$\eta_{eqe}(\lambda) = \frac{I_{ph}}{q n_{ph}}. \quad (1.4)$$

Usually the so-called Differential Spectral Response measurement method is applied; during this measurement the solar cell is illuminated by a continuous bias light (usually white light approximating the AM1.5 spectrum) upon which a monochromatic chopped probe light beam is superposed. The solar cell response to the chopped probe light is measured with a lock-in technique. By varying the wavelength of the probe light a spectrum is measured. The bias light is needed to keep the solar cell in a well-defined bias condition. The external quantum efficiency of the solar cell is determined by comparing its response with a calibrated diode.

Figure 1.11c shows an example of an EQE spectrum, measured at different forward bias voltages. The following physical processes influence an EQE spectrum:

- absorption losses in non-active layers, such as the p-layer and TCO.
- reflection losses at the front surface of the cell.
- effectiveness of light-trapping techniques, such as the application of textured substrates and highly reflective back contacts.
- recombination losses, incomplete collection of photo-generated carriers.

In principle, information about these processes can be extracted from measured External Quantum Efficiency spectra. However, it is often difficult or impossible to decouple the contributions of the individual processes.

There are numerous variations on the above-mentioned three standard measurement techniques. These variations are less commonly used, but can provide additional physical information about the solar cells. A few examples are:

- Illumination-intensity-dependent IV-measurement.
- Temperature-dependent measurement of dark IV-, illuminated IV- and EQE-characteristics.
- Capacitance as a function of bias voltage (CV) measurements at different excitation frequencies (with and without bias illumination).

- Open Circuit Voltage decay (transient of V_{oc} after abrupt termination of the illumination).
- Short circuit current transient (transient of I_{sc} after abrupt termination of the illumination).

Finally, a kind of cell characterisation method that is purely optical is the cell reflectance measurement. This measurement is used to obtain a reflection spectrum, which gives quantitative information about the optical reflectivity losses. It is especially useful if used in combination with an EQE spectrum. To determine the detailed properties of cells on textured substrates, reflection measurement can be carried out as a function of the angle of the incident and the reflected light (angle-resolved reflectance).

Degradation experiments:

In Sect. 1.2 the metastable behaviour of *a*-Si:H has been discussed. Recombination or charge trapping lead to the creation of metastable defects. This phenomenon can be studied by carrying out degradation experiments. Bulk materials can be degraded by exposing them to optical (or other forms of) irradiation; in addition to this type of stress condition it is also possible to stress *pin* diodes and other devices by using current injection (*e.g.* forward biasing of diodes). The stressing conditions in degradation experiments are usually applied for periods that last between several minutes and more than 1000 hours. After application of the stress condition, the material or device is characterised by the methods discussed above and changes due to the stressing can be identified.

In practice, solar illumination is the obvious cause of degradation of *a*-Si:H photovoltaic cells. Hence, the most commonly applied degradation experiment is light stressing. Several standards of light stressing exist for the determination of the stability of solar cells. For instance, a much used standard condition is: AM1.5G spectrum, 100 mW/cm^2 irradiance, 1000 h stressing, 50 °C sample temperature and solar cell in V_{oc}-condition. Other standards for the determination of cell stability may use different total degradation times or accelerated degradation conditions, for example higher intensities at shorter stressing times.

1.4 Modelling of amorphous silicon solar cells

Physical modelling of semiconductor devices involves the development and application of a detailed mathematical model describing all physical processes that are relevant to the device operation. In the specific case of solar cells the model

must include both the optical and electronic processes, because of its function as optical-to-electrical energy converter. The device model can simulate measurable external optical and electrical quantities (such as electric currents and voltages, photon fluxes etc.) by a detailed representation of the internal quantities and processes that generally cannot be measured directly (*e.g.* charge carrier densities, recombination rates etc.). Except for the most simple cases, which allow approximate analytic solutions, in general the mathematical system of a device model has to be solved numerically with the aid of a computer. Therefore, terms as *device simulation program* or *device simulator* are often used to designate this type of models. The ultimate device model for *a*-Si:H based solar cells can simulate all electrical and optical device characteristics as discussed in Sect. 1.3 accurately and consistently.

There are several motivations to be involved in device modelling. In the first place, developing the model and using it for simulations enhances the detailed understanding of the basic physics controlling the device operation. The model can be applied to explain experimental observations. If the model fails to reproduce the experiment accurately, one can conclude that the physical processes controlling the experiments are not described adequately by the model. Hence, this is an indication that the model needs further refinement. The development of more accurate models leads inherently to better understanding of the physics of the device. On the other hand, if the model can reproduce an *extensive* set of device measurements *consistently*, one can be confident that the model is a good approximation of the physics (which must have been explained in the first place because otherwise it would not be possible to implement this as a physical model!). The data set must include measurements obtained with different experiments (using *e.g.* various biasing conditions and temperatures), and further it should preferably contain redundant information, obtained from independent measurements. As soon as a well-calibrated device model is established, it can be used for computer-aided device design and optimisation. In practice, this will often lead to new experimental observations that do not match the simulated predictions; as, for instance, technologies develop further the model no longer provides an accurate description of the physics, and hence model output diverges from the experimental evidence. These new discrepancies are incentives for further model refinement and physical understanding. For instance, the forth-going miniaturisation in micro-electronics calls for a constant enhancement of the simulation models. Thus, the cycle (1) model development, (2) calibration (3) prediction (4) mismatch model vs. experiment forms a closed loop that has proven its value in many fields of scientific research.

In semiconductor device simulators usually the semiconductor equations are

solved in conjunction with physical models that describe the material properties and physical processes [68, 115]. Simulators for *a*-Si:H-based devices are also based on this approach [46, 103]. However, there are some distinct differences in the way the recombination rates and space charge are computed.

In crystalline semiconductors the bandgap contains a relatively low density of electronic states that act as recombination centres. Therefore, in many cases the recombination processes can be described by the conventional Shockley-Read-Hall model and other recombination models that require only effective carrier lifetimes as physical parameters. Usually, the contribution of the charges trapped in the gap states to the total space-charge may be neglected due to its low density. In contrast, the bandgap of amorphous silicon-based semiconductors contains a quasi-continuum of electronic states which strongly influences the electronic properties of the material. The high density of gap states requires a different modelling approach to compute the charge trapping and recombination processes. The contribution of the trapped space charge density cannot be neglected because of its high density. Furthermore, carrier lifetimes depend to a great extent on the actual biasing condition of the device, because the number of states that contribute to the recombination process is bias-dependent (note that in a solar cell the biasing signal can be both electrical and optical). Therefore, in amorphous semiconductor modelling much attention is paid to the detailed representation of the gap states.

We can identify some specific issues that complicate the modelling of *a*-Si:H solar cells. Some of these have already been mentioned shortly in Sect. 1.3, because these obscure the interpretation of measurements as well. First of all, the complicated electronic material properties hampers straightforward interpretation of measurements and model development (the latter is in fact closely related to interpretation of experiments). Consequently, attempts to capture the physical properties of, *e.g.* , the gap state distribution in a detailed model results in the introduction of a large number of model parameters, which makes the model complex. Secondly, amorphous silicon is not a single, well-defined material, but it encompasses a broad range of materials with continuously varying properties. It is generally accepted that, even inside a *pin* solar cell, the properties of the *i*-layer close to the interfaces differ from those in the central region of this layer. Furthermore, because the layers in solar cells (*e.g.* the doped layers) are very thin, these often have different properties than thick layers; however, material properties are usually characterised by using thick layers, which exhibit bulk properties, and consequently these measurements may not be representative for the layers as applied in cells. Despite these complicating factors device modelling is a very useful tool for *a*-Si:H-based device research. Especially the closed loop of iterative

model refinement as discussed above constitutes an excellent way to enhance the understanding of *a*-Si:H device physics further, because discrepancies between the model and the experiment show that our physical picture is not yet complete and needs further refinement.

Because of the complexity of the materials, modelling of *a*-Si:H-based devices requires simplifying assumptions. The following assumptions are made in all amorphous silicon device simulators that are based on the solution of the semiconductor equations:

1. Charge carrier transport only takes place in the extended electron and hole states. The possibility of tunneling transport between localised states is neglected.

2. The transition from localised to extended states is abrupt, which means that the carrier mobilities as a function of energy is a step function at the mobility edge: below the mobility edge carriers have zero mobility and above the mobility edge they have a constant mobility. A gradual transition from localised to extended states, as sketched in Fig. 1.4b is not accounted for.

3. The occupation of localised states by trapped electrons and holes is governed by the mobile, extended-state electrons and holes. Only capture and emission processes between extended and localised states are accounted for. The possibility of transitions between localised states is neglected.

Street [126] discusses each of these assumptions and concludes that they are valid model approximations for *a*-Si:H at room temperature and above. With these assumptions it is possible to develop a device simulator that is based on well-established simulation programs for crystalline semiconductors. Only relatively simple extensions have to be made, such that the basic structure of the crystalline device simulator is maintained.

Different simulation modes can be distinguished: steady-state, transient, and small-signal mode. Most of the *a*-Si:H device models can only carry out steady-state simulations. With this type of simulation the steady-state (time-invariant) response of the device as a function of different steady-state biasing conditions is computed. Examples are: the model of Hack and Shur [46] and AMPS, developed at Penn State University [79]. The popularity of the steady-state simulator is logically explained by the steady-state character of photovoltaic power conversion; the most important solar cell parameter — the conversion efficiency, η — can be computed by using this type of simulator. Many material and device characterisation measurements, as listed in Sect. 1.3, can be simulated in this mode as

well (*e.g.* steady-state photoconductivity, dark and illuminated IV-characteristics, quantum efficiency spectra, etc.). In contrast, the other two simulation modes — transient and small-signal — are relatively rare. Transient simulations give the time-dependent response to a time-dependent excitation signal, such as a step in the applied voltage or the illumination intensity. In the small-signal mode the response to a sinusoidal excitation is computed; it provides the complex response (real and imaginary part) in the frequency domain. Small-signal simulation models have been developed by Caputo *et al.* [17] and Furlan *et al.* [36]. Recently, a device simulator for transients in amorphous silicon has been published by Popović *et al.* [97]. Simulations in these modes do not correlate directly to a solar cell as a power converter. Nevertheless, they can be utilised to analyse and explain measurement data, such as capacitance *vs.* voltage and frequency ($CV(f)$) characteristics, Time-of-Flight (TOF) responses, and results of transient and modulated photoconductivity measurements. Furthermore, application of these simulation modes to calibrate model parameters is very useful: these modes offer additional degrees of freedom in addition to the steady-state simulations and experiments. As discussed above, a well-calibrated device model must be able to simulate a large variety of experiments accurately; therefore, modelling of the experiments requires all three simulation modes. Up to now no systematic use has been made of the three simulation modes for comprehensive model calibration.

For the simulation of a semiconductor device it is necessary to describe its physical structure. This can be done in one, two of three spatial dimensions (denoted as 1D, 2D and 3D, respectively). If the device operation is strictly dominated by 1D processes a simulation in only one dimension is sufficient. For example, flat parallel-layered structures having gradients in relevant material properties and physical quantities only perpendicular to the planes of the layers show 1D behaviour. If the device behaviour depends on physical processes in more than just one dimension, the system can only be described accurately with a 2D or even 3D device simulator.

Almost all *a*-Si:H solar cell device simulators are one dimensional. However, amorphous silicon solar cells are intentionally made non-1D. They are deposited on textured substrates to enhance the optical absorption in a very thin *pin* structure. Because the practical aim of the application of textured substrates is only the enhancement of the optical absorption, the common simulation approach is as follows: an optical model that accounts for light scattering effects (such as those developed by Tao [133] and Leblanc *et al.* [71]) is used to simulate the optical behaviour and produces an 1D optical generation-rate profile, which is subsequently used as input for an 1D electrical device model. In this approach possible non-1D effects of the electrical-optical system are ignored. However, the schematic

cross-sectional picture in Fig. 1.7 shows that a textured *a*-Si:H solar cell is far from being an ideal 1D system, mainly because the "feature" size of the substrate texture is in the same order of magnitude as the thickness of the *pin* structure. To support this intuitive motivation, we mention several experimental and modelling results to indicate that the common quasi-1D modelling approach *cannot* describe all aspects of the physical system accurately. For example, the thickness of an *a*-Si:H layer on a textured substrate is generally inhomogeneous, because the *a*-Si:H layer tends to smoothen the substrate texture as the layer becomes thicker [145]. Further, detailed 2D modelling [108, 109] has shown that the optical generation does not only depend on the depth in the *a*-Si:H layer, but also on lateral position: in the TCO valleys the generation rates are very different from the rates around the peaks. Similar dependence is shown by the electric field inside the device: near sharp peak-like features the field is much higher than in valleys [35, 108, 109]. Finally, formation of localised, highly defective regions in the "valleys" of the TCO structure is reported [65, 106]; this kind of texture-related effects cannot be modelled by 1D models.

These issues indicate that the often-used quasi-1D approach is not suited for the *quantitative* studies of *a*-Si:H solar cells on textured substrates. It can be applied in *qualitative* studies such as the prediction of trends and the comparison of different physical mechanisms. However, to get the accurate quantitative simulations required by model calibration and parameter extraction one has to use 1D experiments and 1D models to avoid the uncertainties caused by the random 3D structure of textured substrates.

The Sanyo group [108, 109] has developed an integrated optical and electrical 2D device simulator, which has an optical model based on the solution of the Maxwell equations. The results obtained by using this model clearly show that scattering caused by TCO texture leads to 2D inhomogeneity of the optical carrier generation rate. Currently a group at NREL [72] is developing an optical model also based on Maxwell's equations. This type of model can be used to optimise the optical absorption by determining the optimal grain structure of textured substrates.

In conclusion, we discuss the main advantages and drawbacks of 1D simulations in comparison to 2D and 3D simulations. In general, 1D models have the advantage of shorter computation times and relatively low complexity. They allow the identification of trends of many physical processes, but are not suited for parameter extraction, model verification, or calibration using non-1D experimental data of textured solar cells; for this type of work experiments on 1D structures are necessary. On the other hand, 2D and 3D models can represent the physical structure of a textured solar cell more accurately and allow the identification and

assessment of typical non-1D effects, such as layer thickness inhomogeneities, influence of defectuous regions, and inhomogeneities of optical generation rates. Further, they can be applied to study substrate scattering properties in detail and to optimise texture.

1.5 Scope and outline of this thesis

This thesis is our contribution to the development of *a*-Si:H solar cell device modelling. The primary goal of this modelling work is to optimise amorphous silicon tandem cells. Modelling aids optimisation in two different ways: (1) the use of device modelling enhances the researcher's insight in the physical aspects of solar cell operation which leads to improved experimental cell designs, and (2) a well-calibrated, accurate physical model can be utilised directly for the design of optimised cells. This latter approach, which is also called Computer Aided Design (CAD) is not yet feasible, but modelling can provide explanations for physical effects, and thereby increases insight in, for example, degradation behaviour of cells.

More specifically our contribution can be distinguished in three topics: (1) model calibration and verification, (2) development of a tandem cell model, and (3) study of accurate experimental techniques to provide high-quality experimental data for model verification and model calibration.

Because of reasons outlined in the previous section the experimental and modelling work is restricted to one-dimensional structures. In this way the complex electro-optical system formed by a solar cell deposited on a randomly textured substrate does not have to be considered in full detail and attention can be focused on accurate, quantitative model verification and calibration by the use of a simplified structure. Further, this work is restricted to the steady-state electrical part of the solar cell simulator. Not much emphasis is put on the optical models.

This thesis is organised in seven chapters. Chapter 2 gives an overview of models used in *a*-Si:H solar cell simulators. It discusses the semiconductor transport equations, the different models for the density of localised states and the models for the computation of the space charge and recombination. In Appendix B we compare in detail the physical models that are described in Chapter 2 and are implemented in different simulators for *a*-Si:H-based devices.

In Chapter 3 we present our device simulator Amorphous Semiconductor Analysis (ASA). All relevant aspects such as the modelling capabilities, the implemented physical models and numerical solution methods are discussed.

The topic of Chapter 4 is the determination of *a*-Si:H-based solar cell model parameters. It starts with a theoretical study of the current mechanisms in forward-

and reverse-biased *pin* diodes without illumination. A study of the dependences between model parameters follows. Next, it discusses the generally made assumption of the abrupt mobility edge, followed by the presentation of our model parameter sensitivity study. Finally, we discuss the results obtained from two calibration exercises.

Chapter 5 treats the modelling of *a*-Si:H tandem solar cells. It first discusses the device physics of tandem cells, followed by a review of tunnel-recombination-junction technologies and a review of the existing models for tandem cell simulations. Subsequently, we introduce a new model to describe the transport and recombination processes in the tunnel-recombination junction. We apply our new modelling approach to tandem cell simulations illustrating two 'fundamental' properties of tandem cells: high fill factors and improved stability.

Chapter 6 discusses our experimental work that emphasises the acquisition of high-quality experimental data such as required for model calibration. First we discuss techniques to measure *IV*-characteristics of *pin* diodes accurately. We propose a method for the characterisation of doped layers *inside* devices. This is followed by the determination of the *a*-Si:H mobility gap from temperature-dependent dark *IV*-characteristics. Finally, we discuss the experimental results of our study of metal-back-contact stability.

To conclude this thesis Chapter 7 summarises the main conclusions of this thesis and gives suggestions for further work.

Chapter 2

Review of amorphous silicon solar cell simulation models

Since Swartz [130] introduced numerical device modelling in 1982 to study hydrogenated amorphous silicon solar cells, device simulators are widely used in the a-Si:H photovoltaics research community. In the course of time various simulation programs have been developed especially for a-Si:H solar cells. In this chapter we give a review of the basic semiconductor device equations and the physical models used in a-Si:H solar cell device simulators in general and our work in particular.

First, we describe the general simulation framework consisting of the semiconductor transport equations and models for the electrical contacts to the device. A discussion of the various models for the localised density of states in the a-Si:H mobility gap follows which includes the main points of the defect-pool model. The physical models for the recombination and charge trapping in the gap states in amorphous silicon and related materials are reviewed; this includes a brief introduction to the Shockley-Read-Hall theory and simplifications to this theory as developed by Taylor and Simmons. After that the Sah-Shockley theory and the decoupled approach for multi-level traps are discussed. Finally an introduction to the trap-assisted tunneling recombination model is given.

2.1 Transport equations

In a semi-classical approach the electron and hole current conduction within semiconductors is described by a set of differential equations generally known as the semiconductor equations [68, 115]. In the following we assume an isothermal situation and the absence of magnetic fields. The semiconductor equations

comprise the Poisson equation (2.1) and the continuity equations for electrons (2.2) and holes (2.3), respectively:

$$\nabla \cdot (\varepsilon \nabla \psi_{vac}) = -\rho \tag{2.1}$$

$$\frac{\partial n}{\partial t} = \frac{1}{q} \nabla \cdot \vec{J}_n + G - R \tag{2.2}$$

$$\frac{\partial p}{\partial t} = -\frac{1}{q} \nabla \cdot \vec{J}_p + G - R \tag{2.3}$$

where ψ_{vac} is the potential related to the local vacuum level, and the carrier concentrations n and p refer to the free carriers. For a definition of symbols we refer to Appendix A. In amorphous semiconductors the space charge, ρ, is not only determined by the concentrations of ionised donors, N_D, and acceptors, N_A, and the free electron and hole concentrations, n and p, respectively, but also by trapped charge density, ρ_{trap}, in the gap states, hence $\rho = q(p - n + N_D - N_A) + \rho_{trap}$.

The electron and hole current densities, $\vec{J}_n$ and $\vec{J}_p$, are governed by the gradients in the corresponding quasi-Fermi levels of the free carriers, E_{fn} and E_{fp}, respectively

$$\vec{J}_n = \mu_n n \nabla E_{fn} \tag{2.4}$$

$$\vec{J}_p = \mu_p p \nabla E_{fp}. \tag{2.5}$$

In amorphous silicon the quasi-Fermi levels are always separated more than three times kT from their corresponding band edges. For this reason it is justified to use the Maxwell-Boltzmann approximation to calculate the free carrier concentrations. By using this approximation we can substitute the expressions relating the free carrier densities to the quasi-Fermi levels and the effective density-of-states (DOS) in the extended conduction and valence band states, N_c and N_v respectively,

$$n = N_c \exp\left(\frac{E_{fn} - E_c}{kT}\right) = N_c \exp\left(\frac{E_{fn} - (E_{vac} - q\chi)}{kT}\right), \text{and} \tag{2.6}$$

$$p = N_v \exp\left(\frac{E_v - E_{fp}}{kT}\right) = N_v \exp\left(\frac{(E_{vac} - q\chi - E_g) - E_{fp}}{kT}\right), \tag{2.7}$$

in Eqns. 2.4 and 2.5. With this substitution we obtain for the current densities:

$$\vec{J}_n = qD_n \nabla n + q\mu_n n \left[\vec{E} - \nabla\chi - \frac{kT}{q}\nabla \ln\left(\frac{N_c}{N_{c0}}\right)\right] \tag{2.8}$$

$$\vec{J}_p = -qD_p \nabla p + q\mu_p p \left[\vec{E} - \nabla\chi - \frac{1}{q}\nabla E_g + \frac{kT}{q}\nabla \ln\left(\frac{N_v}{N_{v0}}\right)\right]. \tag{2.9}$$

In these equations N_{c0} and N_{v0} are reference values for the effective DOS, χ is the electron affinity, E_g is the mobility gap and E_{vac} is the energy level corresponding with the local vacuum level. The Einstein relations, $qD_{(n,p)} = kT\mu_{(n,p)}$, are used to derive these equations. The electric field, $\vec{E}$, is defined as $\frac{1}{q}\nabla E_{vac}$.

In Eqns. 2.8 and 2.9 the first term describes the diffusion current and the second the drift current. The terms in square brackets can be considered as *effective drift* fields; in addition to the electric field, $\vec{E}$, these contain terms applying to cases where inhomogeneities of the material properties result in the presence of heterojunctions. In those cases the currents are also determined by gradients in the electron affinity, χ, mobility gap, E_g, and effective densities of states, N_c and N_v.

The electrical contacts of a semiconductor device can be modelled in different ways. The type of contact model sets the boundary conditions for the differential Eqns. 2.1, 2.2 and 2.3.

Ideal Ohmic contacts. In this case zero space charge and thermal equilibrium concentrations of both types of carriers is assumed at the contacts. This is equivalent with the absence of a Schottky barrier at the surface and infinite surface-recombination velocities of carriers.

Generic contacts. In this case the current densities through the contacts are determined by the carrier concentrations and finite surface-recombination velocities. This is described mathematically by:

$$\vec{J}_n \cdot \vec{n} = -qR_n^{surf} = -qS_n(n - n_{eq}) \tag{2.10}$$

$$\vec{J}_p \cdot \vec{n} = qR_p^{surf} = qS_p(p - p_{eq}) \tag{2.11}$$

where $\vec{n}$ is the normal unit vector pointing outward from the semiconductor surface, and S_n and S_p are the surface-recombination velocities of electrons and holes, respectively. n_{eq} and p_{eq} denote free-carrier equilibrium concentration.

Schottky contacts. In general, there is a Schottky-barrier at the interface between a semiconductor and a metal. The current transport across this interface is in most cases dominated by the majority carriers and is governed by the mechanism of thermionic emission [131]. Thermionic-emission limited transport can be modelled by using the *generic* contact model, where the surface recombination velocity of the majority carriers has to be set to $v_{th}/\sqrt{6\pi}$. For the derivation of this approach and the value of the recombination velocity, we have to consider the equation for an ideal Schottky diode [131] (here, an n-type Schottky diode is considered)

$$J_n = A^* T^2 \exp\left(-\frac{q\phi_{bn}}{kT}\right)\left[\exp\left(\frac{qV_a}{kT}\right) - 1\right] \tag{2.12}$$

where the effective Richardson constant $A^* = \frac{4\pi q m^* k^2}{h^3}$ and ϕ_{bn} is the Schottky barrier height. Using Eqns. 2.10, 2.12, the expression for the effective DOS in the conduction band, $N_c = 2(\frac{2\pi m^* kT}{h^2})^{1.5}$, and the thermal velocity, $v_{th} = \sqrt{\frac{3kT}{m^*}}$, the above result is readily obtained. Here, the usual assumption of quasi-equilibrium is made, so that the majority-carrier quasi-Fermi level is considered constant in the depletion layer.

Application of an external bias voltage results in principle in a shift of the Fermi-levels at the contacts, with respect to each other. Equivalently, this can be described as a departure of the boundary values of the vacuum potential ψ_{vac} from their thermal equilibrium values.

2.2 Modelling of the gap states

In amorphous semiconductors numerous states are present in the mobility gap that act as trapping and recombination centres. In this section, we will discuss the two different types of localised states in the mobility gap of amorphous silicon-based materials and the density-of-states distribution functions that are used for modelling. The present-day models for the electronic states are based on the Cohen-Fritsche-Ovshinsky model [27], and the modifications to this to include the dangling-bond states as well (see for instance Mott and Davis [84] and Street [126]).

Tail states

In crystalline semiconductors periodic variations of the lattice potential give rise to sharply-defined bands of electron states. In contrast, the potential variations in amorphous semiconductors do not show this strict periodic behaviour leading to the existence of tails of localised electron states that penetrate into the bandgap. The conduction band tail states are considered as *single*-electron states that show an acceptor-like behaviour: they are neutral when empty and negatively charged when occupied. The states in the valence band tail behave like donor states.

Based on experimental evidence such as the exponential form of the sub-bandgap absorption spectrum (the Urbach edge) and the characteristics of the Time-of-Flight current transients, it is generally assumed that the density of tail states decreases exponentially into the gap. The slope of the conduction band tail is much steeper than the valence band tail [126]. This results in the following density-of-states functions for the conduction-band tail,

$$N_{cbt}(E) = N_{c0} \exp\left(\frac{E - E_c}{E_{c0}}\right) \tag{2.13}$$

and valence-band tail,

$$N_{vbt}(E) = N_{v0} \exp\left(\frac{E_v - E}{E_{v0}}\right) \tag{2.14}$$

where N_{c0} and N_{v0} is the tail-state DOS at the mobility band edges, and E_{c0} and E_{v0} are the characteristic energies of the exponential decreasing DOS function.

Dangling bond states

In the disordered network of *a*-Si:H there are defects in the form of dangling bonds that give rise to electronic states near the centre of the mobility gap. These energy levels can be removed from their position in the bandgap by hydrogen passivation. Nevertheless, in device quality material about 10^{16} cm^{-3} dangling bonds remain unpassivated, and are the physical origin of the so-called defect states or dangling-bond states.

Dangling bond states show an *amphoteric* (from Greek: αμφότερως: both) character, which means that they simultaneously show a donor- and acceptor-like behaviour. Hence, these states can occupy three different charge states: positively charged when unoccupied, neutral when singly occupied and negatively charged when doubly occupied. A dangling bond can be characterised by two energy levels in the mobility gap: one level, $E^{+/0}$, related to the $+/0$ transition and

another level, $E^{0/-}$, related to the $0/-$ transition. The energy difference between these levels is called the correlation energy, U, which is the energy needed to add a second electron to a singly occupied dangling bond. The correlation energy is the sum of the Coulomb repulsion of the two electrons and the spin attraction caused by the opposite spins of the electrons [84,87]. It is generally accepted that in amorphous silicon-based materials the correlation energy has a positive value.

At present the two most frequently used approaches to model of the dangling-bond density-of-states are:

Gaussian distribution. This simple approach assumes a Gaussian distribution of the dangling-bond transition-energy levels. This is based on the idea that the structural disorder results in a distribution of the dangling-bond energy states. Usually for simplicity no distribution of the correlation energy is assumed, so that both the $E^{+/0}$ and $E^{0/-}$ transition levels have the same Gaussian distribution.

$$N_{db}^{+/0}(E) = N_{db}\frac{1}{\sigma_{db}\sqrt{2\pi}}\exp\left(\frac{-(E-E_{db0}^{+/0})^2}{2\sigma_{db}^2}\right) \quad (2.15)$$

where $N_{db}^{+/0}$ is the distribution of the energy levels related to the +/0 transition, N_{db} is the total number of dangling bonds, $E_{db0}^{+/0}$ is the energy around which the distribution is centred and σ_{db} is the width of the distribution. The distribution of 0/- transition levels is similar to Eq. 2.15 and is centred around $E_{db0}^{0/-} = E_{db0}^{+/0} + U$.

Defect-pool model. In recent years the defect-pool model has been developed. This elaborate thermodynamic model describes the creation of defects as a chemical equilibration process of different bonding configurations at freeze-in temperature. It is based on the process of weak-bond to dangling-bond transformation [127] (See Fig. 2.1). Weak silicon bonds are also called *strained* bonds and correspond with electronic states in the valence band tail. Breaking a weak bond results in two dangling bonds. Hydrogen plays an important role in the conversion process, because hydrogen passivation of one or both of the newly created dangling bonds prevents back-transformation into a weak bond. Hence, the charge state of a dangling bond after bond-breaking influences the final equilibrium of the electron configurations. Therefore, the position of the Fermi level in the mobility gap also influences the dangling-bond concentration. The equilibrium dangling-bond DOS is computed by minimising the free energy of the system of silicon weak bonds, dangling bonds and hydrogen bonds.

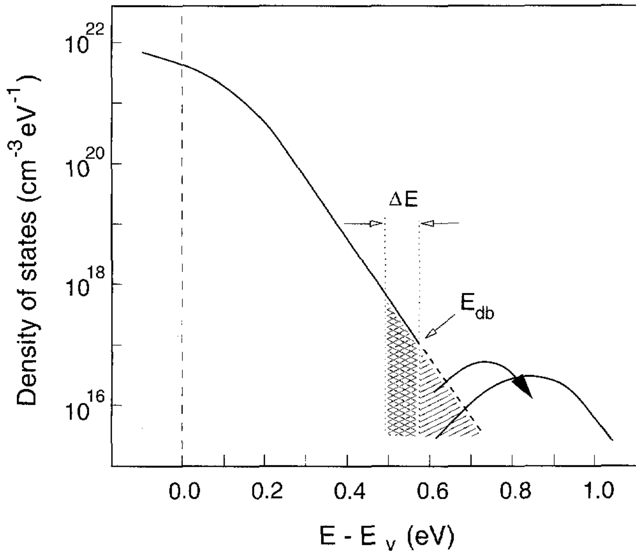

Figure 2.1: Schematic representation of the weak-bond to dangling-bond transformation model. According to this model all weak bonds corresponding to levels in the valence band tail with energies above E_{db} (hatched area in the graph) will decay spontaneously to dangling bonds. The weak bonds in the slightly lower energy range (denoted by the cross-hatched area with width ΔE) will create metastable defects when the material is exposed to stressing conditions (Figure after Stutzmann [127]).

A full derivation of the defect-pool model is beyond the scope of this thesis, and therefore only the basic ideas and formulations will be presented. Powell and Deane [98] published the following expression for the defect distribution, $N_{db}^{+/0}(E)$, derived from their version of the defect-pool model:

$$N_{db}^{+/0}(E) = P(E) N_{v0} \frac{2E_{v0}^2}{2E_{v0} - kT} \exp\left(\frac{-\mu_d(E)}{E_{v0}}\right) \qquad (2.16)$$

where $P(E)$ is the defect-pool function, N_{v0} is the density of states at the valence band mobility edge, E_{v0} is the characteristic slope of the valence band tail, and $\mu_d(E)$ is the defect chemical potential. In the equations of this discussion of the defect-pool model, the energy, E, denotes the $+/0$ transition level. The defect-pool function, $P(E)$, is the distribution of *possible* defect states in the gap; for this

function a Gaussian distribution is assumed

$$P(E) = \frac{1}{\sigma_{db}\sqrt{2\pi}} \exp\left(\frac{-(E-E_p)^2}{2\sigma_{db}^2}\right) \tag{2.17}$$

where σ_{db} is the width of the pool, and E_p is the energy of the peak of defect-pool. The defect chemical potential, μ_d, is the change of free energy in the system caused by the addition of one extra defect. μ_d contains terms to account for the energy of the defect, that depends on its charge state, and on the entropy related to the silicon-hydrogen bonding configurations. Powell and Deane have derived the chemical potential of the defect states as:

$$\mu_d(E) = E + kT\ln\left(\frac{F_{eq}^0(E)}{2}\right) + \frac{ikT}{2}\ln\left(\frac{iN_{db}^{+/0}(E)}{2HP(E)}\right) \tag{2.18}$$

where $F_{eq}^0(E)$ is the equilibrium occupation function of neutral defect states (see page 57), i is the number of hydrogen atoms involved in the defect formation process and H is the hydrogen concentration.

Substitution of μ_d in Eq. 2.16 and rearrangement of terms results in

$$N_{db}^{+/0}(E) = \gamma\left(\frac{2}{F_{eq}^0(E)}\right)^{\rho kT/E_{v0}} P\left(E + \frac{\rho\sigma_{db}^2}{E_{v0}}\right) \tag{2.19}$$

with

$$\gamma = \left(\frac{N_{v0}2E_{v0}^2}{2E_{v0}-kT}\right)^{\rho}\left(\frac{i}{2H}\right)^{\rho-1} \exp\left(\frac{-\rho}{E_{v0}}\left[E_p - E_v - \frac{\rho\sigma_{db}^2}{2E_{v0}}\right]\right) \tag{2.20}$$

and

$$\rho = \frac{2E_{v0}}{2E_{v0}+ikT}. \tag{2.21}$$

The main result of the defect-pool model is that the defect distribution depends on the position of the Fermi-level in the bandgap. To illustrate this dependence, Figure 2.2 shows the defect distribution computed with Eq. 2.19 for three different choices of the Fermi level. The Fermi-level position for each case — p-type, intrinsic and n-type— is indicated by an arrow. Figure 2.2 shows that moving the Fermi-level from the intrinsic position towards one of the band edges increases the concentration of dangling bond states. The displacement of the Fermi-level may be caused either by doping, junction formation (in the i-layer

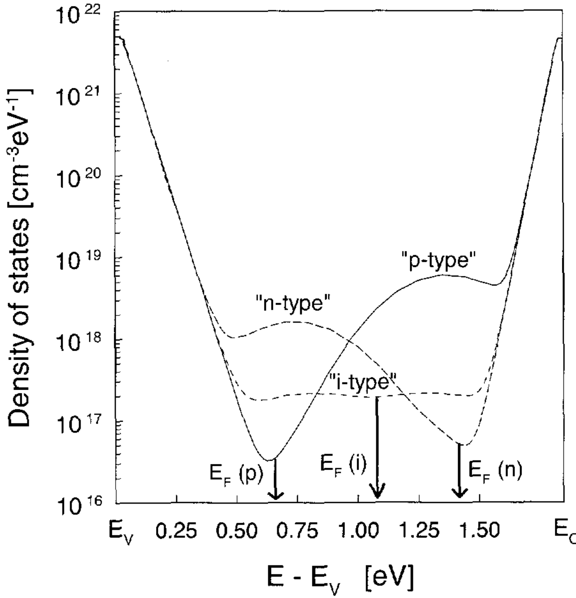

Figure 2.2: Influence of the position of the Fermi-level on the defect distribution. Three different cases are shown: a *p*-type case ($p > n$), intrinsic case, and *n*-type case ($p < n$). The arrows indicate the room temperature positions of the Fermi-levels for each of these cases.

of a *pin* diode), or by application of a gate voltage to a MOS structure. Another characteristic of the distribution of defect states as obtained from the defect-pool model is that the density of states has a minimum near the position of the Fermi-level in non-intrinsic cases (see Fig. 2.2).

The Fermi-level dependence of the defect DOS has consequences for the spatial defect distribution in *a*-Si:H *pin* solar cells. Because the position of the Fermi-level relative to the band edges is position dependent, the defect concentration is position dependent as well. Using the defect-pool model we find that the defect concentration has a minimum in the central part of the *i*-layer and increases towards the doped layers.

2.2.1 Recombination and charge trapping in an arbitrary distribution of states

In crystalline semiconductors usually one discrete energy level in the energy gap dominates the total recombination. Therefore, to model the recombination in these materials one can use models such as the conventional Shockley-Read-Hall

model, which need primarily the carrier lifetimes as input parameters. Amorphous semiconductors require a different approach due to the quasi-continuum of states in the mobility gap. In this type of material the total recombination must be computed by integrating the recombination over all gap states between the valence and conduction band mobility edges, E_v and E_c, respectively. If we define the *recombination efficiency*, $\eta_r(E)$, as the recombination *per* energy state at energy E, we can compute the total recombination as

$$R = \int_{E_v}^{E_c} N(E)\eta_r(E)dE, \tag{2.22}$$

where $N(E)$ is the density of states as a function of energy E in the mobility gap. Equation 2.22 applies both to single-electron levels (tail states) and to two-electron levels (amphoteric states).

The expressions for the space charge trapped in the gap states are similar to Eq. 2.22. However, here we have to distinguish between donor-like and acceptor-like single-electron levels and amphoteric levels. The following two expressions give the space charge in a donor- and an acceptor-like level, respectively.

$$\rho = q\int_{E_v}^{E_c} N(E)[1-f(E)]dE, \tag{2.23}$$

$$\rho = -q\int_{E_v}^{E_c} N(E)f(E)dE. \tag{2.24}$$

In these expressions $f(E)$ is the electron occupation probability. The space charge in an amphoteric states is given by:

$$\rho = q\int_{E_v}^{E_c} N(E)[F^+(E)-F^-(E)]dE, \tag{2.25}$$

where $F^+(E)$ and $F^-(E)$ are the probability functions for empty and doubly occupied dangling bonds, respectively.

From the equations it is obvious that an integration over the gap states is necessary to model the recombination and space charge of amorphous semiconductors. There are different ways to carry out this integration:

- Numerical integration. Using this approach one may use an arbitrary density of gap states distribution and the exact occupation and recombination efficiency functions.

- Analytical integration. Using this approach one is forced to use the so-

called 0 K approximation (step functions approximate the occupation and the recombination efficiency functions) and analytically integrable functions to describe the gap states distribution. This approach is considerably faster than the first one, because no numerical integration is needed.

2.2.2 Recombination and trapping modelling of *a*-Si:H gap states

In general, the approximation is made that localised gap states can only exchange charge carriers with the extended conduction-band and valence-band states. This assumption neglects the possibility of transitions between localised states.

Through this simplification we can use the Shockley-Read-Hall (SRH) model [47, 48, 118] to calculate the occupation function and recombination efficiency of the tail states in *a*-Si:H (single-electron states). For the amphoteric dangling-bond states a more complicated model must be used that takes the possibility of three charge states into account [49, 82, 87, 88, 141]. This model is based on the multi-level statistics, which Sah and Shockley developed [104].

Figure 2.3 schematically depicts the different gap states in *a*-Si:H-based materials and the several models that can be employed for the recombination and charge trapping. These models are discussed in Sect. 2.3. This figure has printed

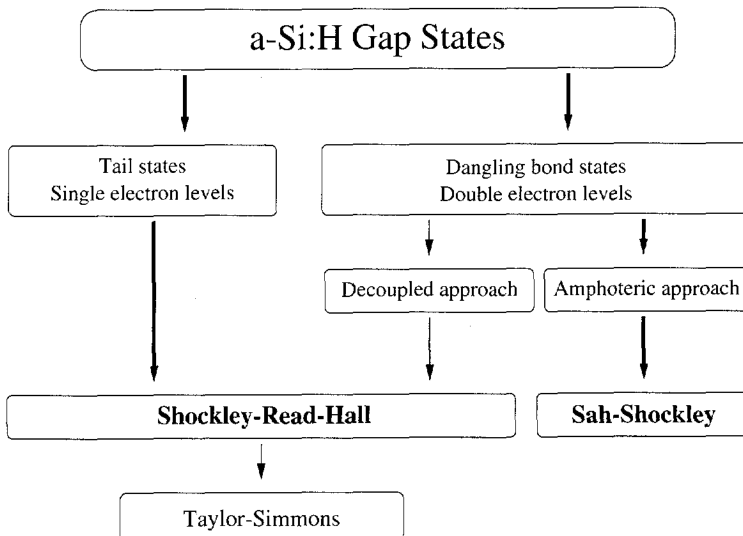

Figure 2.3: The types of amorphous semiconductor gap states and the different models to describe the charge state and recombination. The models printed in boldface are the elementary models to be used in *a*-Si:H device modelling.

in boldface the elementary models to compute charge trapping and recombination in *a*-Si:H devices: Shockley-Read-Hall for the tail states, and Sah-Shockley for the dangling-bond states. The other modelling approaches are simplifications of these: the SRH statistics can be approximated by the approach of Taylor and Simmons [119, 136]. The amphoteric behaviour of the dangling-bond states can be approximated by a pair of single-electron states, which is referred to as the decoupled approach. In turn, the behaviour of the single-electron states can be approximated by the Taylor and Simmons approach. In Appendix B the different modelling approaches and approximations will be subjected to a detailed comparison.

Table 2.1 presents an overview of the recombination models as used in a large selection of published simulation models. It shows whether a certain model uses the complete Shockley-Read-Hall (SRH) statistics or the 0 K Taylor and Simmons (TS) approximation and whether the dangling bonds are described by amphoteric levels (amph.) or by the decoupled approach (decoup.). Simple models that do not take into account both recombination *and* charge trapping (such as the model by Swartz [130]) are not included in the table. The table also shows which dangling-bond DOS distribution is used. If nothing is indicated, these states are modelled by a Gaussian distribution; models which use a different representation of the dangling bond DOS are provided with a note. All simulation models use an exponential function to model the tail states DOS.

2.3 Charge trapping, recombination and thermal generation modelling

2.3.1 Shockley-Read-Hall recombination statistics

The theory of recombination via a single-electron trap has been developed by Hall [47,48] and Shockley and Read [118]. The net recombination through a trap level is determined by the net result of two capture and two emission processes shown schematically in Fig. 2.4. Recombination through a localised state occurs if a state occupied by a hole captures an electron or vise versa. The capture and emission rates are given in Table 2.2. In this table we distinguish donor- and acceptor-like levels, which are denoted by T_d and T_a respectively. The subscripts $+$, 0 and $-$ indicate the charge state, f is the electron occupation function, σ and e are the capture cross section and emission coefficient.

The following derivation of the recombination efficiency and occupation function is limited to donor-like traps; the derivation is analogous for acceptor-like traps. In thermal equilibrium no net recombination occurs and therefore each

Model, author or group	SRH	TS	amph.	decoup.
AMPS, Penn State Univ. [25,79]	•	[a]		•[b]
ASA, Delft Univ. of Techn.	•		•[c]	
ASCA, New Univ. of Lisbon [33,74]		•		•
ASPIN, Ljubljana [120]	•			•[c]
MEDICI, TMI Inc. [137][d]	•			•
SGCSOLAR, Batelle Inst. [12]	•		•	
TFSSP, Purdue Univ. [38,93,114]	•		•	
Bruns *et al.*, Technical Univ. Berlin [15]		•		•
Chatterjee, Indian Ass.Cult.Sci. [22–24]	•			•
Hack *et al.*, ECD Inc. [43–46]		•		[e]
Kreisel, KFA Jülich [67]	•		•[f]	
Misiakos *et al.*, Univ. of Florida [80]		•		[e]
Mittiga *et al.*, La Sapienza, Rome [81]	•			•
Pawlikiewicz *et al.*, ECD Inc. [94,95]		•		•[g]
Sanyo Co. [108]		•		•[h]
Tokyo Institute of Techn. [134,151]		•		•[h]

[a] Early AMPS work contained 0 K Taylor and Simmons approximation [77,78]
[b] Constant or Gaussian dangling-bond DOS
[c] Gaussian or defect-pool dangling-bond DOS
[d] No publications of detailed use for *a*-Si:H solar cells
[e] Tail and defect states not explicitly distinguished
[f] Defect-pool dangling-bond DOS
[g] Exponential dangling-bond distribution
[h] Discrete dangling-bond level, no distribution

Table 2.1: Overview of the recombination and charge trapping models used in a selection of *a*-Si:H simulation programs. The columns *SRH* and *TS* indicate whether the full Shockley-Read-Hall statistics is used or the 0 K Taylor and Simmons approach. The columns *amph.* and *decoup.* indicate whether the amphoteric or decoupled approach is used for the correlated dangling-bond states. Models provided with a note show that not a Gaussian distribution is used, but a different representation of the dangling-bond DOS.

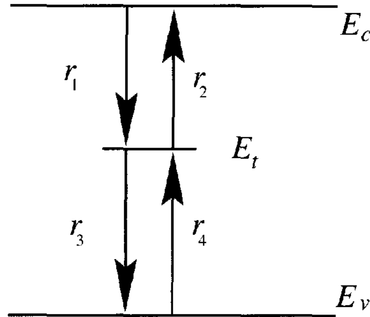

Figure 2.4: Capture and emission processes in a single-electron trap. The rates $r_1 \ldots r_4$ are listed in Table 2.2. Note: the arrows correspond with transitions of *electrons*; the hole transitions are in the opposite direction.

DONOR-LIKE TRAPS

Process		Transition	Rate
electron capture	r_1	$T_d{}^+ + e \rightarrow T_d{}^0$	$n \cdot v_{th} \cdot \sigma_n^+ \cdot N_t \cdot (1-f)$
electron emission	r_2	$T_d{}^0 \rightarrow T_d{}^+ + e$	$e_n^0 \cdot N_t \cdot f$
hole capture	r_3	$T_d{}^0 + h \rightarrow T_d{}^+$	$p \cdot v_{th} \cdot \sigma_p^0 \cdot N_t \cdot f$
hole emission	r_4	$T_d{}^+ \rightarrow T_d{}^0 + h$	$e_p^+ \cdot N_t \cdot (1-f)$

ACCEPTOR-LIKE TRAPS

Process		Transition	Rate
electron capture	r_1	$T_a{}^0 + e \rightarrow T_a{}^-$	$n \cdot v_{th} \cdot \sigma_n^0 \cdot N_t \cdot (1-f)$
electron emission	r_2	$T_a{}^- \rightarrow T_a{}^0 + e$	$e_n^- \cdot N_t \cdot f$
hole capture	r_3	$T_a{}^- + h \rightarrow T_a{}^0$	$p \cdot v_{th} \cdot \sigma_p^- \cdot N_t \cdot f$
hole emission	r_4	$T_a{}^0 \rightarrow T_a{}^- + h$	$e_p^0 \cdot N_t \cdot (1-f)$

Table 2.2: Rates of capture and emission processes in donor- or acceptor-like traps, as schematically depicted in Fig. 2.4.

process is balanced by its inverse process, which means that $r_1 = r_2$ and $r_3 = r_4$. This is called the principle of detailed balancing. In thermal equilibrium the occupation, f, of a single-electron state at E_t is described with the Fermi-Dirac occupation function, $f = [1 + \exp\left(\frac{E_t - E_f}{kT}\right)]^{-1}$. By the application of the principle of detailed balance the emission coefficients are obtained:

$$e_n^0 = v_{th}\sigma_n^+ N_c \exp\left(\frac{E_t - E_c}{kT}\right) \tag{2.26}$$

$$e_p^+ = v_{th}\sigma_p^0 N_v \exp\left(\frac{E_v - E_t}{kT}\right). \tag{2.27}$$

In non-equilibrium steady-state conditions the recombination rate, R, equals the net rate at which electrons disappear from the conduction band and the holes from valence band. Since electrons and holes recombine as pairs both rates should be equal.

$$\begin{aligned} R &= \frac{dn}{dt} = \frac{dp}{dt} \Rightarrow \\ R &= r_1 - r_2 = r_3 - r_4. \end{aligned} \tag{2.28}$$

From the rates in Table 2.2 and Eq. 2.28 the occupation function, f, can be determined,

$$f = \frac{n v_{th}\sigma_n^+ + e_p^+}{n v_{th}\sigma_n^+ + p v_{th}\sigma_p^0 + e_n^0 + e_p^+}. \tag{2.29}$$

Finally, the recombination R is readily found by substituting the rates and occupation function in Eq. 2.28. The recombination efficiency, η_r, follows from $\eta_r = \frac{R}{N_t}$,

$$\eta_r = v_{th}^2 \sigma_n^+ \sigma_p^0 \frac{np - n_i^2}{n v_{th}\sigma_n^+ + p v_{th}\sigma_p^0 + e_n^0 + e_p^+}. \tag{2.30}$$

2.3.2 Taylor and Simmons approximation

Taylor and Simmons [119, 136][1] have derived an elegant approximation for the SRH statistics, for application to recombination problems with a continuous dis-

[1] Ref. 119 contains typographic errors in the equations, but the general idea is correct.

tribution of gap states instead of one or a few discrete recombination levels. This approach reduces the complete SRH expressions to much simpler expressions and thus increases insight into this difficult matter. Especially the 0 K approximation is a widely used approach for modelling SRH recombination through single-electron states inside the mobility gap of amorphous semiconductors. In this approximation the smoothly formed recombination function, Eq. 2.30, and occupation function, Eq. 2.29, are replaced by step functions. Hack and Shur [43–46] first introduced this approach to *a*-Si:H solar cell modelling and many others followed.

For the Taylor and Simmons approximation it is assumed that all traps have the same capture cross section, independent of the energy level of the trap. However, if there are different types of traps each with constant, energy independent capture cross sections, we can apply the Taylor and Simmons approximation to each of these types individually; the total recombination and space charge is obtained by summing the contributions of all types.

From Eqns. 2.26 and 2.27 we can see that the emission coefficient of a carrier decreases with increasing separation from its corresponding band. Hence, we can define an energy level E_{t0} at which the emission coefficients for electrons and holes are equal, $e_n^0 = e_p^+$. (Here, we use the notations for donor-like traps; the results apply analogously to acceptor-like states.) As we can see from its definition, the *intrinsic trap level*[2], E_{t0},

$$E_{t0} = \frac{E_v + E_c}{2} - \frac{kT}{2} \cdot \ln\left(\frac{\sigma_n^+ N_c}{\sigma_p^0 N_v}\right) \tag{2.31}$$

is located near the intrinsic Fermi level; the difference between those levels is determined by the ratio of the capture cross sections.

The electron emission coefficient of a trap level located more than $3kT$ above E_{t0} is much larger than its hole emission coefficient, therefore the latter may be neglected. Consequently, the SRH occupation function, Eq. 2.29, can be approximated by

$$f = \frac{n v_{th} \sigma_n^+}{n v_{th} \sigma_n^+ + p v_{th} \sigma_p^0 + e_n^0}. \tag{2.32}$$

For levels that are more than a few kT below E_{t0} it is more convenient to consider the hole occupation function, which is the complement of the electron occupation

[2] Taylor and Simmons speak about the intrinsic Fermi level in this respect, but here we rather use the term intrinsic trap level to avoid confusion with the usual meaning of intrinsic Fermi level.

function: $1-f$. Analogously, the electron emission coefficient is negligible for these levels, so the hole occupation probability can be written as

$$1-f=\frac{pv_{th}\sigma_p^0}{nv_{th}\sigma_n^+ + pv_{th}\sigma_p^0 + e_p^+}. \tag{2.33}$$

Rearrangement of terms in Eq. 2.32 gives

$$f=\frac{n\sigma_n^+}{n\sigma_n^+ + p\sigma_p^0}\left[1+\frac{e_n^0}{nv_{th}\sigma_n^+ + pv_{th}\sigma_p^0}\right]^{-1} \tag{2.34}$$

where the term between the square brackets is in fact a Fermi-Dirac function, because the emission coefficient depends exponentially on the energy of the trapping level. The quasi-Fermi level for trapped electrons, E_{fn_t}, is defined as the energy at which the condition $e_n^0 = nv_{th}\sigma_n^+ + pv_{th}\sigma_p^0$ is satisfied:

$$E_{fn_t}=E_c+kT\ln\left(\frac{n\sigma_n^+ + p\sigma_p^0}{N_c\sigma_n^+}\right). \tag{2.35}$$

By using this definition we transform Eq. 2.34 into

$$f=\frac{n\sigma_n^+}{n\sigma_n^+ + p\sigma_p^0}\left[1+\exp\left(\frac{E_t-E_{fn_t}}{kT}\right)\right]^{-1} \tag{2.36}$$

which can be considered as a *scaled* Fermi-Dirac occupation function. Analogously, the hole occupation, $1-f$, can be written as

$$1-f=\frac{p\sigma_p^0}{n\sigma_n^+ + p\sigma_p^0}\left[1+\exp\left(\frac{E_{fp_t}-E_t}{kT}\right)\right]^{-1} \tag{2.37}$$

which uses the quasi-Fermi level for the trapped holes, E_{fp_t}, defined by

$$E_{fp_t}=E_v-kT\ln\left(\frac{n\sigma_n^+ + p\sigma_p^0}{N_v\sigma_p^0}\right). \tag{2.38}$$

Combining Eqns. 2.36 and 2.37 we obtain the occupation function according to the Taylor and Simmons approximation. Its main characteristic is that it is a smooth step function that goes from 1 to $\frac{n\sigma_n^+}{n\sigma_n^+ + p\sigma_p^0}$ near E_{fp_t}, and from $\frac{n\sigma_n^+}{n\sigma_n^+ + p\sigma_p^0}$ to 0 near E_{fn_t}. Between the two quasi-Fermi levels for trapped charges the occupation probability is approximately a constant value.

In a similar derivation the recombination efficiency function, η_r, (Eq. 2.30) can be approximated by

$$\eta_r = v_{th} \frac{\sigma_n^+ \sigma_p^0 np}{n \cdot \sigma_n^+ + p \cdot \sigma_p^0} \left[1 + \exp\left(\frac{E_t - E_{fn_t}}{kT} \right) \right]^{-1} \quad \text{for} \quad E_t > E_{t0} \tag{2.39}$$

$$\eta_r = v_{th} \frac{\sigma_n^+ \sigma_p^0 np}{n \cdot \sigma_n^+ + p \cdot \sigma_p^0} \left[1 + \exp\left(\frac{E_{fp_t} - E_t}{kT} \right) \right]^{-1} \quad \text{for} \quad E_t < E_{t0}. \tag{2.40}$$

From these equations we can conclude that only the traps located between the quasi-Fermi levels for trapped charges contribute effectively to the recombination, and that the recombination efficiency, η_r, of those levels is approximately a constant value.

In the 0 K approximation the smooth transitions near the quasi-Fermi levels for trapped charges are replaced by step functions. This renders a staircase function for the occupation and a rectangular block function for the recombination efficiency. The 0 K approximation simplifies the calculation of trapped charge density and recombination in a distribution of traps. For instance the recombination calculation of Eq. 2.22 is replaced by

$$R = v_{th} \frac{\sigma_n^+ \sigma_p^0 np}{n \cdot \sigma_n^+ + p \cdot \sigma_p^0} \int_{E_{fp_t}}^{E_{fn_t}} N(E) dE, \tag{2.41}$$

and the trapped charge computation of acceptor-like localised states (Eq. 2.24) is simplified to

$$\rho = -q \left(\int_{E_v}^{E_{fp_t}} N(E) dE + \frac{n\sigma_n^+}{n\sigma_n^+ + p\sigma_p^0} \int_{E_{fp_t}}^{E_{fp_n}} N(E) dE \right). \tag{2.42}$$

If suitable functions are chosen for $N(E)$a, the integrations in Eqns. 2.41 and 2.42 can be carried out analytically, so that numerical integration over the complete density-of-states is not required. Therefore, this approach is considerably faster than the computation of the complete SRH statistics.

As an illustration of the Taylor and Simmons treatment Fig. 2.5 shows the occupation function and the recombination efficiency function for the parameter sets listed in Table 2.3. The parameters which where kept constant are: temperature $T = 300$ K, effective density of states $N_{c,v} = 3 \cdot 10^{20}$ cm^{-3}, mobility gap $E_g = 1.8$ eV, and thermal velocity $v_{th} = 10^7$ cm/s. The error of the Taylor and Simmons approximation with respect to the SRH expressions is negligible for these choices of parameters. However, in all cases where both capture rate coef-

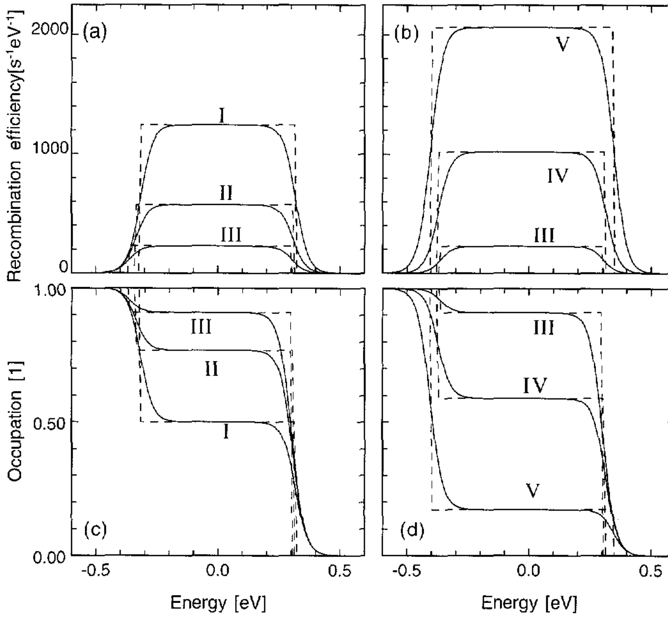

Figure 2.5: (a) and (b) Recombination efficiency, and (c) and (d) occupation function according to the Taylor and Simmons approximation of the SRH statistics (solid lines) for different parameters, as listed in Table 2.3. (a) and (c) show the influence of changing the capture cross sections; (b) and (d) show the influence of changing the free carrier quasi-Fermi levels. Also shown are the 0 K approximations (dotted lines). $E = 0$ eV corresponds with midgap.

Parameter	unit	set I	set II	set III	set IV	set V
σ_n^+	10^{-15} cm^2	10	10	10	10	10
σ_p^0	10^{-15} cm^2	10	3	1	1	1
$E_c - E_{fn}$	eV	0.60	0.60	0.60	0.60	0.60
$E_{fp} - E_v$	eV	0.60	0.60	0.60	0.55	0.50
$E_c - E_{fn_t}$	eV	0.582	0.593	0.598	0.584	0.555
$E_{fp_t} - E_v$	eV	0.582	0.562	0.538	0.527	0.495

Table 2.3: Parameters used for the recombination efficiency and occupation curves of Fig. 2.5. The values of the free electron and hole quasi-Fermi levels are relative to the conduction and valence band mobility edges, E_c and E_v, respectively.

ficients, $n \cdot v_{th} \cdot \sigma_n^+$ and $p \cdot v_{th} \cdot \sigma_p^0$, are *not* much larger than one of the emission coefficients, e_p^+ or e_n^0, considerable errors will be made. This is for instance the case when there is thermal generation and both the electron and hole concentration are much smaller than the intrinsic carrier concentration, or when both free carrier quasi-Fermi levels are close to the intrinsic trap level E_{t0}.

Figure 2.5 also shows the 0 K approximation, in which case the functions show steps at the positions of the quasi-Fermi levels for trapped charges. The 0 K approximation is an elegant and accurate computation procedure in cases where the gap DOS distribution does not change considerably within a range in the order of the thermal energy kT around the trapped charge quasi-Fermi levels. The validity of the 0 K approximation for exponential density of states distributions will be discussed in Appendix B.

2.3.3 Recombination and charge trapping at amphoteric states

The theory of Sah and Shockley [104] developed for states with multiple charge levels is the most accurate method to compute the recombination and charge trapping at an amphoteric three-state level. Figure 2.6 shows schematically the capture and emission processes of an amphoteric state with two transition levels, $E^{+/0}$ and $E^{0/-}$. Table 2.4 lists the rates of these processes. Here, a D denotes a dangling-bond state, and its superscript gives the charge state. The symbols F^+, F^0 and F^- denote the occupation function; these represent the probability that a dangling bond is in a positive, neutral or negative charge state.

Again, the emission coefficients can be determined by the principle of detailed balance. With the thermal equilibrium electron and hole concentrations,

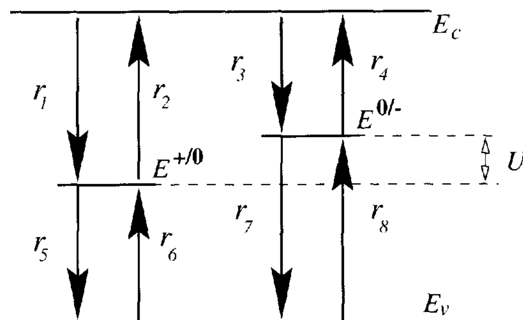

Figure 2.6: Schematic representation of the capture and emission processes for a three-state trap level. The expressions for the transition rates are summarised in Table 2.4. Note: the arrows correspond with transitions of *electrons*; the hole transitions are in the opposite direction.

AMPHOTERIC STATES

Process		Transition	Rate
electron capture	r_1	$D^+ + e \rightarrow D^0$	$n \cdot v_{th} \cdot \sigma_n^+ \cdot N_{DB} \cdot F^+$
electron emission	r_2	$D^0 \rightarrow D^+ + e$	$e_n^0 \cdot N_{DB} \cdot F^0$
electron capture	r_3	$D^0 + e \rightarrow D^-$	$n \cdot v_{th} \cdot \sigma_n^0 \cdot N_{DB} \cdot F^0$
electron emission	r_4	$D^- \rightarrow D^0 + e$	$e_n^- \cdot N_{DB} \cdot F^-$
hole capture	r_5	$D^0 + h \rightarrow D^+$	$p \cdot v_{th} \cdot \sigma_p^0 \cdot N_{DB} \cdot F^0$
hole emission	r_6	$D^+ \rightarrow D^0 + h$	$e_p^+ \cdot N_{DB} \cdot F^+$
hole capture	r_7	$D^- + h \rightarrow D^0$	$p \cdot v_{th} \cdot \sigma_p^- \cdot N_{DB} \cdot F^-$
hole emission	r_8	$D^0 \rightarrow D^- + h$	$e_p^0 \cdot N_{DB} \cdot F^0$

Table 2.4: Capture and emission processes in a three-state amphoteric level

$n_{eq} = N_c \exp(\frac{E_f - E_c}{kT})$, and $p_{eq} = N_v \exp(\frac{E_v - E_f}{kT})$, and with the equilibrium occupation probabilities, F_{eq}^+, F_{eq}^0, and F_{eq}^-, [87,117]

$$F_{eq}^+ = \frac{1}{1 + 2\exp\left(\frac{E^{+/0} - E_f}{kT}\right) + \exp\left(\frac{E^{-/0} + E^{0/-} - 2E_f}{kT}\right)}, \tag{2.43}$$

$$F_{eq}^0 = \frac{2\exp\left(\frac{E^{+/0} - E_f}{kT}\right)}{1 + 2\exp\left(\frac{E^{+/0} - E_f}{kT}\right) + \exp\left(\frac{E^{+/0} + E^{0/-} - 2E_f}{kT}\right)}, \tag{2.44}$$

$$F_{eq}^- = \frac{\exp\left(\frac{E^{+/0} + E^{0/-} - 2E_f}{kT}\right)}{1 + 2\exp\left(\frac{E^{+/0} - E_f}{kT}\right) + \exp\left(\frac{E^{+/0} + E^{0/-} - 2E_f}{kT}\right)}, \tag{2.45}$$

the emission coefficients are readily found as

$$e_n^0 = v_{th} \sigma_n^+ n_{eq} \frac{F_{eq}^+}{F_{eq}^0} = \frac{1}{2} v_{th} \sigma_n^+ N_c \exp\left(\frac{E^{+/0} - E_c}{kT}\right), \tag{2.46}$$

$$e_n^- = v_{th} \sigma_n^0 n_{eq} \frac{F_{eq}^0}{F_{eq}^-} = 2 v_{th} \sigma_n^0 N_c \exp\left(\frac{E^{0/-} - E_c}{kT}\right), \tag{2.47}$$

$$e_p^+ = v_{th}\sigma_p^0 p_{eq}\frac{F_{eq}^0}{F_{eq}^+} = 2v_{th}\sigma_p^0 N_v \exp\left(\frac{E_v - E^{+/0}}{kT}\right), \tag{2.48}$$

$$e_p^0 = v_{th}\sigma_p^- p_{eq}\frac{F_{eq}^-}{F_{eq}^0} = \frac{1}{2}v_{th}\sigma_p^- N_v \exp\left(\frac{E_v - E^{0/-}}{kT}\right). \tag{2.49}$$

The factors 2 and $\frac{1}{2}$ in these equations follow from the twofold degeneracy of the singly-occupied dangling-bond level [28].

In steady-state non-equilibrium conditions there is net generation or recombination and the occupation probabilities are unequal to their thermal-equilibrium counterparts. The statistics can be obtained by the rate equations of the occupation functions,

$$\frac{dF^+}{dt} = -nv_{th}\sigma_n^+ F^+ + e_n^0 F^0 + pv_{th}\sigma_p^0 F^0 - e_p^+ F^+, \tag{2.50}$$

$$\frac{dF^-}{dt} = nv_{th}\sigma_n^0 F^0 - e_n^- F^- - pv_{th}\sigma_p^- F^- + e_p^0 F^0. \tag{2.51}$$

In steady-state these rate equations are equal to zero and in combination with the condition that the sum of the occupation probabilities is unity, $(F^+ + F^0 + F^- = 1)$, the occupation functions can be obtained

$$F^+ = \frac{P^0 P^-}{N^+ P^- + P^0 P^- + N^+ N^0}, \tag{2.52}$$

$$F^0 = \frac{N^+ P^-}{N^+ P^- + P^0 P^- + N^+ N^0}, \tag{2.53}$$

$$F^- = \frac{N^0 N^+}{N^+ P^- + P^0 P^- + N^+ N^0}. \tag{2.54}$$

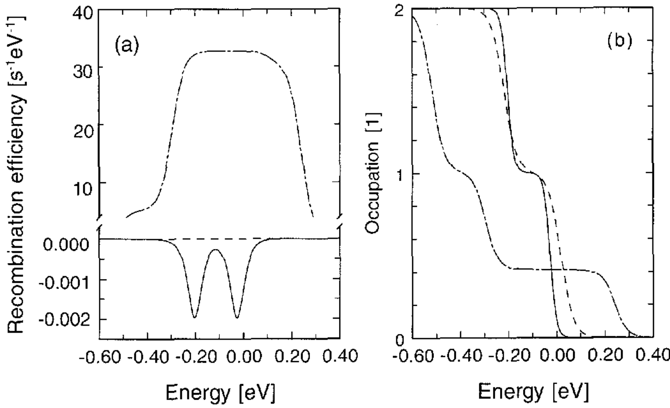

Figure 2.7: Some typical cases of the recombination efficiency function (a) and occupation function (b) in the amphoteric model. The full line corresponds to a case with thermal generation (thus negative recombination), the dashed line corresponds with thermal equilibrium and the dashed-dotted line corresponds with a recombination case. The energy axis corresponds with the position of the transition energy $E^{+/0}$ of the dangling bond. $E = 0$ eV corresponds to midgap. Note the different scales on the positive and negative recombination-axis in (a).

Here, for readability the following variables have been defined:

$$\begin{aligned} N^+ &= nv_{th}\sigma_n^+ + e_p^+ \\ N^0 &= nv_{th}\sigma_n^0 + e_p^0 \\ P^- &= pv_{th}\sigma_p^- + e_n^- \\ P^0 &= pv_{th}\sigma_p^0 + e_n^0. \end{aligned} \tag{2.55}$$

From these occupation functions and the rates of the capture and emission processes, the net recombination efficiency, $\eta_r = r_1 - r_2 + r_3 - r_4$, is obtained

$$\eta_r = v_{th}^2(pn - n_i^2)\frac{\sigma_n^+\sigma_p^0 P^- + \sigma_n^0\sigma_p^- N^+}{N^+P^- + P^0P^- + N^+N^0}. \tag{2.56}$$

The average charge Q per dangling bond is

$$Q = q(F^+ - F^-). \tag{2.57}$$

As an illustration Fig. 2.7 shows the occupation function and the recombination efficiency function of amphoteric states. It includes three different cases: thermal generation, thermal equilibrium, and recombination. Table 2.5 lists the

Quasi Fermi level	unit	Generation	Equilibrium	Recombination
$E_c - E_{fn}$	eV	1.30	0.90	0.70
$E_{fp} - E_v$	eV	1.30	0.90	0.60

Parameter	Unit	Value
σ_p^-	cm^2	$3 \cdot 10^{-15}$
σ_p^0	cm^2	$3 \cdot 10^{-16}$
σ_n^+	cm^2	$1 \cdot 10^{-14}$
σ_n^0	cm^2	$1 \cdot 10^{-15}$

Parameter	Unit	Value
T	K	300
U	eV	0.2
N_c, N_v	cm^{-3}	$3 \cdot 10^{20}$
E_g	eV	1.8
v_{th}	cm/s	10^7

Table 2.5: Parameters used for the graphs in Fig. 2.7.

corresponding parameters. The energy axis corresponds with the $+/0$ transition energy of the amphoteric level with respect to midgap. The occupation plot depicts the average number of electrons that occupies a dangling bond as a function of its transition energy $E^{+/0}$; a value of 1 or 2 means that on the average the dangling bond is singly occupied (neutral) or doubly occupied (negative), respectively. In the case of generation the form of the efficiency and occupation function does not depend to a great extent on the actual values of the quasi-Fermi levels, because in this case the functions are mainly determined by the emission coefficients. On the other hand, in cases of recombination the functions show strongly varying shapes.

2.3.4 Amphoteric states modelled by a pair of uncorrelated states

In many simulation models the behaviour of amphoteric dangling-bond states is modelled by the decoupled approach (*cf.* Table 2.1). Instead of describing a dangling bond as a single defect characterised by two correlated transition energy levels, in the decoupled approach a dangling bond is described by a pair of uncorrelated single-electron states. This pair consists of a donor-like level positioned at $E^{+/0} - kT\ln(2)$ and an acceptor-like level at $E^{0/-} + kT\ln(2)$. The shifts of $kT\ln(2)$ with respect to the transition energies of the original amphoteric level are caused by the twofold degeneracy of the neutral charge state of a dangling bond [98], and can be inferred from a comparison between the emission coefficients of amphoteric states, Eqns. 2.46 – 2.49, and the emission coefficients of single-electron states, Eqns. 2.26 and 2.27 [49]. Hence, in the decoupled approach the *effective* correlation energy separating the T_d and T_a levels is $kT\ln(4)$

larger than the correlation energy of the amphoteric defect [98].

The problem with the decoupled approach is that each single defect, capable of electron and hole capture, is replaced by two traps that are independently capable of trapping carriers. Hence, the decoupled approach gives rise to a higher recombination rate than the amphoteric defect, where the exact deviation depends on the actual values of the capture cross sections. Furthermore, in the decoupled approach it is in principle possible that both the acceptor and donor level are in their charged state, thus giving a net zero contribution to the space charge density. This situation does not actually occur in defect states, since it is physically impossible that zero and two electrons both occupy a dangling bond at the same time. However, if the correlation energy is much larger than the thermal energy kT the probability that this situation occurs is very low.

Halpern [49] has assessed mathematically the validity of the decoupled approximation of the amphoteric defects. To simplify the expressions and to obtain comprehensible results he made several approximations and assumptions. His conclusion is that if the correlation energy U is much larger than the thermal energy the decoupled approach gives under all circumstances accurate values for the space charge trapped by a dangling bond. Further, he concludes that under some restrictive conditions (the ratios of the capture cross sections for charged and neutral states must be approximately equal, *vis.* $\frac{\sigma_n^+}{\sigma_n^0} \approx \frac{\sigma_p^-}{\sigma_p^0}$) the recombination that is due to dangling bonds is approximated fairly accurately.

Suntharalingam *et al.* [129] compare the decoupled approach to the amphoteric approach in an intuitive way. In accordance with the result of Halpern, they conclude that the decoupled approach gives a good approximation of the space charge. They also conclude that the recombination rate will be overestimated. However, their conclusion is that the overestimation is in the order of the ratio of the capture cross sections of neutral states to charged states, $\frac{\sigma_n^0}{\sigma_n^-}$ and $\frac{\sigma_p^0}{\sigma_p^-}$. In this respect the results of Suntharalingam *et al.* and Halpern are contradictory. A detailed comparison of the amphoteric model and the approximation by a pair of decoupled one-electron states is discussed in Appendix B.

2.3.5 Trap-assisted tunnelling recombination model

Hurkx *et al.* [60] have developed a recombination model including tunnelling for use in a numerical device simulator. This model can successfully reproduce the excess-current (including its temperature dependence) in heavily doped diodes under low forward-bias conditions. The main problem with the inclusion of tunnelling mechanisms in a device simulator is that the probability of tunneling through a potential barrier depends on non-local properties. The numerical

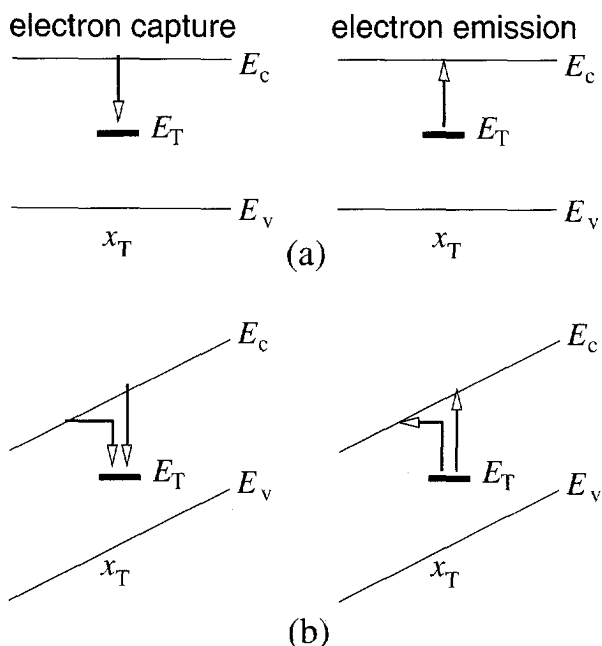

Figure 2.8: (a) Electron capture and emission in absence of electric fields: only electrons that are physically present at position x_T contribute to the processes. (b) Electrons capture and emission in the presence of a high electric field: more electrons can be captured, because of contribution of electrons tunnelling from other positions than x_T. Emission probabilities are increased by phonon-assisted tunnelling.

solution of the semiconductor transport equations, Eqns. 2.1 – 2.3, only requires that the physical variables of the directly neighbouring mesh points are known at each individual mesh point. Therefore, the straightforward implementation of non-local (tunneling) current and recombination mechanisms is complicated.

By making suitable approximations Hurkx *et al.* have developed a model that (1) only depends on local variables, (2) can be expressed with analytic functions, (3) only adds one new parameter, an effective tunnelling mass, and (4) is an extension to the well-established SRH expression (when the electric field is zero the tunneling recombination model equals the SRH model). For all these reasons this model is very suitable for device simulations.

The principles of the trap-assisted tunnelling recombination model are explained with the help of Fig. 2.8. Without accounting for the possibility of tunnelling a trap at position x_T can only capture free electrons and holes, if they occupy this same physical position x_T in the semiconductor. However, if the trap

is located in a region where a high electric field is present, there is a finite probability that carriers from other locations than x_T can reach the trap by tunnelling. On the other hand the emission of trapped electrons or holes in the high field regions is enhanced by the phonon-assisted tunnelling process (in the figure we have neglected the possibility of emission enhancement caused by the Poole-Frenkel effect). Hurkx *et al.* [60] show that the field-dependent enhancement of the emission coefficients and the carrier concentration effectively available for trapping are increased by the same field-dependent factors, Γ_n and Γ_p, for electrons and holes, respectively:

$$\frac{n_{eff}}{n} = \frac{e_n^t}{e_n} = \Gamma_n + 1 \tag{2.58}$$

$$\frac{p_{eff}}{p} = \frac{e_p^t}{e_p} = \Gamma_p + 1, \tag{2.59}$$

where p_{eff} and n_{eff} are the effective concentrations of carriers at x_T , and $e^t_{(n,p)}$ is the emission coefficient which is increased by phonon-assisted tunnelling. With these field-dependent factors the recombination efficiency function Eq. 2.30 is changed into:

$$\eta_r = \frac{v_{th}^2 \sigma_n^+ \sigma_p^0 \cdot (\Gamma_n + 1) \cdot (\Gamma_p + 1) \cdot (np - n_i^2)}{(\Gamma_n + 1) \cdot (n v_{th} \sigma_n^+ + e_n^0) + (\Gamma_p + 1) \cdot (p v_{th} \sigma_p^0 + e_p^+)}. \tag{2.60}$$

From this equation we can infer that an effective increase of carriers at a trap site (Eq. 2.58) can also be attributed to an effective increase of the capture cross sections, *e.g.* $\sigma_{n,eff} = \sigma \cdot (\Gamma_n + 1)$.

By making suitable approximations the factors Γ_n and Γ_p can be written as:

$$\Gamma_{n,p} = \frac{\Delta E_{n,p}}{kT} \int_0^1 \exp\left[\frac{\Delta E_{n,p}}{kT} u - K_{n,p} u^{3/2}\right] du, \tag{2.61}$$

where

$$K_{n,p} = \frac{4}{3} \frac{\sqrt{2m^* \Delta E_{n,p}^3}}{q\hbar |\vec{E}|}. \tag{2.62}$$

Approximate analytic expressions for the field-dependent factors, $\Gamma_{n,p}$, are derived for implementation in device simulators, for which we refer to Hurkx *et al.* [60].

The integration interval, $\Delta E_{n,p}$, depends on the relative position of the trap level to the conduction band minimum or valence band maximum in the neutral regions around the depletion layer. If the trap level is below the minimum of the conduction band, then ΔE_n equals only a part of the total interval $E_c - E_t$, *vis.* $\Delta E_n = E_c - E_{cn}$, where E_{cn} is the minimum value of the conduction band edge from which electrons can tunnel.

Chapter 3

Simulation program for amorphous silicon devices: ASA

In this chapter we introduce our simulation program Amorphous Semiconductor Analysis, ASA. This device simulator is developed for the study of solar cells made of amorphous silicon and related materials. The physical models implemented in ASA and its other features are discussed.

3.1 Simulation modes

The main use of ASA is the simulation of amorphous silicon solar cells for research purposes. The program can simulate different characteristics of these devices:

- Thermal equilibrium state. In this case the electrical state of the device without bias voltage or illumination is computed. In this mode only the Poisson equation is solved; the continuity equations are not solved because there is no current flow in the device.

- Steady-state current-voltage (IV) characteristics of devices with and without illumination. These characteristics result from the solution of the full set of semiconductor equations, Eqns. 2.1–2.5, at different bias voltages. At each bias voltage output can be generated of all internal quantities, such as recombination rates and electric field distributions.

- External Quantum Efficiency (EQE) simulations with and without bias illumination. The EQE is determined from $\Delta I/q\Delta n_{photon}$ as a function of

wavelength, where I is the steady-state current flowing through the terminals of the device, and Δn_{photon} is the differential number of photons between the bias spectrum, S, and the bias spectrum plus the monochromatic probe light, $S + \Delta n_{photon}$. ASA computes generation profiles for both the spectrum S and $S + \Delta n_{photon}$, which are both used to compute the terminal current. The EQE without bias illumination is computed simply by choosing a bias spectrum S with zero intensity. When using a non-zero bias spectrum the differential EQE is computed. The user can define the number of monochromatic photons and the bias voltage of the device.

- Quasi steady-state capacitance-voltage (CV) characteristics, with and without illumination. The capacitance is determined from $\Delta Q/\Delta V$. Two steady-state solutions are computed; one at $V - \frac{1}{2}\Delta V$ and another $V + \frac{1}{2}\Delta V$; ΔQ is determined from the difference of all positive or negative charges (space charge in the device *and* surface charge at the contacts in case of non-zero electric field at the contacts) at these biases.

- Reflection-Transmission (RT) simulation of flat layered structures with normally incident light. Internal reflections at all interfaces and interference of incident and reflected light are taken into account. The user can define one layer in which coherence between incident and reflected light is not taken into account, and thus interference effects are not present.

- Optical carrier generation rate profiles, which bias the device for illuminated IV- and CV-simulations and EQE-simulations. The different models for the optical generation rate are discussed below. Alternatively, generation rate profiles can be imported from other simulators (such as Genpro2 [133]) by means of ASCII data files.

3.2 Definition of the simulation structure

The device structure is defined as follows:

- One-dimensional.

- Two terminal devices.

- The basic unit to define a simulation structure in ASA is the *layer*.

- The electrically-active part of the device is defined as one or more layers of semiconductor material. In addition, layers that are only relevant to the optical behaviour may be added to the front and back of the device.

- Most model parameters can be defined independently for each layer.
- If defined in the main input file, most of the physical properties are constant within the individual layers. However, it is possible to assign position-dependent material parameters by using ASCII data files; these files contain two columns: the coordinate axis and the position-dependent parameter values.
- Very flexible simulation grid generation: equi-distant or exponentially in- or decreasing grid spacings can be defined independently for each layer. The simulation grid can also be read from a data file.

3.3 Heterojunctions

ASA can simulate abrupt and linearly graded heterojunctions. Mobility gap and electron affinity may change abruptly at interfaces or linearly in a layer. The presence of heterojunctions is modelled by the gradient terms of the electron affinity, χ, the logarithm of the effective extended states DOS, $\ln(N_c)$ or $\ln(N_v)$, and the mobility gap, E_g, in Eqns. 2.8 and 2.9. In graded heterojunctions these quantities are continuous functions of the position. On the other hand, these quantities show a step-like change at the position of abrupt heterojunctions; a very narrow simulation grid spacing must be chosen at the position of this heterojunction in order to simulate it correctly.

3.4 Mobilities

The free electron and hole mobilities can be set to constant values in each of the layers, or alternatively, they can be imported using an ASCII data file.

3.5 Doping profile

There are two ways to define a *uniform* doping concentration in a layer:

1. define the net concentration of active acceptors or donors.
2. define the difference between the conduction or valence mobility edge and the Fermi level; this difference is usually referred to as the conduction activation energy, E_{act}. (Note that the experimentally measured value of the E_{act} does not necessarily correspond with the exact position of the Fermi level with respect to the majority-carrier mobility edge.) The actual doping

that corresponds with the user-defined difference between Fermi-level and majority-carrier mobility edge is the concentration that gives *zero* space charge in the material in thermo-dynamic equilibrium conditions; ASA determines this concentration at the first grid point inside a layer and assigns this value to all other points of that layer.

These definitions of the doping concentration are given in the input file of ASA. Alternatively, ASA can read doping profiles from data files; this enables the use of *arbitrary* doping profiles. If the coordinates in the data file do not match the coordinates of the gridpoints, the doping profile will be interpolated logarithmically between two gridpoints (only if the concentrations in the data file are unequal to zero).

3.6 Recombination and charge trapping models

Three types of states are implemented in ASA to describe the properties of amorphous-silicon-based materials in detail:

- *Amphoteric dangling bond states.* There are two models to define the dangling bond density-of-states distribution:

  1. Gaussian density of states (Eq. 2.15).
  2. Density of states according to the defect-pool model of Powell and Deane [98] (see also Sect. 2.2). If this model is chosen the thermal equilibrium state at the freeze-in temperature is computed self-consistently with the Fermi-level-dependent dangling bond DOS; the computed dangling bond distribution is used in subsequent device simulations.

  For both models for dangling bond DOS distributions the amphoteric three-states model is used as recombination and charge trapping model (see Sect. 2.3.3).

- *Acceptor-like conduction band tail states,* and

- *Donor-like valence band tail states.* The distribution of these single-electron states is described by exponential functions, Eqns. 2.13 and 2.14. The full Shockley-Read-Hall model is used to compute the occupation and the recombination (see Sect. 2.3.1).

The following points apply to all three types of states:

- The capture cross sections are *independent* of the energy in the mobility gap. All capture cross sections can be defined independently for each type of gap state.

- In ASA the continuous energy scale of the DOS distributions is discretised in a number of energy intervals of equal extent. The user can define the number of intervals and the total energy range over which a particular type of localised states extends. The DOS within each energy interval is integrated, and the integrated value is assigned to an energy level in the centre of the interval. The discretised DOS distribution is used to compute the total space charge and recombination rate; the contributions of all discrete levels are summed.

Further, the conventional SRH recombination model, which computes the recombination rate through a single midgap level and does not account for charge trapping, is implemented.

ASA is also equipped with the trap-assisted tunneling recombination model of Hurkx *et al.* (see Sect. 2.3.5), which models the field-dependent recombination in high-field regions of the device. This model is implemented in the conventional SRH model and in the SRH model for recombination and trapping in the tail states. The model is implemented in a slightly-modified form in the amphoteric trapping and recombination model for the dangling bond states; modifications are made to account for the tunneling probability to both the $E^{-/0}$ level and the $E^{0/+}$ transition level.

3.7 Contact models

All three types of contacts as described in Sect. 2.1 are implemented in ASA:

- Ohmic contacts (equilibrium concentrations of majority and minority carriers at contact interface).

- Generic contacts (minority carrier concentration unequal to equilibrium due to finite surface recombination at contact interface).

- Schottky contacts (energy barrier in combination with surface recombination for majority carriers, to model the thermionic transport over the barrier).

For the latter two types of contacts the electron and hole surface-recombination velocities and the barrier heights can be set independently.

3.8 Optical models

With ASA optical carrier-generation profiles and reflection-transmission spectra can be simulated. The generation profile can be defined by:

- *Uniform generation rate.*
- *Generation profile simulation.* In these simulations the generation rate is assumed to be equal to the number of absorbed photons per unit volume, so in fact the absorption profile is computed. The wavelength-dependent optical properties of the materials can be taking into account. For absorption simulations two different models are available:

  Lambert-Beer: This model is based on the exponential decrease of the light intensity in an absorbing medium: $I(x) = I_0 \exp(-\alpha x)$, where I is the intensity, α is the absorption coefficient and x is the depth in the medium as measured from its surface. In the model a wavelength-independent reflectivity at the front surface (air-solar cell interface) may be defined for incident light, and at the rear surface (at the *a*-Si:H-metal interface) for the transmitted light. Only a single reflection at the rear surface is accounted for, multiple passes through the device are not simulated. The absorbed energy of incident and reflected light is summed without accounting for interference effects.

  Multi-layer optics model: This model computes reflection and transmission at each interface of a multi-layer structure by using the Fresnel coefficients. Multiple internal reflections and interference due to phase differences of incident and reflected light are accounted for. This model simulates the optical behaviour of thin-film multi-layer structures more realistically than the Lambert-Beer model. The implementation in ASA allows the user to define one layer in which coherence between incident and reflected light is lost. In this layer the intensities of incident and reflected light are added instead of the amplitudes, because in this layer the phase differences are ignored. For details see *e.g.* Tao [133], van den Heuvel [143] or Macleod [73].

  In both models for absorption profile simulations, the optical properties are constant in each layer of the simulation structure. Materials with gradients in optical properties cannot be modelled. There is no model implemented for the coupling between the mobility gap, optical gap and the absorptions coefficient. Further, only normal incidence of the light can be modelled, and scattering at the surfaces is not taken into account.

Either monochromatic light or light with a spectral distribution can be used in absorption simulations. In the case of a continuous spectrum the wavelength axis must be discretised; the number of incident photons per unit area can be defined only at a finite number of wavelengths. The total generation rate is the summation of the contributions at each wavelength of the discretised spectrum.

The reflection-transmission simulation model is also based on the thin-film optical model. The stack of homogeneous layers is reduced to a single optical interface that accounts for the properties of all individual layers; the reflection-transmission properties of the reduced interface represent the properties of the total multi-layer system.

3.9 Temperature-dependent models

In contrast to the number of models available for crystalline silicon device modelling, there are only few models for the temperature dependence of physical *a*-Si:H parameters. In ASA the following temperature dependences are implemented:

- A $T^{\frac{3}{2}}$ temperature-dependence is implemented for the effective DOS of the valence and conduction band extended states, which is the temperature-dependence relation of the effective DOS of a parabolic distribution of energy states. The values are computed as $N_{v,c}(T) = N_{v,c}(T = 300\text{K}) \cdot (\frac{T}{300})^{\frac{3}{2}}$, where $N_{v,c}(T = 300)$ K is the user-defined value at the standard temperature 300 K. Because there is no consensus on the energy distribution of extended states [37], this dependence is chosen as a pragmatic first guess. Further research is needed on this subject.

- In ASA the capture-rate coefficients, which are the products of the capture cross sections, σ, and thermal velocity, v_{th}, are defined in the input at the standard temperature 300 K. We have implemented a $(\frac{T}{300})^{\frac{1}{2}}$-dependence of the capture-rate coefficients to account for the $T^{\frac{1}{2}}$-dependence of the thermal velocity.

- The temperature dependence of the characteristic energies of the exponential tail states is based on the empirical model for the temperature behaviour of the Urbach edge [146]. For the valence band tail the relation by Stutzmann [128] is implemented:

$$E_{v0}^2 = E_{v0(T=0)}^2 + (kT)^2 \tag{3.1}$$

Here, $E_{v0(T=0)}$ is the (extrapolated) characteristic energy of the tail at 0 K. $E_{v0(T=0)}$ is determined from the user-supplied value of the tail slope at 300 K.

Because the conduction band tail is much steeper than the valence band tail [126], we expect that Eq. 3.1 exaggerates the temperature dependence of the conduction band tail. Therefore, we modified this equation to reduce its temperature dependence:

$$E_{c0}^2 = E_{c0(T=0)}^2 + C \cdot (kT)^2 \tag{3.2}$$

where C is a user-definable factor. Further experimental work is needed to provide alternatives to this pragmatic approach.

The temperature-dependent behaviour of the optical gap has been discussed in literature [140,146]. A model accounting for this physical effect is not implemented in ASA. However, implementation is recommended for future versions, because we expect that the mobility gap, which strongly influences device characteristics, shows a similar temperature dependence as the optical gap.

3.10 Numerical and implementational aspects

- In ASA the electric potential of the vacuum level, ψ_{vac}, the free electron concentration, n, and the free hole concentration, p, are used as the independent variables in which the set of semiconductor equations Eqns. 2.1–2.3 is solved.

- The equations are discretised by finite differentiation. To ensure numerical stability we have discretised the continuity equations by using the integral expressions for the current density equations as derived by Scharfetter and Gummel [110,115].

- Two different methods for the iterative solution of the semiconductor equations have been implemented:

  - *Gummel method* [42]: This is the simplest solution method. In each iteration loop the three equations are solved separately in one variable, using the most-recently obtained values of the other two variables. This solution method does not directly take into account the coupling between the equations; therefore, the Gummel method has the advantage that program coding is easier, but the disadvantage is that the

convergence properties are worse, if the equations are strongly coupled. The tri-diagonal matrices representing the discretised second-order differential equation can be inverted by straightforward Gaussian elimination and back substitution, which is very efficient for this sparse band matrix.

- *Newton-Raphson method:* With this method the set of three equations is solved in three variables simultaneously, thus including all couplings between the equations. In this case the Jacobian matrix contains the partial derivatives of the three equations to each of the variables. The resulting matrix equation is inverted in a block-tri-diagonal approach, as discussed by Kurata [68]. If the intermediate results are close enough to the solution the advantage is better (quadratic) convergence behaviour.

The initial guess is more critical when the Newton-Raphson method is used; with this method a bad initial guess is more likely to result in failing convergence, than if one use the Gummel method. Therefore, an option is implemented in ASA to precede the Newton-Raphson method by a few Gummel iteration steps. These initial steps bring the initial guess close enough to the final solution to obtain successful and efficient convergence with the Newton-Raphson method.

- Several damping mechanisms are implemented to avoid convergence problems. The user can activate these mechanisms. In principle, damping reduces the corrections to the independent variables between two iteration steps. For the potential the following two damping strategies are implemented:

  - Clipping of the potential updates if they exceed a certain maximum value.
  - Reduction of large update values according to the damping scheme of Brown and Lindsay [14].

  If the updates for the carrier concentrations are negative and exceed the value of the present concentration, the physically impossible situation of negative concentrations can occur. To avoid this unwanted result the updates of the concentrations can be damped as follows:

  - Clipping of updates that would lead to negative concentrations to a save value of about 90% of the present concentration.

- Linear scaling of the complete update vector to avoid negative concentrations.

Practical experience has shown that the first option of carrier concentration update damping works most efficient.

3.11 Other features

- Frequently, the first bias point of a simulation with optical generation fails to converge, because of a poor initial guess of the independent variables (usually the initial guess is the solution of the previous simulation run, which might for instance be the thermal equilibrium state). The cause of this problem is that there are large differences between the carrier concentrations in the initial guess and the carrier concentrations in the illuminated state. It can be solved by gradually increasing the optical generation rates. In ASA a routine is implemented which carries out automatically a series of simulations with generation rates that increase in exponential steps. With this up-ramping of the generation the convergence behaviour becomes much more robust.
- If ASA fails to converge after an increment in the bias voltage, an intermediate bias point will be inserted automatically. This scheme repeats recursively, if the simulation does not converge at the intermediate point again.
- ASA has a formula parser that allows expressions to be used in the input file. All common arithmetic operations and many mathematical functions such as exponential and goniometrical functions are allowed. Furthermore, the user can define variables which may be used in expressions. The frequently used mathematical and physical constants, such as π, Boltzmann's constant, k, and elementary charge, q, are predefined.

Chapter 4

Amorphous silicon solar cell model parameters

To apply a device simulator in a sensible way one requires good insight in the device physics, and in the role of the device and model parameters. In addition, the simulator must be well calibrated to measured device characteristics. This chapter discusses the detailed analysis and calibration of the *a*-Si:H solar cell device model and its parameters. In Sect. 4.1 we present a theoretical analysis of the recombination and thermal generation processes in an unilluminated *a*-Si:H *pin* diode. This analysis increases the understanding of the influence of the continuous gap-state distribution and related recombination/generation parameters on the dark *IV*-characteristics. Section 4.2 presents the theoretical derivation of parameter dependences amongst a group of important physical model parameters. Based on the findings obtained from this study, suggestions for experiments to be used for model calibration are given. In Sect. 4.3 we discuss the assumption of the abrupt transition from localised to extended states, as is commonly made in *a*-Si:H device simulation models. This is followed by a comprehensive numerical study of model parameter sensitivities in Sect. 4.4. The final section of this chapter discusses the calibration of our *a*-Si:H device model. Here, we show in two calibration exercises that non-linear parameter optimisation or inverse modelling is a useful technique for *a*-Si:H solar cell model calibration. The reasons why very different parameter sets were obtained in the calibration exercises are discussed, and suggestions are given for additional experiments which can lead to a more unique set of model parameters.

4.1 Qualitative discussion of distribution of active recombination states in *pin* structures

Although the 0 K Taylor and Simmons approach is not suited to be used as an accurate and general model for generation and recombination in an *a*-Si:H device simulator (see Appendix B), it is very useful for gaining insight in the device physics of *a*-Si:H devices. In this section we use this model to analyse the recombination processes in an unilluminated *pin* diode, and to identify the most important recombination states and recombination model parameters. This analysis leads to the identification of the dominating mechanism for the current in unilluminated *a*-Si:H *pin* diodes, which is recombination in the depletion layer. We present a simple model that can calculate very efficiently the approximate forward-biased *IV*-characteristics of an *a*-Si:H *pin* diode without illumination. Subsequently, thermal generation in reverse-biased *pin* diodes is discussed; the most important parameters of thermal generation and their mutual influences are identified. Finally, we discuss a few practical issues related to device simulation (such as the choice of the energy discretisation interval for computation of gap-state recombination) based on insight gained by the theoretical analysis of the device model.

Properties of the quasi-Fermi levels for trapped charges

From straightforward mathematical manipulation of Eqns. 2.31, 2.35 and 2.38 the following characteristic properties of the quasi-Fermi levels for trapped charge carriers are found:

- Since $E_{fn_t} + E_{fp_t} = 2E_{t0}$ the quasi-Fermi levels for trapped charges are positioned symmetrically around the intrinsic trap level, E_{t0}. The recombination efficiency function, η_r, which is also controlled by the positions of the quasi-Fermi levels for trapped charge carriers, is therefore symmetrical around E_{t0} as well. Consequently, the energy range that contains the gap states actively involved in the recombination process extends symmetrically around E_{t0}.

- When $n\sigma_n \ll p\sigma_p$ (or $n\sigma_n \gg p\sigma_p$) the quasi-Fermi level for trapped electrons, E_{fn_t}, coincides with the free-electron quasi-Fermi level, E_{fn}, (or, analogously, the quasi-Fermi level for trapped holes, E_{fp_t}, coincides with the free-hole quasi-Fermi level E_{fp}). Because of the above-mentioned symmetry around E_{t0}, the width of the recombination efficiency function is determined by the free-carrier quasi-Fermi level of the *majority* carriers.

In this context the electrons are the majority carrier if $n\sigma_n \gg p\sigma_p$; in the opposite case the holes are the majority carriers. Further, in extrinsic cases the occupation probability of localised gap states is approximated very well by a Fermi-Dirac distribution controlled by the free-majority-carrier quasi-Fermi level. This can be easily derived from Eqns. 2.36 and 2.37.

Analysis of forward-biased *pin* diodes

Based on the characteristics of the quasi-Fermi levels for trapped charge carriers, we discuss which localised states contribute to the recombination process and the dependence thereof on the applied forward bias voltage. To this end two simplifying assumptions are made:

- a uniform electric field in the *i*-layer is assumed: *i.e.* the influence of the space charge density in the *i*-layer on the electric field is not taken into account.
- a quasi-equilibrium situation is assumed so that the free-carrier quasi-Fermi levels are constant throughout the device. The separation of the quasi-Fermi levels equals the applied voltage.

To enhance understanding of the recombination processes inside an *a*-Si:H diode, we split Eq. 2.41 into two factors and consider them separately. Figure 4.1 shows for two different bias voltages the position dependence of

- the energy range enclosed by the quasi-Fermi levels for trapped charge carriers, which contains the 'active' recombination states (shaded area in the band diagrams of the top graph). The extent of this range determines the factor $\int_{E_{fpt}}^{E_{fnt}} N(E)dE$.
- the prefactor $\frac{v_{th}\sigma_n\sigma_p np}{n\sigma_n+p\sigma_p}$ (bottom graphs). This factor has its maximum value at x_p where $n\sigma_n = p\sigma_p$, which coincides with the point where the trapped charge quasi-Fermi levels are closest together. With the above-mentioned assumptions (uniform electric field and constant quasi-Fermi levels) this factor is proportional with $\frac{1}{\cosh(\frac{x-x_p}{x_L})}$ where x_L is a 'characteristic' length depending on the built-in and applied voltages, and on the *i*-layer thickness. From the position dependence of this prefactor can be concluded that an active recombination level is most effective in the recombination process if it is located around x_p.

With increasing forward bias (when going from Fig. 4.1a to Fig. 4.1b, the separation between the trapped charge quasi-Fermi levels increases. Hence, the

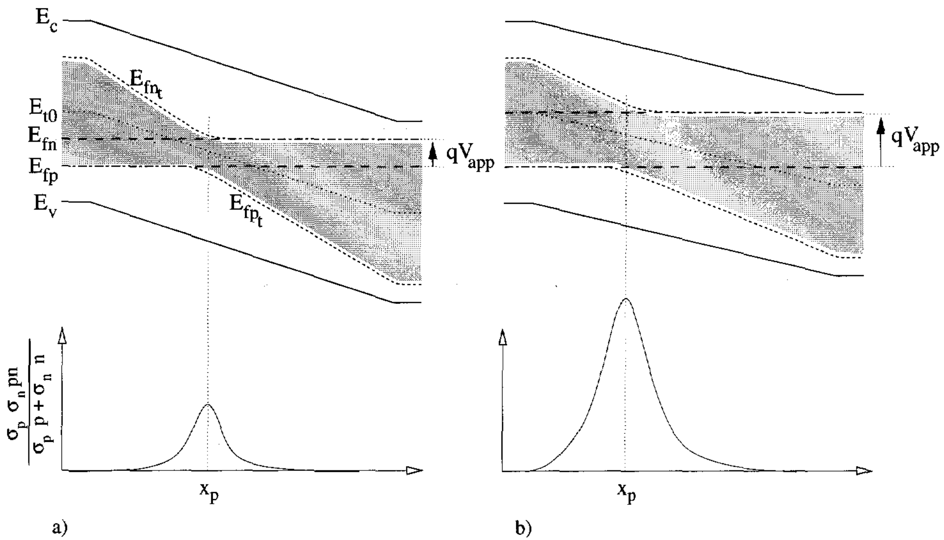

Figure 4.1: Band diagrams of a forward-biased *pin* diode showing the energy range that contains the active recombination states (*i.e.* the shaded area in the top graphs) and the position dependence of the factor $\frac{\sigma_n \sigma_p np}{\sigma_n n + \sigma_p p}$ that determines the 'effectiveness' of an active recombination level. (a) is for low and (b) is for a higher forward-bias condition.

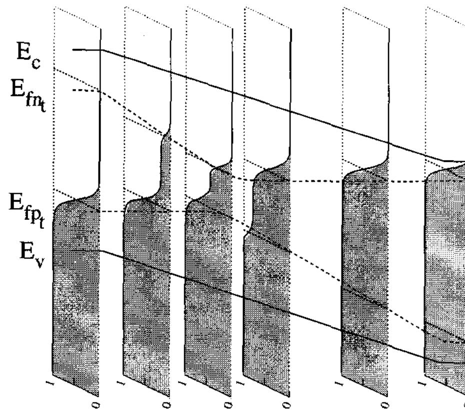

Figure 4.2: Position-dependent occupation function of localised gap states in a forward-biased *pin* diode. The free-carrier quasi-Fermi levels, which are omitted in the graph, coincide with the constant parts of the trapped charge quasi-Fermi levels (see Fig. 4.1).

number of active recombination centres increases, and the carrier lifetimes decrease. It is obvious from the figure that the bias dependence of the lifetimes is the strongest in the centre of the *i*-layer. In this region a bias change influences the distance between the trapped carriers quasi-Fermi levels $E_{fn_t} - E_{fp_t}$ most. Close to the doped layers the separation of the trapped charge quasi-Fermi levels is larger than in the centre of the *i*-layer and less dependent on the bias. Furthermore, we see that the position x_p may change with changing bias, meaning that states in a different part of the device will contribute relatively stronger to the total recombination. The part of the device which dominates the recombination inside the *pin* diode cannot be determined from this qualitative analysis, because it depends on the exact balance between the position dependence and energy dependence of the density of localised states and the position dependence of the prefactor. Nevertheless, we draw the following conclusions, assuming that the distribution of the localised states is independent of the position in the *i*-layer:

- the carrier lifetimes depend on the applied bias, because with increasing bias the separation of the trapped charge quasi-Fermi levels increases.

- the carrier lifetimes decrease from the centre of the *i*-layer towards the doped regions.

- the bias dependence of the carrier lifetimes is the strongest in the centre of the *i*-layer.

- the net recombination per active recombination state is the largest in the central part of the device. Therefore, the addition of a single extra recombination state at x_p causes the strongest increase in the total recombination. As a result, the *IV*-characteristics are most sensitive to changes of the density of states — such as caused by light-induced degradation — in the central part of the *i*-layer.

Figure 4.2 shows schematically the position dependence of the occupation functions in a *pin* device. The figure depicts that in extrinsic regions the free-majority-carrier quasi-Fermi level determines the occupation of the localised states, in accordance with the above-mentioned conclusion. In the central region, where $n\sigma_n \approx p\sigma_p$, the occupation is determined by both types of carriers. Here, the occupation function is not a Fermi-Dirac function, but it shows the step-like character as shown before in Fig. 2.5. This qualitative insight in the occupation of localised states is important for the interpretation of capacitance-voltage (*CV*) measurements and transient measurements on *pin* devices.

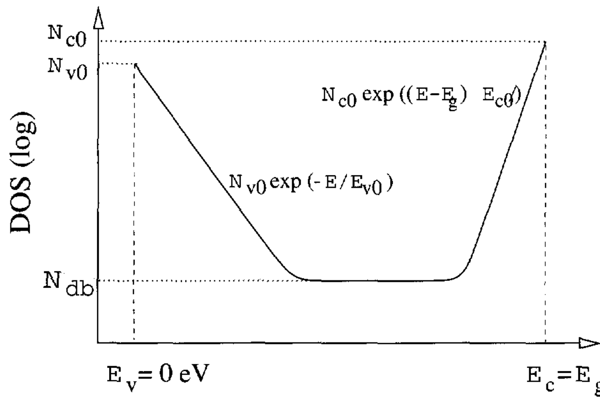

Figure 4.3: Density of states distribution used for approximate calculations of dark IV-characteristics.

Approximate calculation of IV-characteristics

The approximate determination of the active recombination states and the bias-voltage dependence thereof allows us to compute the IV-characteristics of a *pin* diode, when we assume that carrier recombination in the depletion region is the main process that determines the diode current. In an *a*-Si:H *pin* diode the depletion region is comprising almost the complete diode, because the *i*-layer is relatively much thicker than the doped layers. Using the 0 K approximation we compute the recombination current, J, in a diode of thickness, W, as:

$$J(V) = q\int_0^W R(x,V)dx \tag{4.1}$$
$$= qv_{th}\int_0^W \left[\frac{\sigma_n\sigma_p n(x,V)p(x,V)}{\sigma_n n(x,V)+\sigma_p p(x,V)}\int_{E_{fp_t}(x,V)}^{E_{fn_t}(x,V)} N(E)dE\right]dx.$$

For this calculation a simple density of states distribution $N(E)$ is used consisting of a summation of a uniform midgap states density and two exponential tail state distributions (see Fig. 4.3).

$$N(E) = N_{v0}\exp\left(\frac{-E}{E_{v0}}\right) + N_{c0}\exp\left(\frac{E-E_g}{E_{c0}}\right) + N_{db}. \tag{4.2}$$

Since only the recombination is computed, and charge trapping and the influence thereof on the band bending is neglected, the character of the tail states (either donor-like or acceptor-like) is not relevant in this analysis. The free-electron and free-hole concentrations are computed by Eqns. 2.6 and 2.7 where we assume that

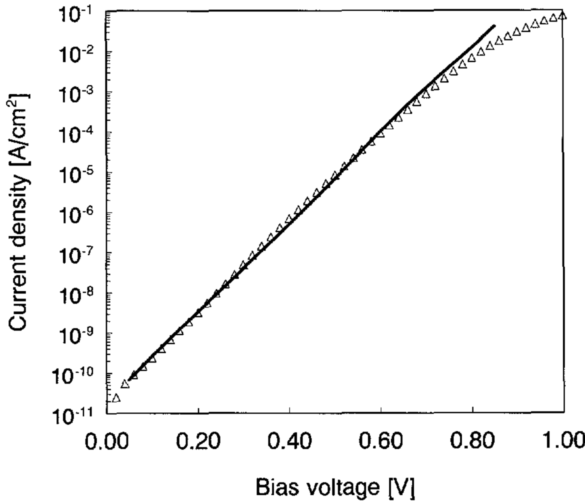

Figure 4.4: Computed forward-bias IV-characteristics of a *a*-Si:H *pin* diode based on a simple model which only accounts for recombination currents (full line). For reference an experimental IV-curve is added (symbols).

the difference between (majority) quasi-Fermi level in the doped region is a fixed value and that $E_c - E_{fn}$ or $E_{fp} - E_v$ increases linearly with increasing distance from the *n*-*i* interface to the *p*-*i* interface or vise versa. This is a direct result of the assumption that the quasi-Fermi levels are constant throughout the device and the electric field is homogeneous in the *i*-layer.

Figure 4.4 shows a simulated IV-curves; the parameters used for this calculation are listed in Table 4.1. Included is also a measured IV-curve. Although the model is very simple the matching between both curves is very good. Only with forward biases exceeding 0.7 V the deviation between the curves increases.

Parameter	Value		Parameter	Value	
E_g	1.76	eV	T	300	K
N_c	$5{\cdot}10^{20}$	cm^{-3}	N_v	$5{\cdot}10^{20}$	cm^{-3}
W	400	nm	N_{db}	$1{\cdot}10^{16}$	cm^{-3}
E_{v0}	0.052	eV	N_{v0}	$1{\cdot}10^{22}$	$\mathrm{eV}^{-1}\,\mathrm{cm}^{-3}$
E_{c0}	0.033	eV	N_{c0}	$1{\cdot}10^{22}$	$\mathrm{eV}^{-1}\,\mathrm{cm}^{-3}$
σ_n	$0.8{\cdot}10^{-14}$	cm^2	σ_p	$0.8{\cdot}10^{-14}$	cm^2

Table 4.1: Model parameters used for the calculations of the dark IV-characteristics shown in Fig. 4.4.

From the good matching of the measured and simulated *IV*-characteristics we can conclude that — for low and moderate forward biases — the *IV*-characteristics of *a*-Si:H *pin* diodes is dominated by recombination processes [142]. This means that the density of states distribution and the capture cross sections are the most important parameters for these characteristics. Other physical parameters, such as the carrier mobilities, have hardly influence on these characteristics. The increasing deviation between simulated and measured curves for high forward biases is due to the fact that in this bias regime the transport (by diffusion) of carriers to the recombination centres becomes a factor that limits the current. In this case the assumption of the constant quasi-Fermi levels is no longer justified.

Typically, *a*-Si:H *pin* diodes have diode ideality factors in the range from 1.4 to 2. A widespread explanation for this experimental observation is that the diode current is a combination of a diffusion-limited current and a recombination-limited current. According to crystalline semiconductor device theory an ideality factor of value one belongs to the first type of current mechanism (diffusion in quasi-neutral regions), whereas the second type of current mechanism (recombination in the space-charge region) has value two [131]. From this theory the straightforward conclusion is drawn that an ideality factor between 1 and 2 indicates a combination of diffusion- and recombination-limited transport. However, based on new insights obtained from our approximate simulation we conclude that this explanation is not correct. Our simulation shows that even with exclusively recombination-limited transport an ideality factor in the intermediate range can be obtained [142]. This is explained by the decrease of carrier lifetimes upon an increase of forward bias voltage. Due to the decreasing lifetimes the recombination current increases more stronger than would be the case with a diode ideality factor of 2.

Analysis of reverse-biased *pin* diodes

In a similar analysis the current behaviour of a reverse-biased *a*-Si:H *pin* diode is studied. In this case, where the current is dominated by generation processes, we use the full expressions for the SRH statistics, because the 0 K Taylor and Simmons approximation is not valid in this regime.

Assuming that everywhere inside the device[1] $np \ll n_i^2$ and using the defini-

[1] This assumption is justified if the free-electron quasi-Fermi level lies at least $3kT$ below the free-hole quasi-Fermi level. As a good approximation this is the case if the device is reverse-biased with a voltage of at least $3kT/q$.

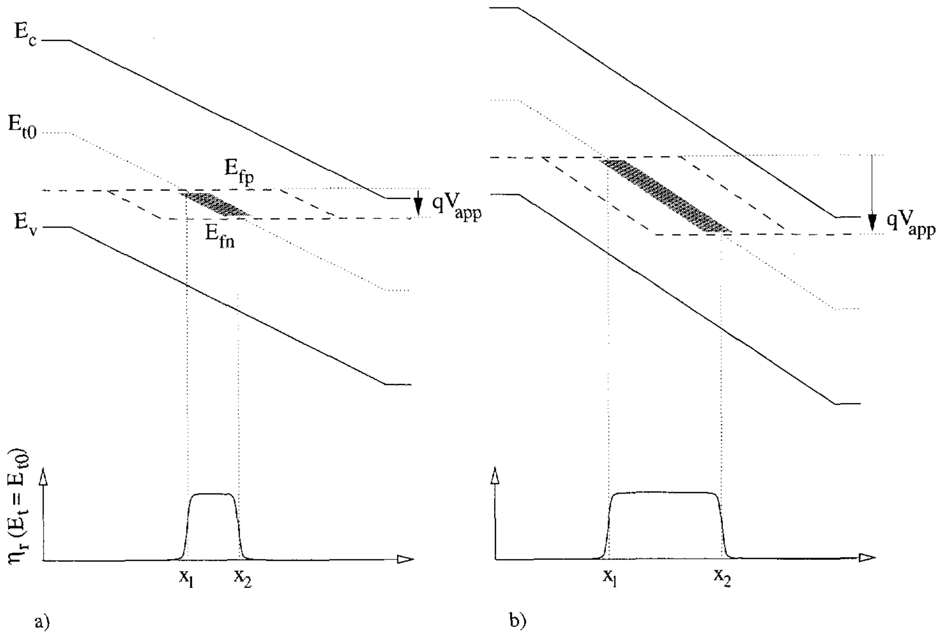

Figure 4.5: Schematic band diagram of a reverse-biased *a*-Si:H *pin* diode (top graphs) at two different bias voltages showing the gap states which are 'active' generation centres (shaded area). In figure (a) the bias is lower than in figure (b). The bottom graphs show schematically the recombination efficiency function η_r for a recombination level at E_{t0} as given by Eq. 4.3.

tion, Eq. 2.31, of the intrinsic trap level, E_{t0}, we can transform Eq. 2.30 into

$$\eta_r = \frac{-v_{th}\sqrt{\sigma_n \sigma_p} n_i}{\exp\left(\frac{E_{fn}-E_{t0}}{kT}\right) + \exp\left(\frac{E_{t0}-E_{fp}}{kT}\right) + 2\cosh\left(\frac{E_t - E_{t0}}{kT}\right)}. \tag{4.3}$$

Straightforward analysis shows that this expression obtains its maximum value if the first two terms in the denominator are much smaller than the third. This is the case if the free-electron quasi-Fermi level, E_{fn}, is positioned below E_{t0} and the free-hole quasi-Fermi level, E_{fp}, above E_{t0}. The schematic band diagrams in Fig. 4.5 show the region $[x_1, x_2]$ where this condition is satisfied. In the lower plots of Fig. 4.5 the position dependence of η_r is shown for a localised state at E_{t0}. As shown, η_r may be approximated by zero outside the range $[x_1, x_2]$ and in reaches, to first-order approximation, a constant value inside this range. Therefore, the states between x_1 and x_2 contribute to the thermal generation. With increasing reverse bias voltage (*cf.* Fig. 4.5a *vs.* Fig. 4.5b) the range $[x_1, x_2]$ increases. Hence,

the region containing states actively involved in the thermal carrier-generation process increases with increasing reverse bias, resulting in a bias-dependent generation current in the a-Si:H *pin* diode. In the range $[x_1, x_2]$ the total thermal carrier generation equals

$$G = \frac{v_{th}\sqrt{\sigma_n \sigma_p} n_i}{2} \int_{E_v}^{E_c} N(E) \frac{1}{\cosh\left(\frac{E_t - E_{t0}}{kT}\right)} dE. \tag{4.4}$$

The function $\frac{1}{\cosh(x/kT)}$ has a narrow peak-like shape that only differs significantly from zero for values of x in the interval between $-2kT$ and $2kT$. Therefore, if the density of states $N(E)$ can be approximated by a constant value N in an energy range of about $4kT$ centred at E_{t0}, Eq. 4.4 can be approximated by

$$G = \frac{v_{th}\sqrt{\sigma_n \sigma_p} n_i}{2} N \pi k T. \tag{4.5}$$

Using this expression we can estimate the reverse current in an a-Si:H *pin* diode by integrating the generation between x_1 and x_2:

$$J = q \int_{x_1}^{x_2} G dx \tag{4.6}$$

of which the upper limit is

$$J = qGW = \frac{q v_{th}\sqrt{\sigma_n \sigma_p} n_i}{2} N \pi k T W \tag{4.7}$$

when we consider that the length of the range $[x_1, x_2]$ can become W at most. Street [125] has derived a similar expression before.

From this analysis we draw several conclusions about the reverse current of an a-Si:H *pin* diode, which is dominated by thermal generation:

- only states in a narrow energy band of about $4kT$ around the intrinsic trap level, E_{t0}, contribute effectively to the thermal generation process.

- the spatial range of active levels increases with increasing reverse-bias voltage. If the distribution of midgap states shows a strong spatial inhomogeneity (*e.g.* increasing strongly towards the *p-i* and *n-i* interfaces as resulting from the defect-pool model) the number of active states depends *supralinearly* on the increase of the range $[x_1, x_2]$. Hence, the bias dependence of the reverse current contains information about the position dependence of the midgap density of states.

- The product $\sqrt{\sigma_n \sigma_p} n_i N$ can be estimated from reverse-bias current measurements of an a-Si:H *pin* diode. Since the reverse-bias current is propor-

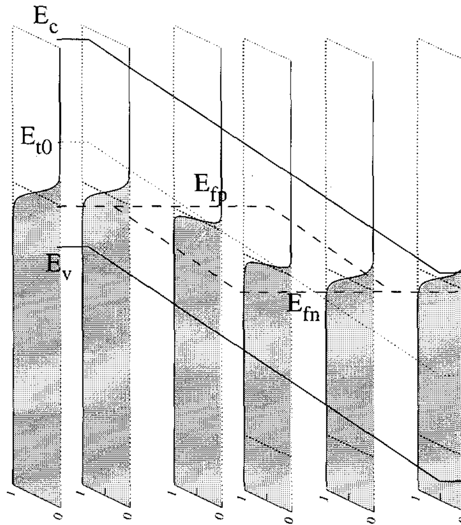

Figure 4.6: Occupation function at several positions inside a reverse-biased *a*-Si:H *pin* diode.

tional to this product the parameters in the product cannot be determined independently by using only this measurement.

- Since the reverse-bias current is proportional to the density of states near the intrinsic trap level E_{t0}, measurement of the reverse current is a very sensitive method to monitor the defect increase due to light- or current-induced degradation.

Figure 4.6 shows the position-dependent occupation function in a reverse-biased *pin* diode. In the regions where E_{fp} and E_{fn} are below resp. above E_{t0} the occupation function is a Fermi-Dirac function determined by the majority-carrier quasi-Fermi level. In the central region (*i.e.* between x_1 and x_2 in Fig. 4.5) the occupation function, f, is

$$f = \frac{1}{1 + \exp\left(\frac{2(E_t - E_{t0})}{kT}\right)} \tag{4.8}$$

as can be readily derived from Eq. 2.29, by using Eqns. 2.26, Eqns. 2.27 and 2.31. We can conclude — as a first-order approximation — that the energy levels up to the intrinsic trap level E_{t0} are occupied in the central part of a reverse-biased *pin* diode.

Final remarks

- It can be shown that — under certain restrictive, but usually satisfied conditions — the density of trapped charge and the recombination as a function of energy of the localised state decreases with decreasing distance from the mobility edges (see Appendix B). Hence, the relative contribution of states close (*i.e.* $\approx$ 100 meV) to the mobility edges to the total trapped space charge and total recombination is small. Therefore, the details about the exact density of state distribution in this part of the mobility gap are not relevant to the device behaviour. The practical consequence of this is that we can choose a rather arbitrary density of states distribution, without much influence on the simulated device characteristics. This conclusion can be considered as the theoretical proof for similar conclusions based on modelling experiments by Arch *et al.* [2].

- The simplified expressions by Taylor and Simmons, Eqns. 2.36, 2.37 and 2.40, show that the occupation and recombination efficiency functions (in case of recombination) basically consist of two Fermi-Dirac functions. The characteristic parameter determining the shape of these Fermi-Dirac functions is kT. From insight in the characteristic properties of the recombination efficiency function and occupation function, we can conclude that an energy sampling interval in the order of kT is required for the accurate numerical calculation of the recombination and space charge. As a rule of thumb an interval of $2kT$ or less will give a sufficiently accurate discretisation of the localised states. This means that in practice about 40 or more equi-distant energy discretisation levels are required for room temperature simulations with a mobility gap $E_g = 1.8$ eV.

- Near the *p-i* and *i-n* interfaces the energy range enveloping the active recombination centres is very wide and does not depend much on the applied voltage (*cf.* Fig. 4.1). Since all recombination levels in this energy range are *equally efficient* in the recombination process, only the *total number of states* between the trapped charge quasi-Fermi levels is relevant for the total recombination in these parts of the device. Hence, specific details of the distribution of recombination states are not relevant for the electrical characteristics of *a*-Si:H *pin* diodes in forward bias, as long as the distribution of states remains primarily between the trapped charge quasi-Fermi levels.

  According to the defect-pool model the total defect density as well as the energy distribution of defects in the gap depend on the position of the Fermi level (see Fig. 2.2): closer to the doped layer the total defect density in

the i-layer increases and the energy in the mobility gap changes at which the defect density of states is maximal. Based on the conclusion of the previous paragraph we conclude that the exact positions of the peaks, as resulting from the defect-pool model, are of subordinate relevance for the device behaviour. Information about these cannot be extracted from electrical measurement data and from a device physical point of view attempts to gain detailed information about the defect distribution in these specific parts of a device are of little use.

- Aiming at a simplification of the theory of recombination processes through energy levels with a continuous distribution, Rose [102] has introduced the concept of *demarcation levels*. These levels play the same role as the trapped charge quasi-Fermi levels of Taylor and Simmons; nevertheless they do not coincide, which is caused by errors in Rose's derivation [119]. Since the demarcation levels are still used frequently in literature (in for instance Halpern [49] or the textbook of Boër [13]), a modest warning is justified. Another frequently used misconception is that — as a fair approximation — the energy states between the *free-carrier quasi-Fermi levels* contribute actively to the recombination process [102, 142]. As shown in Fig. 4.1 this is not correct.

4.2 Analytic analysis of model parameter dependences

In this section an analysis of parameter dependences in a-Si:H device modelling is presented. We derive analytic expressions that give the dependences of five important a-Si:H material parameters, *i.c.* (1) effective densities of states in the extended states, (2) the positions of the mobility band edges (defining the width of the mobility gap), (3) the capture cross sections, (4) the extended state mobilities and (5) the density of states in the band tails at the mobility edges. The density of localised states in the mobility gap is not changed.

In our analysis we distinguish between electron-related and hole-related parameters; dependence relations are derived for both groups of parameters. As electron-related parameters are defined: the effective density of states in the conduction band, N_c, the conduction band mobility edge, E_c, the electron mobility, μ_n, *any* capture cross sections for electrons, here generically denoted by, σ_n, and the density of conduction band tail states at the mobility edge, N_{c0}. The counterparts of these parameters for the hole and valence band properties are designated as the hole-related parameters.

In the five-dimensional parameter space consisting of the above listed model

parameters, the dependence relations define a parameterised line on which the solutions of the semiconductor equations are exactly the same. Relaxation of one of the requirements for the parameter dependences yielding exactly equal solutions results in a second free parameter. With different values for this parameter the solutions of the semiconductor equations are still close approximations of each other. In this case we have two free parameters that span a plane in the 5-dimensional parameter space. In general, two related parameter sets give equal results only at one single temperature, since the temperature is a parameter in the dependence relations. We find that the key parameter amongst the 5 above-mentioned parameter for the temperature-dependent behaviour is the mobility bandgap; therefore, two sets with different bandgaps will show different temperature-dependent simulation characteristics.

4.2.1 Derivation

We define a general requirement that should be met in order to obtain identical simulation output characteristics, irrespective of the actual values of the above-mentioned set of parameters:

> The current density distributions inside a device, as defined by Eqns. 2.4 and 2.5, should not change when the parameter values are changed. Therefore, we require that neither the position-dependent quasi-Fermi levels, E_{fn} and E_{fp}, nor the products of free carrier concentrations and carrier mobilities, $n\mu_n$ and $p\mu_p$ change.

In order to satisfy this requirement, several additional requirements are demanded by the semiconductor equations. When changing the set of parameters, the following quantities must be remain unchanged in order to maintain exactly the same simulation results:

- The distribution of gap states between the mobility edges
- The space charge density distribution; this controls the electric field and potential distributions through the Poisson equation, Eq. 2.1. In other words, the net sum of dopants and trapped and free charges must remain the same when changing from one to the other parameter set.
- The recombination and thermal generations rates; these control the gradients in the current densities through the continuity equations, Eqns. 2.2 and 2.3. As we can see in Table 2.2 and 2.4 the capture rates do not change if the product of capture cross section and free carrier density, $\sigma_n n$ and $\sigma_p p$, is

kept constant. The density of gap states remains unchanged (*cf.* the first requirement of this list). On the other hand, the emission rates do not change if the products $\sigma_n N_c \exp((E_c - E_t)/(kT))$ and $\sigma_p N_v \exp((E_t - E_v)/(kT))$ are kept invariant. The optical generation rates are not affected by the parameter dependence relations.

We can easily see that fulfillment of these requirements results in exactly equal solutions of the semiconductor equations, Eqns. 2.1, 2.2 and 2.3, and current density equations, Eqns. 2.4 and 2.5.

Further, we briefly recall some assumptions and approaches that are generally made in simulation models for *a*-Si:H devices, such as ASA:

- At the mobility edge there is a sharp transition from localised states to extended states. The mobility of carriers in localised states is zero and in the extended states the mobility has a constant value, independent of the electron's energy state.
- The extended states of the conduction and valence band, in which carrier conduction takes place, are described by effective density of states values.
- Only carriers in the extended states can be captured in gap states, and emission takes place from gap states to extended states.

Finally, we remind that the occupation of the extended states as well as the localised tail states close to the mobility edge, the shallow states, can be approximated by the same Maxwell-Boltzmann occupation function, that is controlled by the free carrier quasi-Fermi level. In this analysis the shallow states must be located between $E_{fn_t} + 3kT$ and E_c in the conduction band tail or E_v and $E_{fp_t} - 3kT$ in the valence band tail, where E_{fn_t} and E_{fp_t} are the quasi-Fermi levels for trapped charges, as defined in Sect. 2.3.2 [2]. In the following derivation we also assume that the shallow states do not contribute to the recombination; this conclusion has been drawn in Sect. 4.1 (page 86).

Exact analysis

On the basis of these requirements the dependence relations are derived. Consider a set of electron related parameters, $\{E_{c1}, N_{c1}, N_{c0,1}, \sigma_{n1}, \mu_{n1}\}$, that correspond with the density of states $N(E)$ and mobility $\mu(E)$ of Fig. 4.7a. The hatched area to the right of the mobility edge E_{c1} corresponds to the extended states in the

[2]Strictly speaking this is only valid for biasing conditions that give rise to recombination; in situations with thermal generation the trapped charge quasi-Fermi levels are not defined

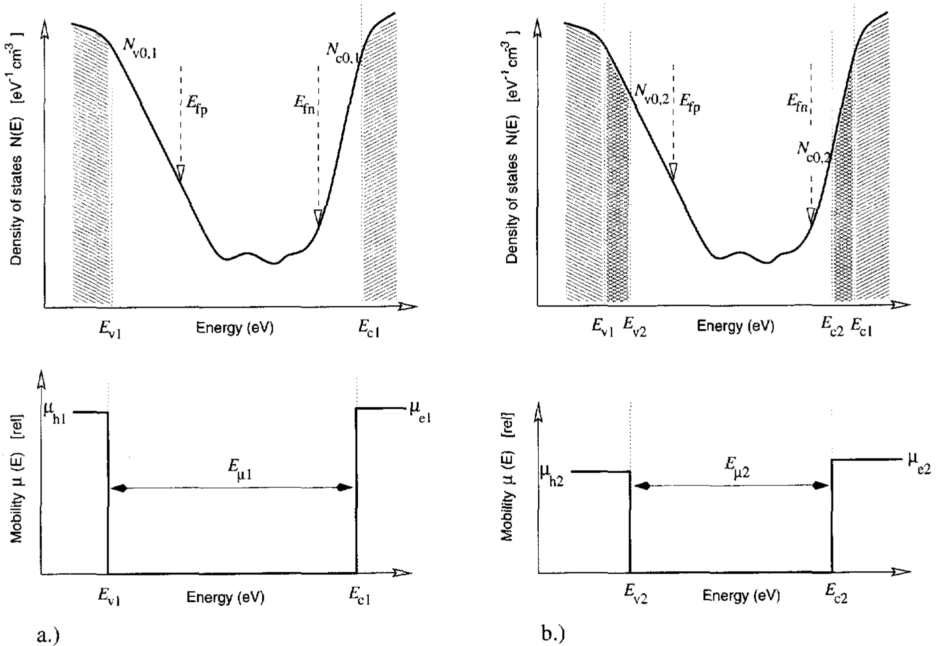

Figure 4.7: Schematic graphs of the *a*-Si:H density of states (top) and mobility as a function of energy (bottom): (a) corresponds to parameter set 1, (b) corresponds to parameter set 2. The extended states in the DOS graphs are hatched. Note that the distribution of localised states between energies E_{v2} and E_{c2} is the same for both parameter sets. The values of the quasi-Fermi levels, E_{fp} and E_{fn}, is arbitrary; they are added to illustrate that they remain at the same energy for both parameter sets.

conduction band. These extended states are modelled by an effective density of states N_{c1}, that is given by:

$$N_{c1} = \int_{E_{c1}}^{\infty} N(E) \exp\left(-\frac{E - E_{c1}}{kT}\right) dE. \tag{4.9}$$

As is shown in Fig. 4.7a the electron mobility is constant for carriers in energy levels above E_{c1}. Figure 4.7b corresponds to model parameter set 2, $\{E_{c2}, N_{c2}, N_{c0,2}, \sigma_{n2}, \mu_{n2}\}$, that should give the same simulation results as set 1. The conduction band mobility edge is shifted from E_{c1} to E_{c2} over $-\Delta E_c$ which is defined as:

$$E_{c1} - E_{c2} = \Delta E_c. \tag{4.10}$$

In the dependence relations for the electron related parameters, we treat ΔE_c as the free parameter. We see that the density of localised states in the gap between E_{v2} and E_{c2} remains unchanged. However, the extended states now extend to the right of E_{c2}. These states are marked as the cross-hatched and hatched regions in the graph. Because the occupation function for shallow tail states and extended states is the same Maxwell-Boltzmann approximation, we are allowed to compute the effective density of states N_{c2} as:

$$\begin{aligned} N_{c2} &= \int_{E_{c2}}^{\infty} N(E) \exp\left(-\frac{E-E_{c2}}{kT}\right) dE \qquad (4.11) \\ &= \int_{E_{c2}}^{E_{c1}} N(E) \exp\left(-\frac{E-E_{c2}}{kT}\right) dE + \int_{E_{c1}}^{\infty} N(E) \exp\left(-\frac{E-E_{c2}}{kT}\right) dE. \end{aligned}$$

The first term in the right hand side of this equation is due to the cross hatched area in Fig. 4.7b, and corresponds to a part of the localised tail states in Fig. 4.7a. The second term is due to the hatched area, which corresponds with the extended states in Fig. 4.7a.

If the localised conduction band tail states of Fig. 4.7a are described by an exponential function, $N(E) = N_{c0,1} \exp((E-E_{c1})/(E_{c0}))$ we can determine the tail state density $N_{c0,2}$ at E_{c2} as

$$N_{c0,2} = N_{c0,1} \exp\left(-\frac{\Delta E_c}{E_{c0}}\right) \qquad (4.12)$$

where E_{c0} is defining the slope of the exponential states distribution. Using the exponential distribution of shallow states we obtain for N_{c2}:

$$N_{c2} = N_{c0,1} \frac{E_{c0}kT}{kT-E_{c0}} \left[\exp\left(-\frac{\Delta E_c}{kT}\right) - \exp\left(-\frac{\Delta E_c}{E_{c0}}\right)\right] + \exp\left(-\frac{\Delta E_c}{kT}\right) N_{c1}. \qquad (4.13)$$

Given a certain value of the electron quasi-Fermi level E_{fn}, the space charge contribution of the electrons in the states above E_{c2} is equal for both sets of parameters. The difference is that with parameter set 1 the electrons between E_{c2} and E_{c1} are localised and only those above E_{c1} are free, whereas with parameter set 2 all electrons above E_{c2} are considered as free electrons (*cf.* the mobility graphs in Fig. 4.7). The free electron concentrations n_1 and n_2 for parameter set 1 and set 2, respectively, are readily computed as: $n_1 = N_{c1} \exp[(E_{fn}-E_{c1})/(kT)]$ and $n_2 = N_{c2} \exp[(E_{fn}-E_{c2})/(kT)]$, respectively. Because of the requirements that the products $n\mu_n$ and $n\sigma_n$ do not change we can easily derive dependence

relations for the electron mobility and capture cross sections:

$$\frac{\mu_{n2}}{\mu_{n1}} = \frac{\sigma_{n2}}{\sigma_{n1}} = \frac{N_{c1}}{N_{c2}} \exp\left(\frac{-\Delta E_c}{kT}\right). \quad (4.14)$$

The set of equations, Eqns. 4.10, 4.12, 4.13 and 4.14 gives the parameter dependences between the electron-related model parameters. The parameter dependences of the hole-related parameters is given by the following set of equations:

$$E_{v2} - E_{v1} = \Delta E_v \quad (4.15)$$

$$N_{v0,2} = N_{v0,1} \exp\left(-\frac{\Delta E_v}{E_{v0}}\right) \quad (4.16)$$

$$N_{v2} = N_{v0,1} \frac{E_{v0} kT}{kT - E_{v0}} \left[\exp\left(-\frac{\Delta E_v}{kT}\right) - \exp\left(-\frac{\Delta E_v}{E_{v0}}\right)\right] + \exp\left(-\frac{\Delta E_v}{kT}\right) N_{v1} \quad (4.17)$$

$$\frac{\mu_{p2}}{\mu_{p1}} = \frac{\sigma_{p2}}{\sigma_{p1}} = \frac{N_{v1}}{N_{v2}} \exp\left(\frac{-\Delta E_v}{kT}\right). \quad (4.18)$$

A close look at the transformation equations for the effective density of states, Eqns. 4.13 and 4.17, reveals two problems:

- There is a singularity if the characteristic tail slopes E_{c0} or E_{v0} equals the thermal energy kT. This can be easily avoided by rewriting the integrand of the first term in the right-hand side of Eq. 4.12 for this particular case. In model parameters sets mostly used, however, the characteristic tail energies are larger than the thermal energy.

- Although for *positive* values of ΔE_c and ΔE_v (giving a reduction of the mobility gap) N_{c2} and N_{v2} are always positive values, we can easily derive that negative values for N_{c2} and N_{v2} are obtained if negative values of ΔE_c or ΔE_v exceed a certain limit. The cause for these unphysical values is that an increase of the mobility gap expands the exponential tails from the old mobility edge, E_{c1} to the new one and that the trapped charge density in this expanded tail states may exceed the charge density of the original extended states. Hence, in order to maintain the same net charge density in the states beyond E_{c1} the excess localised charge density in the tails must

be compensated by a charge density of the opposite sign in the extended states of parameter set 2, thus the effective density of states, N_{c2} or N_{v2}, will get a *negative* value.

Approximate analysis

In the exact derivation given above the effective density-of-states values are transformed in such way that the total contribution to the space charge in states above E_{c2} or below E_{v2} is kept constant. The resulting dependence relations are therefore generally valid, also for crystalline semiconductor model parameters, where no localised states such as tail states or defect states are present in concentrations comparable to amorphous silicon. However, in amorphous silicon the density of gap states is so high that the dominant contribution to the space charge comes from the gap states; with the model parameters normally used the contribution of the charge carriers in the extended states is negligible. This relaxes the requirement that the total space charge in the states above E_{c2} or below E_{v2} should remain unchanged when applying the parameter transformation, since the contribution to the total space charge is negligible in the first place. Therefore, we can consider the effective density of states as another free parameter. Hence, we have two independent parameters, ΔE_c and N_c, and three dependent parameters in the 5 dimensional electron-related parameter space. The same applies to the hole-related parameter space. The range of valid values for N_{c2} and N_{v2} depends on the justification to neglect the contribution of extended states to the space charge density. Since this depends on the actual density and occupation of localised states, the valid parameter range must be determined for each case individually.

4.2.2 Numerical examples

First we show an example of the application of the exact parameter dependence relations. Different sets of i-layer parameters are obtained by application of Eqns. 4.10 to 4.18. In Table 4.2 the set labelled by 'Base' is the baseline set of parameters that is obtained by fitting our device simulator to measured dark IV-characteristics of a *pin* solar cell. In this set the mobility gap is set to 1.85 eV. The other three parameter sets, I, II and III, are derived by application of the exact dependence relations. The tail slope energy parameters, that occur in the dependence relations, are $E_c = 38.3$ meV and $E_v = 63.8$ meV. The temperature parameter, T, was set to 300 K. Different values of the free parameter ΔE_c and ΔE_v have been used. For transformation from the baseline set to set I positive and equal values for these are used. Parameter set II is obtained by only a shift in the valence band mobility edge. Finally, set III is obtained by shifting the

		Parameter set			
		Base	I	II	III
E_g	eV	1.85	1.70	1.75	1.95
ELECTRON-RELATED PARAMETERS					
ΔE_c	eV	0.00	0.075	0.00	-0.05
N_c	cm^{-3}	$7.03 \cdot 10^{20}$	$1.32 \cdot 10^{20}$	$7.03 \cdot 10^{20}$	$1.37 \cdot 10^{21}$
N_{c0}	$eV^{-1}\ cm^{-3}$	$1.36 \cdot 10^{22}$	$1.92 \cdot 10^{21}$	$1.36 \cdot 10^{22}$	$5.02 \cdot 10^{22}$
μ_n	$cm^2V^{-1}s^{-1}$	19.8	5.79	19.8	70.0
σ_n [a]	cm^2	$8.91 \cdot 10^{-16}$	$2.61 \cdot 10^{-16}$	$8.91 \cdot 10^{-16}$	$3.16 \cdot 10^{-15}$
σ_n [b]	cm^2	$1.17 \cdot 10^{-15}$	$3.44 \cdot 10^{-16}$	$1.17 \cdot 10^{-15}$	$4.16 \cdot 10^{-15}$
HOLE-RELATED PARAMETERS					
ΔE_v	eV	0.00	0.075	0.10	-0.05
N_v	cm^{-3}	$7.03 \cdot 10^{20}$	$1.87 \cdot 10^{20}$	$1.26 \cdot 10^{20}$	$2.07 \cdot 10^{21}$
N_{v0}	$eV^{-1}\ cm^{-3}$	$1.36 \cdot 10^{22}$	$4.20 \cdot 10^{21}$	$2.84 \cdot 10^{21}$	$2.98 \cdot 10^{22}$
μ_p	$cm^2V^{-1}s^{-1}$	3.95	0.809	0.462	9.28
σ_p [a]	cm^2	$8.91 \cdot 10^{-16}$	$1.82 \cdot 10^{-16}$	$1.04 \cdot 10^{-16}$	$2.09 \cdot 10^{-15}$
σ_p [b]	cm^2	$1.17 \cdot 10^{-15}$	$2.40 \cdot 10^{-16}$	$1.37 \cdot 10^{-16}$	$2.76 \cdot 10^{-15}$

[a]Dangling bond states
[b]Tail states

Table 4.2: Different parameter sets illustrating the exact dependence relations. Sets I, II and III are obtained by application of the dependence relations. The free parameters are ΔE_c for the electron-related parameters and ΔE_v for the hole-related parameters.

mobility edges outward, as to increase the mobility bandgap. The difference between the lowest and highest mobility bandgap is 0.25 eV and other parameters show differences exceeding one order of magnitude.

Figure 4.8 shows simulated *IV*-characteristics, obtained with the different parameter sets of Table 4.2. The dark *IV*-curves (Fig. 4.8a) and AM1.5G illuminated characteristics (Fig. 4.8b) are the same for the four parameter sets within a very small margin; despite of the large differences of the individual model parameters the relative difference between the curves is less than 0.1%.

Our derivation was based on the requirement that the quasi-Fermi levels, space charge (hence the electric potential as well), and recombination do not change. To illustrate that these requirements are satisfied, we show these quantities in Fig. 4.9. These characteristics correspond with 0.6 V forward bias without illumination. In the band diagram, Fig. 4.9a, the quasi-Fermi levels and the electric potential match very well. The differences between the conduction (valence) band mobility edges are caused by the ΔE_c (ΔE_v) parameter. The space charge

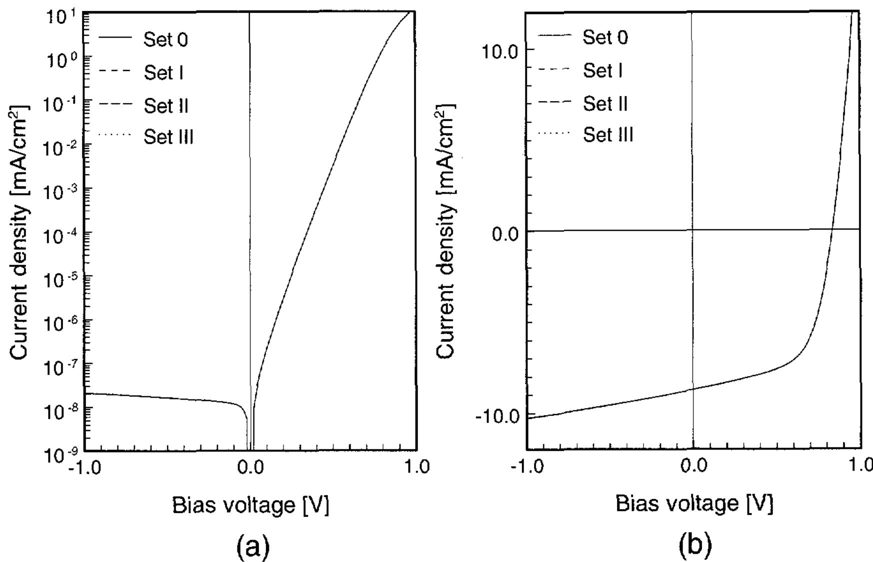

Figure 4.8: Simulation results of a *pin* structure with the 4 different sets of *i*-layer parameters of Table 4.2. (a) Dark IV-characteristics. (b) AM1.5G illuminated IV-characteristics. All curves match within 0.1%, although the parameter values show strong variations.

density (Fig. 4.9b) and recombination rates (4.9c) correspond to each other within a very small margin of $\approx 0.1\%$.

Figure 4.10a shows the difference in temperature behaviour of the dark IV-characteristics obtained with the different sets. The IV-characteristics at 300 K are the same as in Fig. 4.8a. At the other temperatures (here 270 K and 330 K) they show distinctly different results. The differences are caused by the different temperature dependences of the free carrier concentrations depending on the value of the mobility bandgap. The influence of temperature on the dark IV-characteristics is more pronounced in the *diode current activation energy* plot of Fig. 4.10b. The activation energy of the diode current is determined at each bias voltage as the slope of the Arrhenius plot.

An example of parameter transformation by application of the approximate dependence relations are shown in Table 4.3. Here, ΔE_c and N_c are the free parameters for the electron-related parameter dependence relations, and ΔE_v and N_v for the hole-related parameter dependence relations. Parameter set IV shows that the mobility values and capture cross sections do not change if the effective density of states transformation is given by $N_{(c,v)2} = N_{(c,v)1}\exp(\Delta E_{(c,v)}/kT)$. In sets V and VI there is no shift in the mobility edges; here only the effective density

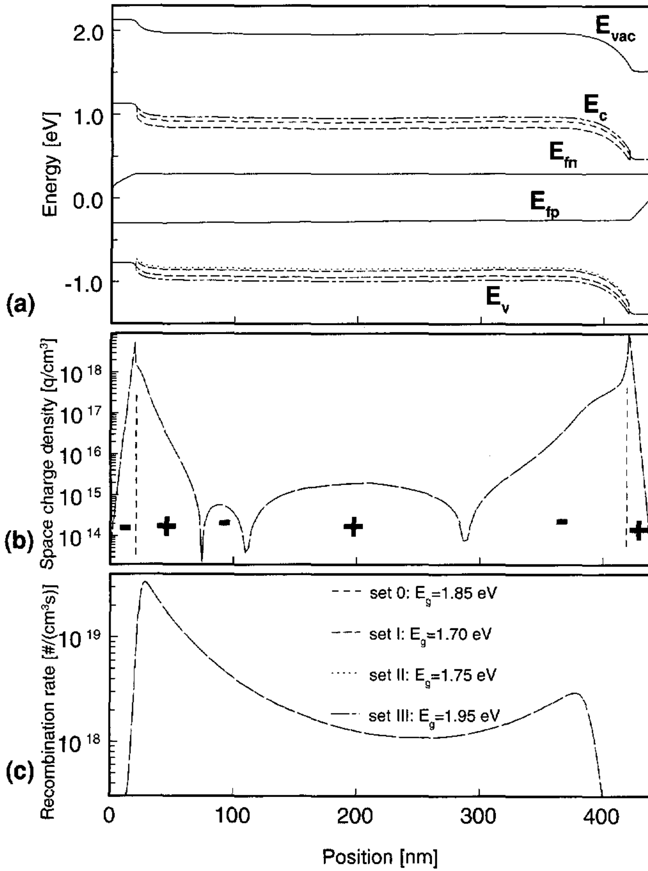

Figure 4.9: Internal quantities of the *pin* structure of Fig. 4.8. Shown are: (a) band diagram; (b) space charge density, and (c) recombination rates for the different parameter values of Table 4.2. All quantities are shown at 0.6 V forward bias without illumination. The four curves in the space charge and recombination graphs overlap exactly.

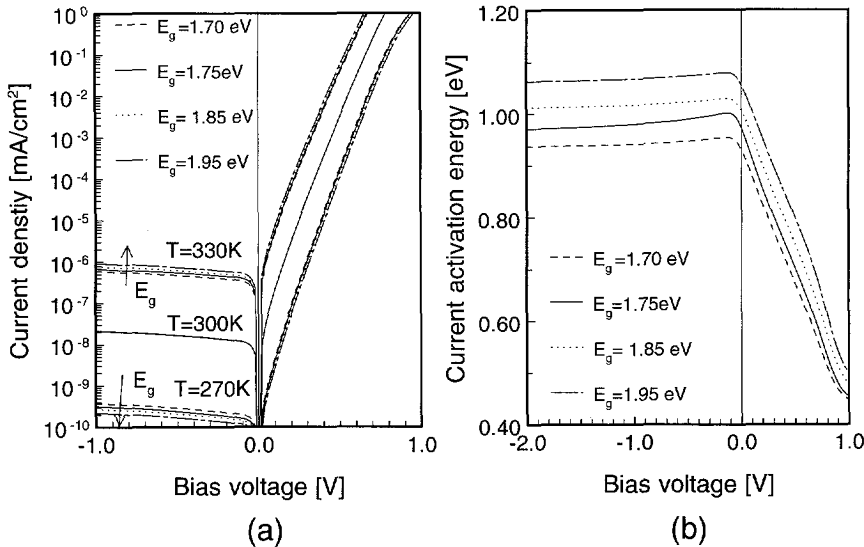

Figure 4.10: Influence of mobility gap on the simulated dark IV-characteristics of a *pin* diode. Figure (a) shows that at 300 K the curves overlap because the parameters depend on each other through the relations derived in this section (parameter sets 0, I, II and III of Table 4.2 are used). At 270 K and 330 K the IV-characteristics are not overlapping. Figure (b) depicts the current activation energy as a function of bias voltage with the bandgap as parameter.

of states are changed by over more than one order of magnitude. In set VII an arbitrary shift in the mobility edges is applied.

Despite the rather extreme changes in parameter values the dark and illuminated IV-characteristics at 300 K (not shown here) are almost equal for each of the parameter sets of Table 4.3. The relative differences are slightly larger than with parameter sets I, II and III, but still considerably less than 0.5%.

We have carried out temperature-dependent simulations of IV-characteristics with all parameter sets presented above. From the simulation results we can draw a very interesting conclusion: two parameter sets which are derived from each other using the dependence relations and which still have equal values for the mobility gap result in equal temperature-dependent behaviour. In other words, the temperature dependence of the IV-characteristics is determined only by the value of the mobility gap. We obtained equal temperature-dependent simulation results using the baseline set and set V and VI, which all have a mobility gap $E_g = 1.85$ eV. The other parameters have very different values in each set. This conclusion shows that mobility gap can be extracted from temperature-dependent

		Parameter set				
		Base	IV	V	VI	VII
E_g	eV	1.85	1.725	1.85	1.85	1.77
ELECTRON-RELATED PARAMETERS						
ΔE_c	eV	0.00	0.050	0.00	0.00	0.030
N_c	cm^{-3}	$7.03 \cdot 10^{20}$	$1.02 \cdot 10^{20}$	$1.00 \cdot 10^{20}$	$3.00 \cdot 10^{21}$	$3.00 \cdot 10^{21}$
N_{c0}	eV^{-1} cm^{-3}	$1.36 \cdot 10^{22}$	$3.69 \cdot 10^{21}$	$1.36 \cdot 10^{22}$	$1.36 \cdot 10^{22}$	$6.21 \cdot 10^{21}$
μ_n	$cm^2V^{-1}s^{-1}$	19.8	19.8	139	4.63	1.45
σ_n [a]	cm^2	$8.91 \cdot 10^{-16}$	$8.91 \cdot 10^{-16}$	$6.26 \cdot 10^{-15}$	$2.09 \cdot 10^{-16}$	$6.54 \cdot 10^{-17}$
σ_n [b]	cm^2	$1.17 \cdot 10^{-15}$	$1.17 \cdot 10^{-15}$	$8.24 \cdot 10^{-15}$	$2.75 \cdot 10^{-16}$	$8.61 \cdot 10^{-17}$
HOLE-RELATED PARAMETERS						
ΔE_v	eV	0.00	0.075	0.00	0.00	0.050
N_v	cm^{-3}	$7.03 \cdot 10^{20}$	$3.86 \cdot 10^{19}$	$1.00 \cdot 10^{20}$	$3.00 \cdot 10^{21}$	$3.00 \cdot 10^{21}$
N_{v0}	eV^{-1} cm^{-3}	$1.36 \cdot 10^{22}$	$4.20 \cdot 10^{21}$	$1.36 \cdot 10^{22}$	$1.36 \cdot 10^{22}$	$6.21 \cdot 10^{21}$
μ_p	$cm^2V^{-1}s^{-1}$	3.95	3.95	27.8	0.926	0.134
σ_p [a]	cm^2	$8.91 \cdot 10^{-16}$	$8.91 \cdot 10^{-16}$	$6.26 \cdot 10^{-15}$	$2.09 \cdot 10^{-16}$	$3.02 \cdot 10^{-17}$
σ_p [b]	cm^2	$1.17 \cdot 10^{-15}$	$1.17 \cdot 10^{-15}$	$8.24 \cdot 10^{-15}$	$2.75 \cdot 10^{-16}$	$3.97 \cdot 10^{-17}$

[a] Dangling bond states
[b] Tail states

Table 4.3: Different parameter sets illustrating the approximate dependence relations. Sets IV, V, VI and VII are obtained by application of the dependence relations. For the approximate dependence relations the free parameters are ΔE_c and N_c for the electron-related parameters and ΔE_v and N_v for the hole-related parameters.

(dark) *IV*-measurements.

4.2.3 Discussion

In the previous two sections we have shown that the parameter space of 5 important *a*-Si:H model parameters show dependences that can be expressed by simple relations. With these relations parameter sets can be transformed, while maintaining the same simulation output of steady-state characteristics. The parameter transformations are controlled by two free parameters, thus leaving three dependent parameters. As electron-related (hole-related) free parameters we have chosen the shift in the conduction-band (valence-band) mobility edge, ΔE_c (ΔE_v), and the effective density of free electron (hole) states, N_c (N_v). If the bandgap does not change between different parameter sets the temperature dependence is equal.

An important conclusion of this work is that it is impossible to find a single

set of model parameters by means of inverse modelling of experimental steady-state *IV*-data at a single temperature. This conclusion has been foreseen, based on the large number of parameters in amorphous silicon modelling; now a quantitative analysis is established, which provides good insight in the parameter dependences. Because of the dependence relations a whole range of parameter values can be found that give exactly the same simulation results. We have illustrated this with a couple of parameter sets that were derived from the same baseline set and were used for the simulation of a *pin* structure. Moreover, our dependence relations are not only applicable to *pin* diodes, but apply also to other experimental data which are often used to characterise *a*-Si:H, such as dark (bulk) conductivity and photoconductivity. The output of models that are used to analyse these experiments also remains unchanged when the parameter transformations are applied.

In the examples it is shown that parameter sets can be transformed into other 'valid' parameter sets, which, however, contain parameters that are generally considered as unphysical for *a*-Si:H and related materials. As an example we mention the extremely high electron mobility value in set V, $\mu_n = 139\ \mathrm{cm^2V^{-1}s^{-1}}$, which is far outside the range of commonly accepted values of the electron mobility in *a*-Si:H.

The band diagrams of Fig. 4.9 show that the parameter transformations may introduce band offsets in the conduction and valence band edge; it is interesting to note that those offset do *not* influence the *IV*-characteristics of the device. Offsets in the band edges are often designated as *heterojunctions*; our example shows that there exists a duality between the introduction of a heterojunction and change of other transport parameters. Thus, at a single temperature a heterojunction can be modelled in either way: change of bandgap or change of other, dependent parameters. However, we must note that the temperature-dependent behaviour is different.

Based on findings of this section we can provide guidelines for parameter extraction and model calibration.

- If steady-state data at only one temperature point is available, the values of the bandgap and effective density of states in the conduction and valence band can be set to chosen, plausible values and kept fixed during the fitting procedure. The other parameters of our parameter dependence relations, *vis.* the mobilities, capture cross sections and density of localised tail state at the mobility edges, and the other parameters of the density of localised states that are not included in our dependence relations, may be determined by fitting the simulation results to the experimental data.

- If steady-state data at various temperatures is available the bandgap can

also be extracted by inverse modelling.

- If time-resolved (transient or small-signal) experimental data is available (and a detailed device simulator allowing these types of simulations) accurate values of the lifetimes of the free carrier can be extracted, thus a decoupling between the capture cross sections (largely determining the life times) and the free carrier concentrations (strongly determined by the effective density of states) can be established.

- Physical meaningful data about bandgap differences at heterojunctions can only be extracted from experiments if the temperature-dependent measurement data are available.

Although we cannot decisively conclude that the use of the proposed extensive set of experiments and simulation modes (steady-state and time-resolved and temperature-dependent) in a calibration step ensures the determination of a unambiguous set of parameters, our analysis clearly points out that *without* such elaborate calibration procedure it is certainly impossible.

4.3 Assessment of the abrupt mobility edge approximation

As pointed out in the introduction of this thesis there exist mobility edges in the conduction and valence bands of amorphous semiconductors such as a-Si:H. At these edges the carrier mobilities change strongly. Hence, the mobility edges are considered as a separation between the localised and extended states (see also Fig. 1.4). The exact change of the mobility as a function of energy is not known. However, one may expect on physical grounds that the carrier mobility increases gradually rather than abrupt, with increase of energy: if we assume that energy levels deep in the tails correspond to states with a stronger localisation than close to the mobility edges, we expect that the mobility increases as the carriers are less deep trapped and that the mobility smoothly increases with increase of energy.

In contrast to the gradual change in mobility, in simulation models the mobility change at the mobility edges is assumed to be abrupt. Below the mobility edge the mobility is assumed to be zero and above it is assumed to have a constant value. In this section we will examine this assumption and the consequences for the device simulation. This analysis is motivated by the following questions, which are highly relevant for modelling:

- does the mobility depend on the concentration of free carriers?

- is the temperature dependence of the mobility influenced by the details of the mobility vs. energy dependence around the mobility edge?

In our search for the answers, we analyse the transport and occupation of free electron states analytically. The analysis is restricted to one type of carriers, the electrons, since the analysis for the other type is completely analogous. We find that the mobility can be expressed as an average mobility that is not dependent on the occupation of free electron states.

If we consider the transport equation for electrons

$$\vec{J}_n = \mu_n n \nabla E_{fn}, \tag{4.19}$$

we note that the electron current density equals the product of mobility μ times carrier concentration n and the gradient of the electron quasi-Fermi level. Since the mobility is a function of energy, the product $\mu_n n$ must be determined by integration over all energy states with mobile carriers. In amorphous silicon the occupation function of shallow tail states and extended states can be approximated by the Maxwell-Boltzmann function, so the integral for a certain value of the quasi-Fermi level, E_{fn}, becomes

$$\mu_n n = \int_{E_c}^{\infty} N(E)\mu(E) \exp\left(\frac{E_{fn} - E}{kT}\right) dE. \tag{4.20}$$

We can define an average, effective mobility μ_{eff} as a mobility weighted by the density of states $N(E)$ and occupation function:

$$\mu_{eff} = \frac{\int_{E_c}^{\infty} N(E)\mu(E) \exp\left(\frac{E_{fn}-E}{kT}\right) dE}{\int_{E_c}^{\infty} N(E) \exp\left(\frac{E_{fn}-E}{kT}\right) dE}. \tag{4.21}$$

In this equation the denominator equals the effective density of states N_c in the conduction band above E_c. Since the concentration of carriers in the states above E_c equals $n = N_c \exp((E_{fn} - E)/kT)$, we can write Eq. 4.20 as

$$\mu_n n = \mu_{eff} N_c \exp\left(\frac{E_{fn} - E}{kT}\right). \tag{4.22}$$

From this equation we can conclude that the mobility, μ_n, in Eq. 4.19 can be approximated by an effective mobility. This μ_{eff} is independent of the occupation of the tail and extended states, and no detailed knowledge of the exact form of the mobility as a function of energy is required. However, from Eq. 4.21 we can conclude that the exact form of $\mu(E)$ and the choice of E_c have influence on

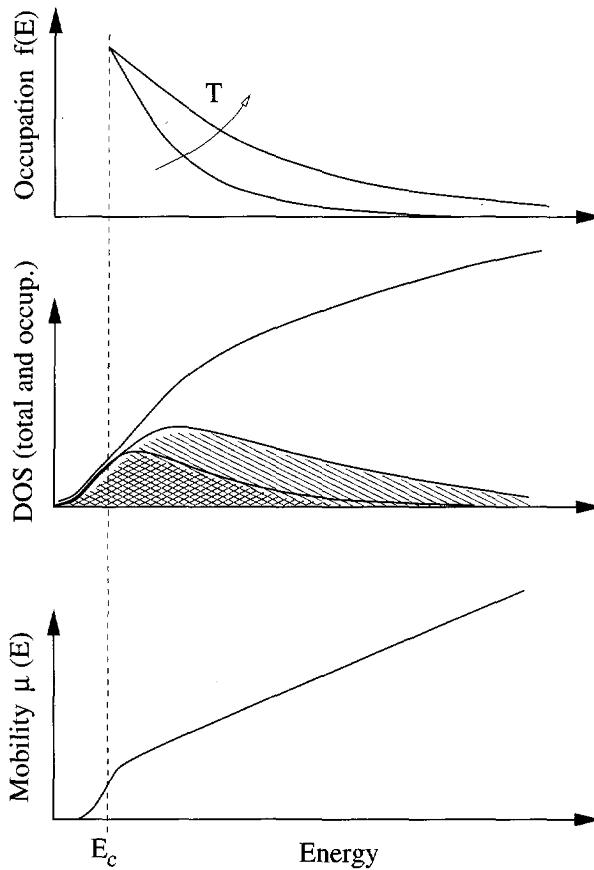

Figure 4.11: Schematic illustration to explain possible temperature dependences of effective mobility, due to a increasing mobility as a function of energy in the extended states. The effective mobility is weighted by the product of density of states N(E) and occupation function f(E) (centre graph). At higher temperatures the weighting function (shaded areas in the centre graph) favours the higher mobility values (lower graph).

the temperature dependence of the effective mobility. This will be illustrated on the basis of Fig. 4.11, that shows a $\mu(E)$ function, that slowly increases with E. If the temperature increases, the "tail" of the Maxwell-Boltzmann function gets longer. Because the effective mobility is weighted by the product of the Maxwell-Boltzmann distribution and the density of states $N(E)$ (which we assume to stay unchanged with increase of temperature), the contribution of relatively higher mobility values is larger at higher temperatures than at lower temperatures. Thus, the weighted average (effective) mobility, μ_{eff} ,increases with increasing temperature if the mobility increases as a function of energy E. In this analysis the assumption is made that the mobility as a function of energy, $\mu(E)$, is *independent* of temperature.

From this analysis we can conclude that for modelling we do not require the exact dependence of the mobility as a function of energy. The mobility can be expressed by an effective mobility value. The temperature dependence of the effective mobility will be determined by detailed properties of the $\mu(E)$ function.

4.4 Model parameter sensitivities

One of the main difficulties of *a*-Si:H device modelling is the need for a large number of parameters to describe the physical properties of the material in sufficient detail. It may be obvious that the responses of material and device characterisation experiments are not all equally sensitive to the same physical material parameters. For instance, a particular parameter which largely determines the result of experiment A, can be without influence on a response of another experiment B. This means that experiment A is very sensitive to the parameter, whereas experiment B is not sensitive at all; this shows that the importance of a model parameter is a relative concept and must be related to a specific experiment. In order to get a good feeling for the sensitivity of *a*-Si:H single-junction *pin* solar cell characteristics to model parameters a comprehensive sensitivity study has been carried out [149]. All parameters of a simple *pin* structure, consisting of three layers with homogeneous properties, are included. This resulted in a ranking of the parameters, based on the relative sensitivity of different solar cell responses. In the first place, the most influential parameters are obtained from the ranking, but equally important is the identification of the parameters without any influence whatsoever. This knowledge is important for parameter calibration by inverse modelling, because it only makes sense to extract the most influential parameters. More generally, a good overview of the influence of model parameters supports experimental work, because it is helpful for the interpretation of experiments and the explanation of trends. Further, it provides insight in which parameters must

be controlled tightly in solar cell technology and which parameters must be measured more accurately, because of their large impact on the modelling results.

In our study we have used the differential response of an output parameter as measure of the sensitivity of this model response to input parameters. The differential response is determined as the difference between the model response to a baseline parameter set and the response to a disturbed parameter set. In the disturbed set one of the parameters is set to an extreme value of its parameter range (either the low or high boundary value); the other parameters keep the same value as in baseline set. The sensitivity is defined as the maximum of the differential response due to changing a particular parameter to either its lower or its upper extreme value. In this procedure only one parameter is changed at a time and it is repeated for each parameter. The obtained sensitivities are classified in different groups, depending on their relative magnitude, in order to get a final ranking of the influence of model parameters.

With our definition of sensitivity we take into account the extent of the parameter space for a particular parameter. This would not be the case if we would use the relative sensitivity instead. The relative sensitivity of a response R to a parameter p is defined as $\frac{dR}{dp} \cdot \frac{p}{R}$, which is in fact a normalised gradient. In our approach a model response can be more sensitive to a parameter p_1 with a small gradient than to parameter p_2, if the parameter space is much larger for parameter p_1 than for parameter p_2; the gradient is less suited to express the sensitivity, unless some normalisation is applied to the parameter space.

Since we change only one parameter at a time, correlation effects between parameters are not taken into account. However, parameters may have a quite different influence on the model behaviour in different parts of the parameter space. In order to include this possibility in our analysis we have repeated the sensitivity analysis for different baseline sets and combined the ranking results of each baseline set to obtain the final ranking. The derived baseline sets are generated randomly from the main baseline set. In this random process we assumed that each parameter has a Gaussian probability distribution around the main baseline set value and that the boundaries of the parameter space are positioned at 3σ from their main value. In case the baseline value is not in the centre of the parameter space the Gaussian distribution is asymmetrical.

Our sensitivity analysis is based on an intuitive approach and is not very efficient in terms of number of experiments (read: simulation runs). More efficient approaches are described in literature; see for instance the review by Kleijnen [64].

Several sensitivity studies for a-Si:H solar cells have been published: McElheny *et al.* [79] have studied the sensitivity of the quantum efficiency of a-Si:H

Schottky barrier solar cells and Chatterjee [23] has studied the sensitivity of the illuminated *IV*-characteristics of an *a*-Si:H *pin* cell. In both papers only few solar cell responses were considered and their sensitivity to parameter changes has been presented in graphs, depicting quantum efficiency or *IV*-characteristics. In the present study a visual interpretation of device characteristics by comparing different graphs is infeasible, because of the large number of solar cell response parameters and model parameters that are included. Therefore, we have chosen a fully automated approach which does not depend on subjective interpretation of graphs by the researcher. In this approach the solar cell responses must be represented by a few characteristic response parameters instead of the full device characteristics, to enable meaningful automated processing of the simulation data.

In this study the sensitivities of three different electrical and electro-optical solar cell characteristics are considered: dark *IV*-characteristics, illuminated *IV*-characteristics, and external quantum efficiency. A limited number of parameters (the response parameters) describes the typical features of each individual device characteristic; we determine the sensitivity of these response parameters to model parameter disturbances. Below we present a list of the response parameters including details about how to determine those from the simulated *IV*- and EQE-curves.

Dark *IV*-characteristics are parameterised by three response parameters:

- *Diode ideality factor, n:* This parameter is determined by fitting a straight line to the $\log(I)$ curve between 0.35 and 0.7 V forward bias. n is proportional to the reciprocal slope of the fitted line.
- *Saturation current, I_0:* In this work the y-axis intercept of the above-mentioned fitted line is considered as the saturation current, I_0. Note that this value is not necessary equal to the reverse current density.
- *Series resistance factor, F_s:* In the high forward-bias range dark *IV*-characteristics deviate from the exponential behaviour shown at lower forward bias voltages. The factor F_s is introduced to quantify this deviation for bias voltages above 0.8 V. The name 'series resistance factor' is chosen, because series resistance is the most obvious physical cause for this kind of effects; however, we have to note that there are many other physical effects that cause this behaviour. The factor F_s is defined as the integral between the fitted straight line and $\ln(I)$: $F_s = \int_{0.8}^{V_{max}} [\ln(I_0) + \frac{qV}{nkT} - \ln(I_{sim}(V))] dV$. This expression is evaluated numerically.

Illuminated IV-characteristics are characterised by three response parameters:

- *Open-circuit voltage,* V_{oc}
- *Short-circuit current,* I_{sc}
- *Fill factor, FF*

These parameters are determined straightforwardly from the simulated IV-curves.

In the present study three different illumination conditions are used for the simulation of IV-characteristics. (1) the standard solar irradiation (AM1.5G spectrum at 100 mW/cm^2), (2) 400 nm wavelength monochromatic illumination (blue light), and (3) 600 nm wavelength monochromatic illumination (red light). The monochromatic illumination is at low intensity (0.1 mW/cm^2).

External quantum efficiencies are characterised by two parameters which allow the comparison of individual EQE-curves in an automated way. These parameters are defined as:

- EQE_{35} is the integrated quantum efficiency spectrum for wavelengths between 300 nm and 550 nm.
- EQE_{58} is the integrated quantum efficiency spectrum for wavelengths between 550 nm and 800 nm.

These parameters do not reflect all typical features of the curves (such as positions of interference fringes). Nevertheless, they are well-suited for a general and easy comparison of EQE-characteristics.

All EQE-simulations use a standard bias illumination, AM1.5G spectrum at 100 mW/cm^2, and two different forward bias voltages, 0.0 V and 0.8 V.

Counting all chosen parameters describing the device characteristics and the different bias conditions yields a total of 16 response parameters which are considered in this sensitivity study. For each of these response parameters we have determined its sensitivity to changes of a large number of the device model input parameters. Both structural parameters, such as layer thicknesses, and physical parameters, such as mobilities and capture cross sections, are considered. Our parameter set contains in total 113 input parameters. The baseline set was obtained by inverse modelling (see Sect. 4.5).

For each parameter we have defined a range in the parameter space. The choices of these ranges are based on (1) differences between various parameter

sets as reported in literature, (2) estimations of the measurement accuracy of each parameter and (3) estimations of technological spread in parameters. In Table 4.4 all baseline parameters and ranges are given. The meaning of the following parameters is not self-explanatory:

- the ratio between the band-tail density-of-states (DOS) at the mobility edge (N_{c0} and N_{v0}, for the conduction band tail and valence band tail, respectively) and the effective extended DOS (N_c and N_v) is used to control the band-tail DOS. This approach is chosen because those two parameters are physically correlated: the complete DOS distribution (see, for instance, Fig. 1.4) is a continuous curve, and therefore, changes of the band tail DOS value at the mobility edge are coupled with changes of the exended (effective) DOS. It can be shown that the ratio between N_{c0} (N_{v0}) and N_c (N_v) must be in the order of $1/kT$.

- the width of the DOS distribution of the valence band tail and conduction band tail, indicated by $E_{range,vt}$ and $E_{range,ct}$, respectively. This input parameter defines the width of the energy range that is occupied by the tail states adjacent to the mobility edge.

- width of the dangling bond states, indicated by $E_{range,db}$. This parameter sets the width of the energy range occupied by the Gaussian distributed dangling bond states. The unit of this parameter is the standard deviation of the distribution function, σ_{db}, as unit.

- the parameter defining the band offset at the *p-i* and *n-i* interface is indicated by "band offset". This parameter can can vary between 0 and 1, where 0 (1) means that the mobility gap difference is exclusively attributed to a step in the conduction (valence) band mobility edge. Intermediate values denote that the mobility gap difference is partially attributed to a valence-band offset and a conduction-band offset.

In the simulations the defect distribution is represented by a Gaussian distribution. In each of the three layers all material properties are position-independent values. For the simulations with 100 mW/cm^2 AM1.5G illumination a fixed set of measured optical parameters for each layer is used. Hence, the sensitivity of the response parameters of the AM1.5G illuminated IV-characteristics to the optical parameters of the layers is not determined. Further, mobility bandgap values are not correlated with the optical bandgap (and thus the absorption coefficients); both parameters are varied independently.

		p-layer		i-layer		n-layer	
STRUCTURE PARAMETERS							
d	nm	10	(5–20)	500	(470–530)	20	(15–25)
OPTICAL PARAMETERS, BLUE LIGHT, 400 NM							
α	μm^{-1}	29.8	(22–38)	47.1	(31–57)	29.5	(22–41)
n	-	3.75	(3.3–4.1)	5.12	(4.8–5.5)	4.6	(4.2–5)
OPTICAL PARAMETERS, RED LIGHT, 600 NM							
α	μm^{-1}	2.26	(1.9–2.9)	2.81	(2.1–3.3)	2.93	(2.1–3.3)
n	-	3.1	(2.9–3.3)	4.3	(4.1–4.5)	4.1	(3.9–4.3)
TRANSPORT, DOPING AND EXTENDED STATES PARAMETERS							
μ_n	cm^2/Vs	1.0	(0.1–10)	10	(1.0–100)	2.0	(0.2–20)
μ_p	cm^2/Vs	0.2	(0.02–2.0)	2.0	(0.2–20)	0.4	(0.04–4.0)
E_{act}	eV	0.46	(0.3–0.55)		(–)	0.29	(0.20–0.40)
E_g	eV	1.83	(1.75–2)	1.7	(1.68–1.9)	1.7	(1.7–1.9)
N_v	10^{20} cm^{-3}	3.2	(0.5–8)	3.2	(0.5–8)	3.2	(0.5–8)
N_c	10^{20} cm^{-3}	3.2	(0.5–8)	3.2	(0.5–8)	3.2	(0.5–8)
ε_r	-	7.2	(5–9)	11.9	(10–13)	11.9	(10–13)
VALENCE BAND TAIL STATES PARAMETERS							
N_{v0}/N_v	eV^{-1}	50	(10–100)	50	(10–100)	50	(10–100)
E_{v0}	eV	0.10	(0.07–0.12)	0.047	(0.033–0.055)	0.047	(0.033–0.055)
σ_p^0	10^{-14} cm^2	1.2	(0.1–12)	1.2	(0.1–12)	1.2	(0.1–12)
σ_n^+	10^{-14} cm^2	12	(1.0–120)	12	(1.0–120)	12	(1.0–120)
$E_{range,vt}$	eV	0.5	(0.5–0.8)	0.5	(0.5–0.8)	0.5	(0.5–0.8)
CONDUCTION BAND TAIL STATES PARAMETERS							
N_{c0}/N_c	eV^{-1}	50	(10–100)	50	(10–100)	50	(10–100)
E_{c0}	eV	0.065	(0.05–0.075)	0.028	(0.020–0.036)	0.028	(0.020–0.036)
σ_n^0	10^{-14} cm^2	1.2	(0.1–12)	1.2	(0.1–12)	1.2	(0.1–12)
σ_p^-	10^{-14} cm^2	12	(1.0–120)	12	(1.0–120)	12	(1.0–120)
$E_{range,ct}$	eV	0.5	(0.5–0.8)	0.5	(0.5–0.8)	0.5	(0.5–0.8)
DANGLING BOND STATES PARAMETERS							
U	eV	0.4	(0.3–0.45)	0.4	(0.3–0.45)	0.4	(0.3–0.45)
$E^{+/0}$	eV	-1.12	(-1.24—1.00)	-1.05	(-1.17—0.93)	-1.05	(-1.17—0.93)
N_{db}	10^{16} cm^{-3}	400	(10–1000)	0.3	(0.03–3.0)	8.0	(1–63)
σ_{db}	eV	0.141	(0.1–0.2)	0.141	(0.1–0.2)	0.141	(0.1–0.2)
$E_{range,db}$	$*\sigma_{db}$	6	(4–8)	6	(4–8)	6	(4–8)
σ_p^0	10^{-14} cm^2	10	(1–100)	10	(1–100)	10	(1–100)
σ_n^0	10^{-14} cm^2	10	(1–100)	10	(1–100)	10	(1–100)
σ_p^-	10^{-14} cm^2	100	($1–10^4$)	100	($1–10^4$)	100	($1–10^4$)
σ_n^+	10^{-14} cm^2	100	($1–10^4$)	100	($1–10^4$)	100	($1–10^4$)

Table 4.4: Values of parameters in the baseline set and their ranges. Parameters of *a*-Si:H-layers.

		Glass	TCO	Silver
		STRUCTURE PARAMETERS		
d	μm	1500 (1000–3000)	0.5 (0.3–0.7)	0.2 (0.05–0.5)
		OPTICAL PARAMETERS, BLUE LIGHT, 400 NM		
α	μm^{-1}	0.0 (0.0–$5 \cdot 10^{-5}$)	0.42 (0.16–0.63)	69 (60–78)
n	-	1.5 (1.4–1.7)	2.086 (1.8–2.4)	0.23 (0.2–0.27)
		OPTICAL PARAMETERS, RED LIGHT, 600 NM		
α	μm^{-1}	0.0 (0.0–$5 \cdot 10^{-5}$)	0.19 (0.10–0.30)	86 (80–92)
n	-	1.5 (1.4–1.7)	1.91 (1.7–2.1)	0.265 (0.25–0.28)

MISCELLANEOUS PARAMETERS		
$S_{n,front}$	cm/s	10^7 (10^2–10^7)
$S_{p,rear}$	cm/s	10^7 (10^2–10^7)
P_{irr}	mW/cm^2	0.1 (0.09–0.11)
T	K	300 (295–305)
p-i band offset	-	0.5 (0.0–1.0)
n-i band offset	-	0.5 (0.0–1.0)

Table 4.4: (Continued) Values of parameters in the baseline set and their ranges. Parameters of TCO, glass and silver and miscellaneous parameters.

The most influential parameters are shown in Table 4.5. The total number of 113 model parameters is reduced to 28 most-important parameters. The symbols indicate the relative sensitivity of the responses to the various parameters. The symbols have the following order: +++, ++, +, -, - -, - - -, 0, where +++ means "largest influence" and - - - means "little influence", 0 means "no influence", n means "not considered". Instead of showing all capture cross sections corresponding to each possible charge state of each type of localised state, we have given only one cross section per type of localised state (σ_{vt}, σ_{ct} and σ_{db} for the valence band tail, conduction band tail and dangling bonds, respectively). Information can be obtained from the table in two different ways:

- the relative sensitivities of a particular response parameter to various model parameters can be analysed by column-wise comparison of the entries for that response parameter. In this way the most influential parameters and the parameters without influence on a particular solar cell response are identified.

- the relative importance of a particular model parameter for the different response parameters can be found by row-wise comparison of the entries. In this way it can be seen which response parameter is most or least sensitive

to changes of a particular model parameter.

Some of the remarkable results of this study are briefly discussed:

- The dark IV-response parameters n and I_0 are most sensitive to the i-layer dangling bond density, N_{db}, and capture cross sections, σ_{db}; somewhat less influential are the mobility gaps, E_g, of the p-layer and i-layer. We note that the dangling bond parameters N_{db} and σ_{db} are most influential on the response parameters n and I_0; therefore, dark IV-curves are the preferred experiments to study the midgap density in the i-layer in a-Si:H *pin* diodes. The strong correlation of the i-layer parameters E_g, N_v, and N_c with the intrinsic free-carrier concentration explains the relatively strong influence of these parameters on the saturation current, I_0, which is approximately proportional to the intrinsic free-carrier concentration (see Sect. 4.1). Further, the relatively strong influence of the valence band tail parameters E_{v0} and σ_{vt} on the ideality factor n is explained by the role that the tail states play in the *bias-voltage dependence* of the current, which is directly related to n (see Sect. 4.1). A bias-voltage increase results in a enlarged separation of the trapped-charge quasi-Fermi levels. Consequently, a larger part of the tail states will start to act as recombination centres. Since the conduction band tail is steeper than the valence band tail the influence of the latter on the recombination current is larger.

  The series resistance factor, F_s, is most sensitive to the p-layer parameters that control the conductivity of this layer: most notably the hole mobility, μ_p, and activation energy, E_{act}. This indicates that the value of F_s is mostly determined by resistance effects of the p-layer. To a lesser extent many parameters of the i-layer influence this response parameter.

- The most important model parameters for the 'blue response' (the external quantum efficiency between 300-550 nm) are the TCO and p-layer parameters. Influential i-layer parameters are the mobilities, μ, and mobility gap, E_g. At 0.8 V forward bias the relative importance of the parameters changes a little: in this case the i-layer effective DOS of the extended states, N_v, and tail states capture cross sections, σ_{vt}, gain importance.

  The large influence of TCO and p-layer parameters is explained by the impact of optical losses in these layers and the losses of photo-generated carriers close to the p-i interface due to unwanted minority-carrier (electron) diffusion towards the p-layer. The transport and recombination properties of the p-layer strongly influences the minority carrier diffusion.

- For the 'red response' (the EQE between 550 and 800 nm) the electrical and optical parameters of the i-layer gain importance over the TCO and p-layer parameters. Since the i-layer is more transparent in this wavelength region, optically relevant parameters such as i-layer absorption coefficient, α, and layer thickness, d, are more important than for the blue response, where all photons are absorbed in the top region of the i-layer. The stronger influence of the hole mobility on the red response than on the blue response is due to the more homogeneous carrier generation by red light. Because of the homogeneous generation the average distance that holes have to travel towards the collecting p-layer is longer than in the case of blue light illumination; in the latter situation electron-hole pairs are generated only in the vicinity of the p-layer, hence the average distance for the holes is less and the importance of hole mobility on the collection efficiency is less.

- Most important parameters for the V_{oc} for all three illumination conditions considered, are the mobility gap, E_g, of the i-layer and the mobility gap, E_g, and the activation energy, E_{act}, of the p-layer. The influence of the i-layer mobility gap and the effective density of extended states, N_v and N_c, is explained by their impact on the maximum obtainable separation of the i-layer quasi-Fermi levels due to optical carrier generation, which is closely correlated with the V_{oc}. Further the relatively strong influence of the valence band tail parameters, E_{v0}, N_{v0}, and σ_{vt} and the defect density, N_{db}, are explained by their strong influence on the carrier recombination in the device.

- The short current densities, I_{sc}, are very sensitive to the optical parameters of each layer and the irradiance of the illumination. The sensitivity to these model parameters is obvious, because of the proportionality between the optical absorption and I_{sc}. Similar to the above discussed blue and red response the 400 nm illuminated IV-characteristics are very sensitive to the TCO and p-layer optical parameters and to the p-layer electrical parameters. Of the i-layer parameters the electron mobility, μ_n, and the mobility gap, E_g, are influential. In the case of 600 nm monochromatic illumination the optical parameters of the TCO and the i-layer are very important. Further, the i-layer hole mobility, μ_p, is very influential, because of reasons outlined above in the discussion of the red response. Note that in case of blue light the i-layer electron mobility, μ_n, and in case of red light the hole mobility, μ_p, is important for the short current response. From this the conclusion can be drawn that for blue light the electron transport is a limiting factor for the carrier collection and for red light the hole transport.

The only response parameter where the n-layer thickness, d, has significant influence is the 600 nm light I_{sc}. This is explained by its role as parasitic absorber of long wavelength light which is transmitted trough the i-layer. Optimally, this light must be reflected without absorption in the n-layer and any reflection losses at the metal back surface.

- the *FF* of *pin* cells with low intensity illumination is most sensitive to the parameters that influence the charge collection: activation energy, E_{act}, and mobility gap, E_g, of the p-layer, and mobilities, mobility gap, E_g, density of valence band tail states parameters, E_{v0}, N_{v0}, and σ_{vt}, and density of dangling bonds, N_{db}, of the i-layer. In addition, the parameters determining the p-layer conductivity show their influence for AM1.5G illumination: E_{act}, N_v, and μ_p. In this case of high current densities the influence of the series resistance caused by the p-layer resistivity on the *FF* is reflected by the importance of these parameters.

Another valuable result of this study is the identification of *unimportant* model parameters. The following parameters have relatively insignificant influence on the device responses included in this study:

- the relative dielectric constants, ε_r, of all three a-Si:H layers. These parameters only influence the dependence of the internal electric field distribution on the space charge distribution (see Eq. 2.1); obviously, their influence on the internal field is small within the ranges that we have chosen for these parameters.

- almost all n-layer parameters, such as the effective density of states, conduction and valence band tail parameters, dangling bond parameters, activation energy, mobilities. The unimportance of the n-layer is reflected in the very little attention that is paid to this specific layer in literature. In a-Si:H *pin* solar cell research the properties of the n-layer are not considered as very critical, in contrast to the properties of the p-layer, i-layer and the interface thereof. Our modelling results are in agreement with this technological experimental observation.

- the conduction band tail parameters. These parameters are less influential than the valence band tail parameters, due to the fact that the density of conduction band tail states is much lower than the density of valence band tail states. This is caused by the smaller exponential characteristic energy of the conduction band tail. This agrees with the findings of Chatterjee [23].

	DARK *IV*			QUANTUM EFFICIENCY			
				300-550 nm		550-800 nm	
Parameter	n	I_0	F_s	0.0 V	0.8 V	0.0 V	0.8 V
TCO PARAMETERS							
d	0	0	0	+++	+	+	-
α	0	0	0	+++	+++	+	+
n	0	0	0	++	++	++	++
***p*-LAYER PARAMETERS**							
d	- -	- -	++	++	++	+	+
α	0	0	0	++	++	−	−
μ_n	+	-	+	+++	++	+	++
μ_p	-	- -	+++	++	+++	++	+++
E_{act}	+	+	+++	+++	+++	++	+++
E_g	++	++	++	+	++	-	++
N_v	-	-	++	++	++	+	++
σ_{vt}	-	-	+	++	++	-	+
σ_{db}	+	+	+	++	+	+	+
***i*-LAYER PARAMETERS**							
d	-	-	-	- -	-	+	-
α	0	0	0	-	-	++	++
n	0	0	0	+	+	++	++
μ_n	-	-	+	++	++	+	-
μ_p	+	-	+	++	+	+++	+++
E_g	++	+++	++	++	++	+	++
N_v	+	++	++	+	++	++	++
N_c	+	++	++	+	+	-	+
N_{v0}	+	-	++	+	+	++	+++
E_{v0}	++	+	++	+	+	++	+++
σ_{vt}	++	+	++	+	++	++	++
N_{db}	+++	+++	++	-	+	+	+
σ_{db}	+++	+++	++	-	-	-	-
***n*-LAYER PARAMETERS**							
d	- -	- -	- -	- -	- -	-	- -
MISCELLANEOUS PARAMETERS							
P_{irr}	0	0	0	-	- -	-	-
T	+	+	-	+	-	+	-

Table 4.5: Influence of model parameters on dark *IV*-characteristics and external quantum efficiency spectra.

ILLUMINATED IV-CHARACTERISTICS

	400 nm			600 nm			AM 1.5G		
Parameter	V_{oc}	I_{sc}	FF	V_{oc}	I_{sc}	FF	V_{oc}	I_{sc}	FF
TCO Parameters									
d	+	+++	--	-	++	-	-	+	-
α	+	+++	-	-	++	-	n	n	n
n	+	++	--	-	+++	-	n	n	n
p-Layer Parameters									
d	+	+++	-	-	+	-	-	+	+
α	-	++	--	--	-	--	n	n	n
μ_n	++	++	+	+	-	-	++	+	+
μ_p	--	-	+	-	--	+	+	+	+++
E_{act}	+++	++	++	++	-	++	++	+	++
E_g	+++	++	++	+++	-	+	+++	+	+
N_v	-	+	-	-	-	+	-	+	++
σ_{vt}	+	+	-	-	-	--	+	+	-
σ_{db}	++	+++	+	+	-	+	-	+	-
i-Layer Parameters									
d	-	--	-	+	+++	+	--	-	-
α	--	+	--	-	+++	+	n	n	n
n	-	+	--	+	+++	-	n	n	n
μ_n	-	++	++	-	-	+	-	+	+
μ_p	+	--	+	+	+++	+++	+	+++	+++
E_g	+++	++	+++	+++	+	+	+++	++	++
N_v	++	-	++	+++	-	++	++	+	++
N_c	++	+	++	++	-	+	++	-	+
N_{v0}	+	-	+	++	-	++	+	+	++
E_{v0}	++	+	+	++	-	+++	+	+	++
σ_{vt}	++	-	+	++	-	++	++	+	++
N_{db}	++	+	++	++	+	++	+	+	+
σ_{db}	+	-	+	+	+	++	--	-	-
n-Layer Parameters									
d	---	0	---	-	++	-	---	--	--
Miscellaneous Parameters									
P_{irr}	+	+++	-	+	+++	-	-	++	-
T	++	--	-	++	--	-	+	-	+

Table 4.5: (Continued) Influence of main parameters on IV-characteristics with three different illuminated conditions: 400 nm and 600 nm monochromatic illumination (low intensity), and standard AM1.5G illumination.

- the minority carrier surface recombinations, $S_{n,front}$ and $S_{p,rear}$. These parameters are not important because practically no excess minority carriers reach the contacts adjoining the doped layers. Because of the very low carrier lifetimes in the doped layer the excess minorities recombine before they can reach the contact surface.

- the optical properties of glass and silver. The uncertainties in the optical parameters of the other layers outweigh the influence of uncertainties in these parameters.

- the parameters describing the density of localised states in the p-layer (of all localised states). Only the capture cross sections are of some importance.

The sensitivity analysis resulted in a ranking of model parameters according to their relative influence on 16 different solar cell response parameters. With the help of this ranking both the *most influential* model parameters and the *unimportant* parameters were identified. Many results correspond to experimental experience of parameters influences.

The obtained insight in the influence of model parameters has several benefits:

- The results support a well-founded selection of a fitting parameter set for model calibration, such as the inverse modelling method (see Sect. 4.5). Careful model calibration leads to physically meaningful a-Si:H model parameters.

- The identified main model parameters can be translated to the main technological parameters, which is advantageous for a-Si:H solar cell technologist and experimentalist.

- With identification of the most influential model parameters also the physical quantities are known, which must be measured (more) accurately.

4.5 Parameter extraction by inverse modelling

Model calibration is essential for the application of a device simulator. For basic device-physical research as well as for device optimisation a simulation model must be carefully calibrated to experimental data. In the field of a-Si:H solar cell research simulation models are usually calibrated by manually adapting the input parameters until a reasonable agreement between measured and simulated IV-characteristics is obtained. With this approach it is very difficult to calibrate the model to more than one experimental characteristic. In this section we discuss the calibration of ASA using a more efficient technique: inverse modelling.

This automated technique allows the simultaneous calibration to to more than one measured characteristic. In principle, the optimisation procedure can results in an optimum fit if it does not get trapped in a local minimum. Inverse modelling is particularly useful for the calibration of *a*-Si:H device simulators, because it is difficult to obtain many of the *a*-Si:H model parameter from direct measurements.

In the section first we will briefly introduce the inverse modelling technique. After that we present the results of two calibration exercises using different models for the dangling bond states. Although good fits are obtained with both models, the sets of calibrated parameters as well as the internal device quantities of the two calibrations show considerable differences, which will be discussed in detail. Finally, we propose a few additional measurements which can be used for model calibration to obtain a more unique set of calibrated model parameters. This research is based on previous work published by the Delft *a*-Si:H solar cell research group [156–158].

4.5.1 Inverse modelling

A detailed discussion of inverse modelling is beyond the scope of this thesis. In this section we only descibe the basics of inverse modelling with the aid of Fig. 4.12; for a full coverage the reader is referred to Ouwerling [91] and the references therein.

Conventionally, simulation tools such as process and device simulators are used to simulate the output response of a physical process as a function of physical model parameters as input. If a simulator is used in this way we call it a forward model. In inverse modelling the roles of input and output data are interchanged: the response of the process is the input of inverse modelling, whereas the model parameters are the output (*cf.* the double framed boxes in Fig. 4.12). For instance, a device simulator as forward model can be used to determine the CV-characteristics of a diode using a particular doping profile as input parameter; in inverse modelling CV-measurement data may be used to determine doping profiles. Inverse modelling can be used in two different ways: (1) it can be applied to calibrate a model by using experimental data to determine the physical input parameters of the model, or (2) it can be used for the design and optimisation of a system by fitting the model to a desired (target) response. When using inverse modelling for optimisation the model must have been calibrated first; then it can be applied to determine the optimum design parameters.

The block diagram (Fig. 4.12) shows the main components of an inverse modelling process: a non-linear optimisation driver and a simulation model. The optimisation driver minimises the error between simulation data and measurement (or target) data. The model is run iteratively, while adapting the model input

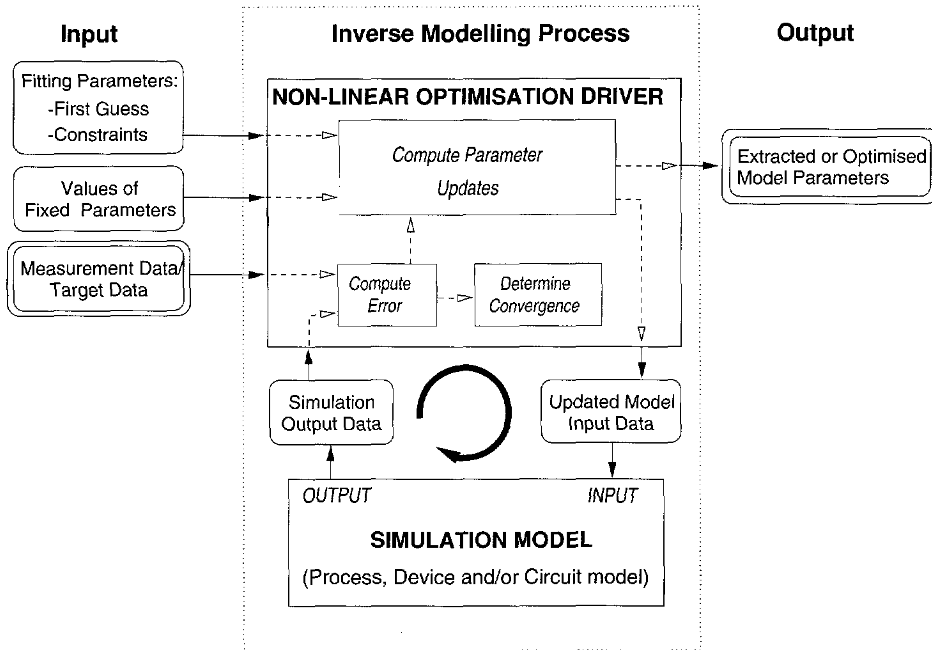

Figure 4.12: Block diagram showing the main components of an inverse modelling optimisation process.

parameters for which the optimum values are sought. The inputs of the inverse modelling process are the measurement or target data, the set of fitting parameters, the initial values and constraints values of the fitting parameters, and the values of the other model parameters which are fixed during the parameter estimation process. The values of the calibrated or optimised fitting parameters are the output.

For the calibration of ASA we use the general measurement-data processor Profile [92] as optimisation driver. In Profile the Modified Damped Least Squares method (a modification of the classic Levenberg-Marquard method) is implemented. This method minimises the weighted mean-square error, χ, of the simulation data, y^s, with respect to the measurement data, y^m,

$$\chi = \frac{1}{N}\sum_{j}^{N} w_j (y_j^m - y_j^s)^2, \tag{4.23}$$

where N is the number of data elements and w_j is a weight factor.

4.5.2 Calibration exercises

We have carried out two calibration exercises. These exercises show that inverse modelling is a useful technique for calibration of an *a*-Si:H-device simulator. The objective of the calibration is validation of our *a*-Si:H device model; if it is not possible to obtain agreement between the model output and the measurements, the model does not describe the physics of the amorphous silicon devices correctly. In this work simulated *IV*-characteristics are fitted to measurement data. To determine which model describes the defect density of states distribution most accurately, we have used two different approaches to model the defect states. This approach allows a direct comparison between the two modelling approaches.

Experimental data

For our model calibration we use the *IV*-characteristics of a single-junction *a*-Si:H solar cell, deposited at Utrecht University (sample # p410). This cell is deposited on specular Indium Tin Oxide (ITO) coated glass and can be considered as an one-dimensional device. Because our device model is 1D we must use 1D experimental structures for calibration purposes. Thicknesses of the *a*-SiC:H *p*-layer, the *a*-Si:H *i*- and *n*-layer are 20 nm, 500 nm and 20 nm, respectively. In this simple device no intentional buffer layer was inserted between the *p*- and *i*-layer.

Four different measurement curves of this device are available: dark *IV*-characteristics and illuminated *IV*-characteristics with AM1.5G solar illumination, blue (400 nm) and red (600 nm) monochromatic illumination. As illumination source an Oriel solar simulator is used. For the measurements with monochromatic illumination the light of the solar simulator is filtered with band-pass interference filters.

Models

The main difference between the two calibration exercises is the choice of the dangling bond density of states distribution model. The following two models are used:

Model 1: Gaussian dangling bond density of states distribution. The defect distribution is position independent in each of the three individual layers of the *pin* diode. The peaks of the Gaussian-distributed $E^{+/0}$ and $E^{0/-}$ transition energies are positioned *symmetrically* with respect to midgap. The set of parameters calibrated by using this model is referred to as 'Set I'.

Model 2: Dangling bond states distribution according to the defect-pool model of Powell and Deane [98]. When using this model, ASA computes the

midgap states distribution self-consistently with the occupancy of the gap states at the equilibration temperature. The set of parameters calibrated by using this model is referred to as 'Set II'.

The optical generation rate is computed with the thin film optics model, which accounts for reflectance at each interface and interference between incident and reflected light beams. The optical model of our device consists of six layers: glass, ITO, *p-a*-SiC:H, *i-a*-Si:H, *n-a*-Si:H, and silver. As optical constants of glass, ITO and silver values from literature are used. The optical constants of the *a*-Si:H and *a*-SiC:H layers are determined by measuring separately grown, thick layers of these materials.

The contacts to the *p*- and *n*-layer are modelled as ideal Ohmic contacts. We have implemented the possibility to add an external series resistance to the device model so that experimental *IV*-data that may include the effects of external resistances are simulated correctly. For instance, the TCO resistance or contact resistance can become relevant when high currents are measured.

Parameter choices

Table 4.6 lists the model parameters that are fitted during the model calibration. We have selected these parameters based on the results of the sensitivity analysis discussed in Sect. 4.4. We assume couplings between some of the parameters to reduce the total number of fitting parameters; the characteristic energy of the conduction band tail, E_{c0}, is set to about $0.6 \cdot E_{v0}$. The capture cross section of the conduction band tail and valence band tail states are assumed to be equal. Further, a contstant ratio between of capture cross sections of charged and neutral states is assumed (1 or 10). Although the mobility gap, E_g, is one of the most-influential parameters (see Sect. 4.4), it is not selected as a fitting parameter, because of the correlation with other parameters, as discussed in Sect. 4.2.

The optical constants (extinction coefficient and refractive index) are not chosen as fitting parameters, despite their relative large influence on the device characteristics. Consequently, the optical carrier generation profile, which depends strongly on the exact values of these parameter, is not calibrated. Eventual (small) differences between the measured and simulated short-circuit currents were corrected by slightly adjusting the optical generation rate with a scaling factor.

All other parameters are fixed during the model calibration, because these parameters are less influential than the parameters listed in Table 4.6. The values used for these parameters are either determined from experiments (such as the optical constants of each layer) or found in other publications on *a*-Si:H solar cell modelling.

p-layer parameters	
Hole mobility	μ_p
Activation energy	E_{act}
i-layer parameters	
Electron mobility	μ_n
Hole mobility	μ_p
Dangling bond density	N_{db}
i- and n-layer parameter	
Characteristic energy of valence band tail	E_{v0}
p-, i- and n-layer parameters	
Effective density of extended states	N_v, N_c
Density of tail states at E_c and E_v	N_{v0}, N_{c0}
Tail states capture cross sections	σ_n^+, σ_p^0, σ_n^0 and σ_p^-
Dangling bond capture cross sections	σ_n^+, σ_p^0, σ_n^0 and σ_p^-

Table 4.6: Model parameters which are fitted in the inverse modelling calibration procedure

The values of the defect-pool model parameters that we use for the simulations with Model 2 are the default values of Powell and Deane [98]. When we use Model 2 the value of the N_{v0} parameter as used for the defect-pool model calculations has a different value than used for the definition of the valence band tail states distribution.

Results

The simulated IV-characteristics are fitted simultaneously to the dark IV-characteristics and to the AM1.5G and red light IV-characteristics. The blue light IV-curve is not used for the calibration, since attempts to fit the simulations to *all four* measured curves simultaneously yielded generally *worse* fits. Figure 4.13 shows the results of the two calibration exercises. We see that with both models very good fits to 3 of the 4 experimental curves could be obtained. Only the dark IV-curves below 0.4 V forward bias do not match the measured data. The large difference in this bias region is caused by the lateral leakage current that hides the

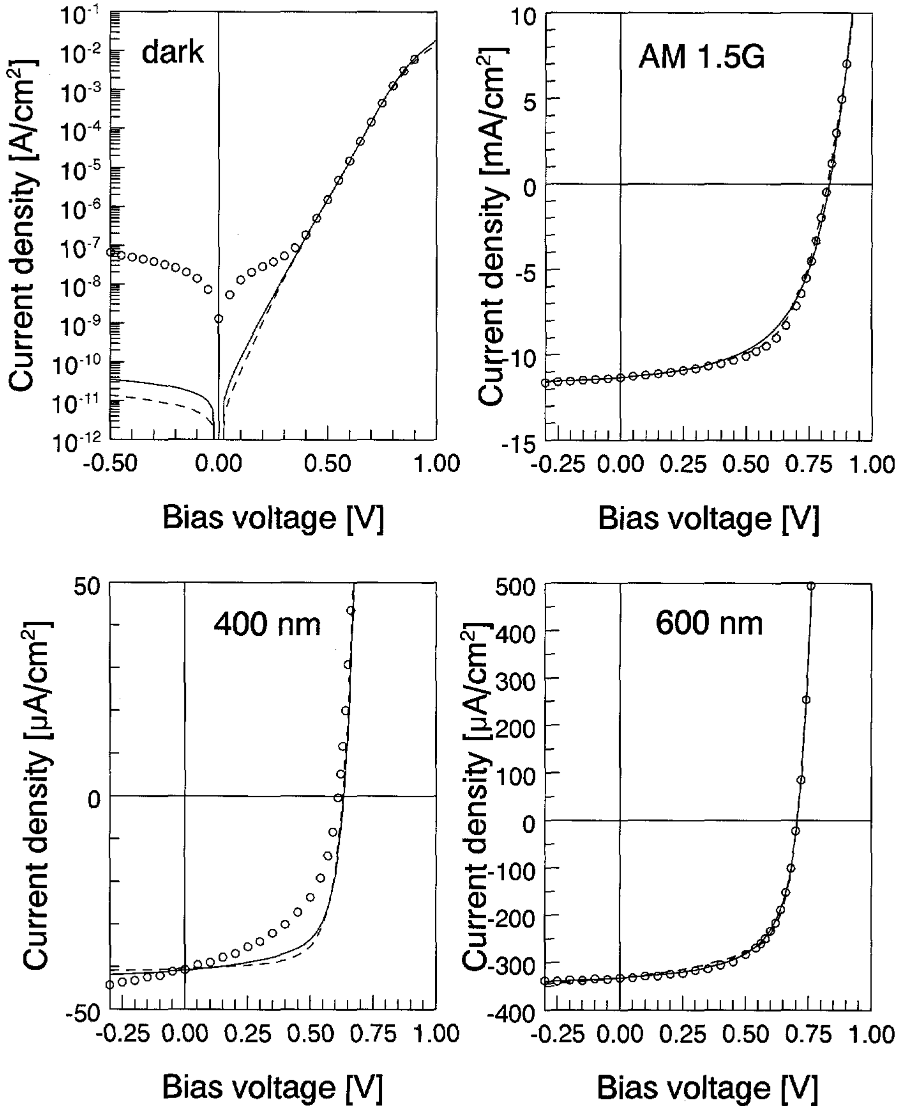

Figure 4.13: Results of the model calibration. The full lines correspond to Model 1 (Gaussian defect distribution), the dashed lines to Model 2 (Defect-pool model defect distribution). The symbols are the experimental data. The models were calibrated to the dark IV-characteristics and the AM1.5G and 600 nm illuminated IV-characteristics.

very low diode currents in this part of the characteristics. To this device we have not applied the n-layer etching that is proposed in Sect. 6.1 to remove the leakage current path. There are two possible causes for the poorer quality of the fits to the blue light IV-characteristics:

- the physics is not adequately represented by the device model, or
- the measurement data with the blue light illumination is of poor quality.

The low fill factor of the blue light IV-characteristic may be an indication that these measurement are not reflecting the true device behaviour; in general, when reducing the light intensity (down from standard AM1.5G illumination) the fill factor increases. This blue-light measurements shows the opposite of this trend: the fill factor of the AM1.5G IV-curve is 0.59, whereas the fill factor with reduced-intensity blue light is only 0.50. Possibly, the low fill factor and the large gradient in the IV-curve at negative biases is also due to the lateral leakage; as we show in Sect. 6.1 low light-intensity IV-measurements are sensitive for these leakage currents and must be carried out cautiously.

In combination with the Gaussian defect distribution model, Model 1, it was necessary to add an external series resistance to obtain a good fits of the AM1.5G illuminated IV-characteristics and the forward-biased dark IV-characteristics above 0.8 V.

Table 4.7 lists the model parameters obtained with the two calibration exercises. The fitting parameters are printed in boldface. There are remarkable differences between the parameter values of set I and set II. Although the mobilities, tail-state capture cross sections and mobility gaps are very different, the fits to the experimental characteristics are equally good. Therefore we can conclude that the used measurement data are not *sufficient* to provide a *unique* set of calibrated parameters. Moreover, additional calibration runs have shown that other very reasonable (in comparison with the presently shown) fits could be obtained with rather different parameters. Based on that observation we conclude that the large differences between set I and set II are not caused by the choice of density of states model for the dangling bond states. An important conclusion that can be drawn from this work, is that dark and illuminated IV-characteristics (such as used in this work) is not sufficient to differentiate between the conventional Gaussian density of states distribution model and the distribution resulting from the defect-pool model.

		SET I			SET II		
Parameter	unit	p-layer	i-layer	n-layer	p-layer	i-layer	n-layer
d	nm	20	500	20	20	500	20
μ_n	cm^2/Vs	1.0	**0.41**	2.0	10	**11.1**	10
μ_p	cm^2/Vs	**0.43**	**0.34**	0.4	**1.47**	**9.25**	1
E_{act}	eV	**0.479**	–	0.29	**0.55**	–	0.30
E_g	eV	1.83	1.7	1.7	1.90	1.85	1.85
N_v, N_c	cm^{-3}	$\mathbf{5.57 \cdot 10^{20}}$			$\mathbf{6.43 \cdot 10^{20}}$		
ε_r	-	7.2	11.9		7.2	11.9	
N_{v0}, N_{c0}	eV^{-1}cm^{-3}	$\mathbf{3.85 \cdot 10^{21}}$			$\mathbf{7.23 \cdot 10^{21}}$		
VALENCE BAND TAIL PARAMETERS							
E_{v0}	eV	0.100	**0.045**		0.080	**0.048**	
σ_n^+	cm^2	$\mathbf{2.16 \cdot 10^{-14}}$			$\mathbf{3.69 \cdot 10^{-15}}$		
σ_p^0	cm^2	$\sigma_n^+/10$			σ_n^+		
CONDUCTION BAND TAIL PARAMETERS							
E_{c0}	eV	0.065	$E_{v0} \cdot 0.6$		0.050	$E_{v0} \cdot 0.63$	
σ_n^0	cm^2	σ_p^0			σ_p^0		
σ_p^-	cm^2	σ_n^+			σ_n^+		
DANGLING BOND PARAMETERS							
U	eV	0.20			0.20		
N_{db}	cm^{-3}	$4 \cdot 10^{18}$	$\mathbf{1.46 \cdot 10^{15}}$	$8.0 \cdot 10^{16}$	Defect-pool model		
σ_{db}	eV	0.20			–		
σ_p^-, σ_n^+	cm^2	$\mathbf{5.05 \cdot 10^{-13}}$			$\mathbf{3.33 \cdot 10^{-13}}$		
σ_p^0, σ_n^0	cm^2	$\sigma_p^-/10$			$\sigma_p^-/10$		

Table 4.7: Overview of the model parameters used in the two calibration exercises. The fitted parameters are printed in boldface.

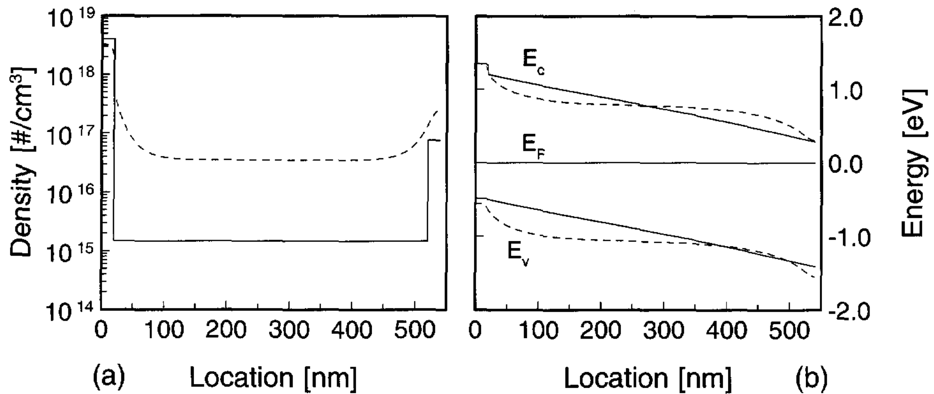

Figure 4.14: (a) Dangling bond density profile, and (b) band diagrams corresponding to the two sets of calibrated model parameters. The full lines correspond with Model 1, the dashed lines with Model 2.

4.5.3 Discussion

Above we concluded that two sets of very different parameter can equally well describe the same experimental *a*-Si:H solar cell *IV*-characteristics. Therefore it is useful to subject the results obtained with the two models to a detailed study. Based on the differences between the results conclusions can be drawn about the experiments that are aditionally needed for model calibration. In Sect. 4.2 we have already discussed this topic; for the calibration exercises, however, we did not use the parameter dependence relations of Sect. 4.2, and still, the simulation output is very similar dispite the largely different input parameters. In this section we will have a closer look at the internal device quantities, such as band diagrams and recombination rate profiles.

Dangling bond density profile

Figure 4.14a shows the profiles of the total density of dangling bonds corresponding to each of the fits. The dangling bond concentration are very different; the dangling bond concentration of Model 2, which used the defect-pool model, is about 25 times higher (in the central part of the *i*-layer) that in Model 1. This is a remarkable difference. In Sect. 4.2 the localised state distribution was not changed when transforming parameter sets that gave equal modelling results. Here, we see that even with difference of a factor 25 in the midgap state concentration approximately equal *IV*-characteristics can be simulated.

Band diagram

The impact of the largely different dangling bond concentrations is best illustrated with the band diagrams for both parameter sets, which is shown in Fig. 4.14b. With the low dangling bond density of the Gaussian distribution set the electric field in the *i*-layer is almost constant, due to the low space charge density in this region. In contrast, with the other parameter set there is a large region around the centre of the *i*-layer, where the electric field is very low in comparison to the field close to the interfaces with the doped layers.

Two important issues are shown in this graph. First, in contrast to the common belief that the field distribution in the *i*-layer is very important for the device operation, our results show that even with strong fields at the interfaces and a low field in the centre the same simulated IV-characteristics can be obtained as with a constant electric field strength. Secondly, we note that the electric field at the contact to the *n*-layer is non-zero. This is only possible if the Fermi-level is pinned at the interface meaning that there must be a Schottky interface and surface charge in the metal layer. This situation is not very likely in an *a*-Si:H solar cell and therefore it shows that the *n*-layer space charge density in the modelled device is not sufficient to cause the required band bending. This shows that the defect and/or the conduction band tail density of states distribution in the *n*-layer is higher in real devices than in our modelling.

Thermal generation rate

In Fig. 4.15a the thermal generation rate as a function of position in the device is shown for different bias voltages. The region in which thermal generation occurs increases with increasing reverse bias voltage, in accordance with the results in Sect. 4.1. With the parameter set fitted with the Gaussian dangling bond distribution the generation rate profile is more or less symmetrical around the centre of the *pin* diode; this is very similar to the schematic graph of Fig. 4.5 in Sect. 4.1. The similarity comes about because the assumed constant gradient in the band diagram of the theoretical derivation is present in the band diagram with parameter set I. On the other hand, with parameter set II the main contribution of the thermal generation is in the front part of the *i*-layer. This results from the fact that the second derivative of the band diagram is not zero due to the presence of space charge in the *i*-layer. Because the largest thermal generation takes place where the electron and hole quasi-Fermi levels are respectively below and above the intrinsic trap level, the region with the strongest contribution to the thermal generation is different is this case.

Further we note that the total thermal generation at a particular bias voltage is

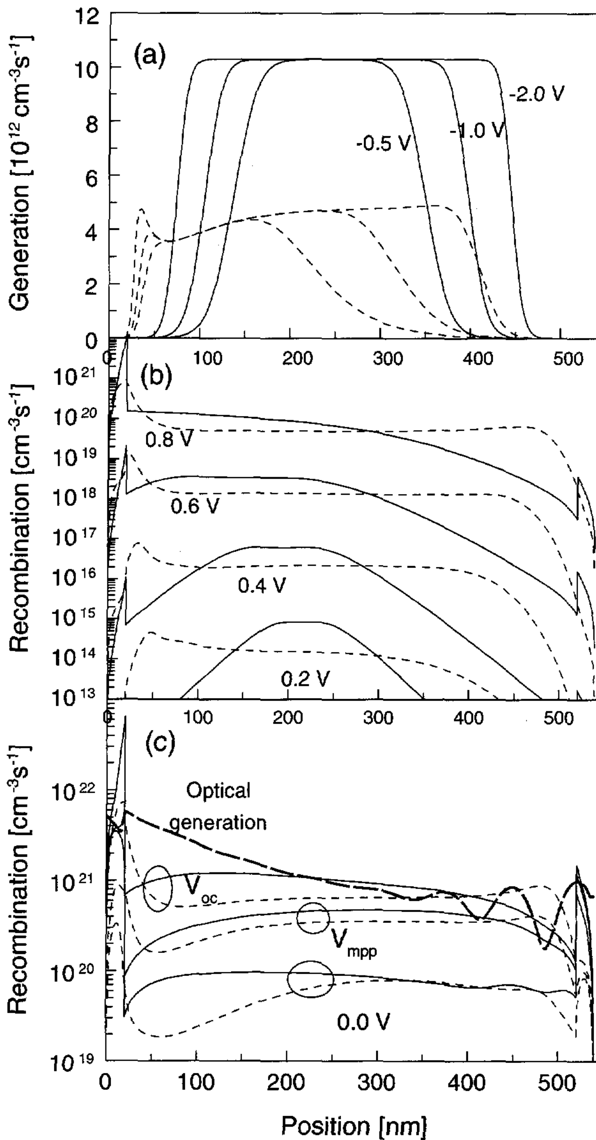

Figure 4.15: Generation and recombination rate profiles in the *pin* diode with two different sets of calibrated model parameters. The full lines correspond with Set I, the dashed lines with Set II. (a) Thermal carrier generation at various reverse bias voltages; (b) Recombination rates at various forward bias voltages without illumination; (c) Recombination rates at $V = 0$, V_{mpp}, and V_{oc} condition in an illuminated *pin* cell. For reference the optical carrier generation profile is added (fat, dashed line).

larger for parameter set I than parameter set II. This difference results in a current that is about 2.5 times higher under un-illuminated reverse-biased conditions (see Fig. 4.13a). However, in the fitting procedure this part of the IV-characteristics was not used, because the intrinsic diode behaviour was masked by the lateral leakage current in the experimental curves. The presence of this difference shows once again the importance of having experimental data for all bias voltages. At first sight it is surprising that parameter set I, in which the defect density is about 20 times *lower* than in set II, gives rise to *higher* thermal generation rates and reverse bias currents. This seemingly contradictory result can be explained with the help of Eq. 4.7, which shows that the reverse bias current is in a first approximation proportional to $\sqrt{\sigma_n\sigma_p}n_iN$. Using the dangling bond density of states near midgap $N = 2.5 \cdot 10^{15}$ cm^{-3} eV^{-1} of Model 1, and $N = 2.8 \cdot 10^{16}$ cm^{-3} eV^{-1} of Model 2, we find a ratio of 2.12 for the above-mentioned proportionality factor, which is very close to the ratio of the reverse bias currents at -2 V (which is 2.19). Therefore, the lower reverse bias current of Model 2 is due to the much lower intrinsic concentration, n_i.

Recombination rate

Figure 4.15b and c show the recombination rate profiles with and without illumination. These graphs also show that depending on the chosen parameters the recombination rate profiles can be very different while the IV-characteristics are very similar. In the case of parameter set I the recombination rate is the strongest is the centre of the device at low forward voltages. The peak of the recombination profile becomes gradually wider and shifts towards the p-i interface with increasing bias voltage. With parameter set II there is a more evenly distributed recombination profile with a small peak close to the p-layer, but in this case we also observe that the distribution becomes wider with increasing bias voltage.

With illumination the recombination profiles show also distinct differences depending on the used model. With Model 1 there are strong peaks in the p- and n-layer, while the main contribution inside the i-layer is relatively nearer to the p-layer. In contrast, the recombination rates with Model 2 show less distinct peaks in the doped layers and here, the main contribution in the i-layer is near the n-layer.

4.5.4 Proposed additional experiments

From the previous discussion it is clear that although the external IV-characteristics are very similar, the internal device characteristics show very distinct differences. Therefore additional experiments are proposed to gain additional

experimental data for parameter extraction. In addition to the un-illuminated *IV*-characteristics in the reverse and low-forward bias regime that we suggested above, we propose the following additional experiments:

1. **Capacitance-voltage (*CV*) characteristics.** In Fig. 4.14a we have shown the large difference in dangling bond density of two parameter sets. Because these differences do not show up in the *IV*-characteristics, other experiments must be added. Since charge trapping is directly related to the density of localised gap states, experiments must be used that provide a more direct measurement of charge trapping. One of the experiments that measures charges is the capacitance-voltage (*CV*) measurement. Although ASA cannot compute the small-signal responses we can show the feasibility of this measurement by carrying out quasi-static capacitance simulations. Figure 4.16 shows the quasi-static *CV*-simulations obtained with the two models and indeed a very large difference between the two characteristics can be seen. For instance, with parameter set I up to about 0.5 V forward bias the capacitance does not significantly exceed the value of the geometric capacitance of the device. In contrast, the *CV*-characteristic with set II starts to increase slowly when decreasing the reverse bias toward zero bias. In the low-forward bias range the differences are significant. This result clearly shows that with *CV*-measurements the total density of localised states is measured more directly. However, application of this measurement for calibration purposes requires the implementation of a small-signal simulation mode in ASA.

2. **Fill Factor dependence on irradiance.** Another measurement that is able to differentiate between set I and set II is an illumination-intensity-level-dependent *IV*-characteristics. As an example we show the fill factor as a function of V_{oc} in Fig. 4.16b. Here, we observe a clear difference between the two parameter sets. Especially notable is the fact that the curves computed with set I are very similar for V_{oc}-s below about 0.5 V, whereas with set II the curves corresponding to the different illumination spectra (either red, blue or AM1.5G) are some distance apart from each other.

3. **Quantum efficiency.** In Fig. 4.16c we show external quantum efficiency curves with the two sets and here again a distinct difference between the curves can be observed. These curves were simulated with exactly the same optical model, therefore all differences are due to differences in the electrical device model. In the wavelength region below 550 nm the quantum efficiency with set II is higher than with set I. In the longer wavelength range there is hardly any difference.

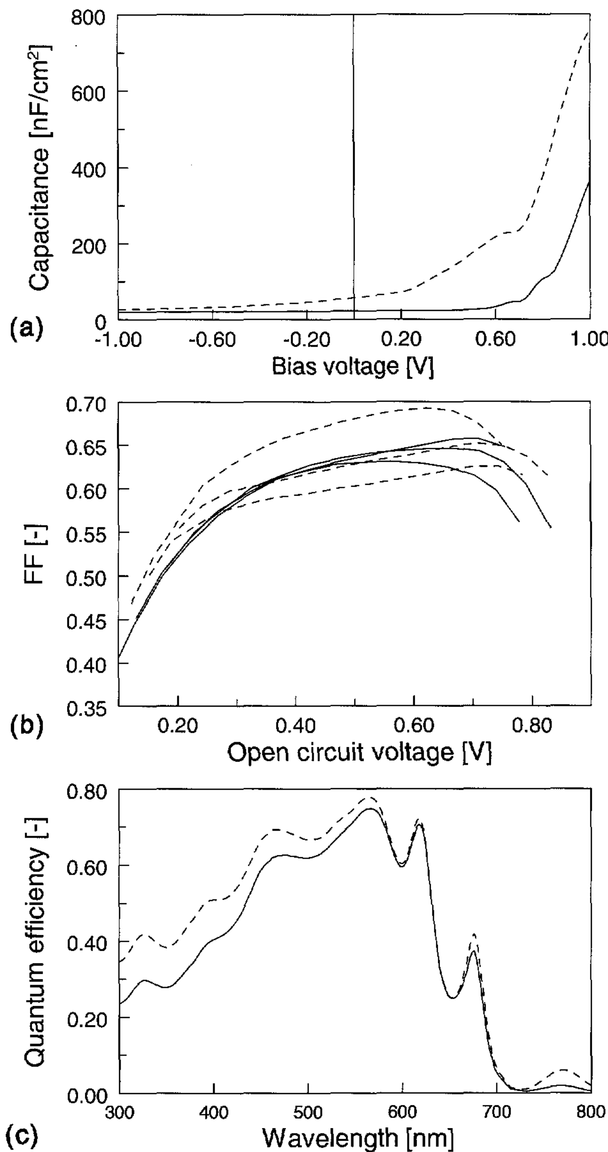

Figure 4.16: Suggested additional device characteristics to be used for model calibration. The characteristics are simulated with 'calibrated' parameter Set I (full lines) and Set II (dashed lines) obtained by fitting to IV-characteristics. (a) Quasi-static capacitance-voltage simulations. (b) Intensity dependent IV-measurements: fill factor as a function of V_{oc}. (c) External quantum efficiency at 0 V.

This list is not complete. It gives a few suggestions for additional experiments for a better calibration of the device model. Other useful experiments may be added.

4.5.5 Conclusion

The conclusions of the model calibration exercises discussed in this section can be summarised as follows:

- inverse modelling is very suitable to calibrate an amorphous silicon device model to experimental data.
- It is not possible to obtain a unique set of model parameters by fitting IV-characteristics only; very different parameter sets can give equally good fits of these characteristics. Moreover, internal device quantities, such as the electric field profile, recombination and thermal generation rate profiles, can be *very* different, and still result in equally well matching simulated and measured IV-characteristics.
- With only IV-measurements it is not possible to differentiate between the conventionally used Gaussian density of dangling bond states distribution and the distribution simulated with the defect-pool model.
- We propose the following additional experiments to reduce the non-uniqueness of the extracted set of calibrated model parameters:
  - dark IV-measurements with reverse and low-forward bias voltages. In Sect. 6.1 we discuss how these measurements must be carried out.
  - CV-measurements. To use the results of these measurements for calibration purposes, a small-signal simulation mode must be implemented in ASA.
  - Illumination-intensity-dependent IV-measurements.
  - External Quantum Efficiency measurement.

Chapter 5

Modelling of amorphous silicon tandem cells

In Chapter 1 of this thesis we have introduced multi-bandgap multi-junction cells as the device structure for stable high-efficiency *a*-Si:H-based solar cells. Because many parameters influence the performance of this type of device (such as material quality, mobility and optical bandgap, subcell thickness) computer modelling is a valuable tool to study and optimise this device.

In this chapter we discuss the modelling of *a*-Si:H-based multi-junction cells. Since there is no fundamental difference between the modelling of tandem and triple-junction cells, the following discussion is restricted to tandem devices. The main problem of tandem cell simulation is the modelling of the interface between the subcells: the tunnel-recombination junction (TRJ). This chapter starts with a discussion of the operating principles of tandem cells and the role of the TRJ. After that, a short review of technologies for TRJ fabrication is given, followed by a review of existing tandem cell models. Subsequently, we introduce a new modelling approach for TRJs. The features of this model are discussed. Finally, it is applied to study a basic tandem cell properties: the enhanced stability and higher fill factors of tandem cells compared to single-junction cells.

5.1 Device physics of tandem cells and tunnel recombination junctions

5.1.1 Operating principles of a tandem cell

To understand the device physics and to identify the performance requirements of tunnel-recombination junctions (TRJs) the basic operating principles of tandem

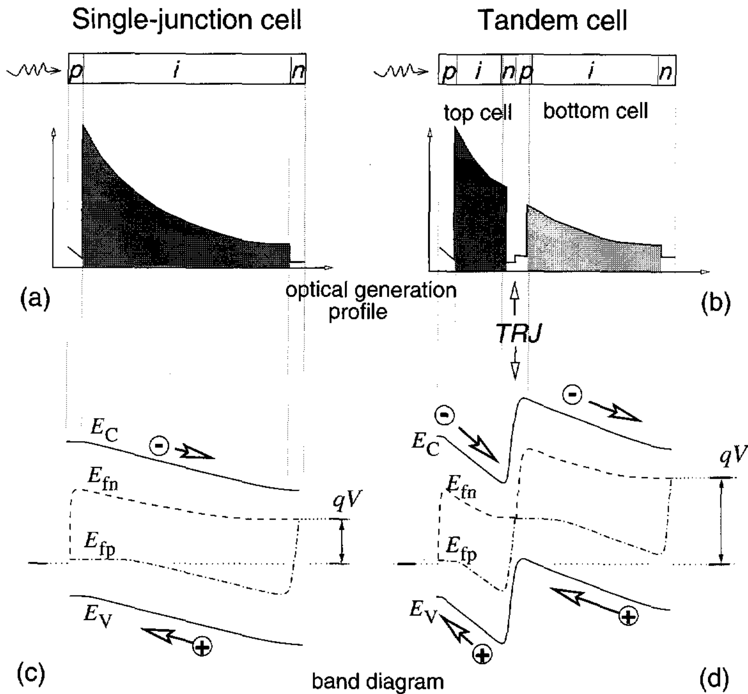

Figure 5.1: Schematic graphs of the generation profiles in (a) a single-junction and (b) a tandem cell, and the band diagrams of a (c) single-junction and (d) tandem cell in a power-generating state. The shaded area of the generation profile is approximately equivalent to the number of electron-hole pairs generated in the *i*-layer. The arrows in the band diagrams depict the direction of the electron and hole currents.

devices must be fully understood. The theory of tandem cell operation is developed by discussing the basic differences between single-junction and tandem cell *IV*-characteristics. On the basis of Fig. 5.1 the operation principles are explained. The figure shows the optical generation rate profiles and band diagrams of a single-junction and tandem solar cell.

A state-of-the-art *a*-Si:H single-junction solar cell has typically the following performance parameters: $V_{oc} = 0.85$ V, $FF = 0.7$, $J_{sc} = 17$ mA/cm^2, $\eta = 10\%$. Under normal operation conditions — in which power is generated by the solar cell — optically generated electron-hole pairs are separated in the *i*-layer; the *n*- and *p*-layer collect the electrons and holes, respectively. The direction of carrier transport is drawn in Fig. 5.1c. If each absorbed photon generates one electron-hole pair and all electrons and holes generated in the *i*-layer are collected, the number of electrons in the external short-circuit current equals the number of

photons absorbed in the i-layer. The total number is equal to the integrated position-dependent optical generation rate in the i-layer; this corresponds the shaded area of the generation profile of Fig. 5.1a.

Next, we consider a tandem cell, which consists of two stacked *pin* cells. This device has two active absorbing i-layers. If the tandem cell delivers photovoltaic power to an external load, the electrons generated in the top *pin* cell are collected by the internal n-layer. The holes generated in the bottom cell move in the opposite direction to be collected by the internal p-layer (*cf.* the arrows in Fig. 5.1d, which depict the carrier flows in a tandem cell). The two types of carriers recombine inside the central np-junction, the TRJ. In this case the TRJ is a forward-biased junction, because electrons are moving from the n- to the p-layer and holes in the opposite direction. If we assume that the all electron-hole pairs absorbed in the i-layers contribute to the short-circuit current, a maximum current can flow in the device when the number of photons absorbed in both i-layers is equal; if there is a mismatch between the number of electron-hole pairs generated in the subcells, the total cell current is limited by the subcell which absorbed the lowest number of photons. In this case a forward 'self'-bias voltage develops across the subcell with the largest carrier generation so that the excess electron-hole pairs recombine. Consequently, as a first order approximation we can conclude that each i-layer must absorb *half* of the total number of absorbed photons for optimal power conversion; hence, the generated external short-circuit current density of the tandem cell is *half* the value generated by a single-junction cell. In Figure 5.1b the parts of the generation profile absorbed in the top-cell and bottom-cell i-layer are shaded. The shaded areas must be approximately equal to get an equal optical generation in each subcell. High optical transparency of the TRJ region is desirable for high efficiency, because photons which are absorbed in the TRJ instead of the bottom cell i-layer are lost for photovoltaic power conversion. The generation profile of Fig. 5.1b shows low optical absorption in the TRJ.

Assuming that the fill factor of the tandem cell and the single-junction cell are equal, the tandem cell V_{oc} must be *twice* the single-junction V_{oc} to obtain the same output power from both types of cells (recall that $\eta = V_{oc} \cdot I_{sc} \cdot FF$). A doubling of the V_{oc} is only possible if the partial V_{oc}-s generated by the top and bottom cell are added without voltage loss in the TRJ. The V_{oc} of a single-junction cell is the difference between the majority carrier quasi-Fermi levels in the doped layers under open-circuit condition. The partial V_{oc} of a subcell can be defined analogously. A loss free addition of partial V_{oc}-s of a tandem cell is only accomplished when the majority-carrier quasi-Fermi levels in the doped layers of the TRJ have (approximately) the same value; in that case there is a nearly zero

internal bias voltage across the TRJ, which we define as the difference between the majority-carrier quasi-Fermi levels at both sides of the TRJ. The loss-free addition of voltages is illustrated in the tandem-cell band diagram of Fig. 5.1d. It shows that the voltage, V, generated by the tandem cell is about twice the value of the single-junction cell of Fig. 5.1c. If the hole quasi-Fermi level in the p-layer of the TRJ would be positioned *below* the electron quasi-Fermi level in the n-layer, there would be a voltage drop over the TRJ resulting in a sub-optimal the total voltage over the tandem cell.

Under V_{oc}-condition the quasi-Fermi levels have in general the same value, because at this bias there is in principle no current flowing in a cell; if there were gradients in the quasi-Fermi levels there would be current (*cf.* Eqns. 2.4 and 2.5). On the other hand, when a solar cell is delivering power to an external load, there is an electrical current flowing in the cell. In this case the partial photovoltages over the subcells of a tandem cell must be added without significant voltage drop over the TRJ in order to perform most efficiently. Hence, in this case again the majority carrier quasi-Fermi levels at both sides of the TRJ must have approximately the same value. Since the typical current of a tandem cell is about 8 mA/cm^2, a good TRJ must be able to conduct this current with only very low bias voltage. In this context "low" means: considerably less than V_{oc}. A TRJ of poor quality will require a larger internal bias voltage and will therefore act like a series resistance; the effect of a non-negligible series resistance is a lowering of the *FF* and thus lowering its conversion efficiency of the tandem cell.

Current transport in a TRJ

A TRJ in a power generating tandem cell is a forward-biased junction, in which electrons move from the n- to the p-layer and holes in the opposite direction. Using Fig. 5.2 we explain the most probable transport mechanism in a TRJ. The graphs show the part of a tandem cell band diagram around the TRJ. Carrier recombination through localised states around position x_{rec} (schematically indicated by the dotted lines) is depicted by the cross.

First, we assume that the current mechanism in an *a*-Si:H *np* junction is the same as in an *a*-Si:H *pin* junction. In Sect. 4.1 we concluded that the current transport in *pin* diodes is dominated by recombination of free electrons and holes in the space-charge region. All carriers move in the extended states until they reach the position (indicated by x_{rec} in Fig. 5.2), where they recombine. To be available for the recombination process, the extended state carriers have to be 'physically' at the position where the recombination takes place.

Using a similar approach to compute the approximate recombination current as discussed in Sect. 4.1 we can estimate the current at a given bias voltage in an

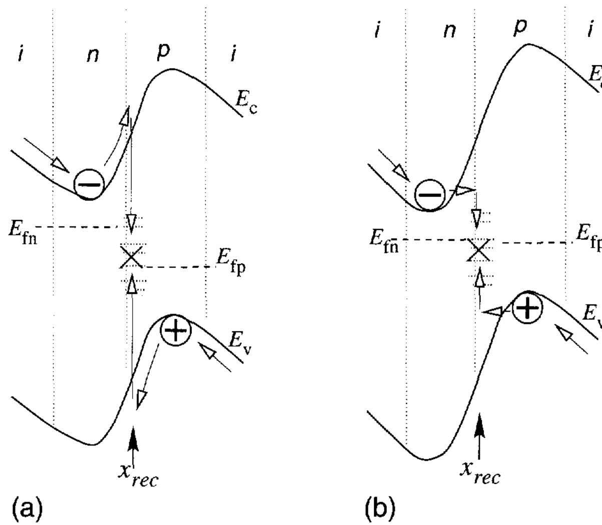

Figure 5.2: Schematic band diagrams illustrating the current and recombination mechanism in a forward-biased tunnel-recombination junction. (a) carrier transport to the recombination region around x_{rec} through the extended valence and conduction band states. (b) carrier transport by tunnelling.

np junction, using typical values for the physical parameters. The recombination current can be approximated by

$$J = qv_{th}W\sigma n_i \exp\left(\frac{qV}{2kT}\right)\int_{E_{fp_t}(x,V)}^{E_{fn_t}(x,V)} N(E)dE \qquad (5.1)$$

which is a simplification of Eq. 4.2, obtained by assuming that the capture cross sections for electron and holes are equal $\sigma_n = \sigma_p = \sigma$, and replacing the term $\sigma\frac{np}{n+p}$ by its maximum value, which is — given a particular bias voltage V — reached if $n = p = n_i \cdot \exp(qV/2kT)$; applying these steps, we find $\sigma\frac{np}{n+p} \leq \sigma n_i \exp(qV/2kT)$. For simplicity we assume that the latter term is constant in a region of width W. Equation 5.1 can be simplified further by assuming that the localised density-of-states distribution, $N(E)$, is a constant value, N. Further, we assume that the width of the integration interval between the quasi-Fermi levels for trapped charge carriers, $(E_{fn_t} - E_{fp_t})$, is equal to the difference between the free-carrier quasi-Fermi levels, $(E_{fn} - E_{fn})$. Figure Fig. 4.1 shows that this approximation is reasonable in the region where $\sigma\frac{np}{n+p}$ reaches its maximum value. The separation between the quasi-Fermi levels for the free carriers is equal to the

applied bias, V. With these assumptions Eq. 5.1 becomes:

$$J = qv_{th}WNV\sigma n_i \exp\left(\frac{qV}{2kT}\right) \tag{5.2}$$

The following values are estimated for the parameters: thickness of recombination region in the TRJ, $W = 10$ nm, density of states $N = 10^{19}$ eV^{-1} cm^{-3}, the capture cross sections are usually in the range 10^{-15}–10^{-13} cm^2 therefore we assume here the largest value $\sigma = 10^{-13}$ cm^2, the intrinsic concentration, n_i, is computed with $n_i = \sqrt{N_v N_c}\exp(E_g/2kT)$, assuming $N_c = N_v = 3 \cdot 10^{20}$ cm^{-3} and $E_g = 1.85$ eV. With these parameter values a recombination current density of 0.1 μA/cm^2 is estimated at a small forward-bias voltage of 0.1 V. From this simple expression we estimate that a bias of about 0.6 V is required to obtain a recombination current density of about 8 mA/cm^2, which is a typical current value for a tandem cell. A voltage drop of this extent across the TRJ would dramatically reduce the efficiency which is not observed experimentally in tandem cells of good quality. Therefore, we conclude that this simple recombination current model does not properly describe current conduction in a TRJ.

The very low current density at low bias voltages is due to the very low concentrations of free carriers available at x_{rec} for recombination. With increasing forward bias the density of free electrons and holes at this position increases exponentially, leading to an exponential increase of the current.

In Fig. 5.2b we show the situation in which free electrons and holes can reach the recombination centres at x_{rec} by tunneling. In this case the recombination centres do not only capture free carriers that are 'physically' present at x_{rec}, but also electrons and holes that originate from parts of the *n*- and *p*-layer, where the carrier concentrations are much higher. If there is a high electric field in the TRJ, the width of the tunnelling barrier is very thin, and can be easily penetrated by the electrons and holes. In this case, the number of carriers available for recombination is already very high at very low bias voltages; therefore, the recombination current can be high at very low bias voltages, if the actual tunnelling transport of carriers from regions with high free carrier densities towards the recombination centres requires only a very low biasing voltage.

It is much more difficult to calculate the approximate current voltage relation with this transport and recombination mechanism, because it is very sensitive to — mostly unknown — issues such as the form and width of the potential barrier, the number of interface states at the *np*-interface, and the question whether the tunnelling occurs in a single step or in multiple steps. Therefore, we limit ourselves to the conclusion that tunnelling must play an indispensable role in the carrier transport of a TRJ, because *without* tunnelling there would be an

unrealistically large voltage drop across the TRJ at normal operating conditions.

Hou *et al.* [57] have called the current conduction mechanism *non-local* recombination, because the free electrons and holes do not have to be at the same physical position, x_{rec}, to recombine. In the first model discussed above electrons and holes had to be in the extended states at x_{rec}, and therefore this recombination mechanism is called *local* recombination. The conclusion about the transport mechanism in a TRJ that we obtained by comparing simple models, has been drawn before by Hegedus *et al.* [54], based on experimental results. Hegedus *et al.* reported a very low temperature dependence of the current-voltage characteristics of TRJ structures and from this results they concluded that tunnelling plays the key role in the current-conduction mechanism of TRJs.

Reverse biasing of a TRJ

The series connection of two *pin* subcells in a tandem solar cell calls into being an *np*-junction of which the biasing polarity is the opposite of the biasing of *pin* subcells. So far we have only considered the case of forward biasing of the TRJ, which occurs when a tandem cell carries a *negative* current; this is the case when the cell is in normal operation conditions as a photovoltaic power generator. However, in cases that a *positive* current flows through the tandem cell the TRJ is biased in *reverse* direction. This happens when an unilluminated tandem cell is forward biased, or when the bias voltage over an illuminated tandem exceeds V_{oc}; These are the cases in which current flows in the other direction than in the normal operational conditions. As we have seen above the current in a forward-biased TRJ is caused by recombination of electron-hole pairs; under reverse biasing conditions the TRJ current is due to thermal generation of electron-hole pairs.

A TRJ can have rectifying properties because it is an *np*-junction. If the junction is rectifying, the current at a particular forward-bias voltage is *much larger* than the current at the same voltage in reverse. The reverse characteristics of a TRJ can influence the tandem characteristics in the above-mentioned bias regions where the TRJ is reverse biased. A rectifying TRJ manifests itself by a downward-bending kink in the IV-characteristics around V_{oc} of an illuminated tandem cell, or by relatively low current densities in the high forward-bias region of the tandem cell's dark IV-characteristics. If a tandem cell shows such characteristics it means the TRJ needs a higher internal bias in reverse direction than in forward direction, because of its rectifying properties. Figure 5.3 illustrates the influence of rectifying TRJs on tandem-cell characteristics. The curves labelled with "bad TRJ" show the influence of TRJs with rectifying properties; the curves labelled "good TRJ" do not show this typical behaviour.

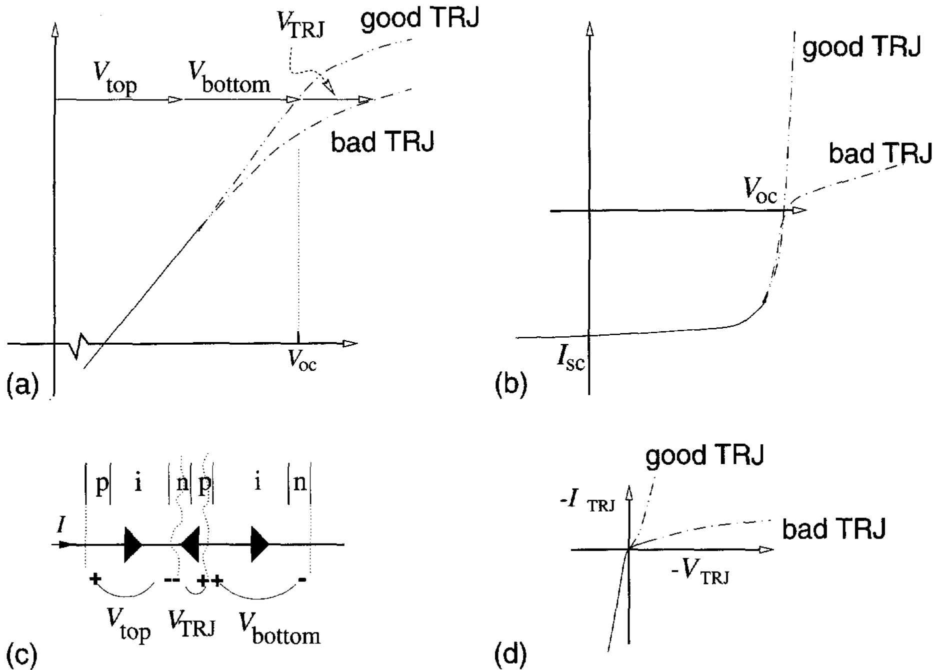

Figure 5.3: The influence of rectifying and non-rectifying tunnel-recombination junctions (TRJ) on tandem cell IV-characteristics. (a) Dark IV-characteristics (on a semi-log scale) of a tandem cell containing a "good" (non-rectifying) and a "bad" (rectifying) TRJ. For a particular current through the tandem cell a high internal voltage across the reverse-biased TRJ is required in the case of a rectifying TRJ. (b) Illuminated IV-characteristics for the same two types of TRJs. (c) Definition of the internal bias voltages across the subcells, V_{top} and V_{bottom}, and across the TRJ, V_{TRJ}. (d) The separated IV-characteristics of a good and a bad TRJ. In this graph the axes are reversed, to facilitate the comparison with graph (b).

Good quality tandem cells *do not* expose these typical properties. Therefore, we must conclude that good quality TRJs do not have rectifying characteristics. This can only be the case if the thermal carrier generation in a reverse-biased TRJ is very efficient.

From this discussion we can conclude that the quality of a TRJ can be determined by examining dark and illuminated IV-curves of tandem cells using bias voltages around V_{oc}.

Space charge and band bending in a TRJ

Above we have seen that TRJs must have high generation and recombination currents at very low reverse and forward bias voltages, respectively. In addition to these transport and recombination properties, the layers of the TRJ must supply the space charge to create a high built-in field and built-in voltage in the *pin* subcells. The built-in voltage is one of the key factors that determine the efficiency of an *a*-Si:H solar cell. The important role as space charge supplier has not received much attention in literature; one of the few papers addressing this issue is the work of Yang *et al.* [153], who carried out a systematic experimental study of TRJ layer thicknesses and doping levels as key factors determining the internal electrostatic properties of a tandem cell.

The role of the space charge in a tandem cell is explained with the help of Fig. 5.4. This figure shows the schematically the space charge density distribution ρ in a *pinpin* structure, along the electric field $\vec{E}$ and the energy band diagram at thermal equilibrium. The curves with full lines show the desired situation in which the space charge in the doped layers of the TRJ suffices to create a high *internal* built-in voltage across both subcells. In this case the layer thicknesses and space charge densities are high enough to produce sufficient band bending and to go from a negative field in the top cell to a very strong positive field in the TRJ and again to a negative field in the bottom cell. There is a strong correlation between layer thickness and space charge density; if one of those parameters decreases, the other must increase to produce the same built-in voltage over the *pin* subcell.

The dashed graphs in Fig. 5.4 represent a situation in which the space charge in the *n*-layer of the TRJ is too low. This means that the layer is either too thin or the space charge density too low (for instance because the active dopant concentration is not sufficient). In this case the built-in voltage across the top cell is seriously reduced, which results in a poor tandem cell operation. This cell will have approximately a V_{oc} of a single-junction cell and an I_{sc} of a tandem. Because of the low built-in potential the separation of optically generated electron-hole pairs is very bad in the top cell, and therefore only very low photovoltage will be

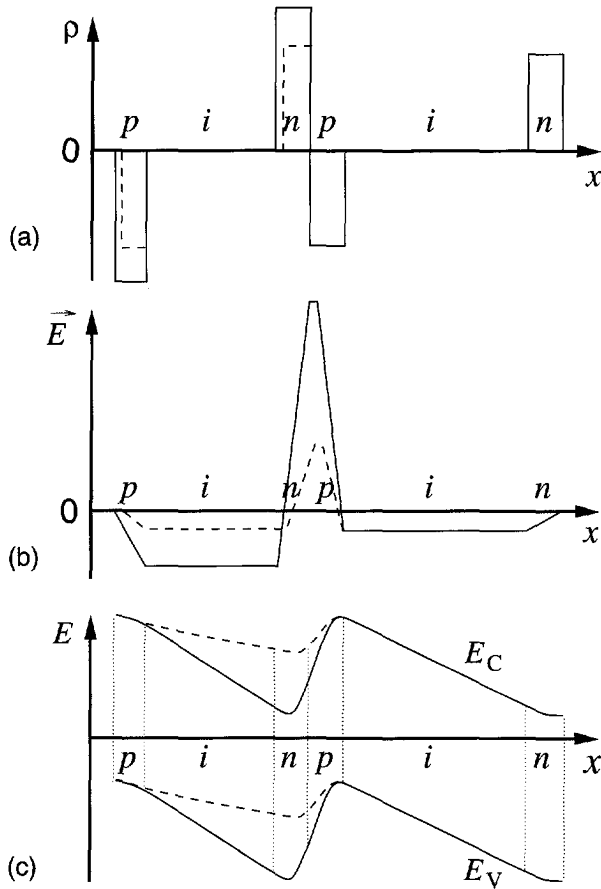

Figure 5.4: Schematic graphs of (a) the space charge distribution, (b) the electric field distribution, and (c) the energy band diagram in a good (full lines) and a bad tandem cell (dashed lines). In the bad cell the space charge density and/or the thickness of the *n*-layer in the TRJ is too low.

generated by this subcell, which causes the low V_{oc}. If we consider an even more extreme case and simply leave away the n-layer in the TRJ, there is no built-in voltage over the top cell.

One of the difficulties of a-Si:H is the impossibility to measure the active doping concentration or space charge density distribution directly. These quantities are very important for the operation of the TRJ, as discussed above. Therefore, we try to estimate the order of magnitude of the required space charge density by simply assuming that the space charge densities in the depleted parts of the n- and p-layer of the TRJ are uniform and have the same absolute value. In this case the well-known expression for the space charge or depletion layer width W_d can be used.

$$W_d = \sqrt{\frac{2\varepsilon_r\varepsilon_0}{q}\frac{N_n+N_p}{N_nN_p}V_{bi}} \tag{5.3}$$

where N_n and N_p are the space charge densities in the n and p-layer, respectively. Estimating the following values for the depletion width $W_d = 15$ nm, built-in voltage $V_{bi} = 1$V, relative dielectric constant $\varepsilon_r = 11.7$ and assuming that $N_n = N_p$, we find for the space charge density $N_n = N_p = 1.15 \cdot 10^{19}$ cm^{-3}. Although the space charge distribution will be far from uniform in an a-Si:H np junction, because of the high density of localised states, this number provides a fair estimation of the order of magnitude.

Moreover, from this number the required doping efficiency of highly doped a-Si:H thin layers can be estimated. Assuming that the chemical doping of a-Si:H is in the order of one percent, meaning that about $5 \cdot 10^{20}$ cm^{-3} dopant atoms are present in the material, *at least* about 2 percent of the dopants must be electrically active and contribute to the space charge in the depletion regions. Because of the assumptions and approximate character of this estimation, a doping efficiency in the range from 1 to 10 percent is be considered as reasonable.

Requirements imposed upon a TRJ

Form the discussions above we can summarise the following requirements for the TRJ

- For effective recombination and thermal generation a high concentration of localised states must be present near the np interface of the TRJ, where the probability for recombination is the highest.
- For an efficient tunnelling transport of charge carriers to recombination

centres, the space charge region must be thin and contain a high concentration of localised states which can serve as hopping centres.

- Layer thicknesses and active dopant concentrations must be sufficient to produce high built-in voltages across both *pin* subcells. The space charge concentration must be in the order of 10^{19} cm^{-3}; the active dopant concentration must be *at least* equal to the required space charge density, but more probably even higher due to the presence of distribution of localised gap states.

- The formation of a compensated region at the *np* interface must be avoided, because it will reduce the built-in field in the TRJ and thus increase the width of the tunnelling barrier [57]. This impedes the tunnelling carrier transport and thus increase voltage loss due to the TRJ.

- The TRJ must be optically as transparent as possible, therefore its thickness and optical absorption in the relevant wavelength range must be minimised.

Optimisation of TRJs needs the optimisation of each of these requirements. However, some of the requirements are conflicting (*e.g.* the requirement of space charge versus layer transparency: the first requires thicker layers, the latter thinner layers). Therefore, optimisation is needed to find the trade off between conflicting requirements.

5.2 Review of tunnel-recombination junction technologies

While studying the modelling of tunnel-recombination junctions (TRJ) attention should be paid to the experimental and technological work done on these devices. Only from those results one can gain knowledge about *what* has to be modelled and *how* a good physical model for use in a device simulator has to be developed. Therefore, we give a critical review of technological TRJ results reported in literature.

The deposition process of the TRJ is a critical step in the fabrication of a tandem cell. Doped layers giving optimised single-junction cell performance are not necessary suited for application in the TRJ of a tandem cell. Therefore, the layers and interfaces of the TRJ must be carefully optimised to obtain maximum tandem-cell efficiency.

The main part of this section discusses microcrystalline silicon μc-Si:H as material of choice for use in the TRJ. For completeness, we shortly mention

other approaches for improvement of the TRJ, before starting the discussion of μc-Si:H. In the early days of the tandem cells the TRJs were made of n-type and p-type a-Si:H layers. In order to improve the contact properties of this junction some research groups proposed the insertion of transparent conductive metal oxide layers between the n-layer and p-layer. Materials used are TiO_x [29, 107] and NbO_x [116]. A very efficient TRJ is formed if the metal oxide is optically transparent and electrically conductive and forms Ohmic contacts with both types of layers. A disadvantage of this technology is that metal oxide deposition is not compatible with a-Si:H deposition technologies. Another approach is the surface oxidation after the deposition of the first TRJ layer, either by exposure to air [70, 111–113] or by applying a CO_2 plasma in the PECVD a-Si:H deposition system [100]. Exposure to air has been applied both to n-type a-Si:H layers [112] as to n-type μc-Si:H layers [70, 111, 113]; this processing step increases the V_{oc}. The effect of this treatment is the creation of additional states at the interface of the n-type and p-type layer of the TRJ, which enhances the recombination in the junction, yielding a higher junction conductivity. Instead of the creation of an oxidised interface in the np junction the insertion of a thin heavily p-type a-Si:H layer (without carbon) improves the TRJ characteristics [154].

Although good tandem cells can be fabricated with amorphous n- and p-layers in the TRJ, there is consensus that the best performance is reached when at least one of the TRJ layers is grown with microcrystalline growth conditions. With these layer the absolute value of the conversion efficiency increases by about 1-2 %. This improvement is mainly due to the increase of the I_{sc} and FF. Most groups reported an increase of the V_{oc} [105, 138, 154], but decreasing V_{oc}-s have been reported too [66].

In principle, for improvement of the TRJ properties only one or both of the n- and p-layer may be made of microcrystalline silicon. In practice, most research groups use microcrystalline n-layers [3, 30, 34, 66, 96, 105, 113, 138, 155]. The United Solar Systems Corp. (USSC) group uses microcrystalline p-layers [6, 8, 40, 41]. Application of fully microcrystalline np TRJs is described in Ref. 99, 138, 139, 152, and 155.

We have noticed that — when applying μc-Si:H in the TRJ — generally the layer which is grown first, is replaced by microcrystalline material;hence, if an n-i-p-n-i-p sequence is grown (using an opaque substrate) a μc-Si:H p-layer is used, while in the opposite sequence p-i-n-p-i-n (on transparent substrates) microcrystalline n-layers are applied. From the literature it is not clear whether this is done intentionally or not. Therefore this topic deserves a detailed study. The findings of Yang *et al.* [152] may give a clue. They have reported that a tandem cell grown in n-i-p-n-i-p sequence with a *fully* microcrystalline TRJ showed a lower V_{oc} than

a tandem cell with only a μc-Si:H *p*-layer in the TRJ. After insertion of unspecified buffer layers at the *p*-*n* and *n*-*i* interface they could restore the V_{oc} to a value slightly higher than the V_{oc} of a cell with an amorphous *n*-layer. Rath *et al.* [99] have published similar results for fully microcrystalline TRJs; however, they deposited an inverted structure (a *p-i-n-p-i-n* cell). Terzini *et al.* [138] also reported a decreased V_{oc}, but in their publication the decrease was less. From these reports it seems that tandem cell characteristics are worse if μc-Si:H is used for the second layer of the TRJ. The underlying physical mechanism must be studied in detail.

To our opinion there is no good physical model to explain *why* TRJs with μc-Si:H layers yield better tandem cells. Most of the research aimed at performance optimisation is carried out in empirically and experimentally. Because of the empirical character of the research and lack of a detailed physical model it is difficult to explain why some TRJs are better than others, even when both contain μc-Si:H layers. In the literature the following explanations are provided to account for the — in general — superior performance of tandem cells with μc-Si:H TRJ layers:

- higher optical transparency of μc-Si:H, increases the I_{sc}, due to its lower absorption coefficients. We think this explanation is plausible.

- the higher electrical conductivity of μc-Si:H layers yields less electrical (resistive) loss in the TRJ and therefore increases the FF. To our opinion this explanation is not correct, because the properties of the *np* junction rather than the conductivity of a single layer determine the performance. We think that there is no correlation between a *very large* conductivity increase (of several orders of magnitude) and the FF; The FF shows only a rather marginal improvement of several percents absolute. Furthermore, if it is the conductivity increase that improves the performance, replacement of an amorphous *p*-layer by a microcrystalline *p*-layer should give a much more pronounced efficiency enhancement. Because of the simple fact that the amorphous *p*-layer has a lower conductivity than the amorphous *n*-layer, there is more to gain by the improvement of the *p*-layer conductivity. Nevertheless, in most tandem cells the *n*-layer is replaced by microcrystalline material.

- the lower activation energy of μc-Si:H doped layers in comparison with *a*-Si:H layers leads to higher built-in voltages, which improves the cell performance. This explanation should be considered as questionable: the value of V_{bi} does not depend exclusively on the separation between equilibrium Fermi level and conduction or valence band mobility edge (this separation

is usually assumed to be equal to the conduction activation energy), but also on the values of the mobility bandgaps and the band offsets at interfaces between the different materials. Since the bandgap of μc-Si:H is much lower than that of a-Si:H, the positive effect on the V_{bi} of the much lower activation energy is compensated by the negative effect of the mobility gap reduction. Therefore, μc-Si:H doped layers do not necessary lead to higher V_{oc}-s.

A major problem of the application of microcrystalline layers to the TRJs is the difficulty to grow thin layers with microcrystalline properties. Several groups have developed special surface treatments that enable a fast nucleation of microcrystalline material on amorphous layers and thus enable a sharp transition from amorphous to microcrystalline material. The USSC group has used fluoridation of the their p-layers in order to promote microcrystalline growth in very thin layers [41]. The groups of Neuchâtel and Jülich have successfully applied a CO_2-plasma interface treatment to initiate microcrystalline growth [96]. An unspecified method with the same effects is reported by the Solarex group [154].

The term microcrystalline material embraces a large variety of materials with differing properties. It is reported by many research groups that not all types of microcrystalline materials are optimally suited for TRJs. The USSC group [6, 8] found that two types of microcrystalline material that give equally good single-junction cell characteristics, do not necessarily both give optimal multi-junction cell characteristics. The Jülich group reported that a hydrogen dilution exceeding a some critical limit resulted in a in a non-reproducibly varying V_{oc} between 1.3 and 1.7 V [9]. To a lesser extend this has also been observed by the Neuchâtel group [96]. They found that the microcrystalline phase in an n-layer has to be controlled carefully in order to maintain high V_{oc}. A too high content of microcrystalline phase in the layer, resulting from a excessive hydrogen dilution of the process gases, resulted in a lowering of the V_{oc}. They successfully applied a bi-layer structure consisting of an amorphous and a microcrystalline part to get a high V_{oc} by relaxing the very strict control of the microcrystalline fraction in the n-layer that would be required if a homogeneous n-layer was applied. From these observations it is obvious that a too high microcrystalline content affects the multi-junction cell characteristics adversely.

5.3 Review of tandem cell models

In literature three different models have been used for the modelling of a-Si:H tandem and triple-junction solar cells. These models are briefly discussed below.

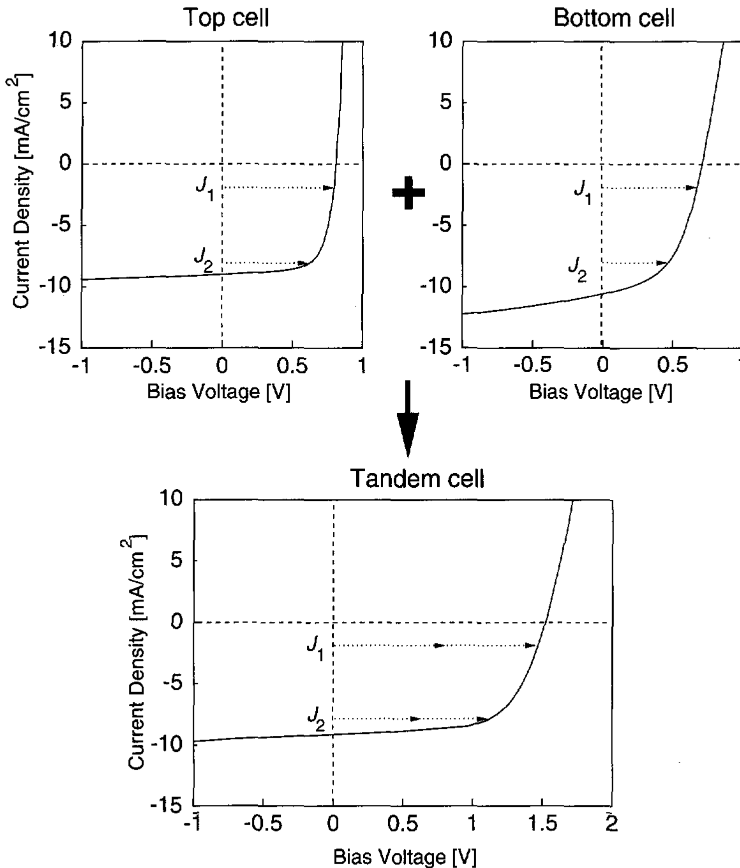

Figure 5.5: Calculation of tandem cell characteristics by addition of separately simulated *IV*-characteristics of the subcells. The bias voltages giving rise to equal current densities (*e.g.* J_1 and J_2) in the subcells are added.

- The simplest model is the "construction" of tandem cell *IV*-characteristics from separately simulated *IV*-characteristics of the subcells. This approach is applied by Block *et al.* [11] and Pawlikiewicz *et al.* [94, 95]. In this approach each subcell is simulated using the corresponding part of the generation rate profile of the tandem cell. The bias voltage for a particular tandem cell current is computed by addition of the (partial) bias voltages over each subcell for that current. By repeating this for all cell currents of the *IV*-curve the tandem cell *IV*-characteristic is determined. This procedure is illustrated in Fig. 5.5.

  The advantage of this method is its simplicity; no special models are needed

for the tunnel-recombination junction. However, there are some disadvantages: (1) the TRJs are modelled as ideal junctions, without loss; physical mechanisms causing losses are not taken into account and therefore the model cannot provide knowledge about making a good TRJ, and (2) only IV-characteristics can be simulated in this way; it is not possible to simulate other device characteristics, such as Quantum Efficiency or Capacitance *vs.* Voltage characteristics.

- An other approach, in which multi-junction cells are modelled as an entity, is the model of Kida *et al.* [63]. They introduce internal boundary conditions at the TRJ interfaces. However, in their model the TRJs are considered as ideal ohmic contacts, similar to the previous approach, and consequently their model does not provide any physical insight into the operation of the TRJ. The only advantage over the previous approach is the ability to treat the multi-junction cell as one entity. Therefore, this approach is not limited to the computation of IV-characteristics only.

- The third method which — like Kida's approach — considers the multi-junction cell as a single device, is the approach introduced by the Pennsylvania State University (Hou *et al.* [58], Bae [5]), which is later applied by Bruns *et al.* [16]. In this modelling approach the recombination in the TRJ takes place in a heavily defective interface region between the doped layers of the TRJ. In the model the mobility gap of this layer is strongly reduced (*e.g.* Bruns *et al.* [16] use a mobility gap of 0.52 eV in the recombination layer). The band edges of the n-layer conduction band and the p-layer valence band are graded towards the recombination layer, in order to model the tunnelling transport of electrons (from the n-layer side) and holes (from the p-layer side) towards the recombination layer. Figure 5.6 illustrates this approach. Bruns *et al.* [16] uses a slightly modified approach, since he grades *both* mobility edges in the doped layers. In the model the mobility gap of the recombination layer is adjusted to fit the simulated open-circuit voltage to the experimental data [4].

  The advantage of this model is that it takes into account the effect of the space charge on the band bending in the TRJ. Because of the large gradings of the mobility edges it is difficult to model the distribution of the localised states and to study the influence of the localised states on the device behaviour.

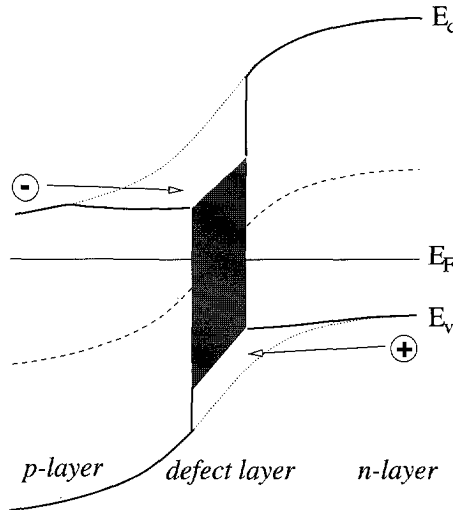

Figure 5.6: Schematic band diagram of the tunnel-recombination junction applying the Penn State model. The shaded region is the defect layer, where the recombination takes place effectively. The mobility edges without grading are indicated with dotted lines, the dash line corresponds to the midgap energy level.

5.4 New model for tandem cells

In this section we introduce a new approach for the simulation of tandem cells [148]. Like the Penn State University tandem cell model, our model enables the simulation of a tandem cell as a single device.

Trap-assisted tunnelling recombination model

As we have discussed in the previous sections tunnelling is important for the operation of a tunnel-recombination junction. The review of approaches reported in literature for the simulation of tandem cells shows that there has been no serious effort to model the tunnel process in a physically realistic way. To model the physics of the TRJ as realistically as possible, we have implemented the trap-assisted tunneling (TAT) recombination model of Hurkx *et al.* [60] in our device simulator ASA. It is one of the few tunnelling models available for application in device simulation programs. This model has already been introduced briefly in Sect. 2.3.5.

The TAT model was originally derived as an extension of the conventional SRH recombination equation using effective carrier lifetimes. In the original implementation carrier lifetimes are divided by field-dependent factors which are

larger than one; an increase of the electric field brings about a reduction of the carrier lifetimes. In the present work the field-dependent factors enlarge the capture cross sections and emission coefficients of trap states, which is basically analogous to the original implementation. Because in ASA not only the recombination through (single electron) traps is computed, but also the charge occupation of traps, in our implementation both the Shockley-Read-Hall recombination function, Eq. 2.30, and the occupation function Eq. 2.29 are modified by the field-dependent factors. Further, the TAT model has been extended for the amphoteric dangling bond occupation and recombination model for the two-electron levels of the dangling bonds. In this model, the capture cross sections and emission coefficients of the two different transition energy levels, $E^{+/0}$ and $E^{0/-}$, also depend on the electric field. The field-dependent factors may have a different value for the two transition energy levels.

Enhanced carrier transport in the TRJ

Preliminary simulations using the TAT model yielded tandem cell IV-characteristics deviated considerably from measured tandem cell characteristics. A study of the parameter sensitivities showed that this could not be improved by tuning the model; adjusting the relevant parameters (such as the defect states density and tunnelling effective electron mass) did not result in more realistic tandem characteristics. Further investigation of the internal device quantities revealed imperfections of the model. We found that the TAT model enhances the recombination depending on the field, but it does *not* model the (very efficient) tunnelling carrier transport in the high field region towards the location of the states where they actually recombine. Although the recombination is much stronger because there are more free carriers available for recombination, the electrons and holes still have to move to the physical position in the simulated device where the recombination takes place. If high recombination current densities are flowing, large gradients in the quasi-Fermi levels (the driving force for carrier transport) are still necessary. Therefore, considerable applied biases are still needed to obtain high current densities when only the trap-assisted tunneling recombination model is applied.

We tried a new approach to model the tunneling transport in high field regions, without having to change the structure of the device simulator drastically. We found that this could be accomplished by also making the extended states mobilities field-dependent. With increasing field the mobility increases as well.

In device simulation models for a-Si:H devices only the carriers in the extended states are mobile and contribute to the current transport. For instance, the electron current density, J_n, is driven by the gradient of the free electron quasi-

Fermi level E_{fn}:

$$J_n = \mu_n n \frac{dE_{fn}}{dx}, \tag{5.4}$$

where μ_n is the *extended* state electron mobility and n is the concentration of *free* electrons in the extended states. This is the general model for electron current as used in device simulators for crystalline as well as for amorphous semiconductors. Conventional drift- and diffusion-driven carrier transport takes place in the extended states; this model only accounts for that type of transport. In the case of tunneling transport there are mobile carriers that do not move in the extended states, but at energies between the mobility edges; those carriers are not included in the model.

Assuming that the tunneling carrier transport is also driven by the gradient in the quasi-Fermi level the following qualitative model is proposed to include tunneling carriers. Instead of only taking into account the carriers inside the extended states, the tunneling carriers can be included in the transport if Eq. 5.4 is modified into:

$$J_n = \left\{ \int_{-\infty}^{+\infty} \mu_n(E) n(E) dE \right\} \cdot \frac{dE_{fn}}{dx} \tag{5.5}$$

This equation accounts in principle for the presence of tunnelling and thus for mobile electrons below the mobility edge. If tunneling carriers are present, the integration over *all energies* gives a larger $\int \mu_n(E) \cdot n(E) dE$ term than just the product of free electrons n and extended state mobility μ_n, as is used in Eq. 5.4. This higher integrated $\mu_n(E) \cdot n(E)$ product is implemented in a pragmatic way to avoid drastic changes in the structure of the simulator; as current conducting carrier concentration still the extended state concentration, n, is used, but to enhance the $\mu_n n$ product the extended state mobility, μ_n, is replaced by an increased field-dependent effective mobility, $\mu_{n,eff}$.

A detailed physical model for the field-dependent effective carrier mobility, based on the physics of tunnelling transport, has not yet been developed. Instead, a pragmatic approach is chosen. There is much experimental evidence, that the conductivity and (drift) mobility of *a*-Si:H increases more or less exponentially with the electric field, for field strengths higher than about 10^5 V/cm [1, 62, 85]. Although the transport in the TRJ is not exactly comparable to the experiments showing the strong conductivity increase, we adopted a similar field dependence

as a first guess for the field-dependent effective carrier mobility, μ_{eff}:

$$\mu_{eff} = \mu \exp\left(\frac{|\vec{E}|}{E_0}\right) \tag{5.6}$$

where E_0 is a parameter determining the strength of the field dependence.

Tandem cell simulation results

Tandem cell simulations are carried out to study the influence of the trap-assisted tunneling model and field-dependent enhanced carrier mobilities model. A simulation structure is defined with a top cell thickness of 90 nm, including 10 nm p-layer and 15 nm n-layer, and a bottom cell thickness of 416 nm, including 11 nm p-layer and 20 nm n-layer. The material parameters used for this simulation study have in general similar values as those in set II of Fig. 4.7. A difference is however, that in the present simulations Gaussian distributions for the dangling bonds are used. The density of dangling bonds is similar to that used in the calibration exercise with the defect-pool model, as presented in Sect. 4.5, except the dangling bond density in the TRJ-layers, which is set to 10^{19} cm^{-3}. Further exceptions are the values of the TRJ n-layer conduction band tail and TRJ p-layer valence band tail characteristic energy. These parameters are strongly increased to: $E_{c0} = 0.095$ eV and $E_{v0} = 0.130$ eV.

Increase of the characteristic energies of the tail states is necessary to ensure the presence of sufficient space charge in the TRJ layers. Without increasing those parameters the band bending in the TRJ was not sufficient, which results in low internal built-in voltages over the *pin* subcells (*cf.* Fig. 5.4). In principle, to obtain space charge densities in the order of 10^{19} cm^{-3}, the density of gap states must be rather *high and flat* near the Fermi level in the doped layers. In that case the required high space charge density is available, if the Fermi level is removed from its equilibrium position, such as is the case in the space charge region of the TRJ. An other possibility to generate sufficient space charge density is to decrease the activation energy of the doped, *amorphous(!)* layers to unrealistically small values. For instance, using a characteristic energy of about 0.030 eV for the n-layer an activation energy of about 0.005 eV is necessary. Therefore, we conclude that the density of localised states should be high and flat in the vicinity of the thermal-equilibrium position of the Fermi level in doped layers. This is in contradiction with the results of the defect-pool model, which gives density of states distributions with a *minimum* value near the equilibrium position of the Fermi level (see Fig. 2.2).

The only adjustable parameter of the TAT model is the effective tunnel mass

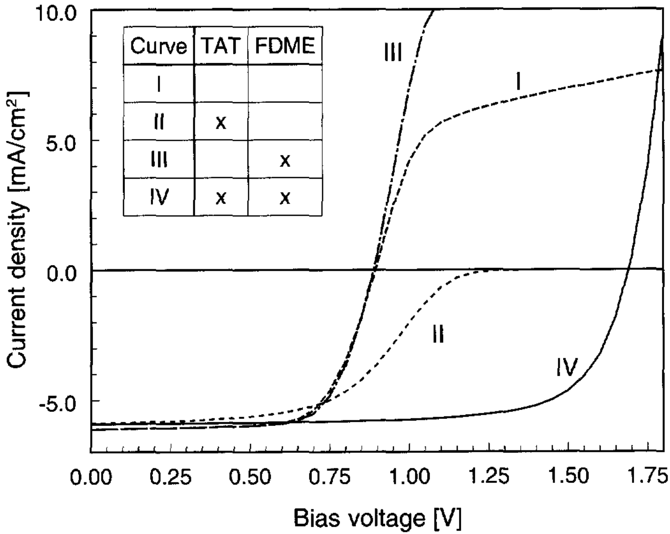

Figure 5.7: Simulated tandem cell IV-characteristics with or without the use of the trap-assisted tunneling (TAT) recombination model and field-dependent mobility enhancement (FDME) model. Curve I is simulated with both models switched off; for curve II only the TAT model is used; for curve III only the FDME model is used; for curve IV both models are applied.

of electrons. This parameter is kept at the default value of Hurkx *et al.* [60]: 0.25 times the electron rest mass. The model parameter of the enhanced-mobility model E_0 is set to $1.2 \cdot 10^5$ V/cm. The field-dependent mobility enhancement was only applied in the TRJ layers. Further, the enhancement factor was computed only once, using the thermal-equilibrium electric-field distribution. During the calculation of the IV-characteristics the mobility values were *not* adapted to actual field strengths in the TRJ that may be slightly off the thermal equilibrium values.

The results of four different simulations are shown in Fig. 5.7. The impact of the TAT and enhanced-mobility models on the simulated IV-characteristics is very obvious. Only if both models are applied the simulated illuminated IV characteristics approaches measured tandem characteristics, in all other cases the fill factor and the open-circuit voltage is much too small. This shows that the physics of the TRJ can be only described realistically with both the TAT and mobility-enhancement model.

To further elucidate the origin of the low fill factor and open-circuit voltage, the band diagrams of the illuminated tandem cells at zero bias voltage are shown in Fig. 5.8. The part close to the TRJ is enlarged. From the differences between the majority carrier quasi-Fermi levels at both sides of the TRJ the internal volt-

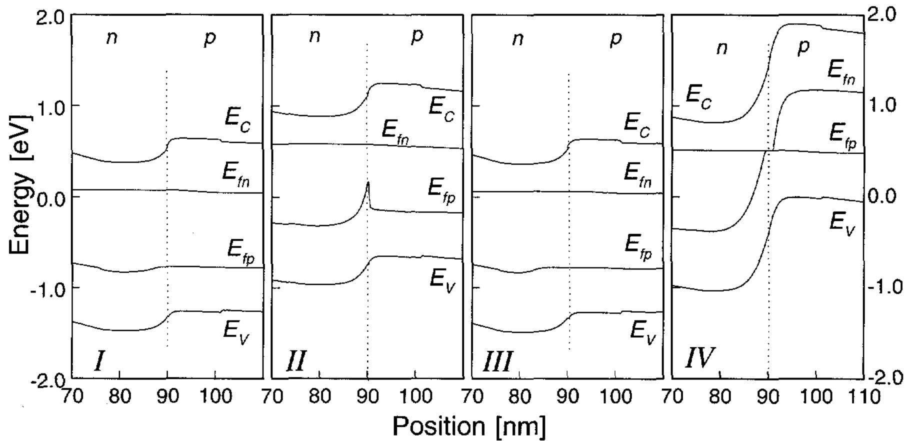

Figure 5.8: Band diagrams in the vicinity of the tunnel-recombination junction of an illuminated tandem cell in short-circuit conditions. The graphs I to IV correspond to the same four cases as shown in Fig. 5.7.

age over this junction can be estimated. In all band diagrams except the one for which both models were used a large difference between the majority carrier quasi-Fermi levels is observed. Since the presence of a large internal voltage causes significant loss of the voltage generated by the tandem cell, this explains the bad *IV*-characteristics.

In conclusion, we summarise that the modelling of the tunneling transport and recombination in the TRJ can be simulated by the combination of the trap-assisted tunnelling recombination model and the field-dependent mobility-enhancement model. Application of both models enables the simulation of realistic tandem cell *IV*-characteristics. Further, to obtain a sufficient space-charge density in the TRJ layers a high density of states around the equilibrium position of the Fermi level is required.

5.5 Modelling of tandem cell degradation

Tandem cell stability and optimum design

Tandem cells are the preferred structures for stable *a*-Si:H solar cells. The simulation approach presented in the previous section is applied to clarify why tandem cells exhibit less degradation.

We have simulated the *IV*-characteristics of an illuminated tandem cell. The material parameters used in the simulations are the same as used in the previous

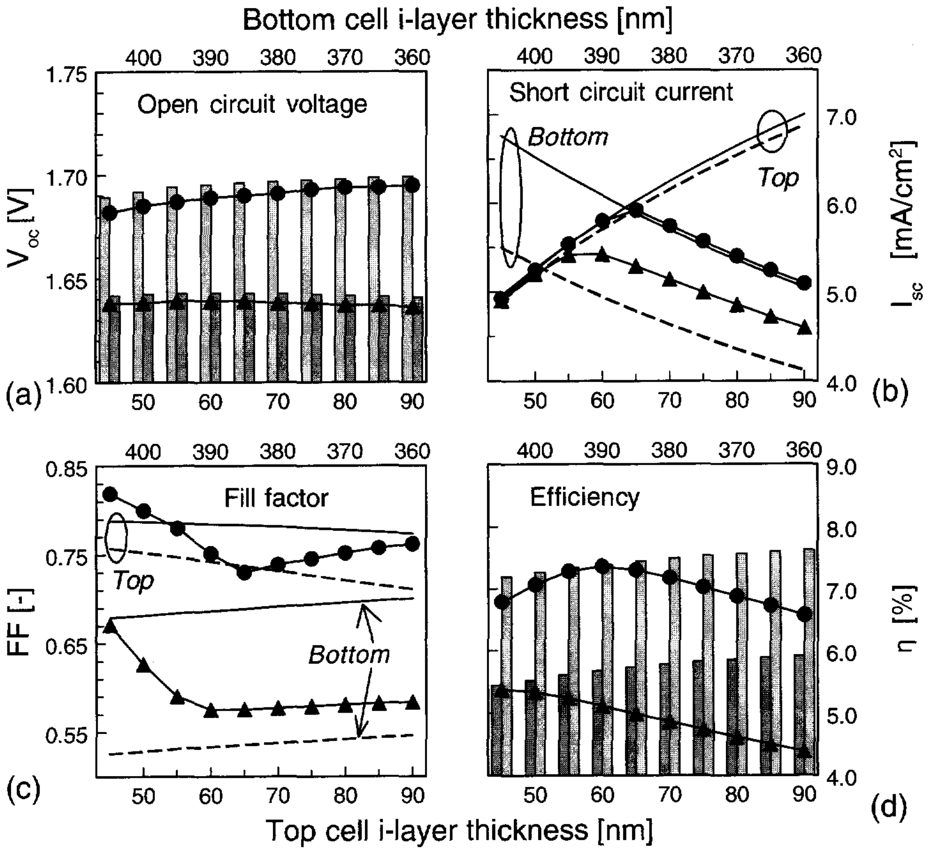

Figure 5.9: Tandem cell parameters as a function of subcell thicknesses; before degradation (lines with round symbols) and after degradation (lines with triangle symbols). (a) Open circuit voltage (here the bars represent the sum of the V_{oc}s of the separately simulated top and bottom cell), (b) short circuit current (the curves without symbols represent the I_{sc}s of the top and bottom cell), (c) fill factor (the curves without symbols represent the FFs of the top and bottom cell), and (d) efficiency (bars represent the sum of the efficiencies of the top and bottom cell).

section. The cells are simulated both in initial state and degraded state. In the degraded state the density of dangling bond states is assumed to be 8 times higher than the initial density. In the initial state the dangling bond concentrations in the top and bottom cell are set to $4 \cdot 10^{16}$ cm^{-3} and $3 \cdot 10^{16}$ cm^{-3}, respectively.

A series of simulations has been carried out in which the thicknesses of the top and bottom cell *i*-layers have been varied. The sum of the thicknesses is kept constant at 450 nm. In addition to the tandem cell simulations, the subcells are simulated individually, using the corresponding part of the optical carrier generation profile of the tandem cell.

The results of the simulations are presented in Fig. 5.9. The graphs show the tandem cell performance parameters along with the parameters of the separately simulated single-junction subcells. Figure 5.9a shows the tandem cell open-circuit voltage as a function of the subcell thickness. The V_{oc} does not depend much on the subcell thicknesses. In the degraded state the V_{oc} is about 50 mV lower than in the initial state. The bars in this graph represent the sum of the V_{oc}-s of the separately simulated subcells. The differences between the tandem cell and summed subcell V_{oc}-s are very small.

The behaviour of the short-circuit current is shown in Fig. 5.9b. In the initial state the tandem cell I_{sc} is approximately equal to the *minimum* of the (separated) top and bottom cell I_{sc}. The maximum is reached for a top cell thickness of 65 nm, where the I_{sc} of both subcells are equal. In the degraded state the maximum tandem I_{sc} does not coincide with the thickness ratio giving equal top and bottom cell I_{sc}-s. This is caused by the relatively large reduction of the bottom cell fill factor: because there is a significant gradient in the degraded bottom cell IV-curve around I_{sc}, the maximum tandem I_{sc} is obtained with a current limiting bottom cell. In this situation a negative internal bias develops across the bottom cell, resulting in a slightly higher current than the short-circuit current of the 'isolated' bottom cell.

Figure 5.9c shows the dependence of the fill factor on the subcell thicknesses. In the initial state the *FF* clearly increases if one of the subcells becomes current limiting and has a lower I_{sc} (*cf.* Fig. 5.9b). In the degraded state the increase of the fill factor is most pronounced if the highest quality subcell (which is usually the top cell) becomes current limiting.

In Fig. 5.9d the initial and degraded tandem-cell efficiencies are shown. The bars depict the sum of the conversion efficiencies of the individually simulated subcells. In the initial state the maximum efficiency is attained approximately with the thickness ratio corresponding to short-circuit current matching. At the optimal efficiency the sum of the bottom-cell and top-cell efficiency is equal to the tandem-cell efficiency. Because from a tandem cell with these *i*-layer thicknesses

all photovoltaic power generated in the subcells is extracted, this is indeed the most efficient tandem cell. In all other cases a part of the generated power must be dissipated in the subcell itself.

In the degraded state the optimum performance is attained with quite different i-layer thicknesses than in the initial state. The best cell after degradation has a sub-optimal initial efficiency and short-circuit current; in the initial state there is a large mismatch between the short-circuit currents of the subcells, meaning that the top cell is initially strongly current limiting.

This modelling study clearly shows that an optimum tandem-cell efficiency in the degraded state does not coincide with the current matching condition in the initial state. Therefore, tandem cells cannot be optimised by purely optical modelling; a full device model of the tandem cell is required to find the optimal design in degraded state. To obtain maximum performance after degradation the best subcell (usually the top cell) must be made current limiting.

The superior stability of tandem cells is usually explained as follows:

- The subcells in a tandem are thinner than a single cell, thus they are more stable themselves.
- The still relatively thick bottom cell which shows still significant degradation if measured as a single cell with this thickness, degrades less if incorporated in a tandem cell. The degradation is reduced because the light intensity reaching the bottom cell is reduced by the top cell.

These explanations do not reveal the most important factor causing the smaller relative degradation: tandem cells are more stable because the instability of the worst, most degrading cell is hidden by the better, more stable cell. Another often made misconception is that there is less degradation in thinner cells, because there is *less recombination* in thinner cells. This is not the case; modelling shows that the recombination rate is not smaller in thinner cells. The reason for better stability is the higher built-in field in thinner cells, which results in more efficient carrier collection, even if the density of metastable dangling bonds states has increased. In other words, thinner cells are more stable because they are less sensitive to the presence of a large concentration of dangling bonds. This is confirmed by modelling the degradation behaviour of cells with different thicknesses.

Chapter 6

Experiments for modelling

This chapter covers three different measurement topics that are relevant to modelling and parameter extraction. First we discuss the accurate measurement of dark IV-characteristics in Sect. 6.1. A large part of measured dark IV-curves is usually not reflecting the intrinsic behaviour of the a-Si:H *pin* diode, but rather a leakage current. This is followed by the extraction of the mobility gap, E_g, from temperature-dependent dark IV-measurements in Sect. 6.2. For these measurements the technique described in Sect. 6.1 are applied. Finally, Sect. 6.3 discusses the thermal stability of the reflective properties of a-Si:H/metal interfaces. This is especially relevant for of a-Si:H solar cell degradation experiments in which also thermal annealing steps are applied. In these experiments the thermal anneal must not affect the optical properties of the back contact, that serves as a reflector for long wavelength light.

6.1 Accurate measurements of dark and light IV-curves

For the analysis of the device physics of a-Si:H solar cells high-quality measurements are required. The measurements must reflect the intrinsic device behaviour and must not be dominated by parasitic effects. As outlined in the introduction a large part of the dark IV-characteristics is usually dominated by parasitic effects. The current in excess of the theoretical exponential characteristic in the voltage region below 0.5 V forward bias is commonly ascribed to shunting, without further specification of the physical origin of the shunts. A possible explanation is the presence of pinholes or other defective regions in the a-Si:H layers below the metal contact dots, which gives rise to non-ideal IV-characteristics. However, if this were the case one would expect either a random variation of the 'shunt' current of different dots on a single sample (due to a statistical distribution of a small

number of shunt creating defects in the sample), or a linear scaling with contact dot area (if the shunting defect density is so high that the total contribution scales with the dot area). Neither of these trends is observed in the measurements of our samples. Instead, we found that the 'shunt' currents are within a small band (less than one order of magnitude in width), which is significantly less than the range of contact dot areas, which ranged between 0.01 and 1 cm^2. A weak, sub-linear correlation between contact dot area and 'shunt' current is present. These observations lead to another explanation for the shunt currents.

6.1.1 Lateral leakage currents in *a*-Si:H *pin* cells

Due to the observation that the 'shunt currents' of devices with considerable spread in area do not show very much variation, we concluded that the parasitic current must have its origin outside the contact dot, which defines a single *pin*-cell. The contribution of the periphery of the dot to the current is explained as follows: the metal contacts are deposited on the *n*-layer which has a relatively high sheet resistivity. If a bias voltage is between over a contact dot and the TCO contact a current flows in the *pin* diode below the dot. However, due to the presence of a conductive *n*-layer the area around the contact gets biased as well and in the *pin*-structure in the periphery of the contact a current will flow, which laterally flows through the *n*-layer to be collected in the contact. In the case of forward bias voltages exceeding 0.6 V the current densities become too high to be collected through the *n*-layer, because of the resistivity of this layer. For bias voltages below 0.4 V the currents are so small that the lateral current flow through the *n*-layer from the periphery to the contact is not causing a significant potential gradient over this layer. In fact, the *n*-layer has practically become an equipotential surface and the total *n*-layer serves as the contact.

In order to remove the contribution of the periphery to the measurement of the *IV*-characteristics of the 'intrinsic' device two possibilities are investigated: (a) the application of a guard ring around the contact, or (b) removal of the *n*-layer around the metal contact [75, 76]. By photo-lithographic techniques and lift-off patterning we have defined contacts surrounded by guard rings. The spacing between contact and guard is 10 μm, in order to define the contact dot area precisely. This results in a considerable extension of the range of useful bias voltages, but at low currents there is still considerable deviation between the theoretical exponential *IV*-characteristics and measurements, and at zero bias voltage a non-zero current flow is observed. This behaviour is due to the (inevitable) small difference (in the order of 1 mV) between the measurement probe and the guard probe of the HP 4145b semiconductor parameter analyser. This small offset voltage gives rise to an offset current through the *n*-layer between the measurement contact and

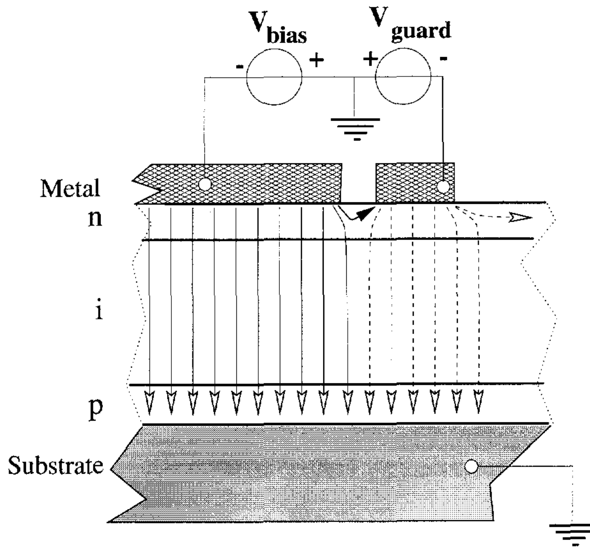

Figure 6.1: Influence of voltage offset between measurement and guard terminal.

the guard contact, as is illustrated in Fig. 6.1. This offset current can be several orders of magnitude larger than the current to be measured and thus masks the characteristics of the intrinsic device. Therefore, the option of guard rings is not suitable for accurate dark IV-measurements in reverse and low forward bias region. However, it can be useful for measurements on tandem cells, as will be discussed below.

The second option — etching the n-layer— has also been employed. Using the contact metallisation as etch mask the n-layer is etched by reactive ion etching (Alcatel type GIR 300, etch gas SF_6 diluted by He, flowrate SF_6: 45 sccm, flowrate He: 50 sccm, RF power: 50 W, pressure = 0.09 mbar, duration 15 s). The etch time is chosen to slightly over-etch the n-layer. To avoid the creation of a bare a-Si:H surface between the n-layer and the p-layer, that may introduce another path for leakage currents, we chose not to etch through the total *pin* structure. By a surface reactive ion measurement it was verified that the n-layer was slightly over-etched.

Figure 6.2 illustrates the effect of the removal of the n-layer. An example of the measured IV-characteristics before and after etching of the n-layer is given in Fig. 6.3. This figure shows that by this preparation technique the lateral leakage current contribution to dark IV-characteristics can be removed. The difference between the current densities before and after etch, is more than 4 orders of magnitude. This is much larger than the ratio of the contact dot area (0.6 cm^2) and

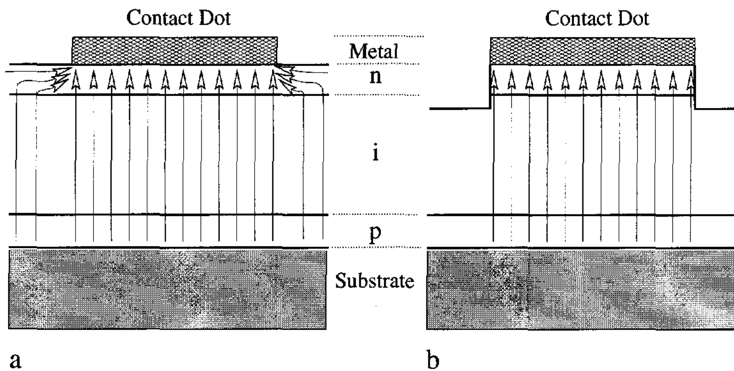

Figure 6.2: Contribution of the lateral leakage current from the periphery of a contact dot. Etching of the *n*-layer outside the metallisation removes the path for the leakage current.

the total sample area ($\approx$ 25 cm^2). This indicates that the lateral leakage current is not just a geometrical effect, in the sense that the effective contact area is increased from the dot area to the sample area, but that there also must be a physical shunt between the n-layer and the TCO-layer. This shunting contact is most probably present at the edges of the *pin* structure, where the deposition is very inhomogeneous. The value of the lateral leakage current is therefore closely related to the sheet resistance of the n-layer and/or the resistance of the shunt path connecting the n-layer locally to the TCO. However, if the latter resistance is the limiting factor in the leakage current path, no correlation with the sample area would be observed. Because of the presence of this correlation in our experiments, we ascribe the leakage current to the shorting of the relatively conductive n-layer. The leakage current value is therefore a measure for the sheet resistance of the n-layer. Any change in the lateral leakage current caused by for instance a temperature treatment of a sample is therefore due to a change in the n-layer conductivity or the conductivity of the shunt between the n-layer and the TCO.

6.1.2 Influence of trap charging on dark IV-measurements

The removal of the n-layer outside the contact area allows us to measure the very low current densities in reverse and slightly forward biased a-Si:H *pin* diodes. We have found that the measurement at these biases is very sensitive to the delay time between the change of the bias voltage and the current measurement. The influence of the delay time is shown in Fig. 6.4. The graphs show the IV-characteristics measured between -0.3 V and 0.2 V with an upward sweep and a downward sweep of the bias voltage. For the measurement of Fig. 6.4a the de-

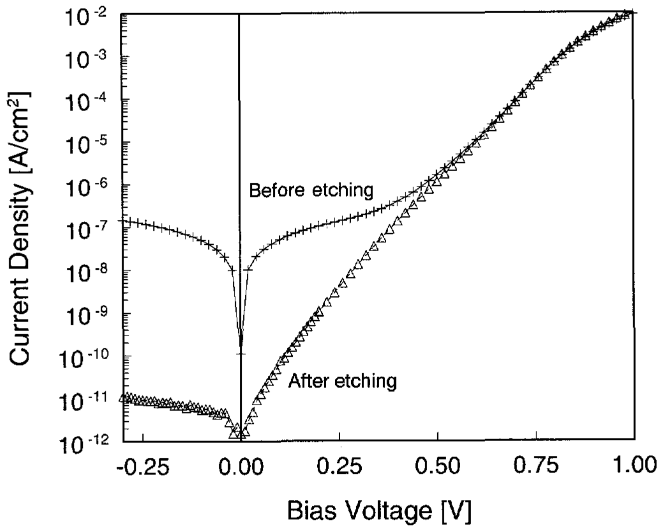

Figure 6.3: Dark IV-measurement results of an *a*-Si:H *pin* diode, before and after etching the *n*-layer.

lay time was set to three seconds. The large difference between the up-sweeping and down-sweeping curves shows that this delay time is not sufficient to reach a steady-state situation after a bias voltage transient. When a delay time of sixty seconds is used the up-sweeping and down-sweeping measurements overlap, implying that after each bias change a steady-state is reached.

To study these transients in more detail we have measured the transient response. The lower curve in Fig. 6.5 shows the current response of an un-degraded *a*-Si:H *pin* diode following a step in the bias voltage at $t = 0$ s from 0 to 25 mV. Street reported very similar measured transients [125]. Our measurement is obtained with a Keithley 5617 electrometer, which has the capability to do a sequence of measurements at predetermined time intervals. To avoid the change of measurement range during the measurement, which was found to give incorrect measurement values in the first few seconds after the change, all measurements were carried out in the 200 pA range. Due to currents in excess of 200 pA during the first few seconds of the transient, no measurement values for this time span are obtained. Analysis of the transient shows that the transient behaviour cannot be characterised by a single time constant. In the first 5 to 10 seconds the time constant is much shorter than after 10 seconds. After that the time constant is in the order of 10 seconds. The question arises as to what causes this very long time constant.

It may be obvious that such long time constant is not caused by the charging

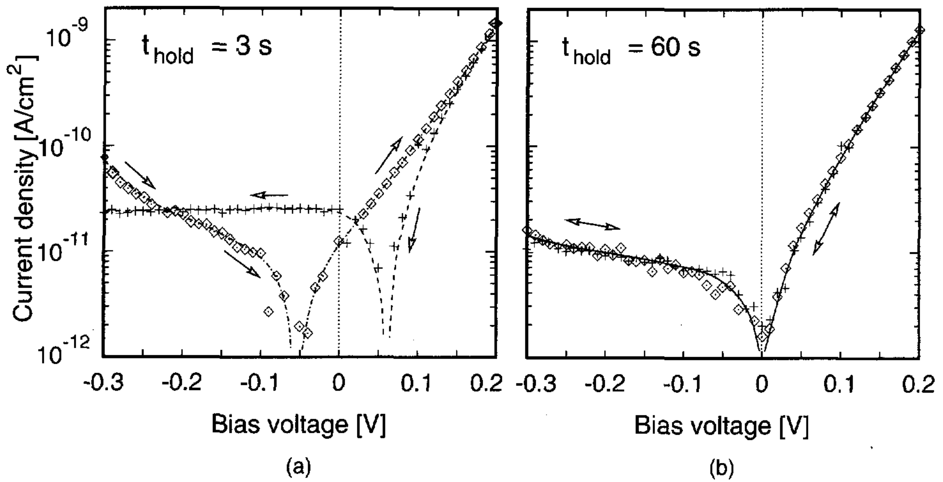

Figure 6.4: Dependence of the IV-measurement on the delay time between bias voltage adjustment and current measurement during a biases sweep. In Fig. (a) a delay time of 3 seconds was applied, which resulted in non-overlapping measurements of upward-sweeping and downward-sweeping bias voltages. In Fig. (b) the delay time was set to 60 seconds, resulting in overlapping measurements.

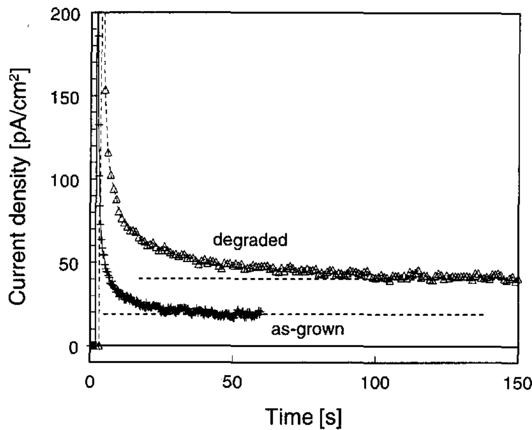

Figure 6.5: Current transients after a step in the bias voltage from 0 to 25 mV. Lower curve: before degradation of the device, upper curve: after light soaking of the device.

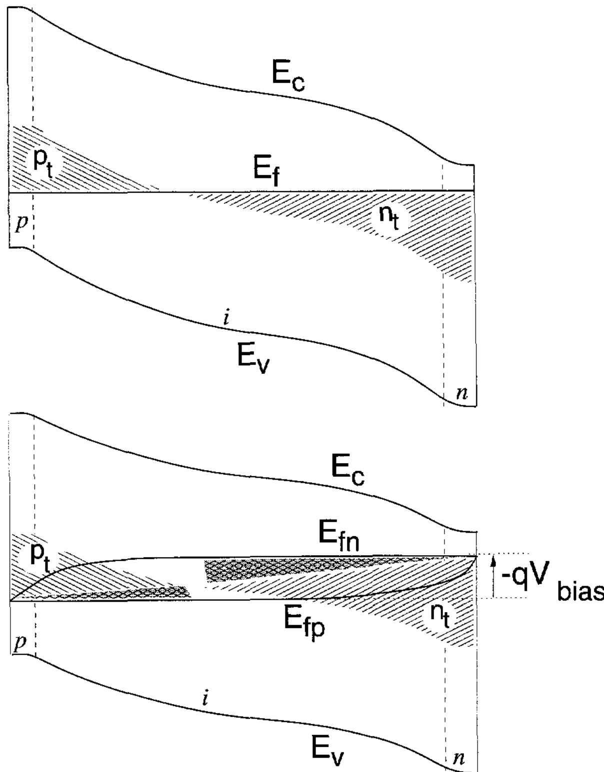

Figure 6.6: Schematic picture of the influence of a bias step on the occupation of the localised gap states. Top figure: thermal equilibrium situation. Bottom figure: after application of a bias voltage, V_{bias}. The states in the cross-hatched region are charged following a change of the biasing voltage.

of the geometric, parallel-plate capacitance, formed by the contacts on both sides of the *pin* diode ($\approx$ 25 nF/cm^2 for an *a*-Si:H structure with 400 nm thickness), since this capacitance is connected to a low-impedance voltage source, through a series resistance of at most 100 Ω. Therefore, the long time constant must be related to an intrinsic property of charge trapping in the *a*-Si:H *pin* diode.

In Fig. 6.6 we show schematically the influence of a bias change on the trap occupation in an *a*-Si:H *pin* diode. For this analysis we assume that all states below midgap are donor-like states and states above midgap are acceptor-like states. In Fig. 6.6a the thermal equilibrium situation is depicted: localised states above the Fermi level and below midgap are donor-like states, occupied by trapped holes (marked by p_t), and states below the Fermi level and above midgap are acceptor-like states, occupied by trapped electrons (marked by n_t). If a forward bias, V_{bias},

is applied the quasi-Fermi levels inside the *pin* diode will separate and a charging of additional localised states will take place. In regions where the hole concentration is higher than the electron concentration the occupation of localised states is controlled by the hole quasi-Fermi level. Analogously, if the electron concentration exceeds the hole concentration the occupation is determined by the electron quasi-Fermi level. The charging of additional states is depicted in Fig. 6.6. The cross-hatched areas mark the states that will be charged if the biasing condition of the device goes from 0 V to V_{bias}. The device changes to a condition in which there is net recombination in the *pin* diode, the additionally trapped charges will not be supplied by thermal generation, but they must be supplied by an external loading current.

By integration of the current transient in excess of the steady-state current value (indicated by the horizontal dotted lines in Fig. 6.5), we can estimate the additional charge that is trapped when a step in the bias voltage is applied. Further, from this charge the capacitance, dQ/dV, due to charge trapping inside the *pin* diode can be determined. The total charge in the current transient is 0.51 nC/cm^2 (start of the integration interval 2.1 s after the bias voltage step). Division by the voltage step gives an estimation of the capacitance of the midgap states: $5.1 \cdot 10^{-10}/0.025 = 20.4$ nF/cm^2. An estimation of the number of charges in the cross-hatched areas of Fig. 6.6 correlates very well to the charge supplied by the current transient. Assuming a midgap density of states of 10^{16} cm^{-3}eV^{-1} and that the states which are charged with this long time constant are located in a region of about 200 nm in the centre of the device, and that the quasi-Fermi levels in this range shift over 12.5 mV (*i.e.* half the externally applied voltage), the charge which will be trapped in these states is about 0.4 nC/cm^2. Despite the rough estimation this value is surprisingly close to the total charge in the current transient (0.51 nC/cm^2).

Although we could explain where the charges are trapped the origin of the large time constant is still unclear. In principle, there are two possible causes: (1) the supply of carriers to the traps is the limiting factor, or (2) the trapping process itself is slow. If the trap charging process is considered as the charging of a capacitor C through a resistor R limiting the supply of charge carriers (loading current), the resistor R can be computed from the time constant and the capacitance of the midgap states as R = 490 MΩcm^2. This resistor value corresponds with a slab of *intrinsic* a-Si:H with a thickness of about 50 μm (assumed is a intrinsic a-Si:H conductivity $\sigma = 10^{-11}$ S/cm). Since the i-layer of the *pin* diode of our measurements has a thickness of only 400 nm (which is for the most part *more* conductive than neutral intrinsic a-Si:H, because the carrier concentrations increase towards the doped layers), it is very unlikely that there is such a high

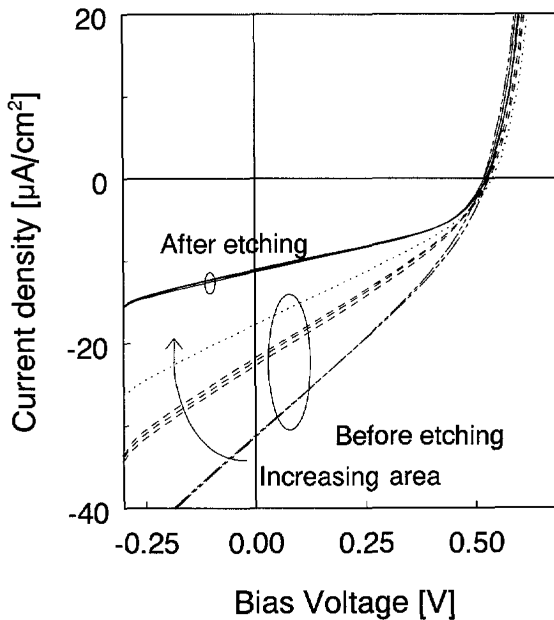

Figure 6.7: Influence of lateral leakage currents on low illumination level IV-measurements. Before n-layer etch the short-circuit current density and apparent shunt resistance depend on the area of the cell. After n-layer etch the current densities of all cells with different areas are equal.

resistance for the loading of the capacitor of localised states. Therefore, the first mentioned cause for the long time constants has to be rejected, and the second must be the real origin. The slow trapping process is explained by the presence of very low carrier concentrations and since the capture process is proportional to the free-trap concentration and the free-carrier concentration, this process will be slow for low forward and reverse bias voltages. With increasing forward bias voltages the densities of carriers available for the trapping process increases, because electrons and holes are injected into the i-layer and the quasi-Fermi levels move closer to their corresponding band edges. Therefore, at higher biases the trap-charging process becomes much faster.

6.1.3 Influence of lateral leakage currents on low illumination level IV-measurements

The lateral leakage current does not only affect the measurements of dark IV-characteristics, but also measurements with low illumination intensities. Samples of which the n-layer has not been etched away, show — depending on the illumi-

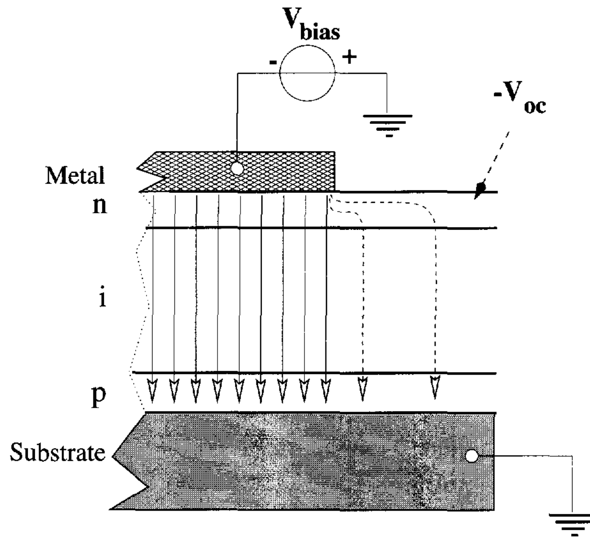

Figure 6.8: Origin of the low apparent shunt resistance in low-light-intensity IV-measurements. In the non-contacted surroundings of a contact dot the solar cell is practically biased at V_{oc}. Therefore, the current flow through the n-layer between surroundings and metal dot depends on the bias voltage on the contact, giving rise to the low apparent shunt resistance.

nation level and sheet resistance of the n-layer— a large gradient in the IV-curve around I_{sc} which reduces the fill factor. The reduction of the fill factor depends on the area of the contact dot, as is shown in Fig. 6.7. After etching the n-layer the current densities of all contacts are equal.

The gradient in the IV-curve at I_{sc} results from the bias-voltage-dependent collection of the photocurrent generated in the periphery of the contact. This mechanism is explained with the help of Fig. 6.8. Far away from the contact dot the cell is biased with V_{oc}, since no external current is flowing in this region of the solar cell. In the direct surroundings of the contact a voltage gradient is present in the n-layer, depending on the value of the bias voltage applied to the contact. Because of the voltage gradient a current flows laterally in the n-layer. Whether this effect will be visible in the measurement results depends depends on the illumination level and the sheet resistivity of the n-layer. For instance, LBIC (Light-Beam Induced Currents) measurements by Kolter [66] show that the contribution of the periphery of the metal contact is much higher with a microcrystalline n-layer than with a amorphous n-layer, which has a much lower conductivity.

Because the gradient of the IV-characteristics around I_{sc} depends on the sheet resistivity of the n-layer, low-illumination-level measurements can be applied to

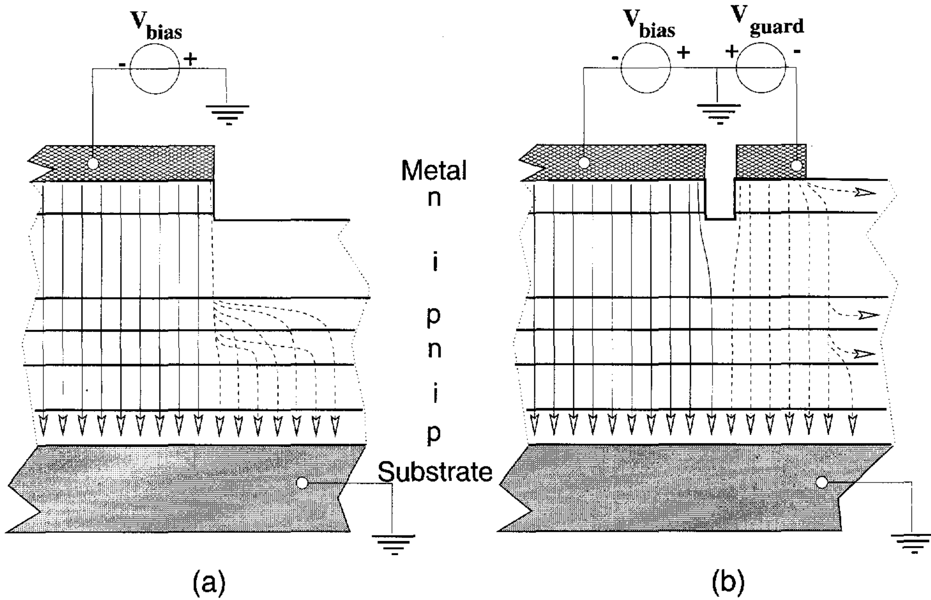

Figure 6.9: (a) Lateral leakage currents in the doped layers of the tunnel-recombination junction of a tandem cell with etched top n-layer. (b) Reduction of the lateral leakage current in the tunnel-recombination junction, by application of a guard ring contact structure in a tandem cell.

characterise the conductivity of the n-layer *in* a solar cell. It is desirable to further investigate this effect and to develop a characterisation method for the n-layer; it will be very valuable since it provides a very simple means to measure the quality of an n-layer as applied inside a solar cell.

6.1.4 Accurate measurements of tandem cell IV-characteristics

In tandem cells the etching of the backside n-layer will not remove the lateral leakage current, because there are layers with a low sheet resistivity in the tunnel-recombination junction. Therefore, these layers give rise to lateral currents which will show up in low current-density measurements, as is depicted by Fig. 6.9a. To obtain high-quality low-current measurements of tandem cells, the guard ring approach can be applied in combination with the etching of the n-layer. This approach is illustrated in Fig. 6.9b.

Measurement of the low illumination-level IV-characteristics of tandem cells can be utilised to assess the quality of the doped layers in the TRJ. For this measurement the back-side n-layer has to be removed such that the configuration of Fig. 6.9a is obtained. From the illumination-intensity dependence of the gradient

in the illuminated *IV*-characteristics the sheet resistivity of the most conductive layer in the TRJ can be estimated. Development of this proposed measurement is highly recommended because it will provide a method to characterise the TRJ layers present in a complete tandem cell.

6.2 Extraction of mobility gap

In Sect. 4.2 we concluded that the mobility gap is the key parameter determining the temperature dependence of dark *IV*-characteristics of *a*-Si:H *pin* diodes. Therefore, temperature-dependent measurements of diode characteristics can be used to extract the mobility gap of *a*-Si:H.

Temperature-dependent *IV*-characteristics have been measured. The dark *IV*-characteristics measured at 300K was utilised to calibrate the model parameters. The set of calibrated parameters was adapted to different values of the mobility gap with the parameter dependence relations derived in Sect. 4.2. These parameter sets, which are equivalent at one temperature, are used to simulate the diode current activation energy as a function of energy. From the measured temperature-dependent dark *IV*-characteristics the activation energy curve has been determined. (Characteristics measured at 300K, 310K and 320K were

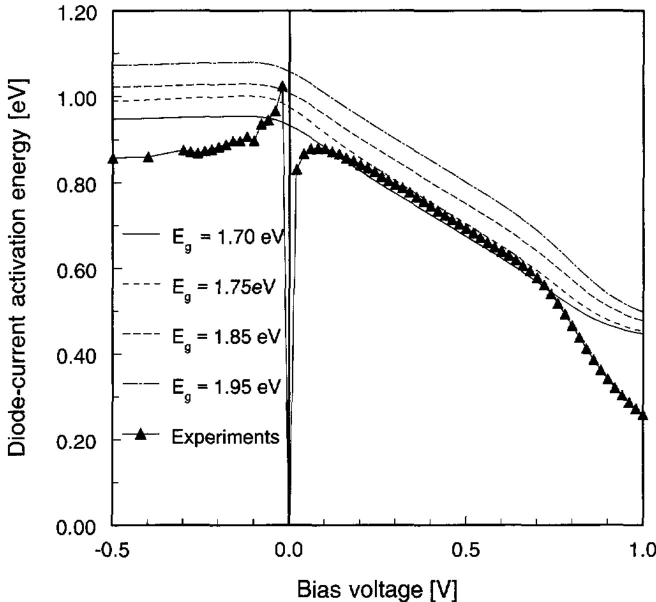

Figure 6.10: Simulated and measured diode current activation energy.

used.) In Fig. 6.10 the simulated and the experimental activation energies are shown. In a large part of the forward bias voltage region there is good agreement between the simulation and the measurements. From this graph we can conclude that the mobility gap of our material is 1.73 ± 0.02 eV, which is the same as the Tauc optical bandgap of our *i*-layer material: 1.74 ± 0.02 eV Thus, the mobility gap is about the same as the optical gap.

This conclusion is in contradiction with the conclusion of Wronski *et al.* [150], who concluded that the mobility gap must be about 0.16 eV higher than the optical gap. This value of the mobility gap was determined by internal photoemission experiments by which the distance between the Fermi level in a metal and the extended conduction and valence band states in *a*-Si:H has been determined. In this work we have shown that the exact value of the mobility gap is only relevant for the temperature dependence of the device characteristics, and therefore the mobility gap must be determined from these characteristics.

6.3 Stability of back contacts

In experimental studies of amorphous silicon material and solar cells the properties of contacts to a device or test structure must be well understood and stable. Especially, degradation experiments in which cells are repeatedly measured, subjected to stressing conditions and annealed, impose strong demands on the quality of the back contact. When carrying out such a sequence degradation and annealing steps to study the Staebler-Wronski effect in solar cells eventual changes of contact properties must be avoided; otherwise, it is not clear what is measured: *a*-Si:H material degradation or changing contact properties. In this section the stability of several metal back contacts for *a*-Si:H solar cells is discussed. We have thermally annealed amorphous silicon/metal structures and measured the reflectivity of these structures.

To obtain useful experimental data about the degradation of material or cell properties due to the Staebler-Wronski effect an eventual influence of changing contact properties must be excluded.

In a discussion of the stability of back contacts we can consider the stability of (1) the mechanical properties, (2) the electrical contact properties, and (3) the optical properties. The back contacts of solar cells to be used for research are mechanically stable if they can withstand the normal handling required by the experiments. More specifically, the metal contact must not be damaged by repeated contacting with measurement probes. Especially in experiments with many individual measurements (such as degradation experiments) this property is important.

A back contact is considered electrically and optically stable if the electrical and optical properties do not alter during annealing steps or aging. A change of those properties can for instance be caused by a changing composition of layers forming the amorphous silicon/metal interface, by the physical formation of an intermediate interface layer, or by chemical changes of one of the materials, for instance by oxidation.

Our main interest is in stable contacts for degradation experiments, in which thermal annealing steps are applied. In the present discussion we concentrate on the stability of mechanical and optical properties of back contacts made of the following materials:

Silver In terms of reflectivity this is the preferred material. However, the mechanical stability is poor: it requires cautious handling to prevent physical damage by measurement probes. These inferior properties are caused by the relatively bad adhesion to *a*-Si:H and the relative softness of the material. Further, changes of unprotected surface of silver contacts on *a*-Si:H structures is always observed: the silver is covered by a brown film after some time of exposure to air. It is not known if the oxidation processes that bring about this changes at the unprotected surface also occur at the silver/*a*-Si:H interface, and if it influences the electrical and optical properties of the contact.

Aluminium This material is worse than silver if the reflectivity is considered, but better in terms of mechanical stability. It does not have the staining problems of silver.

Silver covered by Aluminium This contacting scheme is introduced to combine the advantages of both metals: a highly reflective silver layer is deposited directly on the *a*-Si:H, which is covered by an aluminium layer to improve the mechanical properties and prevent oxidation processes at the surface caused by exposure to the atmosphere.

Sample preparation

Phosphorus doped *a*-Si:H layers of appr. 200 nm thickness are deposited on Corning 1737 glass substrates. Depositions are carried out at DIMES in the AMOR amorphous silicon PECVD deposition system with standard process settings. Prior to metallisation the samples are dipped in a buffered-HF solution to remove the native oxide layer. This step is to exclude possible effects of a silicon oxide interface layer on the properties of the *a*-Si:H/metal interface. The metal contacts are deposited by evaporation. For aluminium deposition electron beam

evaporation is used, for silver thermal evaporation. Bi-layer Ag/Al contacts are deposited without breaking the vacuum of the reactor. The thicknesses of the metal layers that were used are: Al: 500 nm, Ag: 250 nm, and Ag/Al: 100 nm (Ag)/200 nm(Al).

Experimental

The samples with different metals are measured before and during a sequence of thermal anneal treatments. During this experiment changes of the optical reflection spectra due to the heat treatment are monitored.

The samples are annealed on a hot plate at 150 °C in vacuum. During annealing the samples are covered by a metal cap to avoid radiative heat loss that would result in a poorly defined temperature. At different times during the anneal the sample was transferred from the hot plate oven to the reflection-transmission (RT) measurement setup.

The RT setup of the ECTM group at DIMES consists of a tungsten halogen lamp as a light source, a double-grating monochromator, several filters and optics, a beam splitter and two photodetectors for the measurement of the transmitted and reflected light beam. The setup is computer controlled. The system is calibrated by measuring the RT spectrum of a piece of Corning 7059 glass. The different measurements were carried at approximately the same position of the sample.

Results and discussion

In Fig. 6.11 the reflectivity spectra of the different samples after various times of annealing is shown. The discrete steps are due to imprefections of the RT measurement setup; since these are highly reproducible the do not introduce errors in the shown reflectivity changes if they are considered as *relative* changes. The top graph shows that the optical properties of silver back contacts are stable for temperature treatments at 150 °C. Even after the longest anneal time (90 minutes) there is no change in the reflectivity. This result shows that the optical properties of silver back contacts are stable. This type of contact withstands a thermal anneal at 150 °C for 1.5 hours without any change in its high optical reflectivity.

The maximum reflectivity values in the near infrared region are very high and stable. Therefore, we think the proposed reduced reflectivity due to intermixing of Ag and Si at the semiconductor/metal interface [7,40,124,132] does not occur in our samples. Moreover, the extremely low solid solubility of Ag in Al [51] makes the reduction reflective properities due to the formation of an 'interfacial alloy layer' between these metals very unlikely.

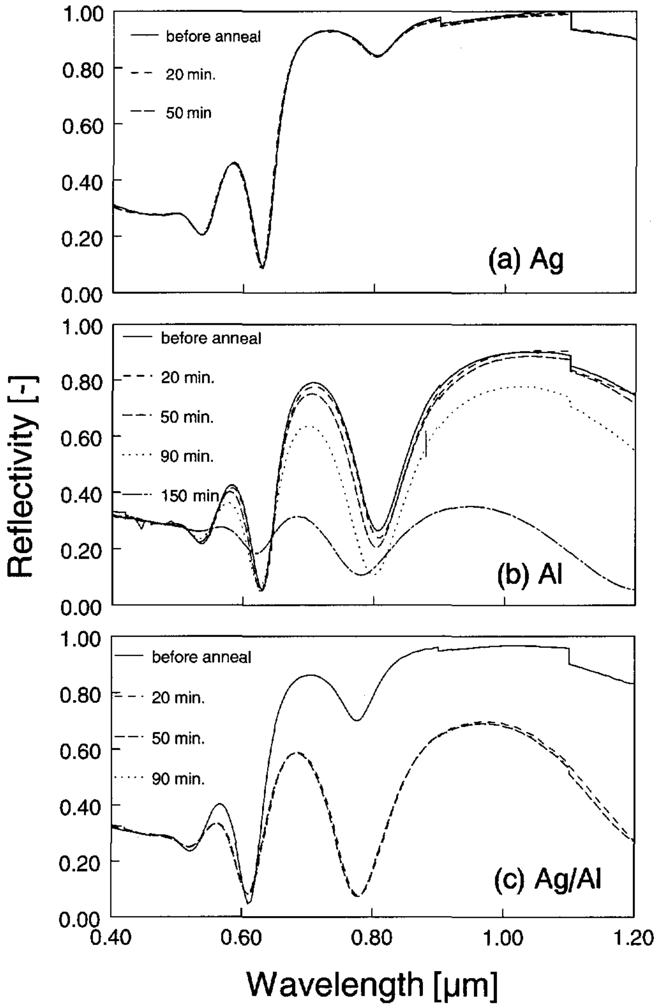

Figure 6.11: Reflectivity degradation of Glass/*a*-Si:H/metal structures caused by thermal annealing at 150 °C. (a) Silver, (b) Aluminium, and (c) Silver/aluminium bi-layer.

The middle graph shows the influence of annealing on the reflectivity of an aluminium back contact. Here, a strong deterioration of the reflectivity after an annealing of 2.5 hours is clearly visibly. Thus we conclude that the reflective properties of an a-Si:H/Al interface are sensitive to heat treatments. Thermal degradation effects of this interface in a temperature range of 150–300 °C has been reported before. For example Haque *et al.* [52,53] reported changes in electrical characteristics of aluminium covered single n-type a-Si:H layers and *pin* devices at temperatures as low as 150 °C. For temperatures higher than 170 °C Si crystal formation is clearly observed at the a-Si:H/Al interface. They concluded that the Al acts as a catalyst for the crystallisation of a-Si:H by solid phase reactions. Like the findings of Morris *et al.* [83], our result shows that also the optical properties of the a-Si:H/Al interface alter due to annealing at these (relatively) low temperatures.

The fastest change in optical properties by thermal anneallling is shown in the bottom graph, which depicts the results for the Ag/Al bi-layer contact scheme. Already after the shortest anneal time (20 minutes) the reflectivity has dropped strongly and does not change anymore with further annealing. The initial reflectivity is high due to the excellent reflection properties of silver. The deterioration of the reflectivity is ascribed to the formation of an AgAl-alloy. The phase diagram of AgAl systems [51] shows that alloying of aluminium and silver occurs already at temperatures well below 200 °C. Hirasaka *et al.* [55] have also reported alloy formation the Ag/Al system, but did not find the bad reflectivity of the degraded a-Si:H/AgAl interface. They have shown that the reflectivity of the AgAl alloy in air is still very high.

The influence of back contact reflectivity degradation on the solar cell performance is most obvious in the quantum efficiency spectra. Figure 6.12 shows an external quantum efficiency of a a-Si:H *pin* cell with a Ag/Al bi-layer back contact. The same cell was measured before and after an annealing step of 2h15m at 150 °C. In the red part of the spectrum the decrease of the quantum efficiency due to annealing is clearly visible. In this part of the spectrum the reflectivity of the back contacts is especially important, because the light is not completely absorbed in the a-Si:H and it partly reaches the back interface of the cell. Good reflectivity of the back contact increases the total absorption of light in this wavelength range in the solar cell. The decrease of reflectivity also influences the short-circuit current of this particular sample.

Conclusion

From this study we conclude that silver has to be applied for back contacts with good thermal stability of optical properties. However, the problem with this

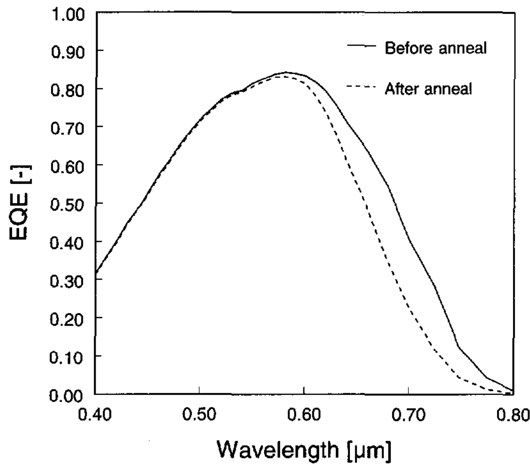

Figure 6.12: Influence of back contact reflectivity degradation on the external quantum efficiency of an *a*-Si:H cells with a bi-layer Ag/Al metal contact. EQE is measured before and after thermal anneal step.

metal is the relatively poor mechanical properties, which make it very susceptible to physical damage during experiments. Covering the silver contact by an aluminium film improves the mechanical properties, but is thermally very instable due to alloying of Al and Ag at relatively low temperatures. Pure aluminium contacts are optically not degrading as fastly as the Ag/Al bi-layer contacts but these contacts have the problem of intermixing of *a*-Si:H and Al and the metal-induced recrystallisation of *a*-Si:H. After prolonged annealing the optical properties of these contacts deteriorate strongly. It is recommended to study the behaviour of contact of sputtered Al:Si as commonly used in IC technologies.

Good mechanical and optical stability can be obtained by inserting an appropriate buffer layer between the Ag and Al layers of the bi-layer contacting system. This buffer layer must form a diffusion barrier between Ag and Al. In literature the use of Ti has been proposed [55]. As an alternative we suggest to use Cr for the intermediate layer, since this material does not tend to alloy with Ag and Al at the temperatures of interest. Our preliminary experiments have shown that the optical reflectivity properties of this proposed contact are indeed not affected by thermal annealing. However, with this approach stress in the layers appears to be a serious problem, which causes cracking of the layers or poor adhesion. The stress may be significantly reduced if the layers are deposited sequentially without breaking the vacuum of the reactor chamber. Layer thickness optimisation may also give better results, which is a topic for further research.

Chapter 7

Conclusions

The main contributions of this work to the modelling of a-Si:H solar cells are summarised.

- A theoretical study of the generation and recombination processes was carried out. This led to the following insights in the device physics of unilluminated a-Si:H *pin* diodes:
  - In a forward-biased diode the recombination occurs through the energy levels that are enclosed by the quasi-Fermi levels for trapped charge carriers.
  - The number of energy levels actively involved in the recombination process depends on the applied voltage. Consequently, the carrier lifetimes depend on the bias as well. This is directly related to the bias dependence of the quasi-Fermi levels for the trapped charge carriers. The bias dependence of the lifetimes is most pronounced near the centre of the i-layer; in this region the *average recombination rate per active recombination centre* is the largest as well.
  - In reverse-biased diodes, energy levels occupying a narrow energy band around the intrinsic trap level are most effective as thermal generation levels. The width of this band does not depend on the bias voltage; however, its spatial extent increases with increasing reverse bias, which leads to a bias dependent reverse current.
  - A simple model that only accounts for the bias-dependent carrier recombination can realistically reproduce measured dark IV-characteristics, which leads to conclusion that carrier *recombination* in the space-charge region largely determines the forward current. The experimentally observed typical value of the diode ideality factor, which

is usually between 1 and 2, results from the above-mentioned bias dependence of the carrier lifetimes. Based on the measured value of the ideality factor usually the conclusion is drawn that the forward current is both due to carrier diffusion (as in an ideal diode) and to recombination in the space-charge region; our result shows that this explanation is not correct.

- The dependences between important model parameters have been studied. The result of this theoretical work is a set of analytic expressions that describe the dependences between the mobility gap, E_g, the effective density of extended states, N_v and N_c, the (free carrier) capture cross sections of the localised gap states, σ_p and σ_n, and the density of tail states at the mobility edge, N_{v0} and N_{c0}. We have shown that two hole-related and two electron-related parameters can be chosen rather arbitrarily from a large parameter range, while the others are adapted using the dependence relations; the results of simulations using parameter sets that satisfy the dependence relations show almost no change in the steady-state IV-characteristics and internal device quantities, if a constant temperature is assumed. Hence, it is not possible to determine each of those parameters independently if only measured steady-state characteristics at a single temperature are available. However, if we consider the temperature dependence of the simulated characteristics, we observe the influence of the mobility gap value on these device characteristics. Based on this observation and other insights, we propose the use of additional experimental data to obtain independent calibrated parameters; for instance temperature-dependent as well as time-resolved and small-signal device characteristics can provide the additional data needed.

- The exact dependence of the mobility on the energy of the charge carriers in *a*-Si:H is not known. For simplicity an abrupt mobility edge is assumed in simulators for *a*-Si:H devices. We have investigated this assumption and have concluded that the exact energy dependence is not directly relevant to the device operation. Hence, the assumption of an abrupt mobility edge is justified. However, a gradually changing mobility may introduce temperature dependences of other material parameters if it is approximated by an abrupt step.

- We have carried out a numerical sensitivity study of the model parameters of an *a*-Si:H *pin* cell. This study has revealed the most important parameters for different steady-state characteristics. Further, the parameters that do not or hardly influence device characteristics are identified as well.

The results aid the selection of fitting parameters to be used for model calibration.

- Two calibration exercises using different modelling approaches for the dangling bond states resulted in good fits to measured IV-characteristics of a single-junction cell. Because both models fitted equally well we cannot draw a conclusion about which model — a Gaussian defect states distribution or a defect distribution resulting from defect-pool model — represents the defect states most realistically. The fitted parameter sets and internal device quantities are very different, which is remarkable since the IV-characteristics are very similar. (E.g. the defect concentration differ by a factor 20.) Based on additional simulations that revealed differences between the models, we suggest as additional experiments: external quantum efficiency, capacitance-voltage measurements, and light-intensity-dependent IV-measurements.

- The device physics of the tunnel-recombination junction, which is the internal junction between the subcells of a tandem cell, has been discussed. Although not all physical details are fully understood, we conclude that carrier transport from regions with relatively high free carrier concentrations towards the recombination centres must take place by tunneling. Furthermore, we have estimated a value for the space charge that must be present at both sides of the junction; for a proper functioning of the tandem cell this must be in the order of 10^{19} q/cm^3. For practical tandem cells this means that in particular the density of states in the conduction band tail of n-doped layers must be much larger than usually assumed in simulations.

- A new device modelling approach for the simulation of tandem cells is developed. It uses the trap-assisted tunneling recombination model and a field-dependent mobility enhancement model to account for the physical mechanisms in the tunnel-recombination junction. A pragmatic approach is chosen for the field-dependent mobility enhancement model, because at present the tunnel-recombination junction is not understood well enough to be modelled in full detail. Nevertheless, this approach has led to better insight in the tandem cell physics. Both models must be applied at the same time to obtain a realistic simulation of tandem cell characteristics. If only one of the models is used the characteristics are very different from the experimental data. This emphasises that not only high recombination is required for the proper functioning of a tunnel-recombination junction but also an efficient carrier transport towards the recombination centres.

- The new modelling approach for tandem cell simulation is used to study the degradation behaviour of tandem cells. We have found that the top cell of a tandem must be 'current limiting' both in the initial and in in the degraded state to give in the best efficiency in the degraded state. (By current limiting is meant that that particular subcell generates less photocurrent.) Further, these simulations nicely illustrate that the optimum thickness ratio of a tandem cell in the degraded states is different from the initial optimum; this must be taken into account when experimentally optimising tandem cells.

- The (relatively) low sheet resistance of the *n*-layer in a *pin* cell is a current conduction path giving rise to lateral leakage currents. These leakage currents usually hide the very low 'intrinsic' *a*-Si:H *pin* diode currents at reverse and low forward biases. However, after etching the part of the *n*-layer that is not covered by the metal contact dots, dark *IV*-characteristics can be measured accurately. When carrying out these measurements in reverse bias and low-forward-bias ranges one has to use very long (in the order of 60 seconds) delay times between bias-voltage adjustments and the actual measuring; the filling and emptying of the gap states is a very slow process in these bias ranges. The lateral leakage effect is also affecting *IV*-measurements with low illumination levels. Here, it causes a gradient in the *IV*-curves in the reverse bias range.

- A characterisation method is proposed to determine the conduction properties of doped layers inside *a*-Si:H single-junction and tandem solar cells. It is based on the measurement of the lateral leakage currents that are related to the conductivity of the doped layers. This technique may even be applied to determine the properties of the (most conductive) layer in the tunnel-recombination junction.

- The mobility gap of *a*-Si:H is determined by means of temperature-dependent dark *IV*-measurements and simulations of *pin* solar cells. The value of the extracted mobility gap is comparable to the optical bandgap: 1.74 $\pm$ 0.02 eV. This is much lower than the usually assumed value, which is between 1.85 and 1.90 eV.

- The influence of thermal annealing at 150 °C on the reflective properties of *a*-Si:H/metal interfaces is investigated. We concluded that the silver/*a*-Si:H interface is stable, unlike the aluminium/*a*-Si:H interface that degrades due to metal-induced recrystallisation of the amorphous silicon and silicide formation. The reflectivity of bi-layer contacts consisting of silver covered

with aluminium also decreases; this is due to alloying of silver and aluminium at these low temperatures. Insertion of a thin chromium barrier layer between the silver and the aluminium prevented alloying, but introduced mechanical stress in the metal layer.

Based on our work we do the following recommendations for future work:

- Implementation of small-signal and transient simulation modes in ASA. These simulation modes should be based on the same basic physical principles on which steady-state models are based.

- Systematic use of illumination-intensity-dependent measurements, temperature-dependent measurements, small-signal measurements and transient measurements in addition to presently-used steady-state IV-characteristics for the comprehensive calibration of the *a*-Si:H device model.

- Development of a characterisation method to determine the conductivity properties of relatively conductive, doped *a*-Si:H layers in single-junction and tandem cells, based on low illumination level IV-measurements.

- Furter development of the field-dependent mobility enhancement model to strengthen the physical basis for the present pragmatic model. For instance, this model should account for the density of localised states that may serve as intermediate points in a multi-step tunnelling process.

- Systematic sample design, sample preparation, measurements, and modelling of individual *n*-*p*-junctions that show the *same* behaviour as the tunnel-recombination junctions that are used in tandem cells. It is likely that only such a study will enable the development of real understanding of the tunnel-recombination junction physics.

- Investigation of the metastable behaviour of *a*-Si:H solar cells by accurate steady-state and transient current measurements under reverse and low forward bias conditions.

- Development of 'in-situ' (read: in-device) characterisation methods for the layers as they are present in *a*-Si:H solar cells.

- Model development and implementation of the temperature dependence of material parameters, such as the mobility gap.

- Extraction of the mobility band gap of microcrystalline material by temperature dependent measurements and simulations of μc-Si:H *pin* diodes.

Appendix A

List of symbols

Symbol	Description	Unit
d	Thickness	cm
D_n	Electron diffusion coefficient	cm^2/s
D_p	Hole diffusion coefficient	cm^2/s
e_n^0	Electron emission coefficient neutral states	s^{-1}
e_n^-	Electron emission coefficient negatively charged states	s^{-1}
e_p^0	Hole emission coefficient neutral states	s^{-1}
e_p^+	Hole emission coefficient positively charged states	s^{-1}
$\vec{E}$	Electric field	V/cm
$E^{+/0}$	+/0 transition level of dangling bond	eV
$E_{db0}^{+/0}$	Centre of Gaussian distribution of +/0 transition levels	eV
$E^{0/-}$	0/- transition level of dangling bond	eV
$E_{db0}^{0/-}$	Centre of Gaussian distribution of 0/- transition levels	eV
E	Energy	eV
E_{act}	Activation energy	eV
E_c	Conduction band (mobility) edge	eV
E_{c0}	Characteristic energy of conduction band tail	eV
E_f	Fermi level	eV
E_{fn}	Electron quasi-Fermi level	eV
E_{fp}	Hole quasi-Fermi level	eV
E_{fn_t}	Quasi-Fermi level for trapped electrons	eV

Symbol	Description	Unit
E_{fp_t}	Quasi-Fermi level for trapped holes	eV
E_g	Bandgap energy, mobility gap energy	eV
E_t	Trap energy level	eV
E_{t0}	Intrinsic trap energy level	eV
E_{vac}	Vacuum energy level	eV
E_v	Valence band (mobility) edge	eV
E_{v0}	Characteristic energy of valence band tail	eV
f	Occupation function	1
FF	Fill factor	1
F^0	Occupation probability of neutral dangling bonds	1
F^+	Occupation probability of positively charged dangling bonds	1
F^-	Occupation probability of negatively charged dangling bonds	1
G	Generation rate	$eV^{-1}cm^{-3}$
h	Planck's constant	eV s
$h\nu$	Photon energy	eV
I	Current	A
I_{mpp}	Current at maximum power point	A
I_{ph}	Photocurrent	A
I_{sc}	Short-circuit current	A
I_0	Saturation current	A
$\vec{J}_n$	Electron current density	A/cm^2
$\vec{J}_p$	Hole current density	A/cm^2
k	Boltzmann's constant	eV/K
kT	Thermal energy	eV
m^*	Effective density-of-states electron mass	g
m^*	Effective tunnelling electron mass	g
$\vec{n}$	Normal unit vector	1
n	Free electron concentration	cm^{-3}
n	Diode ideality factor	1
n	Refractive index	1
n_{eq}	Equilibrium free electron concentration	cm^{-3}
n_i	Intrinsic carrier concentration	cm^{-3}
n_{ph}	Number of photons	1
N	Density of states distribution	$eV^{-1}cm^{-3}$
N_A	Acceptor concentration	cm^{-3}

Symbol	Description	Unit
N_c	Conduction band effective density of states	cm^{-3}
N_{cbt}	Conduction band tail density of states	$eV^{-1}cm^{-3}$
N_{c0}	Conduction band tail density of states @ E_c	$eV^{-1}cm^{-3}$
N_D	Donor concentration	cm^{-3}
N_{db}	Concentration of dangling bond states	cm^{-3}
$N_{db}^{+/0}$	Distribution of dangling bond +/0 transition levels	$eV^{-1}cm^{-3}$
$N_{db}^{0/-}$	Distribution of dangling bond 0/- transition levels	$eV^{-1}cm^{-3}$
N_t	Concentration of traps	cm^{-3}
N_v	Valence band effective density of states	cm^{-3}
N_{vbt}	Valence band tail density of states	$eV^{-1}cm^{-3}$
N_{v0}	Valence band tail density of states @ E_v	$eV^{-1}cm^{-3}$
p	Free hole concentration	cm^{-3}
p_{eq}	Equilibrium free hole concentration	cm^{-3}
P_{irr}	Irradiant power	W
P_{max}	Maximum power	W
q	Unit charge	C
Q	Charge	C
R	Recombination rate	$cm^{-3}s^{-1}$
R_n^{surf}	Electron surface recombination	$cm^{-2}s^{-1}$
R_p^{surf}	Hole surface recombination	$cm^{-2}s^{-1}$
S_n	Electron surface recombination velocity	cm/s
S_p	Hole surface recombination velocity	cm/s
t	Time	s
T	Temperature	K
U	Correlation energy	eV
v_{th}	Thermal carrier velocity	cm/s
V	Voltage	V
V_a	Applied bias voltage	V
V_{mpp}	Voltage at maximum power point	V
V_{oc}	Open-circuit voltage	V
W	Thickness	cm
x	Position	cm
α	Absorption coefficient	cm^{-1}
$\Gamma_{(n,p)}$	Field-dependent factor for electrons or holes, respectively.	1
ε	Dielectric constant	F/cm

Symbol	Description	Unit
ε_r	Relative dielectric constant	1
ε_0	Dielectric constant of vacuum	F/cm
η	Power conversion efficiency	%
η_{eqe}	External quantum efficiency	1
η_r	Recombination efficiency	1
λ	Wavelength	cm or μm
μ_d	Defect chemical potential	eV
μ_n	Free electron mobility	$cm^2V^{-1}s^{-1}$
μ_p	Free hole mobility	$cm^2V^{-1}s^{-1}$
χ	Electron affinity	V
ρ	Space charge density	C/cm^3
ρ_{trap}	Space charge density of trapped charges	C/cm^3
σ	Capture cross section	cm^2
σ_d	Dark conductivity	S/cm
σ_{db}	Defect-pool width	eV
σ_{ph}	Photoconductivity	S/cm
σ_n	Electron capture cross section	cm^2
σ_n^+	Electron capture cross section of positively charged states	cm^2
σ_n^0	Electron capture cross section of neutral states	cm^2
σ_p	Hole capture cross section	cm^2
σ_p^-	Hole capture cross section of negatively charged states	cm^2
σ_p^0	Hole capture cross section of neutral states	cm^2
σ_{db}	Standard deviation of Gaussian dangling bond distribution	eV
ϕ_{bn}	Schottky barrier height for electrons	V
ψ	Electronic potential	V
ψ_{vac}	Vacuum potential	V

Appendix B

Comparison of different physical models

In this appendix we will compare the different models for charge trapping and recombination as implemented in the various device simulation models for a-Si:H based devices. An overview of the models is given in Sect. 2.2.2. The models were discussed in detail in Sect. 2.3.

B.1 Shockley-Read-Hall vs. Taylor and Simmons approximation

In many simulation models the Shockley-Read-Hall recombination statistics is simplified by the 0 K Taylor and Simmons approximation. By evaluation and comparison of the complete SRH and the TS approximation we could identify a few difficulties, which are mainly due to the assumptions and approximations made by Taylor and Simmons:

- The approach is not usable in or very close to thermal equilibrium and in general cases where thermal carrier generation plays a role. Hack and Shur [46], whose approach was adopted by many others after them, had adapted the Taylor and Simmons expressions to include thermal generation. In their modification they only reintroduce the emission coefficients to the numerator of Eq. 2.40 (by replacing np by $np - n_i^2$), but still neglect the emission coefficients in the denominator. In this way the thermal generation are grossly overrated when both electron and hole concentrations are much smaller than the intrinsic carrier concentration. This shortcoming has also been reported by Mittiga *et al.* [81] and by Block [12].

- The Taylor and Simmons approach can only be applied if the ratio between the capture cross sections of neutral and charged states σ_n^+/σ_p^0 is invariant with energy position of trap in the bandgap; this slightly reduces its general applicability. However, there is no physical argument in favour of a variation in capture cross section ratios at present.

- The 0 K approximation replaces the smooth occupation and recombination efficiency functions by staircase and block functions, respectively. Figure 2.5 showed both the real and approximated functions; the differences between those are very obvious in a region of a few kT around the trapped charge quasi-Fermi levels. Less obvious are the differences in the regions which are not enclosed by the trapped charge quasi-Fermi levels: analogous to the Maxwell-Boltzmann approximation of the Fermi-Dirac distribution the occupation function f and the recombination function η_r can be approximated by an exponential function if the energy difference with the trapped electron quasi-Fermi level (or below the trapped hole quasi-Fermi level) is more than a couple of kT. In these regions f and η_r can be approximated by an exponential function which is characterized by the thermal energy kT. However, in the 0 K approximation gives f and η_r are set to zero for these energy values. For the assessment of the accuracy of the 0 K approximation, the differences between the real and approximated functions are subjected to a critical analysis.

  The accuracy of the 0 K approximation has been discussed by different authors before, however with different conclusions. For instance, Hack and Shur [46] state that the underestimation (when applying the 0 K approximation) of the space charge trapped in tail states with an exponential DOS distribution is not significant provided that the characteristic slopes of the tail state distributions (E_{c0} and E_{v0} in Eqns. 2.13 and 2.14) are larger than kT. This conclusion is commonly cited in discussions of the accuracy of the approximation (see *e.g.* Bruns [15]). In contrast, Gray [38] concludes that with tail state characteristic energies close to kT the 0 K approach *strongly* underestimates the space charge trapped in the tail states. Block [12] also concludes that the 0 K approximation is not suited for cases where the tail states characteristic energy is close to kT. Because of this conflicting conclusions the question remains: for what density of states distributions is the approach accurate and what is the order of the errors made.

  The integrand of Eqns. 2.22-2.24 contains the product of the recombination function $\eta_r(E)$ or occupation function $f(E)$ and the density of states distribution $N(E)$. As we have shown in Sect. 2.3.2 under certain conditions

(in cases of net carrier recombination) the functions $\eta_r(E)$ and $f(E)$ are (locally) symmetric around the trapped charge quasi-Fermi levels E_{fn_t} and E_{fp_t}. Because of this symmetry the substitution of the smooth functions η_r and $f(E)$ by their 0 K approximations will give a very well approximated integral value if the density of states distribution $N(E)$ is a 'smooth' function and does not change very much in the vicinity (*i.e.* in a range of 6 kT) of the trapped charge quasi-Fermi levels. Due to their exponential distribution the tail states do *not* generally satisfy this general statement.

Due to the neglect of the exponentially decreasing parts of $\eta_r(E)$ and $f(E)$, the errors introduced by the 0 K approximation can become substantial exponentially distributed gap states. Considering for instance the conduction band tail in the energy range above E_{fn_t}, the occupation function and recombination function decrease proportionally with $\exp(-(E-E_{fn_t})/kT)$ whereas the tail states density increases proportional with $\exp(E/E_{c0})$. In a large range of E_{c0} values the product of these functions results in a non-negligible values, which are neglected in the 0 K approximation. Straightforward analysis shows that the error will be approximately a factor two for an tail state slope of $E_{c0} = 2 \cdot kT$. For smaller values of E_{c0} the error will increase, because now the largest contribution of trapped charge or recombination is due to states *above* rather than *below* the trapped electron quasi-Fermi level E_{fn_t}. In order to illustrate this Fig. B.1 shows the product $N(E) \cdot f(E)$ for different values of the conduction band tail states slope E_{c0}. The characteristics or the product $N(E) \cdot \eta_r(E)$ are analogous. In this figure the y-axis is normalised in such way that the tail states distributions corresponding to different slopes coincide, and the differences in the relative contribution of energy states to the recombination or charge trapping process can be compared directly. As shown, the product is symmetrical around E_{fn_t} in case $E_{c0} = 2kT(51.8\text{meV})$ and becomes approximately a constant value above $E = E_{fn_t}$ when $E_{c0} = kT$. For even smaller values of E_{c0} the main contribution is due to states which are closest to the mobility edge E_c.

From this analysis we can conclude that for tail slopes equal to $2kT$ the 0 K underestimation of the recombination or trapped charge is about a factor 2. For energy states distributions with slopes *less* than $2kT$ the underestimation increases *strongly* (see the inset of Fig. B.1). This result shows the incorrectness of the common assumption that the 0 K approximation is accurate for tails with $E_{c0} > kT$. Instead, a good approximation will only be obtained for states distributions with slopes $E_{c0} > 2kT$. However, for the tail slopes E_{c0} and E_{v0} usually values in the range $kT \cdots 2kT$ are used.

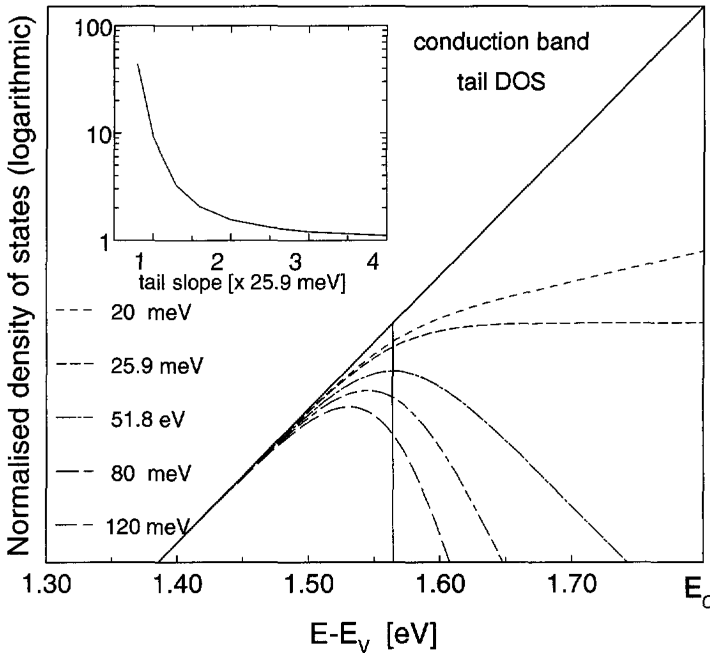

Figure B.1: Normalised exponential conduction band tail density of states N (thick line) and products $N \cdot f$ (or $N \cdot \eta_r$) (dashed lines) for different values of the tail slope parameter E_{c0}. In this specific case the trapped electron quasi-Fermi level is positioned at $E_{fn_t} = 1.56$eV. In the 0 K approximation the triangular function below $E = E_{fn_t}$ corresponds with the products $N \cdot f$ and $N \cdot \eta_r$. The inset shows the relative underestimation of space charge density and recombination rate (for this particular case) in the 0 K approximation with respect to the full SRH approach, as a function of the tail slope (in units kT).

An important implication of this analysis is that with a *single* parameter set *very different* simulation output results can be obtained for the total recombination rate and space charge density with the full SRH model and the 0 K Taylor and Simmons approximation. Consequently, device simulators will give different simulation results depending on which model is used.

These points show that there are many restrictions to the general applicability in device modelling of the Taylor and Simmons approach and its 0 K approximation.

B.2 Amphoteric dangling bonds model vs. decoupled approach

As outlined in Sect. 2.3 many simulators for *a*-Si:H devices use the decoupled model for recombination and occupation of dangling bond states. The errors introduced by this approach instead of the physically correct amphoteric model have been discussed before by Halpern [49] and Suntharalingam *et al.* [129]. In both papers assumptions *c.q.* intuitive reasoning is applied to assess the accuracy of the decoupled approach as an approximation for the amphoteric model. Therefore, these papers do not provide a satisfactory answer to the question of accuracy of the decoupled approach. In this section the errors of the decoupled approach with respect to the amphoteric dangling bond model are studied numerically. In this way there is no need to make a-priori assumptions and simplifications in order to reduce the complexity of the model equations. By considering different choices of parameters good insight into the differences between both approaches is obtained.

We define the *net occupation function* f of amphoteric dangling bond states as the (average) number of electrons per two-electron level: $f = F^0 + 2F^-$. Here, F^0 and F^- are the probabilities that the level is occupied by one and two electrons, respectively. In the decoupled approach the net occupation is the sum of the occupation f^d of a donor-like level at $E^{+/0} - kT\ln(2)$ and the occupation f^a of an acceptor-like level at $E^{0/-} + kT\ln(2)$, hence $f = f^d + f^a$. The difference between the net occupation functions of the two cases equals the absolute error made by the decoupled approach. Using Eqns. 2.29, 2.53, 2.54 and 2.55 the following expression for the *absolute* error Δf in the occupation function due to use of the decoupled approach is obtained:

$$\Delta f = \frac{N^0N^+ - P^0P^-}{N^+P^- + P^0P^- + N^+N^0} - \frac{N^0N^+ - P^0P^-}{P^0N^0 + N^+P^- + P^0P^- + N^+N^0} \tag{B.1}$$

This equation allows the exact evaluation of the error for arbitrary combinations of parameter values.

Similarly, an exact expression for the error $\Delta\eta_r$ in the recombination efficiency is obtained:

$$\Delta\eta_r = \frac{R^t - R^a}{R^a} = \frac{\sigma_n^+\sigma_p^0 N^0N^+(N^0 + P^-) + \sigma_n^0\sigma_p^- P^0P^-(P^0 + N^+)}{(\sigma_n^+\sigma_p^0 P^- + \sigma_n^0\sigma_p^+ N^+)\cdot(P^0N^0 + N^+P^- + P^0P^- + N^+N^0)} \tag{B.2}$$

Here, R^a is the recombination rate computed with the amphoteric model. R^t in the

PARAMETER CHANGES PER COLUMN

Quasi Fermi level	unit	p-type	intrinsic	n-type
$E_c - E_{fn}$	eV	1.00	0.60	0.30
$E_{fp} - E_v$	eV	0.30	0.60	1.00

PARAMETER CHANGES PER ROW

Row	σ_p^-	σ_p^0	σ_n^+	σ_n^0
I	1.0	1.0	1.0	1.0
II	1.0	0.1	1.0	0.1
III	1.0	0.1	1.0	1.0
IV	0.1	0.1	1.0	0.1
V	0.1	0.1	1.0	1.0

Table B.1: Parameters used for the graphs in Fig. B.2. The unit of the capture cross sections is: 10^{-14} cm^{-2}. Parameters not occurring in this table have the same values as in Table 2.5.

recombination through a pair of an acceptor-like and a donor-like single-electron state in the decoupled approach. For $\Delta\eta_r$ the *relative* error is chosen, because the large range of values that η_r can adopt.

The errors in occupation and recombination of dangling bonds due to the use of the decoupled approach are determined by analysing the behaviour of Eqns. B.1 and B.2. The influence of the parameters (free electron and hole concentrations, capture cross sections and correlation energies) in many different combinations has been studied. The typical behaviour of the errors Δf and $\Delta\eta_r$ is illustrated in Fig. B.2. In the graphs Eqns. B.1 and B.2 are plotted as a function of energy of the $E^{+/0}$ transition level of the dangling bond. In this figure only cases in which *recombination* occurs are considered. Each graph corresponds to a different combination of parameters. Between the different columns only the free electron and hole concentrations are varied: from the left to the right the columns correspond with an p-type case ($p \gg n$), an intrinsic case ($p \approx n$) and n-type case ($n \gg p$). In each of the five rows a different combination of the capture cross sections is applied. In the graphs of top row all capture cross sections are set to the same value. In this case the recombination efficiency using the decoupled approach is twice that of the amphoteric approach, which means that the error is 100%. The second row depicts the error in case that *both* capture cross sections of the *neutral* states are set to a *ten times lower* value than in the previous case. Now, the error $\Delta\eta_r$ is reduced to 10%. The observed trend, that the error equals the ratio of the capture cross section of neutral and charged states, has been con-

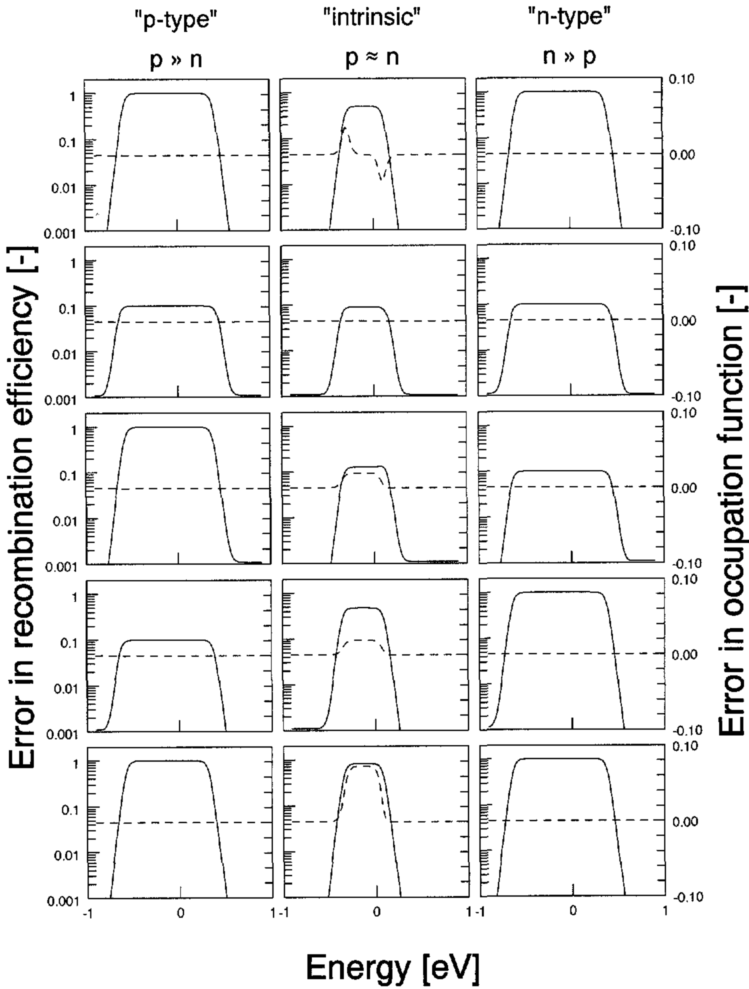

Figure B.2: Errors introduced by use of the decoupled approach instead of the amphoteric model for the dangling bond states. The full lines represent the relative error $\Delta\eta_r$ in the recombination efficiency (left y axis); the dashed lines represent the absolute error Δf in the occupation function (right y axis). The 3 columns correspond with different concentrations of free carriers ($p \gg n$, $p \approx n$ and $n \gg p$), and each row corresponds with a different set of capture cross sections. The parameters are listed in Table B.1. The x-axes correspond with the energy level of the $E^{+/0}$ transition of an amphoteric state and zero coincides with midgap.

firmed by further experiments. Unlike the first two rows, where $\sigma_n^+ = \sigma_p^-$ and $\frac{\sigma_n^0}{\sigma_n^+} = \frac{\sigma_p^0}{\sigma_p^-}$, the capture cross sections for the graphs of row three to five were varied more randomly. From these graphs we draw the conclusion that the error in recombination efficiency equals the ratio of capture cross sections of the *minority* carriers. For instance, in row four the ratios are $\frac{\sigma_n^0}{\sigma_n^+} = 0.1$ and $\frac{\sigma_p^0}{\sigma_p^-} = 1$, which results in an error of 10% for a p-type case and 100% for an n-type case. In the case of near intrinsic material the error is between 10% and 100%.

Also shown in the graphs of Fig. B.2 are the errors Δf in the occupation function (dashed lines). We can conclude from the figure that the error gets significant values only in the near intrinsic cases. Depending on the values of the capture cross sections the errors can be in the order of 10%. This is in contradiction with the findings of Halpern [49] and Suntharalingam *et al.* [129], who concluded that the decoupled approach approximates the amphoteric occupation function very well, if the correlation energy is positive and larger than a few kT.

In cases of thermal generation (not shown) the errors of the decoupled approach with respect to the amphoteric approach are in general very small. Therefore, for these cases the decoupled approach is an excellent approximation. On the other hand, when the correlation energy U is set to a negative value the errors in both the recombination efficiency and the occupation will become very large; in this case the decoupled approach is not usable, neither for generation nor for recombination conditions.

From this study we draw the conclusion that the amphoteric model, which models the behaviour of the dangling bond states correctly, can be approximated well by a pair of a donor-like and an acceptor-like state under the condition (1) that the capture cross sections of the neutral states are much smaller than those of the charged states and (2) that the correlation energy U is positive and considerably larger than the thermal energy kT. If the capture cross sections for neutral and charged states come in the same order of magnitude the overestimation of the decoupled approach may become as high as 100% or even higher for more unfavourable ratios. This can be explained as follows: assume a situation in which the concentration of one type of carriers — *e.g.* the electrons — is much higher than the other. In this case the capture rate of minorities (here the holes) controls the net recombination rate. An amphoteric dangling bond state that contributes to the recombination process, is most probably in a twofold charge state and can capture holes. In the decoupled approach there is a pair of states: a negatively charged acceptor-like state *and* a neutral donor-like state, which both can capture minority carriers. If now the hole capture cross section of the negative state is much larger than the cross section of the neutral state, the recombination rate due

to the neutral donor-like state can be neglected in comparison with the rate due to the negative acceptor-like state. Hence, the recombination rates of the amphoteric model and the decoupled model are approximately equal. On the other hand, if the ratio of the hole cross sections is close to one, the recombination rate will be overestimated by a factor two. Thus, the ratio of the minority carrier capture cross section of charged and neutral states determines the overestimation of the recombination rate. Further, we find — in contradiction with previous publications — that in some cases the errors in the occupation function can become in the order of 10% when using the decoupled approach as approximation for the amphoteric model.

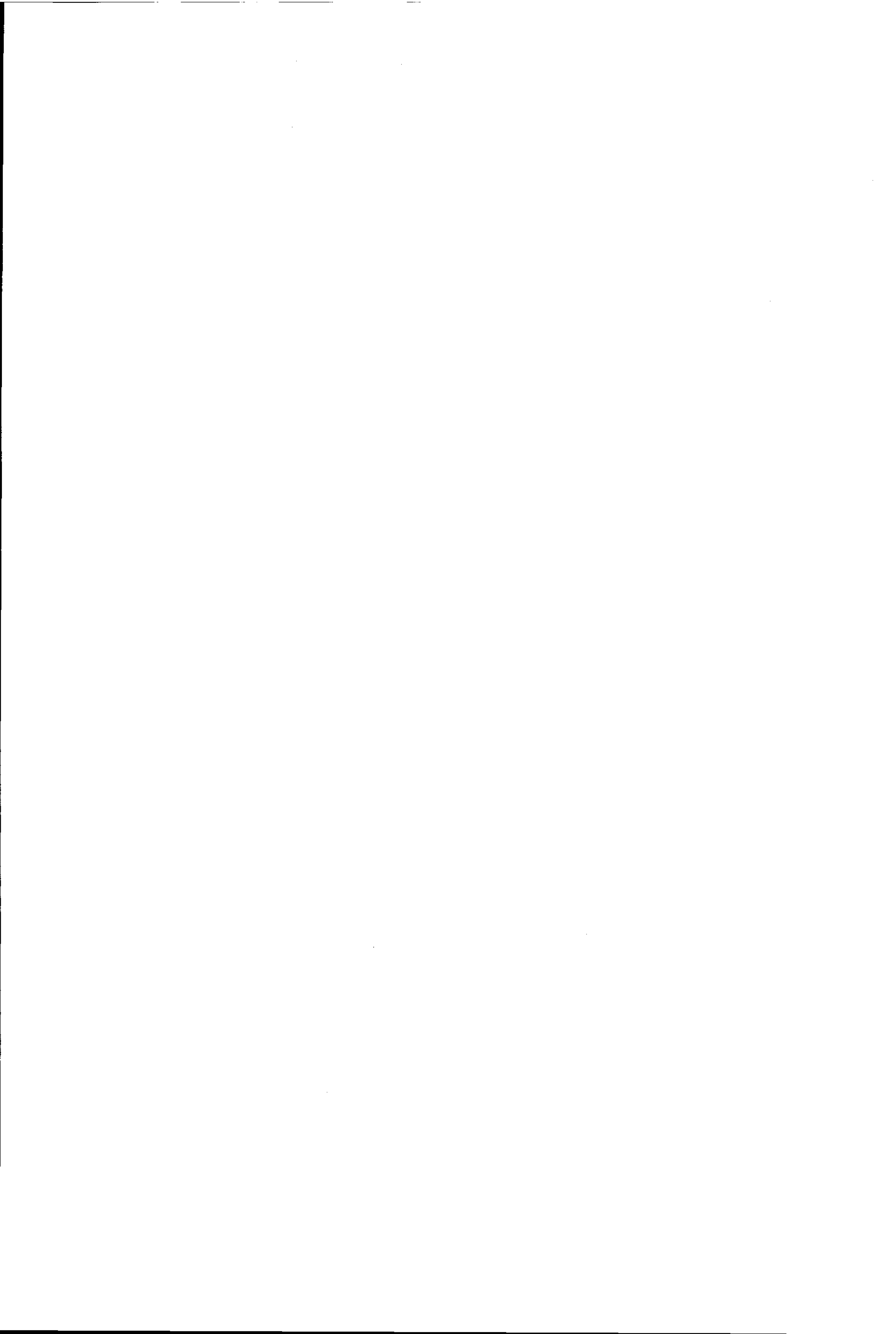

References

[1] Antoniadis, H., R.I. Devlen, S. Esipov, and S. Guha. High-field electron drift in *a*-Si:H. In *ICAS-14*, 1991.

[2] Arch, J.K., F.A. Rubinelli, J.Y. Hou, and S.J. Fonash. First principles computer model showing the effect of p-layer thickness and front contact barrier height on the performance of a-Si:H p-i-n solar cells. In *Proc. of the 21th IEEE PVSC*, pp. 1636–1641, 1990.

[3] Arya, R.R., L. Yang, M. Bennett, J. Newton, Y.M. Li, B. Fieselmann, L.F. Chen, K. Rajan, G. Wood, C. Poplawski, and A. Wilczynski. Status, progress and challenges in high performance, stable amorphous silicon alloy based triple junction modules. In *Proc. of the 23th IEEE PVSC*, pp. 790–794, 1993.

[4] Bae, S. Personal communication, 1994.

[5] Bae, S. and S.J. Fonash. Examination of optimized structures for a-Si:H based triple junction solar cells. In *Proc. of the 1st WCPEC*, pp. 484–487, 1994.

[6] Banerjee, A., E. Chen, R. Clough, T. Glatfelter, S. Guha, G. Hammond, K. Hoffman, M. Hopson, N. Jackett, M. Lycette, J. Noch, T. Palmer, K. Parker, I. Rosenstein, D. Wolf, X. Xu, J. Yang, and K. Younan. 10.8% efficient one-square-foot-area multijunction amorphous silicon alloy photovoltaic module. In *Proc. of the 23th IEEE PVSC*, pp. 795–802, 1993.

[7] Banerjee, A. and S. Guha. Study of back reflectors for amorphous silicon alloy solar cell application. *J. Appl. Phys.*, 69(2), pp. 1030–1034, 1991.

[8] Banerjee, A., J. Yang, T. Glatfelter, K. Hoffman, and S. Guha. Experimental study of p layers in "tunnel" junctions for high efficiency amorphous sil-

icon alloy multijunction solar cells and modules. *Appl. Phys. Lett.*, 64(12), pp. 1517–1519, 1994.

[9] Beneking, C., B. Rech, T. Eickhoff, Y.G. Michael, N. Schultz, and H. Wagner. Preparation and light stability of a-Si/a-Si stacked solar cells. In Hill, R., W. Palz, and P. Helm, editors, *Proc. of the 12th EPVSEC*, pp. 683–686, Amsterdam, the Netherlands, 1994.

[10] Bennett, M.S. and K. Rajan. Stability of multijunction *a*-Si:H-based solar cells. *J. Appl. Phys.*, 67(9), pp. 4161–4166, 1990.

[11] Block, M., D. Bonnet, and F. Zetzsche. Modeling of multilayer amorphous thin film silicon-gemanium single and tandem solar cells. In *Proc. of the 22th IEEE PVSC*, pp. 1275–1280, 1991.

[12] Block, Meinolf. *Modellierung von Dünnschichtsolarzellen aus amorphem Silizium.* PhD thesis, Fachbereich Physik der Phillips-Universität Marburg, 1993.

[13] Böer, K.W. *Survey of Semiconductor Physics, Electrons and Other Particles in Bulk Semiconductors.* Van Nostrand Reinhold, New York, 1990.

[14] Brown, G.W. and B.W. Lindsay. The numerical solution of poissons's equation for two-dimensional semiconductor devices. *Solid State Electronics*, 19, pp. 991–992, 1976.

[15] Bruns, J. *Die Entwicklung eines numerischen Simulationsmodells für a-Si:H Solarzellen und seine Anwendung zur Analyse experimentell ermittelter Spektralcharakteristiken.* PhD thesis, Fachbereich Elektrotechnik der Technische Universität Berlin, 1993.

[16] Bruns, J., M. Choudhury, and H.G. Wagemann. The influence of working conditions on the current matching in a-Si:H stacked solar cells. In *Proc. of the 13th EPVSEC*, pp. 230–233, Nice, France, 1995.

[17] Caputo, D., U. Forghieri, and F. Palma. Numerical analysis of differential capacitance in a-Si:H Solar cells: monitoring of light-soaking experiment. In *Proc. of the 13th EPVSEC*, pp. 187–190, Nice, France, 1995.

[18] Carlson, D.E. Amorphous silicon solar cells. *IEEE Transactions of Electron Devices*, ED-24, pp. 449–453, 1977.

[19] Carlson, D.E., R.R. Arya, M. Bennett, L.-F. Chen, K. Jansen, Y.-M. Li, J. Newton, K. Rajan, R. Romero, D. Talenti, E. Twesme, F. Willing, and L. Yang. Commercialization of multijunction amorphous silicon modules. In *Proc. of the 25th IEEE PVSC*, pp. 1023–1028, 1996.

[20] Carlson, D.E. and C.R. Wronski. Amorphous silicon solar cell. *Appl. Phys. Lett.*, 28(11), pp. 671–673, 1976.

[21] Carlson, D.E., C.R. Wronski, J.I. Pankove, P.J. Zanzucchi, and D.L. Staebler. Properties of amorphous silicon and a-Si solar cells. *RCA Rev.*, 38, pp. 211–225, 1977.

[22] Chatterjee, P. Origin of the modulated photocurrent in the presence of bias light in quantum efficiency measurements. *J. Appl. Phys.*, 75(2), pp. 1093–1097, 1994.

[23] Chatterjee, P. Photovoltaic performance of a-Si:H homojunction p-i-n solar cells: A computer simulation study. *J. Appl. Phys.*, 76(2), pp. 1301–1313, 1994.

[24] Chatterjee, P. A computer analysis of the effect of a wide-band-gap emitter layer on the performance of a-Si:H-based heterojunction solar cells. *J. Appl. Phys.*, 79(9), pp. 7339–7347, 1996.

[25] Chatterjie, P., P.J. McElheny, and S.J. Fonash. Influence of illumination conditions on the spectral response of hydrogenated amorphous silicon Schottky barrier structures. *J. Appl. Phys.*, 67(8), pp. 3803–3809, 1990.

[26] Chittick, R.C., J.H. Alexander, and H.F. Sterling. The preparation and properties of amorphous silicon. *J. Electrochem. Soc.*, 116, pp. 77–81, 1969.

[27] Cohen, M.H., H. Fritsche, and S.R. Ovshinsky. Simple band model for amorphous semiconducting alloys. *Phys. Rev. Lett.*, 22(20), pp. 1065–1068, 1969.

[28] Deane, S.C. and M.J. Powell. Defect-pool model parameters for amorphous silicon derived from field-effect measurements. *J. of Non-Cryst. Solids*, 164-166, pp. 323–326, 1993.

[29] Delahoy, A.E., J. Kalina, C. Kothandaraman, and T. Tonon. Advanced technology amorphous silicon photovoltaic modules. In Palz, W., G.T. Wrixon, and P. Helm, editors, *Proc. of the 9th EPVSEC*, pp. 599–603, Freiburg, FRG, 1989.

[30] Dutta, J., Z.Y. Wu, E. Turlot, E. Cornil, J.P.M. Schmitt, and A. Ricaud. Stability and reliability of amorphous silicon pin/pin encapsulated modules. In Guimarães, L., W. Palz, C. De Reyff, H. Kiess, and P. Helm, editors, *Proc. of the 11th EPVSEC*, pp. 545–548, Montreux, Switzerland, 1992.

[31] Edwards, D.F. Silicon. In Palik, E.D., editor, *Handbook of Optical Constants of Solids*, pp. 547–569. Academic Press, Inc., 1985.

[32] EnergieNed,. De energiedistributiesector. Internet page: http://www.energiened.nl, 1997.

[33] Fantoni, A., M. Vieira, and R. Martins. Spatial microscopic/macroscopic control and modelling of the p.i.n. devices stability. In Razeghi, M., Y.-S. Park, and G.L. Witt, editors, *Optoelectronic Integrated Circuit Materials, Physics and Devices*, volume 2397, pp. 695–702, 1995.

[34] Fujikake, S., S. Saito, H. Sato, T. Yoshida, Y. Ichikawa, and H. Sakai. 30x40 cm^2 double-junction tandem cells with ZnO coated SnO_2 transparent electrodes. *Solar Energy Materials and Solar Cells*, 23, pp. 289–296, 1991.

[35] Furlan, J., S. Amon, P. Popović, and F. Smole. Internal opto-electric properties of p-i-n a-Si:H solar cell on grooved TCO texture. In *Proc. of the 1st WCPEC*, pp. 658–661, 1994.

[36] Furlan, J., I. Skubic, F. Smole, P. Popovič, and M. Topic. Small-signal capacitance and conductance of biased a-Si structures. *J. Appl. Phys.*, 80(7), pp. 3854–3859, 1996.

[37] Furlan, J., F. Smole, and P. Popović. Effective densities of states in conduction and valence bands in a-Si. In Schiff, E.A., M.J. Thompson, A. Madan, K. Tanaka, and P.G. LeComber, editors, *Amorphous Silicon Technology — 1993*, volume 297 of *Materials research society symposium proceedings*, pp. 363–368, 1993.

[38] Gray, J.L. A computer model for the simulation of thin-film silicon-hydrogen alloy solar cells. *IEEE Transactions of Electron Devices*, 36(5), pp. 906–912, 1989.

[39] Guha, S. Amorphous silicon alloy solar cells and modules — opportunities and challenges. In *Proc. of the 25th IEEE PVSC*, pp. 1017–1022, 1996.

[40] Guha, S., J. Yang, A. Banerjee, T. Glatfelter, K. Hoffman, S.R. Ovshinsky, M. Izu, H.C. Ovshinsky, and X. Deng. Amorphous silicon alloy photovoltaic technology – from R&D to production. In Schiff, E.A., M. Hack, A. Madan, M. Powell, and A. Matsuda, editors, *Amorphous Silicon Technology — 1994*, volume 336 of *Materials research society symposium proceedings*, pp. 645–655, 1994.

[41] Guha, S., J. Yang, P. Nath, and M. Hack. Enhancement of open circuit voltage in high efficiency amorphous silicon alloy solar cells. *Appl. Phys. Lett.*, 49(4), pp. 218–219, 1986.

[42] Gummel, H.K. A self-consistent iterative scheme for one-dimensional steady state transistor calculations. *IEEE Transactions of Electron Devices*, ED-11, pp. 455–465, 1964.

[43] Hack, M. and M. Shur. Computer simulation of amorphous silicon-based alloy p-i-n solar cells. *IEEE Electron Device Letters*, EDL-4(5), pp. 140–143, 1983.

[44] Hack, M. and M. Shur. Theoretical modeling of amorphous silicon-based alloy *p-i-n* solar cells. *J. Appl. Phys.*, 54(10), pp. 5858–5863, 1983.

[45] Hack, M. and M. Shur. The role of boron profiling in enhancing the performance of amorphous silicon-based alloy p-i-n solar cells. *IEEE Transactions of Electron Devices*, ED-31(5), pp. 539–542, 1984.

[46] Hack, M. and M. Shur. Physics of amorphous silicon alloy p-i-n solar cells. *J. Appl. Phys.*, 58(2), pp. 997–1020, 1985.

[47] Hall, R.N. Germanium rectifier characteristics. *Physical Review*, 83, page 228, 1951.

[48] Hall, R.N. Electron-hole recombination in germanium. *Physical Review*, 87, page 387, 1952.

[49] Halpern, V. The statistics of recombination via dangling bonds in amorphous silicon. *Phil. Mag.* **B**, 54(6), pp. 473–482, 1986.

[50] Hamakawa, Y., H. Okamoto, and Y. Nitta. A new type of amorphous silicon photovoltaic cell generating more than 2.0 V. *Appl. Phys. Lett.*, 35(2), pp. 187–189, 1979.

[51] Hansen, M. and K. Anderko. *Constitution of Binary Alloys*. McGraw-Hill Book Company, Inc., New York, 1958.

[52] Haque, M. Shahidul, H.A. Naseem, and W.D. Brown. Interaction of aluminum with hydrogenated amorphous silicon at low temperatures. *J. Appl. Phys.*, 75(8), pp. 3928–3935, 1994.

[53] Haque, M.S., H.A. Naseem, and W.D. Brown. Degradation and failure mechanisms of a-Si:H solar cells with alumium contacts. In *Proc. of the 1st WCPEC*, pp. 642–645, 1994.

[54] Hegedus, S.S., F. Kampas, and J. Xi. Current transport in amorphous silicon n/p junctions and their application as "tunnel" junctions in tandem solar cells. *Appl. Phys. Lett.*, 67(6), pp. 813–815, 1995.

[55] Hirasaka, K., K. Suzuki, and M. Hashiba dna T. Yamashina. Characterization of electrode materials adopted for a-Si:H solar cells by means of auger electron spectroscopy. *Solar Energy Materials*, 19, pp. 199–210, 1989.

[56] Hishikawa, Y., K. Ninomiya, E. Maruyama, S. Kuroda, A. Terakawa, and K. Sayama. Approaches for stable multi-junction a-Si solar cells. In *Proc. of the 1st WCPEC*, pp. 386–393, 1994.

[57] Hou, J., J. Xi, F. Kampas, S. Bae, and S.J. Fonash. Non-local recombination in "tunnel junction" of multijunction amorphous Si alloy solar cells. In Schiff, E.A., M. Hack, A. Madan, M. Powell, and A. Matsuda, editors, *Amorphous Silicon Technology — 1994*, volume 336 of *Materials research society symposium proceedings*, pp. 717–722, 1994.

[58] Hou, J.Y., J.K. Arch, S.J. Fonash, S. Wiedeman, and M. Bennett. An examination of the "tunnel junctions" in triple junction a-Si:H based solar cells: modeling and effects on performance. In *Proc. of the 22th IEEE PVSC*, pp. 1260–1264, 1991.

[59] Hulstrom, R., R. Bird, and C. Riordan. Spectral solar irradiance data sets for selected terrestrial conditions. *Solar Cells*, 15, pp. 365–391, 1985.

[60] Hurkx, G.A.M., D.B.M. Klaassen, and M.P.G. Knuvers. A new recombination model for device simulation including tunneling. *IEEE Transactions of Electron Devices*, 39(2), pp. 331–338, 1992.

[61] Jongerden, G.J. Doorbraak: roll-to-roll productie van flexibele zonnecellen. Presentation at NOZ-PV Uitvoerders Bijeenkomst, Utrecht, The Netherlands, Oct. 29 1997.

[62] Juška, G., J. Kočka, K. Arlauskas, and G. Jukonis. Electron drift mobility in *a*-Si:H under extremely high electric field. *Solid State Comm.*, 75, pp. 531–533, 1990.

[63] Kida, H., M. Itoh, S. Fukazawa, T. Ohta, and K. Yamamoto. A device modeling of amorphous silicon based tandem solar cells. *Jap. J. Appl. Phys.*, 28(9), pp. L1499–L1501, 1989.

[64] Kleijnen, J.P.C. Sensitivity analysis and related analyses: A review of some statistical techniques. *J. of Statistical Computation and Simulation*, 57, pp. 111–142, 1997.

[65] Knoesen, D., R.E.I. Schropp, and W.F. van der Weg. Structural defects in thin film amorphous silicon films deposited on textured TCO material. In Hack, M., E.A. Schiff, A. Madan, M. Powell, and A. Matsuda, editors, *Amorphous Silicon Technology — 1995*, volume 377 of *Materials research society symposium proceedings*, pp. 597–602, 1995.

[66] Kolter, M., C. Beneking, D. Pavlov, T. Eickhoff, P. Hapke, S. Frohnhoff, H. Münder, and H. Wagner. Highly conductive microcrystalline n-layers for amorphous silicon stacked solar cells: preparation, properties, and device application. In *Proc. of the 23th IEEE PVSC*, pp. 1031–1036, 1993.

[67] Kreisel, Andreas. Numerische Modellierung der Degradation von Dünnschicht-Solarzellen aus amorphem Silizium. Master's thesis, Forschungszentrum Jülich, Institut für Schicht- und Ionentechnik, May 1995.

[68] Kurata, M. *Numerical Analysis for Semiconductor Devices.* Lexington Books, 1982.

[69] Kuwano, Y., T. Imai, M. Ohnishi, and S. Nakano. A horizontal cascade type amorphous Si photovoltaic cell model (integrated type amorphous Si photovoltaic cell module). In *Proc. of the 14th IEEE PVSC*, pp. 1408–1409, 1980.

[70] Landweer, G.E.N., C.H.M. van der Werf, R.W. Stok, J.W. Metselaar, and R.E.I. Schropp. The application of micro-crystalline n-type Si in amorphous silicon tandem solar cells. In Hill, R., W. Palz, and P. Helm, editors, *Proc. of the 12th EPVSEC*, pp. 1284–1287, Amsterdam, the Netherlands, 1994.

[71] Leblanc, F., J. Perrin, and J. Schmitt. Numerical modeling of the optical properties of hydrogenated amorphous-silicon-based p-i-n solar cells deposited on rough transparent conducting oxide substrates. *J. Appl. Phys.*, 75(2), pp. 1074–1087, 1994.

[72] Luft, W., H.M. Branz, V.L. Dalal, S.S. Hegedus, and E.A. Schiff. Progress in amorphous silicon pv technology: an update. In Ullal, H.S. and C. E. Witt, editors, *13th NREL Photovoltaics Program Review*, volume 353, pp. 81–100, 1996.

[73] Macleod, H.A. *Thin-file optical filters.* Hilger, London, 1969.

[74] Martins, R., A. Fantoni, and M. Vieira. Tailoring defects on amorphous silicon pin devices. *J. of Non-Cryst. Solids*, 164-166, pp. 671–674, 1993.

[75] Martins, R. and E. Fortunato. Dark current-voltage characteristics of transverse asymmetric hydrogenated amorphous silicon diodes. *J. Appl. Phys.*, 78(5), pp. 3481–3487, 1995.

[76] Martins, R., E. Fortunato, A. Bicho, and G. Lavareda. Role of the lateral leakage current on amorphous silicon solar cells. In *Proc. of the 1st WCPEC*, pp. 587–590, 1994.

[77] McElheny, P.J., J.K. Arch, and S.J. Fonash. Assessment of the surface-photovoltage diffusion-length measurement. *Appl. Phys. Lett.*, 51(20), pp. 1611–1613, 1987.

[78] McElheny, P.J., J.K. Arch, H.-S. Lin, and S.J. Fonash. Range of validity of the surface-photovoltage diffusion length measurement: A computer simulation. *J. Appl. Phys.*, 64(3), pp. 1254–1265, 1988.

[79] McElheny, P.J., P. Chatterjee, and S.J. Fonash. Collection efficiency of a-Si:H Schottky barriers: A computer study of the sensitivity to material and device parameters. *J. Appl. Phys.*, 69(11), pp. 7674–7688, 1991.

[80] Misiakos, K. and F.A. Lindholm. Analytical and numerical modeling of amorphous silicon *p-i-n* solar cells. *J. Appl. Phys.*, 64(1), pp. 383–393, 1988.

[81] Mittiga, A., P. Fiorini, M. Falconieri, and F. Evangelisti. Dark J-V characteristic of p-i-n a-Si:H solar cells. *J. Appl. Phys.*, 66(6), pp. 2667–2674, 1989.

[82] Morgado, E. Recombination at correlated dangling bonds and the effects of Fermi level position on steady-state photoconductivity in amorphous silicon. *Phil. Mag.* **B**, 63(2), pp. 529–542, 1991.

[83] Morris, J., R.R. Arya, J.G. O'Dowd, and S. Wiedeman. Absorption enhancement in hydrogenated amorphous silicon-based solar cells. *J. Appl. Phys.*, 67(2), pp. 1079–1087, 1990.

[84] Mott, N.F. and E.A. Davis. *Electronic Processes in Non-Crystalline Materials, 2nd edition.* The International Series of Monographs on Physics, ed. W. Marshall and D.H. Wilkinson. Clarendon Press, Oxford, 1979.

[85] Nebel, C.E., R.A. Street, N.M. Johnson, and C.C. Tsai. High-electric-field transport in *a*-Si:H. II. Dark conductivity. *Phys. Rev.* **B**, 46(11), pp. 6803–6814, 1992.

[86] Neudeck, G.W. and A.K. Malhotra. Field effect conductance modulation in vacuum-evaporated amorphous silicon films. *J. Appl. Phys.*, 46(1), pp. 239–246, 1975.

[87] Okamoto, H. and Y. Hamakawa. Electronic behaviors of the gap states in amorphous semiconductors. *Solid State Comm.*, 24(1), pp. 23–27, 1977.

[88] Okamoto, H., H. Kida, and Y. Hamakawa. Steady-state photoconductivity in amorphous semiconductors containing correlated defects. *Phil. Mag.* **B**, 49(3), pp. 231–247, 1984.

[89] Ostendorf, H.-C., W. Kusian, W. Krühler, and R. Schwarz. Light and current degradation of a-Si:H pin, nin and pip diodes detected with CPM. *J. of Non-Cryst. Solids*, 164–166, pp. 659–662, 1993.

[90] Ostendorf, H.-C., R. Schwarz, W. Kusian, and W. Krühler. CPM-characterization of light and current stressed a-Si:H diodes with nin, pip and pin structures. In *Proc. of the 23th IEEE PVSC*, pp. 872–877, 1993.

[91] Ouwerling, G.J.L. *Nondestuctive one- and two-dimensional doping profiling by inverse methods.* PhD thesis, Delft University of Technology, 1989.

[92] Ouwerling, G.J.L., F. van Rijs, B.F.P. Jansen, and W. Crans. Inverse Modelling with the PROFILE optimisation driver. In Crans, W., editor, *Digest NASECODE VI Software Forum, Part: Short Course on Software Tools for Process, Device and Circuit Modelling*. Boole Press, Dublin, 1989.

[93] Park, J.W., R.J. Schwartz, J.L. Gray, and G.B. Turner. A self-consistent numerical model of thin film silicon hydrogen-alloy solar cells. In *Proc. of the 20th IEEE PVSC*, pp. 55–60, 1988.

[94] Pawlikiewicz, A.H. and S. Guha. Numerical modeling of multijunction amorphous silicon based p-i-n solar cells. In *Proc. of the 20th IEEE PVSC*, pp. 251–255, 1988.

[95] Pawlikiewicz, A.H. and S. Guha. Performance comparison of triple and tandem multi-junction a-Si:H solar cells: a numerical study. *IEEE Transactions of Electron Devices*, 37(7), pp. 1758–1762, 1990.

[96] Pellaton Vaucher, N., B. Rech, D. Fischer, S. Dubail, M. Goetz, H. Keppner, C. Beneking, O. Hadjadj, V. Shklover, and A. Shah. Controlled nucleation of thin microcrystalline layers for the recombination junction in a-Si stacked cells. In *Technical digest of the int. PVSEC-9*, pp. 651–652, 1996.

[97] Popović, P., E. Bassanese, F. Smole, J. Furlan, S. Grebner, and R. Schwarz. Numerical analysis of the transient response in amorphous silicon. *Appl. Phys. Lett.*, 82(9), pp. 4504–4507, 1997.

[98] Powell, M.J. and S.C. Deane. Improved defect-pool model for charged defects in amorphous silicon. *Phys. Rev.* **B**, 48(15), pp. 10815–10827, 1993.

[99] Rath, J.K., F.A. Rubinelli, and R.E.I. Schropp. Microcrystalline n- and p-layers at the tunnel junction of a-Si:H/a-Si:H tandem cells. *J. of Non-Cryst. Solids*, 227–230, pp. 1282–1286, 1998.

[100] Rech, B. Personal communication, 1996.

[101] Rech, B. *Solarzellen aus amorphen Silizium mit hohem stabilem Wirkungsgrad. Zum Einfluß des p/i-Grenzflächenbereichs und der intrinsischen Absorberschicht.* PhD thesis, Forschungszentrum Jülich, Institut für Schicht- und Ionentechnik, 1997.

[102] Rose, Albert. *Concepts in Photoconductivity and Allied Problems*, volume 19 of *Interscience Tracts on Physics and Astronomy*. Interscience Publishers, 1963.

[103] Rubinelli, F.A., S.J. Fonash, and J.K. Arch. Computer modelling of solar cell structures. In *Proc. of the int. PVSEC-5*, pp. 811–819, 1992.

[104] Sah, C.T. and W. Shockley. Electron-hole recombination statistics in semiconductors through flaws with many charge conditions. *Physical Review*, 109(4), pp. 1103–1115, 1958.

[105] Saha, S.C. and S. Ray. Development of highly conductive n-type μc-Si:H films at low power for device applications. *J. Appl. Phys.*, 78(9), pp. 5713–5720, 1995.

[106] Sakai, H., T. Yoshida, T. Hama, and Y. Ichikawa. Effects of surface morphology of transparent electrode on the open-circuit voltage of a-Si:H solar cells. *Jap. J. Appl. Phys.*, 29(4), pp. 630–635, 1990.

[107] Sakai, Y., K. Fukuyama, M. Matsumura, Y. Nakato, and H. Tsubomura. The effect of interposing thin oxide layers on the photovoltaic properties of *a*-Si:H solar cells II Between the middle *n* and *p* layers of a tandem-type cell. *J. Appl. Phys.*, 64(1), pp. 394–398, 1988.

[108] Sawada, T., H. Tarui, N. Terada, M. Tanaka, T. Takahama, S. Tsuda, and S. Nakano. Theoretical analysis of textured thin-film solar cells and a guideline to achieving higher efficiency. In *Proc. of the 23th IEEE PVSC*, pp. 803–810, 1993.

[109] Sawada, T., N. Terada, T. Takahama, H. Tarui, M. Tanaka, S. Tsuda, and S. Nakano. Numerical approach for high-efficiency a-Si solar cells. *Solar Energy Materials and Solar Cells*, 34, pp. 367–372, 1994.

[110] Scharfetter, D.L. and H.K Gummel. Large-signal analysis of a silicon read diode oscillator. *IEEE Transactions of Electron Devices*, ED-16(1), pp. 64–77, 1969.

[111] Schropp, R.E.I. Efficiency optimization techniques for amorphous silicon solar cells. *Diffusion and Defect Data – Solid State Data B. Solid State Phenomena*, 44–46, pp. 853–862, 1995.

[112] Schropp, R.E.I., D. Leone, J. Hyvärinen, J. Skarp, T. Suntola, J.W. Metselaar, M. Zeman, D. Guillardeau, W. Loyer, and E. Fabre. Cost-effective large area integrated multijunction amorphous silicon solar cell structures (CLIMAX). In Hill, R., W. Palz, and P. Helm, editors, *Proc. of the 12th EPVSEC*, pp. 1253–1256, Amsterdam, the Netherlands, 1994.

[113] Schropp, R.E.I., J. Daey Ouwens, G.E.N. Landweer, M.B. von der Linden, and C.H.M. van der Werf. Bandgap-, dopant, and defect-graded dual-junction amorphous silicon solar cells. In Hill, R., W. Palz, and P. Helm,

editors, *Proc. of the 12th EPVSEC*, pp. 699–702, Amsterdam, the Netherlands, 1994.

[114] Schwartz, R.J., J.L. Gray, G.B. Turner, D. Kanani, and H. Ullal. Numerical modeling of p-i-n hydrogenated thin film silicon solar cells. In *Proc. of the 17th IEEE PVSC*, pp. 369–373, 1984.

[115] Selberherr, S. *Analysis and Simulation of Semiconductor Devices*. Springer-Verlag, Wien New York, 1984.

[116] Shen, D.S., R.E.I. Schropp, H. Chatham, R.E. Hollingsworth, P.K. Bhat, and J. Xi. Improving tunneling junction in amorphous silicon tandem solar cells. *Appl. Phys. Lett.*, 56(19), pp. 1871–1873, 1990.

[117] Shockley, W. and J.T. Last. Statistics of the charge distribution for a localized flaw in a semiconductor. *Physical Review*, 107(2), pp. 392–396, 1957.

[118] Shockley, W. and W.T. Read, Jr. Statistics of the recombinations of holes and electrons. *Physical Review*, 87(5), pp. 835–842, 1952.

[119] Simmons, J.G. and G.W. Taylor. Nonequilibrium steady-state statistics and associated effects for insulators and semiconductors containing an arbitrary distribution of traps. *Phys. Rev.* **B**, 4(2), pp. 502–511, 1971.

[120] Smole, F. and J. Furlan. Effects of abrupt and graded a-Si:C:H/a-Si:H interface on internal properties and external characteristics of *p-i-n a*-Si:H solar cells. *J. Appl. Phys.*, 72, pp. 5964–5969, 1992.

[121] Spear, W.E. and P.G. LeComber. Substitutional doping of amorphous silicon. *Solid State Comm.*, 17, pp. 1193–1196, 1975.

[122] Staebler, D.L. and C.R. Wronski. Reversible conductivity changes in discharge-produced amorphous Si. *Appl. Phys. Lett.*, 31(4), pp. 292–294, 1977.

[123] Sterling, H.F. and R.C.G. Swann. Chemical vapour deposition promoted by r.f. discharge. *Solid State Electronics*, 8, pp. 653–654, 1965.

[124] Stiebig, H., A. Kreisel, K. Winz, N. Schultz, C. Beneking, Th. Eickhoff, and H. Wagner. Spectral response modelling of a-Si:H Solar cells using accurate light absorption profiles. In *Proc. of the 1st WCPEC*, pp. 603–606, 1994.

[125] Street, R.A. Thermal generation currents in hydrogenated amorphous silicon *p-i-n* structures. *Appl. Phys. Lett.*, 57(13), pp. 1334–1336, 1990.

[126] Street, R.A. *Hydrogenated Amorphous Silicon.* Cambridge Solid State Science Series, ed. R.W. Cahn, E.A. Davis and I.M. Ward. Cambridge University Press, 1991.

[127] Stutzmann, M. The defect density in amorphous silicon. *Phil. Mag.* **B**, 60(4), pp. 531–546, 1989.

[128] Stutzmann, M. A comment on thermal defect creation in hydrogenated amorphous silicon. *Phil. Mag. Lett.*, 66(3), pp. 147–150, 1992.

[129] Suntharalingam, V. and H.M.Branz. On modeling trivalent dangling bonds with bivalent levels. In Schiff, E.A., M. Hack, A. Madan, M. Powell, and A. Matsuda, editors, *Amorphous Silicon Technology — 1994*, volume 336 of *Materials research society symposium proceedings*, pp. 153–158, 1994.

[130] Swartz, G.A. Computer model of amorphous silicon solar cell. *J. Appl. Phys.*, 53(1), pp. 712–719, 1982.

[131] Sze, S.M. *Physics of Semiconductor Devices, 2nd edition.* John Wiley & Sons, New York, 1981.

[132] Tabuchi, K., W.W. Wenas, M. Yoshino, A. Yamada, M. Konagai, and K. Takahashi. Optimization of ZnO films for amorhous silicon solar cells. In Guimarães, L., W. Palz, C. De Reyff, H. Kiess, and P. Helm, editors, *Proc. of the 11th EPVSEC*, pp. 529–532, Montreux, Switzerland, 1992.

[133] Tao, G. *Optical Modeling and Characterization of Hydrogenated Amorphous Silicon Solar Cells.* PhD thesis, Delft University of Technology, 1994.

[134] Tasaki, H., W.Y. Kim, M. Hallerdt, M. Konagai, and K. Takahashi. Computer simulation model of the effects of interface states on high-performance amorphous silicon solar cells. *J. Appl. Phys.*, 63(2), pp. 550–560, 1988.

[135] Tauc, J., R. Grigorovici, and A. Vancu. Optical properties and electronic structure of amorphous gemanium. *Phys. Stat. Sol.*, 15, pp. 627–637, 1966.

[136] Taylor, G.W. and J.G. Simmons. Basic equations for statistics, recombination processes, and photoconductivity in amorphous insulators and semiconductors. *J. of Non-Cryst. Solids*, 8–10, pp. 940–946, 1972.

[137] Technology Modeling Associates, Inc. *Medici, Two-dimensional Device Simulation Program, Version 2.0*, 1994.

[138] Terzini, E., G. Cavaliere, G. Conte, A. Mastrogiacomo, G. Nobile, and A. Rubino. Device quality materials for single/double junction a-Si:H solar cells. In Hill, R., W. Palz, and P. Helm, editors, *Proc. of the 12th EPVSEC*, pp. 1276–1279, Amsterdam, the Netherlands, 1994.

[139] Trijssenaar, M., G.E.N. Landweer, L.L.A. Vosteen, and J.W. Metselaar. Highly conductive micro-crystalline p- and n-type layers for amorphous silicon tandem solar cells. In Guimarães, L., W. Palz, C. De Reyff, H. Kiess, and P. Helm, editors, *Proc. of the 11th EPVSEC*, pp. 564–567, Montreux, Switzerland, 1992.

[140] Tsang, C. and R.A. Street. Recombination in plasma-deposited amorphous Si:H. Luminescence decay. *Phys. Rev.* **B**, 19(6), pp. 3027–3040, 1979.

[141] Vaillant, F. and D. Jousse. Recombination at dangling bonds and steady-state photoconductivity in a-Si:H. *Phys. Rev.* **B**, 34(6), pp. 4088–4098, 1986.

[142] van Berkel, C., M.J. Powell, A.R. Franklin, and I.D. French. Quality factor in *a*-Si:H *nip* and *pin* diodes. *J. Appl. Phys.*, 73(10), pp. 5264–5268, 1993.

[143] van den Heuvel, J. *Optical Properties and Transport Properties of Hydrogenated Amorphous Silicon.* PhD thesis, Delft University of Technology, 1989.

[144] van der Veer, J. and J. Dawson. Shell International Renewables — Bringing together the Group's activities in solar power, biomass and forestry. Web page: http://www.shell.com, 1997. Transcript of a Press conference in Londen, 6 October 1997.

[145] Wanka, H.N., E. Lotter, and M.B. Schubert. Characterization and optimization of the TCO/a-Si:H(,B) interface for solar cells by in-situ ellipsometry and SIMS/XPS depth profiling. In Schiff, E.A., M. Hack, A. Madan, M. Powell, and A. Matsuda, editors, *Amorphous Silicon Technology — 1994*, volume 336 of *Materials research society symposium proceedings*, pp. 657–662, 1994.

[146] Weiser, G. and H. Mell. Temperature dependence of the optical absorption edge in a-Si:H. *J. of Non-Cryst. Solids*, 114, page 298, 1988.

[147] Wentinck, H.M. *Carrier Injection in Amorphous Silicon Devices*. PhD thesis, Delft University of Technology, 1988.

[148] Willemen, J.A., M. Zeman, and J.W. Metselaar. Computer modeling of amorphous silicon tandem cells. In *Proc. of the 1st WCPEC*, pp. 599–602, 1994.

[149] Willemen, J.A., M. Zeman, and J.W. Metselaar. Sensitivity study of a-Si:H solar cell model parameters. In *Technical digest of the int. PVSEC-9*, pp. 359–360, 1996.

[150] Wronski, C.R., S. Lee, M. Hicks, and Satyendra Kumar. Internal photoemission of holes and the mobility gap of hydrogenated amorphous silicon. *Phys. Rev. Lett.*, 63(13), pp. 1420–1423, 1989.

[151] Yamanaka, S., M. Konagai, and K. Takahashi. Numerical study of amorphous silicon based solar cell performance toward 15% conversion efficiency. *Jap. J. Appl. Phys.*, 28(7), pp. 1178–1184, 1989.

[152] Yang, J., A. Bannerjee, and S. Guha. Triple-junction amorphous silicon alloy solar cell with 14.6% initial and 13.0% stable conversion efficiencies. *Appl. Phys. Lett.*, 70(22), pp. 2975–2977, 1997.

[153] Yang, J., R. Ross, R. Mohr, and J. Fournier. Physics of high efficiency multijunction solar cells. In Madan, A., M. Thompson, D. Adler, and Y. Hamakawa, editors, *Amorphous Silicon Semiconductors — Pure and Hydrogenated*, volume 95 of *Materials research society symposium proceedings*, pp. 517–525, 1987.

[154] Yang, L., L. Chen, S. Wiedeman, and A. Catalano. Microcrystalline silicon in a-Si:H based multijunction solar cells. In Fauchet, P.M., C.C. Tsai, L.T. Canham, I. Shimizu, and Y. Aoyagi, editors, *Microcrystalline Semiconductors: Materials Science & Devices*, volume 283 of *Materials research society symposium proceedings*, pp. 463–470, 1993.

[155] Yoshida, T., K. Maruyama, O. Nabeta, Y. Ichikawa, H. Sakai, and Y. Uchida. High efficiency a-Si:H two-stacked tandem solar cell. In *Proc. of the 19th IEEE PVSC*, pp. 1095–1100, 1987.

[156] Zeman, M., G. Tao, M. Trijssenaar, J.A. Willemen, J.W. Metselaar, and R.E.I. Schropp. Application of the defect pool model in modelling of a-Si:H solar cells. In Hack, M., E.A. Schiff, A. Madan, M. Powell, and

A. Matsuda, editors, *Amorphous Silicon Technology — 1995*, volume 377 of *Materials research society symposium proceedings*, pp. 639–644, 1995.

[157] Zeman, M., J.A. Willemen, S. Solntsev, and J.W. Metselaar. Amorphous silicon solar cell parameters extraction by inverse modelling. In *Technical digest of the int. PVSEC-7*, pp. 609–610, 1993.

[158] Zeman, M., J.A. Willemen, S. Solntsev, and J.W. Metselaar. Extraction of amorphous silicon solar cell parameters by inverse modelling. *Solar Energy Materials and Solar Cells*, 34, pp. 557–563, 1994.

Summary

A device simulator based on physical models is a powerful tool to study the fundamental operation of semiconductor devices. Especially for devices made of hydrogenated amorphous silicon (*a*-Si:H), which is a very complex material, physical device modelling can lead to better insight in the material and device properties. Furthermore, a complete and well-calibrated device simulator can be applied to optimise *a*-Si:H solar cell performance, which is the ultimate goal of the research discussed in this thesis.

The device simulator for *a*-Si:H solar cells, Amorphous Semiconductor Analysis (ASA), has been used and developed further. This simulator solves the semiconductor equations in combination with physical models for the material properties of amorphous silicon. The simulator and its physical models are described in detail.

To use a device simulator in a useful way one must understand the basic physics and the impact of the model parameters in full detail. Further, the model must be calibrated carefully to measured device characteristics. This thesis contributes to a better insight in solar cell operation and model calibration

From the results of a simple approximate model of an *a*-Si:H *pin* diode we conclude that the dark *IV*-characteristics are dominated by recombination and generation (R-G) processes in the depleted *i*-layer. The main parameters for the R-G processes are identified. Further, a set of analytic relations describing the dependence between important parameters is derived from a theoretical analysis of the semiconductor equations and the recombination models. Based on the found parameter dependences we conclude that it is impossible to obtain *independent* parameter values for, *e.g.* , the mobility gap, effective density of extended states and carrier mobilities, if *only* steady-state *IV*-data at one measurement temperature are available. We conclude that additional temperature- and time-dependent measurements are required for model calibration.

For simulations of *a*-Si:H-based devices it is generally assumed that the mobility edge is abrupt. This assumption has been critically examined. We conclude

that the exact energy dependence of the mobility near the mobility edge is not relevant for the device behaviour. Hence, the abrupt mobility edge assumption does not introduce errors in the simulations.

A comprehensive numerical study of parameter sensitivities has revealed the most-influential and the unimportant model parameters. Two calibration exercises have been carried out; we successfully used inverse modelling to fit three simulated *IV*-characteristics simultaneously on experimental data of an *a*-Si:H *pin* diode. Based on the large differences between the two fitted parameter sets we conclude that the used steady-state *IV*-data are not sufficient to calibrate the chosen parameters independently. Furthermore, we conclude from this study that it is impossible to examine which model (a Gaussian distribution or a distribution according to the defect-pool model) is best representing the defect density of states. Additional measurements are needed to calibrate the parameters, *e.g.* capacitance-voltage measurements, external quantum efficiency measurements and illumination-intensity-dependent *IV*-measurements.

A new model for the simulation of *a*-Si:H-based tandem solar cells has been introduced. This model uses the trap-assisted tunnelling model and a field-dependent mobility enhancement to describe the physics at the interface between the two subcells of a tandem cell, the tunnel-recombination junction. Using this model we analyse the degradation behaviour of tandem cells and conclude that these cells show less degradation than single junction cells, because the more stable top cell masks the stronger degradation of the less stable bottom cell. This masking effect is also the cause for the high fill factors of tandem cells.

IV-characteristics in the dark and with low-illumination intensities can be measured accurately after etching the part of the *n*-layer that surrounds the back contacts of an *a*-Si:H *pin* cell. The partial removal of the *n*-layer eliminates the lateral leakage current that hides the intrinsic behaviour of the diode. Since correlating with the conductivity of the *n*-doped layer, the lateral leakage current can be used to characterise the properties of this layer as a part of a complete *pin* structure.

We have extracted the mobility gap of intrinsic *a*-Si:H by using accurate temperature-dependent *IV*-measurements and simulations; a value of 1.70 to 1.75 eV is found, which is considerably lower than the commonly accepted value of 1.85 to 1.90 eV.

Finally, a study of the optical properties of different metal back contacts has shown that the reflectivity properties of silver are not degraded by thermal annealing at 150 °C. In contrast, the reflectivity of aluminium contacts and silver-aluminium bi-layer contacts decreases strongly due to solid state reactions, such as alloying and silicon crystallisation.

Joost Willemen

Samenvatting

Een simulatieprogramma dat is gebaseerd op fysische modellen, is een krachtig hulpmiddel voor het bestuderen van de fundamentele werkingsprincipes van halfgeleidercomponenten. Omdat gehydrogeneerd amorf silicium (*a*-Si:H) een uiterst complex materiaal is, geldt in het bijzonder voor dit materiaal dat fysisch modelleren tot een beter inzicht in de materiaaleigenschappen en eigenschappen van de componenten kan leiden. Verder kan een complete en goed gekalibreerde simulator worden toegepast voor het optimaliseren van *a*-Si:H zonnecellen, hetgeen het uiteindelijke doel is van het onderzoek dat in dit proefschrift is beschreven.

Het simulatieprogramma voor *a*-Si:H zonnecellen, Amorphous Semiconductor Analysis (ASA), is toegepast en verder ontwikkeld. Deze simulator lost de halfgeleidervergelijkingen op in combinatie met fysische modellen voor de materiaaleigenschappen van amorf silicium. Het programma en de modellen zijn in detail beschreven.

Om een simulatieprogramma op een zinnige wijze toe te passen, dient de gebruiker zeer goed bekend te zijn met de fysische principes en de invloed van de modelparameters. Verder is het noodzakelijk dat het model goed gekalibreerd is aan gemeten karakteristieken. Dit proefschrift draagt bij aan het vergroten van het inzicht in de werking van zonnecellen en de kalibratie van het zonnecelmodel.

De resultaten, verkregen met een eenvoudig, benaderend model dat alleen de recombinatie- en generatieprocesses (R-G) beschrijft, tonen aan dat de stroom-spannings (*IV*) karakteristieken van een *a*-Si:H *pin* diode zonder belichting bepaald worden door R-G-processen in de ruimteladingszone van de *i*-laag. De belangrijkste parameters die van invloed zijn op de R-G-processen, zijn geïdentificeerd. Verder is een aantal analytische relaties afgeleid die de afhankelijkheden tussen belangrijke modelparameters beschrijven. De afleiding is gebaseerd op een theoretische analyse van de halfgeleidervergelijkingen en de recombinatiemodellen. De relaties tonen aan dat het onmogelijk is om onafhankelijke parameterwaarden te bepalen voor, bijvoorbeeld, de mobiliteits-bandafstand, de effectieve dichtheid van vrije toestanden en de beweeglijkheden van de ladingsdragers,

als uitsluitend stationaire IV-meetgegevens bij één meettemperatuur beschikbaar zijn. Dit laat zien dat aanvullende temperatuur- en tijdafhankelijke metingen noodzakelijk zijn voor modelkalibratie.

In simulatoren voor a-Si:H halfgeleidercomponenten wordt aangenomen dat de mobiliteit als functie van energie een abrupte sprong vertoont. Een theoretische, analytische beschouwing van deze aanname laat zien dat de exacte energieafhankelijkheid van de mobiliteit niet relevant is voor het electrisch gedrag van een a-Si:H component, en dat derhalve de aangenomen abrupte sprong geen fouten in de simulaties veroorzaakt.

De modelparameters die de grootste invloed hebben op de simulaties van a-Si:H componenten zijn bepaald met een uitgebreide numerieke studie van de parametergevoeligheden. Twee kalibratie-oefeningen met 'inverse modellering' zijn beschreven; drie gesimuleerde IV-curven van een a-Si:H *pin* diode zijn tegelijkertijd gefit aan eperimentele meetgegevens. De grote verschillen tussen de twee verzamelingen 'gekalibreerde' parameters geven aan dat de gebruikte meetdata niet voldoende informatie bevatten om de gekozen parameters onafhankelijk van elkaar te kalibreren. Hieruit wordt tevens geconcludeerd dat het niet mogelijk is om uit deze studie te bepalen welk model de toestandsverdeling van de bengelende bindingen het meest-realistisch beschrijft (een Gaussische verdeling of een verdeling volgens het 'defect-pool' model). Aanvullende metingen zijn nodig om meer modelparameters te kunnen kalibreren, zoals bijvoorbeeld metingen van de capaciteit als functie van spanning, externe quantum-efficiëntie-metingen of lichtintensiteit-afhankelijke IV-metingen.

Een nieuw simulatiemodel voor a-Si:H tandem-zonnecellen is ontwikkeld. Dit model beschrijft de fysica van de tunnel-recombinatie-grenslaag tussen de twee enkelvoudige cellen in een tandem-zonnecel door middel van het "trap-assisted tunneling"-model en een veldafhankelijke toename van de ladingsdragermobiliteiten. Het model wordt toegepast om de degradatie-eigenschappen van tandem-zonnecellen te bestuderen. Dit onderzoek laat zien dat dit tandem-zonnecellen minder degraderen dan enkelvoudige cellen, omdat de stabielere voorste cel de sterkere degradatie van de minder stabiele achterste cel maskeert. Dit maskeringseffect is ook de oorzaak van de betere vulfactoren van tandem-zonnecellen.

De IV-karakteristieken zonder belichting en met lage belichtingsintensiteiten kunnen nauwkeurig gemeten worden indien de n-laag in het gebied rondom de achtercontacten is weggeëtst. Het gedeeltelijk verwijderen van de n-laag heft de laterale lekstroom op die het intrinsieke gedrag van de diode maskeert. Doordat deze lekstroom correleert met de weerstand van de n-gedoteerde laag, kan meting van deze stroom informatie verschaffen over de eigenschappen van de n-laag

zoals deze in een *pin*-structuur aanwezig is.

Aangetoond is dat met nauwkeurige, temperatuur-afhankelijke *IV*-metingen en simulaties de mobiliteits-bandafstand van intrinsiek *a*-Si:H bepaald kan worden. Toepassing van deze methode heeft voor deze materiaal parameter een waarde tussen 1.70 en 1.75 eV opgeleverd, hetgeen aanzienlijk lager is dan de algemeen aanvaarde waarde tussen 1.85 en 1.90 eV.

Tot slot laat een onderzoek naar de optische eigenschappen van verschillende metalen achtercontacten zien dat de reflectie-eigenschappen van zilver niet degraderen na blootstelling aan een uitstookbehandeling bij 150 °C. In tegenstelling tot het gedrag van zilver, neemt de reflectiviteit van aluminium contacten en tweelaags, zilver-aluminium contacten sterk af door vaste-stof reacties, zoals legering en kristallisatie van het silicium.

Joost Willemen

Acknowledgements

Having arrived at the last page of my thesis I wish to look back on the past five years that I spent at the Laboratory of Electrical Components, Technology and Materials (ECTM) and the Delft Institute of Microelectronics and Submicron-technology (DIMES) working towards my PhD. During this time numerous people supported me and contributed to this thesis. I sincerely wish to thank all who contributed to the completion of this work. In particular I like to thank:

- Prof. M. Kleefstra for offering me the opportunity to start my PhD research, and for critically and patiently reading one draft version of this thesis after the other.

- Prof. Jan Slotboom for his critical attitude, the fruitful discussions, and his constant encouragement to put more emphasis on the experimental part of this work.

- Prof. Kees Beenakker for support of any kind and maintaining the good working atmosphere in DIMES.

- Wim Metselaar for providing the right research environment and giving me the opportunity to do this research.

- Miro Zeman for his daily supervision, discussions, assistance and carefully reading the manuscript.

- Bert Huizing and Raymond Hueting for all the good years, discussing numerous topics, and sharing the same office and thesis frustrations. Special thanks to Ray for his continuous concern for my coffee supply after leaving DIMES.

- Barry van Dijk and Martin Kroon, who had to undergo numerous lectures about topics covered in this thesis. Special thanks to Martin for etching of the solar cells, and special thanks to Barry for the steady coffee supply.

- René van Swaaij and Egbert Schroten who proved to be very pleasant and good discussion partners, although we started working together rather recently. I am much indebted to René who meticulously read my thesis and suggested many many many improvements. Thanks!

- Amir Vosteen for the discussions, providing data, and the assistance with various measurements setups.

- Jan Chris Staalenburg for his 'interrupt-based' assistance for measurement and computer problems. I have learned a lot from his large knowledge of measurements and electronics.

- Ben Girwar, Jan van Staden and Bram v.d. Male for making samples and technical assistance.

- Jeanne-Marie Sirks and Marian Roozenburg for the secretarial support and the pleasant atmosphere at DIMES.

- All other students and colleagues of ECTM and DIMES for the friendly working atmosphere.

- The colleagues of Utrecht University, in particular Ruud Schropp for providing experimental data, samples and suggestions, and Frank Achten for our lengthy discussions on spectral-response measurement setups (unfortunately, spectral response measurements have not become a significant part of this thesis).

- All participants of the NOZ-PV meetings and the Euregional workshops.

- Mirjam Nieman, for correcting the English of the largest part of this thesis and greatly increasing its readability.

- My 'new' colleagues at Robert Bosch GmbH for their flexible attitude and giving me the time to complete this thesis in parallel to my new job.

- Ad, Marie-José, Katelijne, Atalja, Simon and Katrien for their support and encouragement.

- My friends for their moral support and understanding.

- Kirstin for her eternal support, understanding and taking care of the household and our children alone, during the last year or so.

- Felien and Jiri for just being there and showing me the joy of life.

Biography

Joost A. Willemen was born in Schijndel, the Netherlands, on 26 December 1967. He obtained the Gymnasium β degree at the Mill Hill College in Goirle, and started his studies at the Faculty of Electrical Engineering at the Delft University of Technology in 1986. During his studies he did a student's research project on Junction CCDs as X-ray imaging devices, and worked as a trainee at Philips Semiconductors in Nijmegen, the Netherlands. The topic of his master's research work, carried out at the Laboratory of Electrical Materials (presently named the Laboratory of Electronic Components, Technology and Materials) was the modelling of bandgap narrowing in heavily doped, compensated silicon. In 1993 he obtained his master's degree and subsequently started working as a research assistant at the Delft Institute of Microelectronics and Submicrontechnology (DIMES) of the Delft University of Technology. Until mid 1998, he carried out research on the modelling of amorphous silicon solar cells and assisted at several lectures on semiconductor and device physics. Recently, he joined Robert Bosch GmbH in Reutlingen, Germany, to work on the development of ASICs and micromachined sensors for automotive applications.